



2012

# NANOCRYSTALS OF CHEMOTHERAPEUTIC AGENTS FOR CANCER THERANOSTICS: DEVELOPMENT AND IN VITRO AND IN VIVO EVALUATION

Christin P. Hollis

University of Kentucky, [christin.hollis@gmail.com](mailto:christin.hollis@gmail.com)

**[Click here to let us know how access to this document benefits you.](#)**

---

## Recommended Citation

Hollis, Christin P., "NANOCRYSTALS OF CHEMOTHERAPEUTIC AGENTS FOR CANCER THERANOSTICS: DEVELOPMENT AND IN VITRO AND IN VIVO EVALUATION" (2012). *Theses and Dissertations--Pharmacy*. 17.  
[https://uknowledge.uky.edu/pharmacy\\_etds/17](https://uknowledge.uky.edu/pharmacy_etds/17)

This Doctoral Dissertation is brought to you for free and open access by the College of Pharmacy at UKnowledge. It has been accepted for inclusion in Theses and Dissertations--Pharmacy by an authorized administrator of UKnowledge. For more information, please contact [UKnowledge@lsv.uky.edu](mailto:UKnowledge@lsv.uky.edu).

**STUDENT AGREEMENT:**

I represent that my thesis or dissertation and abstract are my original work. Proper attribution has been given to all outside sources. I understand that I am solely responsible for obtaining any needed copyright permissions. I have obtained and attached hereto needed written permission statements(s) from the owner(s) of each third-party copyrighted matter to be included in my work, allowing electronic distribution (if such use is not permitted by the fair use doctrine).

I hereby grant to The University of Kentucky and its agents the non-exclusive license to archive and make accessible my work in whole or in part in all forms of media, now or hereafter known. I agree that the document mentioned above may be made available immediately for worldwide access unless a preapproved embargo applies.

I retain all other ownership rights to the copyright of my work. I also retain the right to use in future works (such as articles or books) all or part of my work. I understand that I am free to register the copyright to my work.

**REVIEW, APPROVAL AND ACCEPTANCE**

The document mentioned above has been reviewed and accepted by the student's advisor, on behalf of the advisory committee, and by the Director of Graduate Studies (DGS), on behalf of the program; we verify that this is the final, approved version of the student's dissertation including all changes required by the advisory committee. The undersigned agree to abide by the statements above.

Christin P. Hollis, Student

Dr. Tonglei Li, Major Professor

Dr. Jim Pauly, Director of Graduate Studies

---

NANOCRYSTALS OF CHEMOTHERAPEUTIC AGENTS FOR CANCER  
THERANOSTICS: DEVELOPMENT AND *IN VITRO* AND *IN VIVO* EVALUATION

---

DISSERTATION

---

A dissertation submitted in partial fulfillment of the requirements for the degree of  
Doctor of Philosophy in the College of Pharmacy at the University of Kentucky

By

Christin Pramudiati Hollis

Lexington, Kentucky

Director: Dr. Tonglei Li, Professor and Allen Chao Chair in Industrial and Physical  
Pharmacy, Purdue University

and Co-Director: Dr. Paul M. Bummer, Associate Professor of Pharmaceutical Sciences,  
University of Kentucky

Lexington, Kentucky

2012

Copyright © Christin Pramudiati Hollis 2012

## ABSTRACT OF DISSERTATION

### NANOCRYSTALS OF CHEMOTHERAPEUTIC AGENTS FOR CANCER THERANOSTICS: DEVELOPMENT AND *IN VITRO* AND *IN VIVO* EVALUATION

The majority of pharmacologically active chemotherapeutics are poorly water soluble. Solubilization enhancement by the utilization of organic solvents often leads to adverse side effects. Nanoparticle-based cancer therapy, which is passively targeted to the tumor tissue via the enhanced permeation and retention effect, has been vastly developed in recent years. Nanocrystals, which exist as crystalline and carry nearly 100% drug loading, has been explored for delivering antineoplastic agents. Additionally, the hybrid nanocrystal concept offers a novel and simple way to integrate imaging agents into the drug crystals, enabling the achievement of theranostics. The overall objective of this dissertation is to formulate both pure and hybrid nanocrystals, evaluate their performance *in vitro* and *in vivo*, and investigate the extent of tissue distribution and tumor accumulation in a murine model. Pure and hybrid nanocrystals of several model drugs, including paclitaxel (PTX), camptothecin, and ZSTK474, were precipitated by the anti-solvent method in the absence of stabilizer, and their size was further minimized by homogenization. The nanocrystals of PTX, which is the focus of the study, had particle size of approximately 200 nm and close-to-neutral surface charge. Depending on the cell type, PTX nanocrystals exerted different level of cytotoxicity. In human colon and breast cancer xenograft models, nanocrystals yielded similar efficacy as the conventional formulation, Taxol, at a dose of 20 mg/kg, yet induced a reduced toxicity. Biodistribution study revealed that <sup>3</sup>H-PTX nanocrystals were sequestered rapidly by the macrophages upon intravenous injection. Yet, apparent toxicity was not observed even after four weekly injections. The sequestered nanocrystals were postulated to be released slowly into the blood circulation and reached the tumor. Tritium-labeled-taxol, in contrast, was distributed extensively to all the major organs, inducing systemic toxicity as observed in significant body weight loss. The biodistribution results obtained from radioactive analysis and whole-body optical imaging was compared. To some degree, the correlation

was present, but divergence in the quantitative result, due to nanocrystal integrity and limitations associated with the optical modality, existed. Despite their promising properties, nanocrystal suspensions must be securely stabilized by stealth polymers in order to minimize opsonization, extend blood-circulation time, and efficiently target the tumor.

KEYWORDS: nanocrystals, theranostics, poorly water soluble, drug delivery, fluorescence

Multimedia Elements Used: TIF (.tif)

Christin P. Hollis

---

Author's signature

November 19, 2012

---

Date

NANOCRYSTALS OF CHEMOTHERAPEUTIC AGENTS FOR CANCER  
THERANOSTICS: DEVELOPMENT AND *IN VITRO* AND *IN VIVO* EVALUATION

By

Christin Pramudiati Hollis

Tonglei Li, Ph.D.

---

Co-Director of Dissertation

Paul M. Bummer, Ph.D.

---

Co-Director of Dissertation

Jim Pauly, Ph.D.

---

Director of Graduate Studies

November 19, 2012

---

Date

*To my beloved parents, husband, and son*

## ACKNOWLEDGEMENTS

I would like to express my sincere gratitude to those who have helped and supported me throughout the course of my graduate work. This dissertation would not have been possible without you.

First, I would like to thank my committee. Each of you has uniquely contributed invaluable guidance and support throughout my graduate study. To my advisor, Dr. Tonglei Li, thank you for challenging me to be a better scientist and step out of my scientific comfort zone, as well as continually encouraging me to expand my knowledge in multiple disciplines. I am grateful for your continuous support and patience throughout my graduate study. To Dr. Paul Bummer, thank you for serving as my co-advisor and generously sharing your laboratory space in the past few months. Your guidance and support to this dissertation work is truly appreciated. To Dr. Brad Anderson, thank you for continually challenging my thought process and inspiring me to be a better scientist. Your advice and support have been very invaluable resources. To Dr. Barbara Knutson, thank you for being my IGERT co-advisor and contributing valuable advice from a different perspective. I would also like to give a special thanks to Dr. Liya Gu for agreeing to serve as my outside examiner.

Beyond my committee, I would like to thank other faculties at the University of Kentucky that have given support and contribution to the advancement of this dissertation. To Dr. B. Mark Evers, thank you for serving as my CNTC co-advisor in the past two years. Our collaborations have expanded my knowledge in cancer research and experience in working with others from different disciplines. To Dr. Piotr Rychahou,

thank you for training and guidance in conducting animal studies. To Dr. Robert Yokel, thank you for teaching and guiding me how to work with radioactive materials. My last part of dissertation work would have not been possible without your contributions and support. To Drs. Younsoo Bae, Heidi Mansour, and Eric Munson, thank you for allowing me to utilize the instruments in your laboratory. To Dr. Heidi Weiss, thank you for assisting me in the statistical analysis and interpretation of the experimental data.

I would also like to thank all the members of Dr. Tonglei Li's lab. Especially to Drs. Alessandra Mattei and Clare Aubrey-Medendorp, thank you for your friendship, support, and help. To Dr. Hua Zhang, I am very fortunate to work with you in the early process of the nanocrystal development and grateful for all your advice and training. To Dr. Rongsheng Zhao, thank you for training me how to design and conduct animal studies. Your contribution in the early part of this project is very invaluable. Dr. Lili Sun, thank you for the training on conducting cell culture studies.

On personal note, I would like to thank my family and friends for their love and support. To my mom and dad, thank you for your unconditional love and sacrifice. I would never have made it thus far if it were not for you. You both have been my inspirations and role models. To my husband, Jason, thank you for continually believing in me. To my precious son, Malachi, you have brought joyfulness that has sustained me through challenging moments. Above all, I acknowledge my Creator, who has given me wisdom, strength, and guidance that have enabled me to work towards the goal of improving the health and wellness of human beings.

## TABLE OF CONTENTS

ACKNOWLEDGEMENT .....	iii
TABLE OF CONTENTS.....	v
LIST OF TABLES .....	x
LIST OF FIGURES .....	xii
LIST OF ABBREVIATIONS.....	xvi
Chapter 1 - Introduction.....	1
1.1. Current Cancer Therapy and Nanomedicine .....	1
1.2. Theranostics .....	4
1.2.1 Definition and Purpose .....	4
1.2.2 Imaging Modalities and Probes .....	5
1.2.2.1 Optical Imaging.....	5
1.2.2.2 Magnetic Resonance Imaging (MRI) .....	8
1.2.2.3 Radionuclide-based Imaging.....	9
1.2.2.4 Computed Tomography (CT).....	9
1.2.2.5 Ultrasound .....	10
1.2.3 Building Theranostic System.....	11
1.2.3.1 Vesicles.....	11
1.2.3.2 Polymeric Nanoparticles.....	12
1.2.3.3 Micelles .....	13
1.2.3.4 Core-shell Nanoparticles .....	14
1.2.3.5 Dendrimers .....	16
1.2.3.6 Carbon Nanotubes .....	17
1.2.4 General Considerations for Translation.....	18
1.3. Nanocrystals.....	19
1.3.1 Introduction.....	19
1.3.2 Various Approaches to Produce Nanocrystals.....	20
1.3.2.1 Top-down Approach.....	20
1.3.2.2 Bottom-up Approaches.....	22
1.3.2.3 Combination Approach.....	28
1.3.3 Particle Stabilization .....	29
1.3.4 Physical Characterization of Nanocrystals .....	31

1.3.4.1	Particle Size .....	31
1.3.4.2	Surface Charge .....	33
1.3.4.3	Crystallinity .....	34
1.3.4.4	Dissolution.....	35
1.3.5	Nanocrystals for Cancer Therapy .....	37
1.3.5.1	<i>In Vitro</i> Evaluation of Nanocrystals .....	41
1.3.5.2	<i>In Vivo</i> Evaluation of Nanocrystals.....	42
1.3.5.3	Clinical Study of Nanocrystal Formulation.....	45
1.4.	Hybrid Nanocrystals for Theranostics.....	45
1.5.	Statement of Problems .....	48
1.6.	Objectives.....	51
Chapter 2 - Preparation and Physicochemical Characterization of Paclitaxel Nanocrystals		55
.....		55
2.1	Introduction .....	55
2.2	Materials and Methods .....	57
2.2.1	Materials .....	57
2.2.2	Preparation of Paclitaxel Nanocrystals .....	58
2.2.3	Particle Size and Surface Charge Measurements of Paclitaxel Nanocrystals	59
2.2.4	Solid-state Characterization of Paclitaxel Nanocrystals.....	60
2.2.5	HPLC Analysis .....	60
2.2.6	Solubility of Paclitaxel Nanocrystals in PBS.....	61
2.2.7	Particle Size Analysis of Paclitaxel Nanocrystals in Different Media .....	61
2.2.8	Storage Stability of Paclitaxel Nanocrystals.....	62
2.3	Results and Discussion.....	62
2.3.1	Particle Size and Surface Charge Measurements of Paclitaxel Nanocrystals	62
2.3.2	Solid-state Characterization of Paclitaxel Nanocrystals.....	66
2.3.3	Solubility of Paclitaxel Nanocrystals in PBS.....	68
2.3.4	Particle Size Analysis of Paclitaxel Nanocrystals in Different Media .....	70
2.3.5	Storage Stability of Aqueous Suspension of Paclitaxel Nanocrystals .....	78
2.3.6	Storage Stability of Freeze Dried Paclitaxel Nanocrystals .....	84
2.4	Conclusion.....	86
Chapter 3 - Cellular Toxicity and Uptake of Paclitaxel Nanocrystals.....		87
3.1	Introduction .....	87

3.2	Materials and Methods .....	90
3.2.1	Materials .....	90
3.2.2	Preparation of Pure and Hybrid Paclitaxel Nanocrystals.....	91
3.2.3	Cytotoxicity Study of Paclitaxel Nanocrystals in HT-29 Cells .....	92
3.2.4	Characterization of Paclitaxel Hybrid Nanocrystals.....	95
3.2.5	Analysis of the Fluorophore Entrapment.....	95
3.2.6	Cellular Uptake Study of Paclitaxel Hybrid Nanocrystals in MCF-7 Cells	96
3.3	Results and Discussion.....	98
3.3.1	Cytotoxicity Study of Paclitaxel Nanocrystals in HT-29 Cells .....	98
3.3.2	Particle Size Measurement.....	100
3.3.3	Analysis of the FPR-648 Fluorophore Entrapment .....	100
3.3.4	Cellular Uptake Study of Paclitaxel Nanocrystals in MCF-7 Cells.....	101
3.4	Conclusion.....	107
Chapter 4 - <i>In Vivo</i> Studies of Paclitaxel Pure and Hybrid Nanocrystals.....		108
4.1	Survival Study in HT-29 Xenograft Model .....	108
4.1.1	Introduction.....	108
4.1.2	Materials and Methods.....	109
4.1.2.1	Materials .....	109
4.1.2.2	Preparation of Pure PTX Nanocrystals and Taxol.....	110
4.1.2.3	Characterization and Analysis of PTX Nanocrystals .....	110
4.1.2.4	Cell Culture of HT-29.....	110
4.1.2.5	Animal Study.....	111
4.1.2.6	Statistical Analysis .....	112
4.1.3	Results and Discussion .....	113
4.1.3.1	Characterization of PTX Nanocrystals .....	113
4.1.3.2	Animal Study.....	115
4.1.4	Conclusion .....	120
4.2	Evaluation of PTX/MMPSense/FPR-648 Nanocrystals in MCF-7 Xenograft	121
4.2.1	Introduction.....	121
4.2.2	Materials and Methods.....	123
4.2.2.1	Materials .....	123
4.2.2.2	Preparation of Pure and PTX/MMPSense/FPR-648 Hybrid Nanocrystals.....	124
4.2.2.3	Physical Characterization and Chemical Analysis of Nanocrystal Systems .....	124

4.2.2.4	Cell Culture of MCF-7 .....	125
4.2.2.5	Animal Study.....	126
4.2.2.6	IVIS <sup>®</sup> Imaging .....	127
4.2.2.7	Statistical Analysis .....	128
4.2.3	Results and Discussion .....	128
4.2.3.1	Characterization and Analysis of PTX Pure and PTX/MMPSense/FPR-648 Hybrid Nanocrystals .....	128
4.2.3.2	Animal Study.....	134
4.2.4	Conclusion .....	142
4.3	Evaluation of PTX/Nicardipine Nanocrystals in MCF-7 Xenograft.....	144
4.3.1	Introduction.....	144
4.3.2	Materials and Methods.....	146
4.3.2.1	Materials .....	146
4.3.2.2	Preparation of Pure and PTX/Nicardipine Hybrid Nanocrystals.....	147
4.3.2.3	Characterization of Nanocrystal Systems.....	148
4.3.2.4	Chemical Analysis.....	148
4.3.2.5	Cell Culture.....	148
4.3.2.6	Animal Study.....	149
4.3.3	Result and Discussion.....	150
4.3.3.1	Characterization and Analysis of Nanocrystals.....	150
4.3.3.2	Animal Studies .....	151
4.3.4	Conclusion .....	154
Chapter 5	- Tumor Accumulation and Tissue Distribution of <sup>3</sup> H-Taxol versus <sup>3</sup> H-Paclitaxel/FPI-749 Hybrid Nanocrystals .....	155
5.1	Introduction .....	155
5.2	Materials and Methods.....	160
5.2.1	Materials .....	160
5.2.2	Preparation and Analysis of <sup>3</sup> H-Taxol and <sup>3</sup> H-PTX/FPI-749 Nanocrystals 160	
5.2.3	Cell Culture.....	162
5.2.4	Animal Study .....	162
5.2.5	Tritium Analysis in Blood and Tissue .....	163
5.2.6	IVIS <sup>®</sup> Imaging .....	164
5.2.7	Statistical Analysis.....	164
5.3	Results and Discussion.....	165

5.3.1	Characterization of Hybrid PTX /FPI-749 Nanocrystals.....	165
5.3.2	Tissue Distribution by Tritium Analysis.....	166
5.3.3	Tumor Accumulation .....	172
5.3.4	IVIS <sup>®</sup> Imaging for Non-Invasive Tissue Distribution .....	175
5.3.5	<i>Ex vivo</i> IVIS <sup>®</sup> Imaging.....	179
5.4	Conclusion.....	182
Chapter 6 - Conclusion and Future Outlook.....		185
APPENDICES .....		188
A.1	Hybrid Camptothecin/Gold Nanocrystals .....	188
A.1.1	Introduction.....	188
A.1.2	Materials and Method .....	191
A.1.2.1	Materials .....	191
A.1.2.2	Preparation of Hybrid Camptothecin Nanocrystals.....	191
A.1.2.3	Chemical Analysis of Hybrid Camptothecin Nanocrystals.....	193
A.1.2.4	Electron Microscopy Imaging and Energy Dispersive X-ray Spectroscopy (EDS).....	194
A.1.3	Result and Discussion .....	195
A.1.4	Conclusion .....	200
A.2	Nanocrystals of ZSTK474.....	201
A.2.1	Introduction.....	201
A.2.2	Materials and Method .....	203
A.2.2.1	Materials .....	203
A.2.2.2	Preparation of ZSTK474 Nanocrystals.....	204
A.2.2.3	Physical Characterization and Chemical Analysis of ZSTK474 Nanocrystals.....	205
A.2.3	Result and Discussion.....	206
A.2.3.1	Characterization and Analysis of ZSTK474 Nanocrystals.....	206
A.2.3.2	Stability of ZSTK474 Nanocrystals in Different Media .....	208
A.2.4	Conclusion .....	210
REFERENCES .....		211
VITA.....		260

## LIST OF TABLES

Table 1.1.	The predicted time to achieve complete dissolution of spherical particles under sink condition based on the Hixson-Crowell cube root law equation. . . . .	36
Table 1.2	Nanocrystal formulations of anticancer drugs. . . . .	40
Table 2.1.	SEM images of PTX nanocrystals incubated in 37°C saline and cell culture media (DMEM + 10% fetal bovine serum (FBS)) at concentration of 0.1 mg/ml. Two images were presented for each time point. Scale bars represent 500 nm. . . . .	69
Table 2.2.	Particle size analysis of SEM images presented in Table 2.1 by SigmaScan. Data represents mean ± S.D. . . . .	72
Table 2.3.	SEM images of PTX nanocrystals incubated in nude mouse whole blood/ buffered sodium citrate (9:1 v/v, 0.109 M, 3.2%, to prevent coagulation) at a concentration of 0.1 mg/ml. At each pre-determined incubation time, two SEM images were presented. Scale bars represent 1 µm . . . . .	73
Table 2.4.	SEM images of PTX nanocrystals suspension in water (at concentration of 1 mg/ml) stored at 4°C and room temperature. Two images were presented for each time point. Scale bars represent 1 µm . . . . .	80
Table 2.5.	Summary of the key parameters of PTX nanocrystals during storage at 4°C. Data represents mean ± S.D. . . . .	82
Table 2.6.	Summary of the key parameters of PTX nanocrystals during storage at room temperature. Data represents mean ± S.D. . . . .	83
Table 2.7.	SEM images of freeze-dried PTX nanocrystals re-suspended in DI water at various time points. Scale bars: 1 µm. . . . .	85
Table 2.8.	Particle size analysis of SEM images presented in Table 2.7 by SigmaScan Data represents mean ± S.D. . . . .	86
Table 3.1.	The 96-well setup for the cellular toxicity study of PTX nanocrystals and dissolved PTX in HT-29 cells. . . . .	93
Table 3.2.	The IC <sub>50</sub> values of PTX nanocrystals and dissolved PTX in HT-29 cells at different incubation times. . . . .	99
Table 4.1.	SEM images of PTX nanocrystals utilized for four weekly treatments during the survival study. Scale bars represent 1 µm. . . . .	114
Table 4.2.	The physical characterizations (mean ± S.D.) of PTX nanocrystals used during the survival study. . . . .	115

Table 4.3.	The details of injections for evaluating MMPSense performance <i>in vivo</i> .....	127
Table 4.4.	SEM images of PTX and PTX/MMPSense/FPR-648 nanocrystals. Scale bars represent 1 $\mu\text{m}$ . .....	130
Table 4.5.	Physical properties of PTX pure and hybrid nanocrystals (mean $\pm$ S.D.).....	130
Table 4.6.	SEM images of PTX and PTX/Nicardipine nanocrystals. Scale bars represent 1 $\mu\text{m}$ . .....	151
Table A.2.1.	SEM images of ZSTK474 nanocrystals suspended in saline (at room temperature) and cell culture media (McCoy's 5A + 10% fetal bovine serum + 1% penicillin streptomycin) at 37°C. Scale bars represent 2 $\mu\text{m}$ .....	208
Table A.2.2.	The stability study of ZSTK474 nanocrystals in different media. The particle size of the nanocrystals were analyzed from the SEM images by SigmaScan. Data represents means $\pm$ S.D.....	210

## LIST OF FIGURES

Figure 1.1.	Free energy diagram for nucleation. (Adapted from Mullin [1]).	23
Figure 1.2.	Predicted time for complete dissolution of spherical particles composed of poorly water soluble compounds in sink condition based on Hixson-Crowell cube root law equation	37
Figure 1.3.	The illustration (left) and examples (right) of hybrid crystals. Rhodamine B (red) and fluorescein (green) were embedded in acetaminophen (top) and aspirin (bottom) crystals, respectively	47
Figure 2.1	Chemical structure of Paclitaxel (PTX).	57
Figure 2.2.	Schematic of nanocrystal preparation method by combination approach.	59
Figure 2.3.	SEM image showing typical morphology and size of PTX nanocrystals produced with combination approach.	63
Figure 2.4.	Particle size measurements of PTX nanocrystals suspended in DI water at 0.1 mg/mL by Nano-ZS. The three lines represent the triplicate measurements.	63
Figure 2.5.	Zeta potential measurements of PTX nanocrystals suspended in 10 mM NaCl at 0.1 mg/mL by Nano ZS. The three lines represent the triplicate measurements.	64
Figure 2.6.	Powder X-ray diffractograms of PTX nanocrystals, dihydrate, and anhydrous	67
Figure 2.7.	Modulated DSC thermograms of PTX nanocrystals and dihydrate.	67
Figure 2.8.	TGA analysis of PTX nanocrystals.	68
Figure 2.9.	Solubility profiles of PTX anhydrous, dihydrate and nanocrystals in PBS at 37°C.	69
Figure 2.10.	Particle size analysis of PTX nanocrystals incubated in different media at 37°C by DLS.	74
Figure 2.11.	SEM image of fresh freeze-dried PTX nanocrystals re-suspended in DI water. Scale bar represents 1 $\mu\text{m}$ .	84
Figure 3.1.	The cytotoxicity curve of PTX nanocrystals and dissolved PTX in human colon cancer HT-29 by SRB assay.	99
Figure 3.2.	SEM image of PTX/FPR-648 hybrid nanocrystals for cellular uptake in breast cancer MCF-7. Scale bar represents 1 $\mu\text{m}$ .	100

Figure 3.3. The standard curve of FPR-648 in DMSO measured at $\lambda_{\text{ex}}$ : 650 nm and $\lambda_{\text{em}}$ : 670 nm. ....	101
Figure 3.4. Compilation of confocal microscopy images of MCF-7 cells incubated with PTX/FPR-648 hybrid nanocrystals (cyan) for 0.5, 1, and 2 hours. The cell nucleus and lysosome were stained with DAPI (blue) and LysoTracker Red, respectively. Scale bars in the top panel indicate 2 $\mu\text{m}$ while those in middle and bottom panels indicate 5 $\mu\text{m}$ . The purple, yellow, and white arrows might suggest the formation of membrane ruffles, macropinocytosis, and clathrin-mediated endocytosis, respectively.....	103
Figure 3.5. The confocal images of MCF-7 cells incubated with free FPR-648 dye at concentration of 0.1 $\mu\text{g}/\text{ml}$ for 2 hours.....	106
Figure 4.1. The tumor volume chart from the three different groups: control (saline), 20 mg/kg Taxol, 20 mg/kg PTX nanocrystals up to day 23 after inoculation (prior to euthanization, n=12 for all the groups).....	118
Figure 4.2. The percent of animal survival versus time. Animals were administered either with saline, 20 mg/kg Taxol or PTX nanocrystals at day 10, 16, 24, and 31 after inoculation (n=12 on day 0).....	118
Figure 4.3. Percent body weight change of animals in three treatment groups up to day 23 after inoculation (prior to euthanization, n=12 for all the groups).....	120
Figure 4.4. IVIS <sup>®</sup> images of wells that were filled with standard solutions prepared in DMSO and imaged either with $\lambda_{\text{ex}}$ : 640 nm and $\lambda_{\text{em}}$ : 700 nm or $\lambda_{\text{ex}}$ : 745 nm and $\lambda_{\text{em}}$ : 800. Only the bottom part, FPR-648 solutions, fluoresced at the former excitation/emission window, while the top part, MMPSense 750 solutions, fluoresced at the latter.....	131
Figure 4.5. The standard curve of MMPSense 750 obtained from IVIS <sup>®</sup> Spectrum. ....	133
Figure 4.6. The standard curve of FPR-648 obtained from IVIS <sup>®</sup> Spectrum.....	133
Figure 4.7. IVIS <sup>®</sup> images of non-xenograft mice (n=5) injected with 0.1 nmol MMPSense 750. ....	134
Figure 4.8. IVIS images of mice from different treatment groups at day 2 after injection. MMPSense solution (0.1 nmol) was given to the first three groups with or without the treatment, while approximately 0.2 nmol of MMPSense were entrapped in the injected hybrid nanocrystals given to the last group. The color intensity scale was doubled ( $4 \times 10^{-6}$ to $2 \times 10^{-5}$ ) of the last group in order to match the half amount of the dyes used in the first three groups ( $2 \times 10^{-6}$ to $1 \times 10^{-5}$ ).....	135

Figure 4.9. (A) IVIS images of mice from untreated, Taxol, PTX pure, and PTX hybrid nanocrystal groups from day 0 to day 5. Day 0 images were taken 2 hours post-injection. The color scale from the PTX hybrid nanocrystal group (left) was doubled compared to the other groups (as in Figure 3). (B) The average IVIS efficiency (i.e., IVIS efficiency (cm <sup>2</sup> ) divided by the area of each mouse (cm <sup>2</sup> )) was plotted against the time. The data points indicate mean ± S.D. n=6 for the xenografted mice (Figure 4.8) and n=5 for no-xenograft group (Figure 4.7).....	137
Figure 4.10. IVIS <sup>®</sup> images of mice in the hybrid nanocrystal group viewed at $\lambda_{\text{ex}}$ : 640 nm and $\lambda_{\text{em}}$ : 700 nm signifying the fluorescence signal detected from the near-infrared dye, FPR-648, incorporated in the hybrid nanocrystals. The excised tumors and major organs (liver, spleen, kidneys, lung, and heart) were imaged on day 7 with the same imaging parameter.....	140
Figure 4.11. Percent change in tumor volume measured daily after single injection of treatments on day 0. Each point indicates the mean ± S.D. (n=6). *P<0.01 compared to the untreated group on day 7. All treatments induced tumor suppression (P<0.05) on days 3, 4, 5, and 6.....	141
Figure 4.12. Percent change in body weight measured daily. Each point indicates the mean ± S.D. (n= 6). # P < 0.05 compared to the untreated group on days 2, 3, 4, and 6.....	142
Figure 4.13. The chemical structure of nicardipine.....	146
Figure 4.14. The percent of tumor volume change of animals administered with Taxol, PTX nanocrystals, and PTX/Nicardipine nanocrystals (n=6).....	153
Figure 4.15. The percent of body weight change of animals administered with Taxol, PTX nanocrystals, and PTX/Nicardipine nanocrystals (n=6).....	153
Figure 5.1. SEM image of PTX hybrid nanocrystals without any radioactive payload. Scale bar represents 1 $\mu\text{m}$ .....	165
Figure 5.2. The distribution (% injected dose/gram of blood or tissue) of 20 mg/kg <sup>3</sup> H-Taxol. The term “asap” refers to 5 minutes post-injection time.....	167
Figure 5.3. The distribution (% injected dose/gram of blood or tissue) of 20 mg/kg <sup>3</sup> H-PTX/FPI-749 nanocrystals. The term “asap” refers to 11 minutes post-injection time.....	167
Figure 5.4. The distribution (mean ± S.D.) of <sup>3</sup> H-PTX in female nude mice after a bolus intravenous injection of (A) <sup>3</sup> H-Taxol and (B) <sup>3</sup> H-PTX/FPI-749 nanocrystals at 20 mg/kg .....	169

Figure 5.5. The distribution (% absolute amount in blood or tissue/amount injected, mean $\pm$ S.D.) of 20 mg/kg (A) $^3\text{H}$ -Taxol and (B) $^3\text{H}$ -PTX/FPI-749 nanocrystals. The term “asap” refers to 5 and 11 minutes post-injection time of $^3\text{H}$ -Taxol and $^3\text{H}$ -PTX/FPI-749 nanocrystals, respectively.....	170
Figure 5.6. The tumor accumulation (% injected dose/gram of tumor) comparison between $^3\text{H}$ -Taxol and $^3\text{H}$ -PTX/FPI-749 nanocrystals. The “asap” refers to 5 minutes for $^3\text{H}$ -Taxol and 11 minutes for $^3\text{H}$ -PTX/FPI-749 nanocrystals.....	170
Figure 5.7. IVIS <sup>®</sup> images of the dorsal view of athymic mice injected with $^3\text{H}$ -PTX/FPI-749 nanocrystals.....	178
Figure 5.8. IVIS <sup>®</sup> images of the ventral view of athymic mice injected with $^3\text{H}$ -PTX/FPI-749 nanocrystals.....	178
Figure 5.9. IVIS <sup>®</sup> images of ex-vivo tissues of animals administered with $^3\text{H}$ -PTX/FPI-749 nanocrystals. ....	181
Figure 5.10. The fluorescence distribution (% total efficiency/gram of blood or tissue) of 20 mg/kg $^3\text{H}$ -PTX/FPI-749 nanocrystals. The term “asap” refers to 11 minutes post-injection time.....	182
Figure A.1.1. The two forms of camptothecin (CPT) .....	191
Figure A.1.2 The schematic of filtration and harvesting hybrid nanocrystals .....	193
Figure A.1.3. CPT/gold hybrid nanocrystals without vigorous washing and filtering: (A) TEM images, (B) STEM images.....	196
Figure A.1.4. CPT/gold hybrid nanocrystals with vigorous washing and filtering: (A) TEM image, (B) STEM image, (C) EDS analysis.....	197
Figure A.1.5. CPT/chloroaurate hybrid nanocrystals with vigorous washing and filtering: (A) STEM image of overall structure, (B) high resolution STEM image of imbedded gold clusters, (B*) particle analysis of gold cluster, (C) high resolution STEM image of imbedded gold ions, (C*) particle analysis of gold ion.....	198
Figure A.1.6. (A) HR-TEM of hybrid CPT nanocrystals, (B) FFT filtered image using diffraction patterns (C and D) of a TEM image of hybrid camptothecin nanocrystals .....	199
Figure A.2.1. The chemical structure of ZSTK474.....	202
Figure A.2.2. SEM image of ZSTK nanocrystals. Scale bar represents 2 $\mu\text{m}$ . ....	207
Figure A.2.3. Powder x-ray diffractogram of freeze-dried ZSTK474 nanocrystals. ....	207

## LIST OF ABBREVIATIONS

ATCC	American Type Culture Collection
CME	Clathrin-Mediated Endocytosis
CPT	Camptothecin
CT	Computed Tomography
DLS	Dynamic Light Scattering
DSC	Differential Scanning Calorimetry
EPR	Enhanced Permeability and Retention
HPLC	High Performance Liquid Chromatography
IACUC	Institutional Animal Care and Use Committee
IFP	Interstitial Fluid Pressure
IVIS <sup>®</sup>	<i>In Vivo</i> Imaging System
MDSC	Modulated Differential Scanning Calorimetry
MMP	Matrix Metalloproteinase
MPS	Mononuclear Phagocyte System
MRI	Magnetic Resonance Imaging
PET	Positron Emission Tomography
PTX	Paclitaxel
PXRD	Powder X-Ray Diffraction
RES	Reticuloendothelial System
SEM	Scanning Electron Microscope
SPECT	Single Photon Emission Computed Tomography
STEM	Scanning Transmission Electron Microscope
TEM	Transmission Electron Microscope
TGA	Thermogravimetric Analysis

## Chapter 1 - Introduction

### 1.1. Current Cancer Therapy and Nanomedicine

Cancer remains as a leading cause of death worldwide, and the incidence of cancer increases every year. Surgical removal is often limited to solid tumors that are confined in a limited area. Chemotherapy and some extent of radiotherapy then play important roles in inhibiting the growth of residual or metastasized cancer cells and tissues. Unfortunately, large proportions of pharmacologically active antineoplastic agents emerging from high-throughput drug screening initiatives are poorly water soluble. With the current delivery paradigm focusing on solubilizing drug substances prior to the intravenous administration, organic solvents and co-solvents are commonly used to assist solubilization of an anticancer drug. For instance, Taxol<sup>®</sup> uses the combination of Cremophor EL and ethanol to solubilize paclitaxel, a first-line anticancer drug [2]. This common practice of injecting solubilized drugs in organic solvents or aqueous co-solvents can potentially yield adverse effects due to the following reasons: (a) the inherent toxicity associated with the delivery vehicle (e.g. hypersensitivity reactions, nephrotoxicity, neurotoxicity, and neutropenia [3, 4] due to Cremophor); and (b) additional toxicities that arise due to the lack of tumor selectivity, which can heavily affect the rapidly-growing healthy tissues.

In an effort to minimize the toxicity, chemotherapeutics have been encapsulated in nanovehicles with the intention of increasing the tumor-targeting efficiency. Nano-size particles are particularly aimed to take advantage of the enhanced permeation and retention (EPR) effect [5-7], which refers to the poorly constructed blood vessels and

ineffective drainage of the lymphatic system in solid tumors. Due to their rapid growth, tumor vessels are discontinuous, exhibiting abnormal organization, and hierarchical branching patterns [8, 9] relative to normal vascular networks. As a result, tumor vessels are “leakier”, with relatively slow blood flow. In addition, the lymphatic drainage from tumors becomes ineffective as the tumor size increases. This combination of the leakiness of tumor vasculature and low clearance from the interstitial space of tumor tissue is known as the EPR effect [5-7]. Due to their small size, nanoconstructs can passively extravasate into solid tumors through the gaps between the endothelial cells of the underdeveloped tumor vasculature (“passive targeting”). More recently, studies have shown that as the disease progressed, some receptors or endothelial markers are overexpressed on the surface of tumor cells [10]. This finding has led to an alternative approach of “active targeting”, where the delivery systems are decorated with ligands that can specifically bind to the overexpressed receptors. Though the necessity for ligand attachment is still controversial, previous studies have shown that the presence of tumor-targeting ligand does not always result in an increase in tumor accumulation [11-13]. These findings suggested that active targeting does not necessarily translate into effective delivery to the entire tumor.

A vast number of drug delivery nanosystems, including liposomes [14, 15], micelles [16], solid lipid nanoparticles [17, 18], polymeric nanoparticles [19, 20], and dendrimers [21], have been developed in the past decades. Increasing number of nanoformulations are being evaluated in clinical trials, and some have been approved by the U.S. Food and Drug Administration (FDA). The current marketed nanomedicines for cancer therapy include Doxil<sup>®</sup> (doxorubicin liposomes), Daunoxome<sup>®</sup> (daunorubicin citrate liposomes),

Abraxane<sup>®</sup> (amorphous nanoparticles of albumin-bound paclitaxel), Marqibo<sup>®</sup> (vincristine sulfate liposomes), and NanoTherm<sup>®</sup> (aminosilane-coated superparamagnetic iron oxides for magnetic hyperthermia) [22, 23]. Limitations associated with the current nanoparticle designs still exist. The solubilization and encapsulation approach, in which the drug is dispersed in surfactants, encapsulating polymers and/or solubilizing lipids, results in complex constructs. Such multi-component systems could potentially exhibit vehicle instability and drug leakage. For liposomes, both drug leakage from the formulation and instability have been observed during their preparation, storage, and administration [24, 25]. Micellar systems encountered similar problems [26]. Preparation of such a multi-component system requires multiple, arduous steps of synthesis and purification, which make the scale-up for production extremely challenging, if not impossible. Furthermore, toxicity concerns, which may sprout from the composition of the nanocarriers themselves, are often ignored [27]. More importantly, these existing delivery systems have low drug loading. Polymeric micelles, which are known to have high drug loading [26], can only contain up to 42.5% drug content [28]. Considering the fact that no more than 5% of administered nanoparticles can reach and accumulate at the tumor [29, 30], drug leakage and low drug loading limit the potential benefit of existing nanoparticle designs to cancer patients. Hence, ideal vehicles must have high drug loading capacity, low drug loss, and minimum carrier-inherent toxicity [27]. The feasibility of large-scale manufacturing also needs to be considered. Nano-sized drug crystals, a carrier-free colloidal system, seem to fulfill the aforementioned requirements and may potentially offer effective delivery of antineoplastic agents to tumors.

## **1.2. Theranostics**

### **1.2.1 Definition and Purpose**

Nanomedicines are designed with the intent to improve the tumor-targeting efficiency and attenuate the toxicity of systemically delivered chemotherapeutic agents. Over the past decades, the growth of research in nano-sized drug delivery systems for cancer therapy has been substantial, resulting in numerous products in clinical trials and even some in the marketed products. Concurrently, the development of nano-size particles for diagnostic purposes is also escalating. In recent years, multifunctional systems have been developed by either loading imaging probe(s) into the drug delivery systems or combining active ingredients into nanomaterials with intrinsic diagnostic capability (e.g. gold or iron-oxide-based nanoparticles). The approach to combine the two, therapy and diagnosis, is referred to “theranostics”. In a sense, the diagnosis term is not necessarily referring strictly to the identification, localization, or staging of a given pathology, but rather towards the ability to longitudinally monitor the therapeutic efficacy and predict a potential treatment response. Theranostic nanomedicines can be utilized to validate and optimize the properties of drug delivery systems and enable personalized medicine via pre-screening of treatment in patients in preclinical and clinical settings, respectively [31]. When designed properly, theranostic systems are able to provide real-time, yet non-invasive, information on the tissue distribution and target site (tumor) accumulation of the nanoconstructs. This live feedback can be utilized as a tool to optimize the physical properties of the delivery system, where improved tumor targeting efficiency, thus treatment efficacy, can be achieved with minimal toxicity. In clinics, the post-injection-data gathered from patients can also be further analyzed to stratify group response to the

treatment. Only those that respond well should continue to be treated. Otherwise, alternative treatment should be considered.

## **1.2.2 Imaging Modalities and Probes**

Most of the development and evaluation of cancer theranostic systems still remains in preclinical and clinical settings. Imaging probes and their modalities have been extensively reviewed [32-36] and will be summarized as follows.

### **1.2.2.1 Optical Imaging**

The extension of optical imaging techniques from *in vitro* and *ex vivo* applications to that of non-invasive *in vivo* imaging has been substantial. The progress has been attributed to the development of near-infrared fluorophores, activatable near-infrared fluorochromes, bioluminescence probes, and red-shifted proteins [37]. Optical imaging in living subjects fundamentally based on the ability to detect light, either from fluorescence or bioluminescence emitted from the body. Bioluminescence imaging is used to detect the limited numbers of photons that originate from cells that have been genetically engineered to express luciferase. It plays a significant role in cancer research, particularly in its ability to non-invasively monitor the tumor-cell growth and regression, visualize the kinetics of tumor-cell clearance by chemotherapeutics, and track gene expression [36]. However, the signals are generated from the cells themselves, not from the theranostic agents – thus, it is beyond the scope of this discussion. Fluorescence reflecting imaging (FRI) is broadly used in research settings due to its ability to detect low levels of signal (photon) and allow rapid testing of proof-of-principle in living experimental models [35].

In addition, it can provide high-throughput imaging because of its ease of operation, short acquisition time (i.e. 1 to 60 seconds), and the feasibility to simultaneously measure six or more anesthetized living mice [38]. However, limitations, including significant background from tissue auto-fluorescence, limited efficiency of light transmission through animal tissue (i.e.  $< 1$  cm), and lack of depth information, still exist [35]. The imaging information from this system is also surface-weighted, in that anything closer to the surface will appear brighter [37]. A newer approach via fluorescence-mediated tomography (FMT) allows imaging of deeper structures. With FMT [39, 40], the subject is exposed to a continuous wave or pulsed light from different sources, and the detectors are spatially and orderly arranged in an imaging chamber to capture the emitted light. The algorithm results in a reconstructed tomographic image, with enhanced depth of penetration (i.e.  $< 10$  cm, [36]).

Fluorescence imaging probes are commonly incorporated into theranostic systems because they are sensitive [41, 42], relatively inexpensive, and easy to handle (i.e. compared to radioactive material) [43]. *In vivo* imaging of the fluorescence probes is still limited due to the light scattering and absorption that occurs in tissue constituents, specifically by blood (oxy- (HbO<sub>2</sub>) and deoxyhemoglobin (Hb)) and water. Near-infrared (NIR) fluorophores with wavelength range of 650 and 900 nm are most utilized in optical imaging technologies due to their low absorption and auto-fluorescence, minimal background interference, and improved tissue depth penetration [37, 44-46]. In the field of oncology, the first clinical trials using fluorescence imaging were focused on an image-guiding intraoperative method for sentinel lymph node resection [47-51] using Indocyanine Green (ICG, emission wavelength of  $\sim 800$  nm), the only FDA approved

NIR dye for human use. Based on composition, fluorophores can be categorized into two classes: organic and inorganic (quantum dots). Both classes have been extensively used in the field of nanotheranostics.

The organic ones are generally derived from the class of cyanines, squaraines, phthalocyanines, porphyrins, and BODIPY [42, 52], while quantum dots (QDs) are nanocrystals of semi-conducting materials [53], made from the II-VI (i.e. CdSe, ZnS, CdTe), III-V (InP), or IV-VI (PbS, PbSe, PbTe) semiconductors. Organic dyes, due to their aromatic structure, generally have low water solubility. Solubility may be increased by chemical modification via addition of polar groups, including sulfonate [46, 54] or saccharide [55, 56]. Free organic fluorophores are rapidly cleared *in vivo*. Hydrophilic dyes (e.g. fluorescein) are typically cleared by urinary excretion, while lipophilic ones (e.g. ICG) are cleared by biliary excretion [43]. Compared to organic fluorophores, QDs offer several unique advantages, including significant improvement in the probe brightness (i.e. 10-20 times brighter than organic dyes [57]), resistance against photobleaching, and enhancement in detection sensitivity (e.g. clearly detectable above the tissue auto-fluorescence for animal model) [58]. Despite their advancement as novel fluorescent probes for multiplexed tissue and cell labeling, quantum dots still have several drawbacks, such as toxicity [59] and clearance by the reticuloendothelial system (RES), that still remain unsolved and limit their potential for human clinical applications. Specific details of the synthesis, applications, and toxicity of quantum dots have been reviewed [58-61].

### **1.2.2.2 Magnetic Resonance Imaging (MRI)**

The MRI signal is based on the difference in nuclear magnetic relaxations of the water protons in biological solutions and surrounding solid tissue. During the imaging process, subject is exposed to a radio frequency that allows the hydrogen nuclei to have enough energy to spin and precess. Upon exposure of strong magnetic field, the nuclei spin back in the direction parallel to the field. The relaxation process in which the nuclei return to the original aligned state can be exploited into images. The differentiation between tissues can be enhanced by using contrast agent to shorten the relaxation parameters (T1 and T2) of water. MRI is able to provide excellent tissue contrast without ionizing radiation, offering high spatial resolution [32-34]. Some of MRI limitations are low sensitivity and long acquisition and image processing time, which hinder its use as a high throughput modality [34]. Because MRI suffers from low sensitivity, the administration of high concentrations of contrast agents is often required to produce a detectable signal [32]. Improved signal-to-noise ratio and resolution can also be increased by exposure to high magnetic field strength, which may cause physiological effects (e.g. nausea and visual abnormalities) [33].

Common MRI contrast agents, which include the paramagnetic (e.g. gadolinium (Gd) and manganese (Mn)) and superparamagnetic (e.g. iron-oxide nanoparticles) substances, are commonly incorporated into nano-sized drug delivery vehicles to achieve theranostic functions. Compared to gadolinium-chelates, superparamagnetic iron oxide (SPIO) particles are preferred due to their sensitivity and biocompatibility. In addition, their physical properties can be manipulated by changing their size [62].

### **1.2.2.3 Radionuclide-based Imaging**

Although the hardware and radioisotopes used for positron emission tomography (PET) and single-photon emission computed tomography (SPECT) are different, both approaches rely upon the detection of  $\gamma$ -ray emissions arising from radioisotope decay. Unlike MRI, radionuclide-based imaging techniques have a nominally low background signal and require little signal amplification due to the high energy of gamma rays. Compared to SPECT, PET imaging is approximately ten times more sensitive - picomolar ( $10^{-12}$  M) concentrations of radiolabel can be readily detected and quantified regardless of tissue depth. Although PET imaging is capable to track molecular events, it has poor spatial resolution. Thus, generally PET imaging is often hybridized with high resolution images from computed tomography (CT) for the event localization. SPECT is more widely available than PET, and it is advantageous due to its ability to concurrently image multiple radionuclides. Nonetheless, both SPECT and PET are quantitative techniques, which are advantageous compared to other modalities, such as MRI and optical imaging. For PET imaging, the radiopharmaceuticals utilized generally emit high-energy  $\gamma$ -ray (e.g.  $^{18}\text{F}$ ,  $^{11}\text{C}$ ,  $^{13}\text{N}$ ,  $^{15}\text{O}$ ), while low-gamma  $\gamma$ -ray (e.g.  $^{99\text{m}}\text{Tc}$ ,  $^{111}\text{In}$ ,  $^{125}\text{I}$ ) emitting probes are used for SPECT. Radionuclides used for SPECT are simpler to prepare and usually have a longer half-life than those used for PET [32].

### **1.2.2.4 Computed Tomography (CT)**

CT generally provides complementary anatomical information for radionuclide-based imaging by measuring the absorption of X-rays as they pass through tissues. Within a CT image, one can distinguish the difference between tissues based on the degree of X-ray

attenuation, which is determined by the atomic number of the contrast agent and the electron density of the tissue. Absorption differences between bone, fat, air, and water produce high contrast images of anatomical structures [63]. CT's relatively low tissue contrast for tumors and surrounding tissue can be enhanced by the use of contrast agent. The current CT contrast agent (e.g. iodine) is rapidly extravasated and cleared from the system. Prolonged presence in the blood pool may be achieved by developing nanoparticles which contain electron dense elements with high atomic number (e.g. iodine, bismuth, and gold). Because of gold's atomic number and electron density [63], it provides about 2.7 times stronger contrast per unit weight than iodine. In addition, the low toxicity [64], good biocompatibility, and unique physical and chemical properties of gold (nanoparticles) make it an ideal contrast agent. More importantly, various shapes of the particles can be utilized since the only important parameter in CT imaging is the total amount of gold per unit volume (voxel) [65]. The utilization of gold as a contrast agent *in vivo* was first reported in 2006, and it is being continually explored [66].

#### **1.2.2.5 Ultrasound**

Ultrasound probes typically contain one or more acoustic transducers, which emit high frequency sound waves (>20 kHz). The image is formed based on the sound wave echoed back from the internal organs [67]. Contrast enhancement at the molecular level can be obtained by introducing gas-entrapped-microbubbles, which have different acoustic properties than tissues. Nanoparticle-based contrast agents are currently in various stages of development [32].

### 1.2.3 Building Theranostic System

To form theranostic nanoconstructs, imaging modalities are incorporated in delivery systems via various methods, including encapsulation, intercalation, adsorption, or covalent-bond conjugation, which may be vehicle-specific [31, 32, 68, 69]. Most relevant nanoconstructs, such as vesicles (e.g. liposomes and polymersomes), polymeric nanoparticles, micelles, core-shell structures, dendrimers, and carbon nanotubes will be reviewed below.

#### 1.2.3.1 Vesicles

The two main classes of vesicles, liposomes [70] and polymeric vesicles [71], have the ability to integrate both hydrophilic and hydrophobic moieties either by covalent and non-covalent interaction. The three different approaches to engineer theranostic-based-liposomes have been reviewed [72]: (i) hydrophobic probes can be embedded in the lipid bilayer, (ii) hydrophilic probes can be encapsulated within the internal aqueous-core of the liposome, (iii) probes can be physically adsorbed into the surface of the liposome. Probes that are popularly being incorporated into liposomes are gold nanoshells and nanoparticles, quantum dots, superparamagnetic iron oxide (SPIO) nanoparticles, and radionuclides. For instance, Al-Jamal and Kostarelos designed theranostic liposomes by loading either doxorubicin or artificially enveloped adenoviruses in the core and entrapping the quantum dots into the lipid bilayers [72]. Extended circulation time *in vivo* and minimized non-specific binding were achieved by chemically linking QDs to the surface of doxorubicin-loaded actively-targeted anti-HER2-immunoliposomes by PEG-DSPE [73]. To exemplify the robustness of liposomes as delivery vehicles for both

therapeutic and diagnostic agents, multifunctional liposomal system containing chemotherapeutic agent and multiple imaging probes, including gadolinium (Gd), near infrared fluorescence tracer, or radioisotopes (e.g.  $^{99m}\text{Tc}$ ,  $^{64}\text{Cu}$ ) have been recently developed. The liposome was comprised of DSPC/cholesterol/Gd-DOTA-DSPE/DOTA-DSPE/IRDye-DSPE with ammonium/ pH gradient, whereby radionuclides such as  $^{99m}\text{Tc}$  and  $^{64}\text{Cu}$ , and the antineoplastic, doxorubicin, could be post-loaded to the core [74].

While liposomes are composed of phospholipids that chemically mimic those in eukaryotes, polymersomes result from bilayer self-assembly of a diverse array of synthetic amphiphilic block copolymers containing hydrophilic and hydrophobic blocks [75]. Similar to liposomes, polymersomes have a large hydrophilic reservoir in the core and thick hydrophobic lamellar membranes that are available for functionalization. For instance, ultra-small SPIO and doxorubicin were successfully embedded together into the membrane of vesicles with one-step nanoprecipitation, creating hybrid polymersomes that were able to provide contrast enhancement and a triggered release function in an oscillating radiofrequency field [76]. Further use of polymersomes to host multifunctional modalities has been reviewed [75]. These vesicle-type delivery vehicles are versatile and tunable for the delivery of therapeutic and diagnostic agents. Nonetheless, limitations, including production, complexity, and vehicle toxicity [32], need to be taken into consideration.

### **1.2.3.2 Polymeric Nanoparticles**

In polymeric nanoparticles, the hydrophobic portion of the block copolymer self-associates and concentrates into a semisolid core while the hydrophilic portion of the

copolymer forms a coronal layer [77]. Both hydrophobic and hydrophilic moieties can be either be encapsulated in the core, adsorbed on the surface, or covalently attached to the surface. Superparamagnetic iron oxide nanoparticles and doxorubicin were embedded in YCC-DOX polymer nanoparticles, which were composed of poly (ethylene oxide)-trimellitic anhydride chloride-folate (PEO-TMA-FA) [78]. Compared to conventional MRI contrast agent, Resovist®, YCC-DOX showed higher MRI sensitivity to folate receptor-positive liver tumor cells. Even more, the nanoparticles showed inhibition of tumor growth without inducing adverse side effects. Additional examples of theranostics designed from this group of delivery vehicles have been reviewed by the Peppas group [79].

### **1.2.3.3 Micelles**

Micelles are self-assembled nano-sized colloidal particles with a hydrophobic core and hydrophilic shell [16]. Without the aqueous core, imaging agent has to be bound to the polymer via conjugation or entrapped within the dense hydrophobic core [80]. Similar approaches can be taken to build theranostic systems from polymeric micelles, which consist of self-assembled block copolymers with a densely packed hydrophobic core and hydrophilic shell [81]. A study reported that doxorubicin and SPIO nanoparticles were simultaneously entrapped in the core of a Pluronic F127 micellar system. When tested *in vitro*, the micelles containing SPIO nanoparticles having a diameter of approximately 100 nm had a substantial advantage in the T2 relaxation and decreased cell toxicity compared with Resovist, a commercial SPIO contrast agent [82]. In more complicated unimolecular micelles consisting of the amphiphilic multiarm star block copolymer, H40-

PCL-b-P(OEGMA-Gd-FA), paclitaxel was physically encapsulated within the hydrophobic core while a targeting moiety (folic acid) and MRI contrast agent (DOTA-Gd) were covalently anchored in the hydrophilic outer corona. When tested in a murine model, this theranostic nanoconstruct demonstrated conspicuously positive contrast enhancement and an extended blood circulation time [83].

#### **1.2.3.4 Core-shell Nanoparticles**

Nanoparticles (NPs) constructed from inorganic materials (e.g. SPIOs, quantum dots, gold NPs, silica NPs) are clustered into this large class of core-shell structures. Advances in the development of core-shell structures for theranostics have been extensively reviewed by Xie *et al.* [84]. To link the core-shell structures with other functional entities, various techniques, including conjugation, electrostatic surface interactions, and adsorption, have been employed [84]. In addition, due to their small size, core-shell-nanoparticles can also be incorporated into other nanovehicles as diagnostic probes.

Due to their biocompatibility, inexpensiveness, and superior magnetic properties, SPIOs have a vast number of bio-applications, including their use as contrast probes for MRI [85-87]. In addition, due to their inherent intrinsic properties, SPIOs can serve dual imaging/therapy role. They can be used not only as a contrast enhancer in MRI, but also as a transducer in hyperthermia therapy. In the presence of external alternating magnetic field (AMF) signal, SPIOs can convert the electromagnetic energy to heat [88, 89]. With appropriate coatings, SPIOs can be easily coupled with drug molecules via covalent coupling [90-92]. Drug molecules can also be encapsulated in the polymeric matrices,

which typically used as hydrophilic coating [93-95]. Recently, small molecule entity also has been successfully loaded into hollow SPIOs [96].

Quantum dots (QDs) are semiconductor-based-nanocrystals that have unique and unprecedented optical properties, such as improvement in brightness, resistance against photobleaching and chemical degradation, enhancement in detection sensitivity, and a narrow emission spectrum [84]. Their optical properties can be finely tuned by adjusting their size and composition. Modifications of QDs were mostly achieved via the disulfide linkage on the surface, but concern regarding the fragility of the disulfide bond still exists [97]. However, limitations due to the innate toxicity of QDs have hindered its use in clinical trials [97]. QD applications as bioimaging probes may be further extended with the recent emergence of less toxic Cd-free QDs [98-100].

Gold NPs (including gold nanoshells) has a unique surface plasmon feature that enable its use for photothermal therapy, where gold NPs can transform light into heat and cause ablation to nearby cells. Due to the strong interaction between gold and thiol, surface conjugation is mostly done via the addition of thiolated species [101, 102].

Unlike other core-shell structures, silica nanoparticles do not have an intrinsic diagnostic function, but they offer an excellent platform for loading a broad range of therapeutic and imaging moieties. Generally, tetraethyl orthosilicate (TEOS) is the precursor for building silica NPs. Functional groups can be incorporated into the nanostructures by using aminopropyltrimethoxysilane (APS) or mercaptopropylmethoxysilane (MPS) as co-precursors, which can coagulate with the TEOS matrix and conjugate with amine or thiol groups. Besides small chemical entity [103] and drug molecules [104], other small core-shell structures (e.g. SPIOs, gold NPs, QDs) can be embedded into the silica matrices

[105-107]. Additionally, mesoporous silica nanostructures, which consist of hundreds of empty channels and large surface areas, are promising candidates for drug vehicles as they provide excellent reservoirs for entrapping small molecules [108]. Silica NPs are biodegradable, and they are renally cleared within a short period of time [109].

#### **1.2.3.5 Dendrimers**

Dendrimers are hyper-branched and highly-defined polymer macromolecules characterized by large numbers of end-group functionalities and compact molecular structures. Their starburst structure enables greater loading efficiency for therapeutics and imaging agents [110]. An *in vitro* study of multifunctional poly(amidoamine) (PAMAM) dendrimers conjugated with a chemotherapeutic drug (paclitaxel), imaging agent (fluorescein isothiocyanate, FITC), and targeting moiety (folic acid) showed a targeted delivery of the therapeutic and imaging agents to specific cancer cells [111]. An alternative chemotherapeutic drug, methotrexate, could also be conjugated to the multifunctional PAMAM dendrimer [112]. In PAMAM dendrimers, the leading dendrimer scaffold in biomaterials, the attachment of therapeutics and imaging probes to the amine termini is mainly achieved via a random statistical approach. A more controlled strategy was developed recently by creating polyamide-based dendrimer that contains nine azide termini, nine amine termini, and fifty-four terminal acid groups [113]. The amine termini were reacted with a near infrared cyanine dye, resulting in orthogonal functionalization of a multifunctional dendrimer that showed a relatively high quantum yield, fluorescence signal, and large Stokes shift with minimal toxicity toward T98G human glioblastoma cells.

### 1.2.3.6 Carbon Nanotubes

Carbon nanotubes (CNTs) are cylindrical carbon allotropes. They can be formed either as single-walled or multi-walled, for increased stability [114]. They can be used as a theranostic platform due to their tunable properties and ability to incorporate multiple functionalities. Therapeutic and imaging agents can be linked either covalently via amide bonds [115] or non-covalently due to the hydrophobic nature of the surface [116] or aromatic (i.e. pi-pi) stacking [117]. Similar to core-shell structures, CNTs have a broad excitation profile and high absorption coefficient. One particular study showed that due to their unique intrinsic electronic band structures, single-wall carbon nanotubes (SWNTs) can have a very high optical absorbance in the NIR regime [118]. In addition to their capability to provide optical simulation inside living cells, SWNTs were able to cause cell death upon continuous NIR radiation that caused local heating. In order to spare the healthy cells, SWNTs were functionalized with a folate moiety that allowed selective internalization in cells with overexpressed folate receptor. Thus far, studies on multifunctional CNTs are mainly conducted *in vitro* as cytotoxicity observed from the use of CNTs is still debatable [119]. Nonetheless, a recent report on an immunologically modified nanotube system utilizing glycosylated chitosan (GC) as surfactant, showed a remarkable ability of SWNTs to induce complete tumor regression and long-term survival in a murine EMT6 xenograft model [120]. Upon intratumoral injection, the SWNT-GC system maintained its optical properties and was able to be taken up by cancer cells. When the subcutaneous tumor (in flank) was irradiated by a laser (980 nm),

the SWNTs were able to induce cellular thermal destruction and provide photothermal therapy.

In summary, imaging probe(s) can be embedded in the core of nanovehicles, intercalated in or be part of the nanovehicle's shell, or linked to the exterior side by either adsorption or a covalent bond (conjugation). Encapsulation, either by the entrapment using molecular affinity or covalent conjugation to the material constituting the particle core, offers the advantage of protecting probes from direct interactions with biological fluids.

#### **1.2.4 General Considerations for Translation**

In order for nanomedicine to be useful in clinical practice, evidence of sufficient potency or payload, reduced toxicity and side effects, biodegradability, and adequate stability during formulation, storage, and administration has to be shown. Additionally, pharmacokinetics and biodistribution also play important roles in the performance of the nanoplatform. Even with a promising pharmacological response, a nanomedicine that cannot reach its target will have no clinical utility. The key factors relevant to the design of practical nanomedicines and the regulatory mechanisms to achieve safe and timely realization of clinical benefits have been elegantly reviewed by Duncan and Gaspar [121].

## **1.3. Nanocrystals**

### **1.3.1 Introduction**

Over the last few years, nanocrystal formulations have been of considerable interest for delivering poorly soluble drugs via oral, parenteral, and other routes [122]. Administered directly as nanosized solid particles, drug nanocrystals require no solubilizing and/or encapsulating chemicals, thus circumventing side effects that may have stymied many existing delivery systems. More importantly, production of nanocrystals at a large scale is feasible due to the simplicity of formulation and absence of solubilizing, encapsulating, or conjugating steps. Because no harsh solubilization agents are utilized in the nanocrystal formulation, it is expected to offer less toxicity and improved anticancer efficacy.

The term crystal connotes regular, periodic supramolecular structures assembled by organic or other types of molecules or atoms. Characteristically, a crystal shows distinct X-ray diffraction patterns and has a specific melting point, density, and solubility, in addition to other well-defined physicochemical properties. Compared with the amorphous state, in which molecules are randomly packed, the crystalline state is more stable, exemplified by the fact that amorphous materials can readily undergo spontaneous phase transitions and recrystallization. As such, using crystalline materials in a formulation assures better physical stability than those amorphous formulations.

Nanocrystals of poorly soluble drugs can offer several advantages over solubilized and encapsulated formulations. Aside from their physical stability, the dissolution rate of nanocrystals can be significantly enhanced – under sink conditions – due to their increased surface area. More importantly, manufacturing at the industrial scale is

possible. Below, major approaches for producing nanocrystals of organic molecules are further discussed. The top-down approach produces large crystals that are physically reduced in size by comminution; the bottom-up approach yields nanocrystals from solution by crystallization. Several review articles have focused on the techniques, mainly the top-down approach [122-126].

### **1.3.2 Various Approaches to Produce Nanocrystals**

#### **1.3.2.1 Top-down Approach**

There are two basic diminution techniques: wet milling and high-pressure homogenization. Wet milling involves mechanical attrition, where drug particles are wetted by an aqueous solution of surfactants and subjected to mechanical shearing and grinding by, for example, milling balls in a milling container. The particle size is reduced and may reach a few hundred nanometers. The Nanocrystal<sup>®</sup> technique[127], a wet milling process patented by Élan Co., has been employed in several oral products including Rapamune<sup>®</sup>, Emend<sup>®</sup>, Tricor<sup>®</sup>, and Megace ES<sup>®</sup> [128]. One drawback of the technique is potential contamination from the erosion of metal milling balls or pearls. The amount of contamination is determined by the hardness of drug particles as well as the milling time, which can take up to several days [129]. The use of polymeric beads (e.g., polystyrene derivatives) may be helpful in minimizing the erosion.

High-pressure homogenization is another fragmentation technique. One development is based on jet-stream microfluidization [130], in which two fluid streams of particle suspensions collide under high pressure in a Y-shaped chamber, leading to particle

collision and subsequent particle rupture. The marketed product Triglide<sup>®</sup> developed by SkyePharma Co. is produced by Insoluble Drug Delivery-Particles (IDD-P<sup>TM</sup>) technology, a microfluidization method [131]. Piston-gap homogenizers are also used to produce nanosized solid particles by forcing a suspension of drug particles with a piston through a thin gap under high pressure [132]. The combination of cavitations, high shear forces, and turbulent flow, fractures the particles into smaller pieces. The outcome of particle fragmentation is influenced by several factors, including the power of homogenization, particle hardness, and number of the piston-moving cycles. Compared with wet milling, the homogenization method may yield less contamination during the production process [133]. There are currently two patented technologies for nanocrystal production that employ the piston-gap homogenization method, DissoCubes<sup>®</sup> and Nanopure<sup>®</sup>. In the former, owned by SkyePharma Co., drug powders are dispersed in an aqueous solution of surfactants and subjected to homogenization [132]; in the latter, previously owned by PharmaSol GmbH and now acquired by Abbott Co., drug particles are suspended in either non-aqueous dispersion media (e.g., oils and liquefied polyethylene glycol) or aqueous-organic cosolvents (e.g., glycerol-water, and ethanol-water mixtures) prior to homogenization [132]. These operations require that one start with drug particles no larger than 25  $\mu\text{m}$  so that the blockage of the homogenizer can be minimized [134].

Currently, the top-down approach dominates the production of nanocrystals and is used to manufacture several products in the market [126]. Despite its popularity, there are inherent drawbacks in this approach, including the high energy input, prolonged operation time, possibility of contamination, and decreased crystallinity or stability [135].

The stability concern is particularly critical for a nanocrystal system to be considered for parenteral drug delivery. The amorphous content produced during the high-energy process can lead to phase instability, which in turn causes uncertainty and potential variability in pharmacokinetic behavior which should be tightly controlled.

### **1.3.2.2 Bottom-up Approaches**

Nanocrystals can be grown directly from solution. Nucleation and crystal growth thus play essential roles in the bottom-up approach. To induce nucleation, a solution needs to become supersaturated. Cooling, solvent evaporation, and mixing with an antisolvent, are among several ways to create supersaturation [136]. Still, a solution can become supersaturated to some extent without producing any nuclei. This is because nucleation is energetically unfavorable. According to the classical nucleation theory [137-139], the change in free energy when a nucleus starts to grow includes two energy components, one associated with the creation of the new surface, and another with the packing of molecules in the bulk crystal. As depicted in Figure 1.1, the surface-related term,  $\Delta G_S$ , is always positive (energetically unfavorable) because creation of a new surface of a solid particle requires energy input. On the other hand, the bulk-related term,  $\Delta G_V$ , is negative (energetically favorable) due to the formation of intermolecular interactions between molecules in the nucleus. When a nucleus is small,  $\Delta G_S$  dominates, and the overall free energy change is positive so that the development of the nucleus is not spontaneous. As the nucleus grows and surpasses a so-called critical nucleus size ( $r_c$ ),  $\Delta G_V$  becomes dominant, and the overall free energy change becomes negative. Subsequently, the nucleus can grow freely as long as supersaturation is maintained.

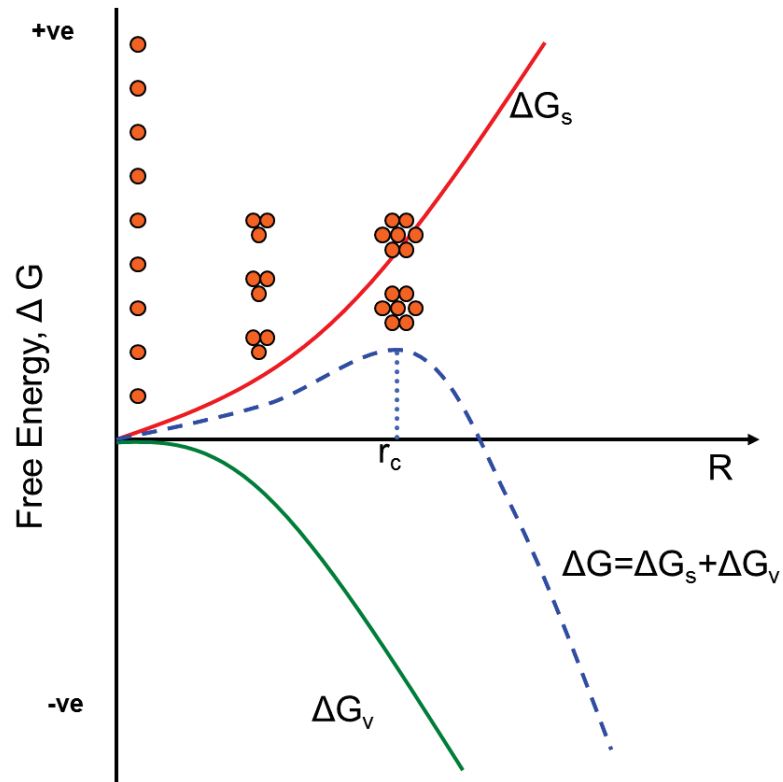


**Figure 1.1.** Free energy diagram for nucleation. (Adapted from Mullin [1]).

In reality, homogeneous nucleation – nucleation without the aid of substances other than the solute molecules – seldom occurs. Foreign materials, impurities, or even the surface of the crystallization vessel often help to induce nucleation, which is denoted as the heterogeneous nucleation [1]. According to the classical nucleation theory, the presence of a foreign surface lowers the  $\Delta G_s$  term for a nucleus to form on the surface. In other words, the nucleus requires less energy for surface creation when it forms on a pre-existing surface.

In order to produce nanosized crystals from solution, it is thus extremely critical to control the nucleation process. It is important not only for controlling the particle size but also for the size distribution. Ideally, nucleation of a large number of crystalline embryos must occur concurrently from the supersaturated solution. Rapid depletion of the solute molecules from the solution limits further growth of each nucleus so as to achieve a nanosize. Having a large number of nuclei produced at the same time also keeps the particle size distribution narrow. Similar particle sizes are not only preferred for ensuring product quality but also important for maintaining the stability of nanocrystals. A narrow distribution of particle size can greatly minimize the so-called Ostwald ripening phenomenon, in which larger particles grow at the expense of re-dissolving smaller ones because of their differences in surface energy [140]. For this purpose, the induction of nucleation needs to be abrupt and homogeneous throughout the growth medium. One common strategy is to mix the solution of a drug compound with an antisolvent, so that the supersaturation is reached immediately; at the same time, the mixture is subjected to intense sonication and/or mechanical stirring. It is known that air cavities created by sonication may trigger nucleation because of the presence of air-liquid interfaces and locally concentrated liquid pockets. Nevertheless, because nucleation is such a difficult process to control [141], subtle changes in growth conditions can result in drastic variations in product quality. For producing nanocrystals, extreme care is particularly needed for identifying a suitable set of peripheral conditions [142], which mostly likely vary for distinct compounds.

There are several approaches that have been developed to create supersaturation and induce nucleation [125]. They include hydrosols [140], high-gravity controlled

precipitation technology (HGCP) [143, 144], confined impinging jets [145], supercritical fluid technology (SCF) [146], and sonoprecipitation [147], as further discussed below.

#### **1.3.2.2.1 Hydrosols**

Considered to be a more mature method, hydrosols or aqueous nanosuspensions of poorly water soluble drugs have been developed by Sandoz (now Novartis) [148]. The active ingredient is dissolved in aqueous-organic miscible cosolvents (e.g., ethanol, isopropanol, and acetone), while various peptisers and/or stabilizing agents (e.g., citric acid, gelatin, ethyl cellulose N7, lecithin) may be added to the aqueous phase to prevent aggregation. A matrix former, generally sugar or sugar alcohol (e.g., mannitol), is also added to the solution to prevent agglomeration and aid in the re-suspension process. In the laboratory setting, solid nanoparticles can be produced by mechanically mixing the various components in a beaker while removing the organic solvent through evaporation. For the industrial production, the organic and aqueous phases are pumped into a static mixer and forced through an atomizing nozzle, leading to the formation and drying of nanoparticles [148-151]. One study reported that spray-dried cyclosporin A contained 38  $\mu\text{m}$  particle agglomerates that were reduced to 120 nm upon re-dispersion in water [149]; the nanoparticles produced by this method were nonetheless amorphous [149, 150].

#### **1.3.2.2.2 High-Gravity Controlled Precipitation (HGCP)**

HGCP is considered to be one of the most promising techniques to produce nanoprecipitations at the commercial scale [125]. The key component in HGCP is a rotating packed bed (RPB), where two liquid streams are pumped in and mixed together

vigorously by centrifugation. Subsequently, the mixture is spread into thin films and ultimately broken into tiny droplets. In addition to using antisolvents, mixing two streams of reactants can also produce precipitates chemically in HGCP. Depending on the compound and conditions, a product may be amorphous or crystalline. Nanoparticles of a few pharmaceutical compounds, including cephadrine [152], danazol [153], and salbutamol sulphate [154, 155], have been successfully produced by this method.

#### **1.3.2.2.3 Flash Nanoprecipitation by Confined Liquid Impinging Jets (CLIJ)**

In this technique, two respective jet streams of a drug solution and an antisolvent are forced together by opposing nozzles that are mounted in a small chamber to create localized, intensified mixing. The mixing causes precipitation of nanoparticles within the residence time of mixing. The velocity, drug concentration, and volume ratio of the two streams are considered to be the factors determining the particle size distribution of a product. CLIJ has been utilized in the production of salbutamol sulphate, ibuprofen, cyclosporin A, and amphotericin B [156-158]. GRAS (Generally Regarded as Safe) additives may be added to assist the production.

#### **1.3.2.2.4 Supercritical Fluid (SCF) Technology**

This method takes advantage of the unique physical properties of supercritical fluids, including low density and viscosity as well as high diffusivity of solute molecules to attain rapid mixing. In addition, quick and easy removal of a SCF without excessive drying can greatly facilitate the precipitation of nanoparticles. Supercritical carbon dioxide (SCO<sub>2</sub>) is mostly used and considered green or environmentally friendly for

processing most pharmaceuticals. Depending on the solubility of a compound in  $\text{SCO}_2$ , production can be accomplished by allowing the drug/ $\text{SCO}_2$  mixture to expand under ambient conditions (method called Rapid Expansion of Supercritical Solution or RESS [159]) or by using  $\text{SCO}_2$  as the antisolvent when the drug is poorly soluble in  $\text{SCO}_2$  (a process called Supercritical AntiSolvent, or SAS [159]). In the both methods, it is critical that other solvents used are miscible with  $\text{SCO}_2$ ; water is actually immiscible. Amoxicillin, ampicillin, and rifampicin nanoparticles were successfully produced by the SCF approach [160]. 100-500 nm nanoparticles of insulin, rhDNase, lysozyme, and albumin were precipitated from aqueous ethanol solution by using ethanol as the co-solvent [161].

#### **1.3.2.2.5 Sonoprecipitation**

Ultrasonic waves can create cavitations that subsequently collapse, releasing shock waves that may assist in rapid and more uniform nucleation [162]. Ultrasound can also reduce particle agglomeration by minimizing particle contacts [147]. Drug microparticles were reportedly produced by the sonocrystallization method [163-165]; it was also shown that the method could produce nanoparticles of amorphous cefuroxime axetil [166]. Factors that influence the quality of a final product include: (i) ultrasound frequency, intensity, and power, (ii) sonication probe size and immersion depth, (iii) solution volume, and (iv) duration. Although the experimental setup appears to be straightforward, this technology has not been adopted for commercial production.

The quality of nanocrystals produced by the bottom-up approach is expected to be superior to that by the top-down method. Particle size and morphology can be better

controlled, and it is possible to produce pure nanocrystals with little or no amorphous content. Shorter production time, less energy consumption, and reduced contamination also make the precipitation techniques desirable. Clearly, the bottom-up approach holds great promise for developing nanocrystals for parenteral delivery, which demands uncompromised quality and stability. Although no such product is currently in the market, there is certainly a growing interest and need in this field. Challenges remain in controlling nucleation and subsequent crystal growth, so that batch-to-batch reproducibility can be achieved. It is certain that, among various methods that are being developed, ones that are simple, reproducible, and yet cost-effective for production scale-up should have great potential in commercial production [140].

### **1.3.2.3 Combination Approach**

There have been efforts to combine the two aforementioned approaches. The NanoEdge™ patent by Baxter claims that nanocrystals, ranging from 400 nm to 2µm, can be prepared by crystallization followed by high pressure homogenization [167]. Our research group used an antisolvent approach to grow nanocrystals by rapidly precipitating anticancer drugs under intense stirring and sonication [168, 169]. To further reduce the size, the nanocrystal suspension can subsequently be homogenized. Nanocrystals with an average particle size ranging from 200 to 800 nm have been successfully produced in our laboratory. The second step of homogenization breaks down larger crystals and, particularly, aggregates, achieving a much narrower particle size distribution.

### 1.3.3 Particle Stabilization

Nanocrystals and nanoparticles of drugs, whether prepared by the top-down or bottom-up approach, often require surfactants to be physically attached to the surface of each particle in order to prevent the particles from aggregation during the preparation, storage, and administration. Particle aggregation mutually facilitates Ostwald's ripening and eventually becomes irreversible, leading to larger particles and precipitates. Surfactant usage is particularly necessary when the surface of nanocrystals is uncharged. In general, polymeric surfactants are commonly used to introduce steric repulsion between particles; electrostatic repulsion also promotes particle segregation when ionic surfactants are used. Povidones, pluronics, and celluloses are the most commonly used surfactants. Natural biological molecules, such as lecithins and cholic acid derivatives, are utilized as well [170].

Finding a suitable surfactant for a particular drug is experimentally demanding [171]. A stabilizer obviously needs to have sufficient affinity for the particle surface and the amount used should provide sufficient steric and/or electrostatic repulsion between the particles [172]. Excess surfactant does not always lead to better coverage due to the tendency of surfactants to form micelles when the concentration surpasses the critical micelle concentration (CMC) [173, 174]. A recent study of the effects of 13 stabilizers during wet milling of nine drug compounds [175] concluded that the semi-synthetic polymers, including hydroxypropylmethylcellulose (HPMC), methylcellulose (MC), hydroxyethylcellulose (HEC), hydroxypropylcellulose (HPC), carboxymethylcellulose sodium salt (NaCMC), and alginic acid sodium salt (NaAlg), yielded rather poor stabilizing performance, likely due to their high viscosity. Less viscous stabilizers,

including linear synthetic polymers (PVP K30 and K90) and synthetic copolymers (poloxamer 188 and Kollicoat IR<sup>®</sup>) showed better stabilizing capabilities, especially at higher concentrations. Tween<sup>®</sup> 80 and TPGS (D- $\alpha$ -tocopherol polyethylene glycol 1000 succinate) gave the best stabilizing performance. Moreover, the timing of surfactant addition may affect particle properties. Stabilizers are commonly added along with the starting microcrystalline materials for wet milling or homogenization. However, the addition of a stabilizer prior to crystallization may alter the nucleation and subsequent crystal growth outcome.

Because the surfaces of nanocrystals undergo consistent dynamic changes due to dissolution and surface recrystallization, albeit at a slow rate, surface coating by surfactants may not be able to sustain stability of nanocrystals for long-term storage. Alternatively, nanocrystal products can be post-processed by freeze-drying, spray drying, or pelletization [124]. In the absence of solvents, the surface dynamics and Ostwald ripening are greatly minimized. Water soluble sugars such as mannitol, trehalose, and dextran are commonly added as matrix formers prior to drying [176]. Nanosuspensions for intravenous use can be sterilized by terminal heat and gamma irradiation [177] as well as filtration [178] and stored as liquid suspensions or lyophilized solids.

### 1.3.4 Physical Characterization of Nanocrystals

Nanocrystals need to be fully evaluated to determine their: (i) particle size and size distribution, (ii) surface charge, (iii) crystallinity, and (iv) dissolution rate [123, 134, 176, 179].

#### 1.3.4.1 Particle Size

When a formulation is intended for intravenous delivery, it is essential to ensure that the particle size is smaller than the smallest blood capillary (a few micrometers) so that potential capillary blockade or emboli formation can be avoided [134]. For rapid and non-invasive determination of the mean particle size and size distribution, photon correlation spectroscopy (PCS) or dynamic light scattering (DLS) is mostly used for particles ranging from 3 nm to 3  $\mu$ m. The size distribution is indicated by the polydispersity index (PI), which is a cumulant-method-derived-parameter that is used for determining the width of the particle size distribution. When particle size population is assumed to follow the Gaussian distribution, the PI relates the standard deviation ( $\sigma$ ) and the intensity-weighted average hydrodynamic size ( $Z_D$ ) of particles in the following equation:

$$PI = \left(\frac{\sigma}{Z_D}\right)^2 \quad (1)$$

PI value of 0.1-0.25 suggests that the size distribution is fairly narrow, while a PI value greater than 0.5 indicates a very broad distribution. To achieve long-term stability, it is important to maintain the PI parameter as low as possible.

The first order output of DLS is intensity distribution of particle size, which is weighted according to the intensity of light scattered by the particle. Using the Rayleigh

approximation, the relative contribution of particles is proportional to the (diameter)<sup>6</sup>. Thus, generally it is difficult to measure the presence of small particles (e.g. 10 nm) in a population that is dominated by larger particles (e.g. 1000 nm) because the total scattered light generated by the large particles overshadows that of the small ones. Intensity-weighted output is ideal for identifying the presence of aggregates in the sample.

The intensity distribution can be converted to volume-weighted distribution when the following assumptions are accepted: (a) all particles are spherical, (b) all particles are homogeneous, (c) particle's optical properties are known (e.g. refractive index), and (d) no error in the intensity distribution [180]. In volume-weighted distribution, the contribution of each particle in the distribution relates to the volume of particle, which is proportional to (size)<sup>3</sup>. Laser diffractometry (LD), which generates volume-based distribution, is suitable for measuring particle size greater than 3  $\mu\text{m}$ . This technique works well for spherical particles; for nanocrystals, which tend to have large aspect ratios (i.e., length/width), the size results often deviate significantly from those determined by electron microscope imaging. For non-spherical particles, LD may overestimate the particle size distribution [181, 182]. Over-prediction of the median diameters is also observed [183]. Thus, caution is needed when measuring and reporting particle size of irregular-shape particles [184].

A coulter counter, which yields the absolute number of particles per volume unit of different size classes, can be used as an additional method, for example, to quantify any contamination from microparticles. In instruments that generates a number-weighted distribution, each particle is given equal weighting irrespective of its size [180].

#### **1.3.4.2 Surface Charge**

Surface charging is important for the stability of nanocrystals in solution. According to the Derjaguin, Verwey, Landau, and Overbeek (DLVO) theory, the stability of a colloidal system depends on the balance between two counteracting forces, attractive (van der Waals) and repulsive (electrical double layer) [185]. The electrical double layer surrounding a particle consists of an inner region (Stern layer), where counter-ions are strongly bound to the particle, and an outer region (diffuse layer), where counter-ions are loosely associated. Within the diffuse layer, there exists a notional boundary, named the slipping plane, which separates counter-ions that move along with the particle and those that stay with the bulk fluid. The electric potential difference at the slipping plane versus a point in the bulk medium is defined as the zeta potential. It can be measured by using light scattering to monitor the electrophoretic mobility when the colloidal system is subjected to an electric field. In addition to the sample's surface chemistry, pH of the medium, conductivity of the fluid, and concentration of additives can influence the distributions of counter-ions surrounding the interface and thereby the zeta potential. To resist flocculation and aggregation, particles need to have sufficiently high repulsion forces. It is generally recognized that a specific value of zeta potential can be useful in predicting the physical stability of a nanosuspension formulation.  $\pm 30$  mV or larger (absolute value) is desired for an electrostatically stabilized suspension. For particles with smaller zeta potentials, surfactants may be needed to provide further steric and/or electrostatic repulsions [186]. Numerous studies have shown that surface potential can have a drastic influence on cellular uptake or even tumor targeting of nanoparticles [187-191]. One study of cationic and anionic polymeric nanoparticles with similar particle

size (90-100 nm) reported that anionic nanoparticles were transited through the degradative lysosomal pathway within the cell, while the cationic particles were transcytosed and accumulated at the basolateral membrane [188]. On the other hand, positively charged micelles caused higher hemolytic activity – due to strong electrostatic interaction between the particles and the anionic erythrocyte membrane – and accumulated in the liver proportionally to the positive charge density; in contrast, negatively charged micelles were not hemolytic [191]. Highly charged nanoparticles had a much higher opsonization rate than neutral or slightly charged nanoparticles of the same size [191, 192]. Thus, it is necessary to balance the surface charge in order to achieve maximum storage stability and minimum opsonization subsequent to intravenous administration.

#### **1.3.4.3 Crystallinity**

Crystallinity of a product is often assessed by X-ray diffraction (XRD), complemented by differential scanning calorimetry (DSC). When a compound is known to form hydrates or solvates, thermogravimetric analysis (TGA) is used as well to determine any weight loss at elevated temperature. These analyses also play a key role in characterizing polymorphic forms of a crystalline formulation. In one study to formulate SN 30191, an anticancer drug (PI3K inhibitor), by high pressure homogenization, the pre-milled form II particles were converted to form I when the sample was subjected to a pressure between 500 and 1500 bar [193]. Further increase in pressure to 1750 bar led the formation of a hydrate. Polymorphic transitions can considerably change the solubility and dissolution rate, which may alter a compound's *in vivo* performance, such as its bioavailability.

#### 1.3.4.4 Dissolution

Dissolution behavior of nanocrystals can be determined by the USP dissolution apparatus 2 (paddle) or similar methods. A large volume of dissolution medium (e.g., more than 500 mL) may be needed to minimize the influence of withdrawing samples during the measurement. Careful attention is needed when carrying out the solubility measurement of nanocrystals. It is reported that solubility results determined by centrifugation, ultracentrifugation, or filtration may be questionable because of poor separation of solid particles from the solution [194]. In the presence of high-concentrations of stabilizers or surfactants, solubility of a drug may be apparently increased, likely due to micellar solubilization of the drug [194]. It must be noted that although the dissolution rate of a nanocrystal formulation can be enhanced considerably because of the increase in surface area, the solubility increase is minimal. For instance, the solubility of loviride nanosuspension was reportedly increased by 15% when the particle size was about 150 nm [194].

The complete dissolution of spherical micronized particles with diameter of less than 50  $\mu\text{m}$  under sink condition can be estimated based on the Hixson-Crowell cube root law in the following equation:

$$\tau = \frac{\rho r_0^2}{2DC_s} \quad (2)$$

where  $\tau$  is the estimated time for complete dissolution,  $\rho$  is the density,  $r_0$  is the particle radius,  $D$  is diffusion coefficient, and  $C_s$  is the solubility of the solid material [195].

Table 1.1 and Figure 1.2 represents the plots and calculated values, respectively, of predicted time for complete dissolution of spherical particles (radius of 100 to 500 nm) composed of poorly water soluble materials, with solubility of 0.5 and 1  $\mu\text{g/ml}$ . As the solubility decreased by half, the time for a complete dissolution is doubled. The reported diffusion coefficient of compounds may vary depending on the method of calculation or analysis. For illustration purposes, the diffusion coefficients of two poorly water soluble compounds, camptothecin and paclitaxel are utilized to calculate the time for complete dissolution in Table 1.1 and Figure 1.2. Camptothecin was reported to have diffusion coefficient ranged from  $7 \times 10^{-7} \text{ cm}^2/\text{sec}$  to  $2 \times 10^{-7} \text{ cm}^2/\text{sec}$  [196], while paclitaxel has approximate diffusion coefficient value of  $2 \times 10^{-7} \text{ cm}^2/\text{sec}$  [197].

**Table 1.1.** The predicted time to achieve complete dissolution of spherical particles under sink condition based on the Hixson-Crowell cube root law equation.

<b>Time for Complete Dissolution of Spherical Particles under Sink Condition (min)</b>				
Radius (nm)	$D = 7 \times 10^{-7} \text{ cm}^2/\text{s}$		$D = 2 \times 10^{-7} \text{ cm}^2/\text{s}$	
	$C_s = 1 \mu\text{g/ml}$	$C_s = 0.5 \mu\text{g/ml}$	$C_s = 1 \mu\text{g/ml}$	$C_s = 0.5 \mu\text{g/ml}$
500	29.8	59.5	104.2	208.3
400	19.0	38.1	66.7	133.3
300	10.7	21.4	37.5	75.0
200	4.8	9.5	16.7	33.3
100	1.2	2.4	4.2	8.3

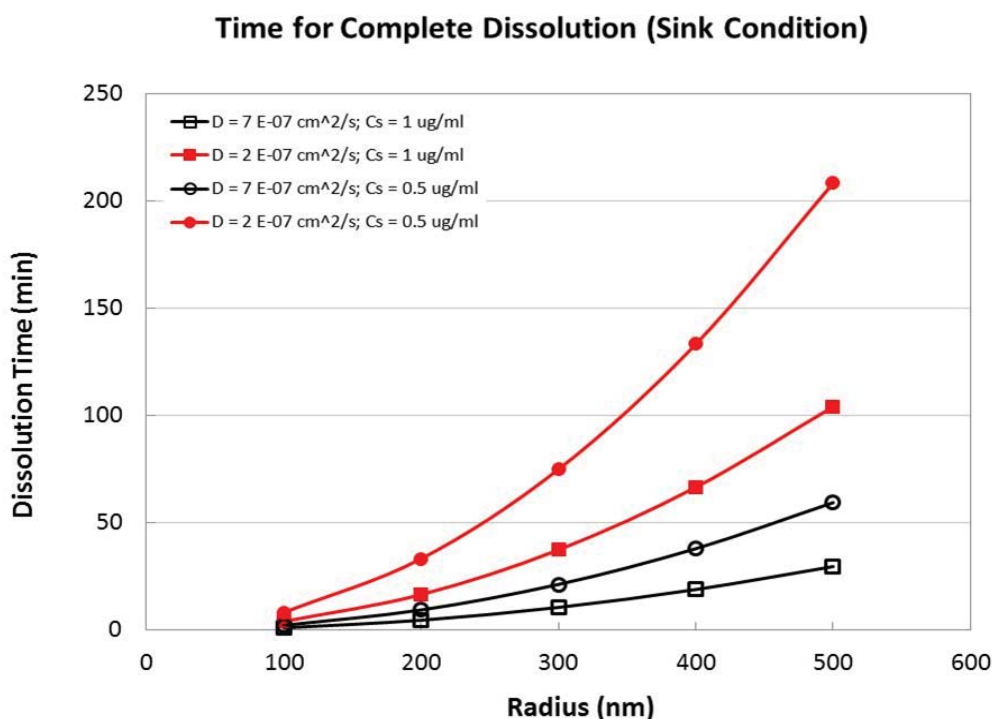


**Figure 1.2.** Predicted time for complete dissolution of spherical particles composed of poorly water soluble compounds in sink condition based on Hixson-Crowell cube root law equation.

### 1.3.5 Nanocrystals for Cancer Therapy

Combinatorial chemistry and high throughput screening have resulted a steady increase in the number of drug candidates over the years, but the majority have been poorly soluble [198-200]. Among various formulation strategies, reducing the size of solid particles of a drug compound has gained considerable attention as a delivery method [176]. Although the marketed nanocrystal-based products are mainly for oral delivery, formulated mostly by the top-down approach, nanocrystals have been exploited for other routes as well, including parenteral, dermal, mucosal, ocular, and pulmonary [122].

Relative to the conventional delivery approaches, nanocrystal formulations are free of organic solvents or other solubilizing chemicals which may cause adverse effects. The administration of escalated doses of nanocrystals, which can be up to three to ten-fold higher than the maximum tolerated dose of a conventional formulation may result in improved patient tolerability and enhanced therapeutic efficacy [201, 202]. Compared to other nano-sized drug delivery systems, nanocrystals contain nearly 100% drug loading (surfactant(s) may be used in some cases). This is a key property of nanocrystals since less than 5% of the total administered dose is delivered to the tumor site [29, 30]. Once delivered to the tumor site, the dissolution rate of drug molecule will mainly be determined by its solubility in the accumulation environment and concentration gradient. Inhibition of cancer cell growth in the delivery site begins when the drug concentration starts to exceed the  $IC_{50}$  value (i.e. half the maximum inhibitory concentration). In addition, because the majority of the nanoconstruct consists of the drug, the additional toxicity and hazard that may be introduced by the delivery carrier [203] is avoided. Depending on the method of preparation, drug nanosuspension products can either be crystalline or amorphous. In order to achieve better physical stability, a final product in crystalline state is generally preferable.

Another advantage of formulating chemotherapeutics as nanocrystals is the ease of manufacturing and scale-up. The top-down approach dominates the production of nanocrystals and has generated several marketed products [126]. Meanwhile, commercial scales of techniques that are based on bottom-up approach is continually being developed [125]. Although no such product is currently in the market, there is certainly a growing interest and need in this field. To date, the number of studies reported to use nanocrystals

for cancer therapy is still limited (Table 1.1). Because of their promising values, more studies are expected to emerge. Some recent studies that characterize the behavior and *in vitro*, *in vivo*, and clinical performance of nanocrystal formulations of antineoplastic agents are reviewed as follows.

**Table 1.2** Nanocrystal Formulations of Anticancer Drugs

Compound	Method <sup>a</sup>	Stabilizer(s)	Average Size (nm)	Zeta Potential (mV)	Ref
Piposulfan	MM	Tween 80, Span80	210.2±38.9	N/A	[201]
Camptothecin	MM	Pluronic <sup>®</sup> F108	202.3±30.5	N/A	[201]
Etoposide	MM	Pluronic <sup>®</sup> F127	256.2±53.0	N/A	[201]
Paclitaxel	MM	Pluronic <sup>®</sup> F127	279.2±29.60	N/A	[201]
Asulacrine	HPH	Poloxamer 188 (Pluronic <sup>®</sup> F68)	702±0.02(d90)	N/A	[204]
SN30191	HPH	Poloxamer 407, Solutol HS15, Mannitol	1200-1300 (d90)	N/A	[193]
Paclitaxel	3PNET	Pluronic <sup>®</sup> F127	122±35	0.82	[202, 205]
Oridonin	HPH	Pluronic <sup>®</sup> F68, lecithin, HPMC, PVP	(i) 322.7; (ii) 103.3±1.5 & 897.2±14.2; (iii) 912.5±17.6	(i) -26.74±2.68; (ii) -20.3±0.4, -21.8±0.8; (iii) N/A	(i) [174], (ii) [206], (iii) [207]
Deacetymyco epoxydiene	HPH	Lecithin, Pluronic <sup>®</sup> F68, HPMC, PVP	423±11	-23.1±3.5	[208]
Quercetin	HPH, EPAS	Pluronic <sup>®</sup> F68, Lecithin	213.6±29.3 (HPH); 282.6±0.02 (EPAS)	-22.48±4.6(HPH); -21.12±2.7(EPAS)	[209]
Paclitaxel	SLbL, US	Polyelectrolytes, BSA	100±20 (SLbL); 220±20 (US)	-45±3	[210]
Camptothecin	Anti- solvent	Without stabilizer	234.4±35.6	-41.8±1.3	[168]
Paclitaxel	Anti- solvent	Without stabilizer	438.5±8.3	-15-22	[169]

<sup>a</sup> HPH: high pressure homogenization; MM: media milling; EPAS: evaporative precipitation into aqueous solution; 3PNET: three-phase nano-particle engineering technology; SLbL: sonication assisted layer-by-layer polyelectrolyte coating; US: ultrasonication.

### **1.3.5.1 *In Vitro* Evaluation of Nanocrystals**

Free drug molecules dissolved from nanocrystals enter cells through passive diffusion. Additionally, nanocrystals can be taken up by cells via endocytosis. Particles having a size of 200 nm or less are preferentially internalized after binding to clathrin-coated pits, while particles between 200 and 500 nm are internalized by the caveolae-mediated pathway [211, 212]. The maximum size of particles that can be endocytosed is 500 nm [213]. In one of our studies, the addition of chlorpromazine (CPZ), which disrupts clathrin and hence clathrin-mediated endocytosis, reduced the cellular uptake of camptothecin (CPT) nanocrystals by about 20% compared with that of CPT nanocrystals without the inhibitor [168]. This finding suggested that clathrin-mediated endocytosis was, in some degree, responsible for the uptake of CPT nanocrystals in cancer cells. Moreover, nanocrystals were observed to exert greater cytotoxicity than a solution formulation, particularly when the incubation time was relatively short. One study showed that, against prostate cancer cells PC-3, the  $IC_{50}$  value of deacetylmycopoxydiene (DM) nanocrystals was much lower than that of the drug solution after a 12-hour incubation; the  $IC_{50}$  value of the nanosuspension and solution converged when observed at 48 hours [208]. The cell internalization of nanocrystals, which were able to provide a higher intercellular concentration of drug, may have been responsible for the increased toxicity in the early incubation period.

### **1.3.5.2 *In Vivo* Evaluation of Nanocrystals**

One of the early *in vivo* studies of nanocrystals was conducted in a murine adenocarcinoma model by testing ball-milled nanocrystals of pipsulfan, camptothecin, etoposide, and paclitaxel [201]. Solubility values of these drugs range from 200 to less than 4  $\mu\text{g/mL}$ . It was found that, when given intravenously using a multiple-dose regimen at the maximum tolerated dose (MTD), the nanocrystal formulations of the four chemotherapeutic drugs were able to suppress the tumor burden with no deaths reported, while control formulations using organic solvents and surfactants to solubilize the drugs caused 20% or more mortality. A significant increase in the MTD of nanocrystals was also reported by a recent study in which paclitaxel nanocrystals were formulated by a three-phase nanoparticle engineering technique and tested in two murine tumor models [202]. The nanocrystals were given at a dose equivalent to the MTD of a Cremophor-EL solubilized dosage form (20 mg/kg), and both formulations showed similar treatment efficacy. The nanocrystals showed a much improved therapeutic outcome when administered at 60 mg/kg. The PTX nanosuspensions were also tested by oral administration but found to be less effective than the parenteral dosage form.

Intravenously administered nanocrystals are expected to reach tumors via the EPR effect. We found that camptothecin nanocrystals, administered in a MCF-7 xenografted murine tumor model, yielded significantly better antitumor activity ( $p < 0.01$ ) than the drug salt solution [168]. Biodistribution results at 24 hour after the injection further revealed that CPT nanocrystals accumulated in the tumor at a much higher level than the salt solution. Note that a majority of nanocrystals (or any nanoparticle drug delivery systems) are still being taken up by the reticuloendothelial system (RES), mainly liver and spleen [214]. A

common practice to reduce the RES uptake and enhance biocompatibility is to modify the surface of a nanosystem, physically or chemically, with biocompatible polymers, such as polyethylene glycol (PEG), which is known to prolong the systemic circulation [215]. Because nanocrystals continue to dissolve after their administration, surface coating by polymeric surfactants onto the nanocrystals may not work. Thus, there is a critical need to investigate new ways to incorporate biocompatible molecules (and other functional molecules) into nanocrystals.

The particle size of a nanoparticle delivery system has a fundamental influence on the pharmacokinetics (PK) and biodistribution of the nanoparticles. It has been suggested that particles between 50 and 300 nm can achieve prolonged blood circulation [214, 216], which helps their accumulation in solid tumors via the EPR effect [214, 217, 218]. With the same surface charge of -25 mV, polymeric nanoparticles with the size of 150 nm were reported to have significantly longer circulation time due to the low uptake by the RES than particles of 500 nm [189]. Compared with a solution formulation, optimally designed nanovehicles are expected to bear improved PK behaviors, including increased half-life ( $t_{1/2}$ ), reduced clearance (Cl), increased area under the curve (AUC), and increased mean residence time (MRT) [218]. The PK of intravenously injected nanocrystals of chemotherapeutics (e.g., paclitaxel, asulacrine, and oridonin) was reported to be quite distinctive, best described by a two-compartmental model, where the elimination was non-zero order [204, 206, 219]. In a rabbit model, the pharmacokinetic profile of 103-nm oridonin nanocrystals, which were shown to dissolve rapidly, was similar to that of the drug solution [174]. On the contrary, the 300-nm paclitaxel [219] and 700-nm asulacrine nanocrystals [204] were rapidly taken up by the RES organs, such

as liver, spleen, and lungs, resulting in shortened distribution half-lives ( $t_{1/2\alpha}$ ) and decreased AUC. The decreased and yet prolonged AUC in plasma was found to be beneficial to minimize the toxic drug exposure. Interestingly, the 900-nm oridonin nanocrystals were found to achieve decreased Cl and  $t_{1/2\alpha}$  and increased AUC as compared with the dissolved drug [174]. Overall, prolonged elimination half-life ( $t_{1/2\beta}$ ) and MRT were observed for nanocrystals between 300 and 900 nm [204, 206, 219]. The sustained blood concentrations likely resulted from slow release of drug molecules from nanocrystals trapped by the RES organs [204, 206]. Size has also been found to affect particle accumulation and retention in the tumor. Small particles may accumulate faster in tumors, but larger ones can be retained longer [29]. Moreover, particle accumulation in the tumor relies on the leakiness of the tumor vasculature, which is further determined by the tumor type [220, 221], histological grade, and malignant severity [222]. The cutoff sizes of pores in the tumor vasculature range from 200 nm to as large as 1.2  $\mu\text{m}$ , with the majority between 380 and 780 nm [221]. Collectively, it has been suggested that in order to take advantage of the EPR effect and target tumors, nanoparticles should be smaller than 400 nm [29]. The particle size is nonetheless one of many factors that determine the pharmacokinetics and biodistribution of nanoparticles. Surface chemistry plays an important role as well. Because their surface is decorated with hydroxyl groups, amorphous silica particles with sizes of 50 and 250 nm exhibited significantly higher blood to liver ratios compared with 180-nm PEG-coated solid lipid nanoparticles in a Wistar rat model [216]. Despite their intrinsic hydrophilicity, which resulted in decreased RES clearance, detailed toxicological studies of amorphous silica particles are still limited [223].

### **1.3.5.3 Clinical Study of Nanocrystal Formulation**

A recent clinical study of Panzem<sup>®</sup>, a nanocrystal dispersion of 2-methoxyestradiol (2ME2), an endogenous estradiol-17 $\beta$  metabolite that bears antimitotic and antioangiogenic activities, demonstrated an improved pharmacokinetic performance and antitumor activity relative to its capsule formulation when given orally to 16 patients with advanced solid malignancies and 14 patients with taxane-refractory, metastatic castrate-resistant prostate cancer [224, 225]. Despite the fact that the 2ME2 nanocrystal formulation was well-tolerated and showed evidence of biologic activity, the active ingredient did not appear to have sufficient clinical activity and the study was terminated at phase II. No other clinical studies to test parenteral nanocrystal formulations for cancer therapy have been reported

## **1.4. Hybrid Nanocrystals for Theranostics**

*In vivo* imaging in animals has been extended tremendously due to the advancement in molecular and cellular techniques, increased numbers of animal models, and development of novel imaging probes. Non-invasive *in vivo* imaging is more advantageous relative to conventional, non-quantitative cytology/histology microscopy techniques [226]. The advancement in *in vivo* imaging has facilitated the ability to: optimize drug and gene therapy, visualize drug response at the molecular and cellular level, and assess disease progression [35]. Besides providing a visualization of the temporal and spatial biodistribution of the molecular probe and its relation to biological pathways, *in vivo* imaging also allow researchers to acquire longitudinal imaging of the same animal at multiple time points. More specifically, *in vivo* imaging can significantly benefit the

development of novel cancer nanotechnologies, in terms of providing early assessment of therapeutic response. Additionally, imaging may also permit the evaluation of biodistribution as well as pharmacokinetics.

Relative to other non-invasive imaging modalities, such as MRI and PET, optical imaging, which is being continuously developed, has several advantages, including high sensitivity, absence of radioactive irradiation, low running cost, and potential application in image-guided surgery [227]. In recent years, optical imaging has been used extensively to provide early assessment of therapeutic response of novel cancer nanotherapeutics. The evaluation of biodistribution and pharmacokinetics of fluorescent-labeled agents *in vivo* has been attempted as well, either by analyzing the excised tissues [228-233] or non-invasively via tomographic imaging [234]. Assuming that the optical probe remains with to the delivery vehicle, optical imaging serves as a fast screening tool for assessing the temporal accumulation in the tumor and comparing percent distribution of different formulations in the same tissue type (e.g. tumor to tumor).

With an objective to gain a better understanding of nanocrystal behavior *in vivo*, our laboratory has developed novel nanosized hybrid crystals containing a physically integrated material. The concept was inspired by a well-known phenomenon in solid-state chemistry wherein impurities are entrapped in the crystal lattice of a host particle. The existence of foreign substances in a host is typically insignificant, having little effect on the structure and integrity of the host crystal structure but capable of casting drastic influence on the optical appearance and other physical properties of the host. Examples are abundant. Colored diamonds are one famous example; synthetic hybrid crystals include alloys and semiconductors. The most relevant examples are “dyeing crystals”,

where guest dye molecules are integrated in organic crystals [235]. As a proof of concept, our laboratory has tested whether or not fluorophores can be entrapped in individual drug crystals. Examples are the incorporation of rhodamine B and fluorescein into acetaminophen and aspirin, respectively, drug crystals (Figure 1.2).

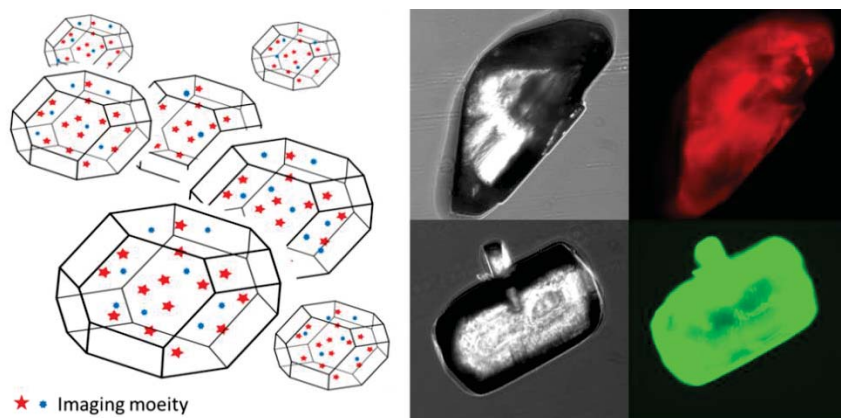


**Figure 1.3.** The illustration (left) and examples (right) of hybrid crystals. Rhodamine B (red) and fluorescein (green) were embedded in acetaminophen (top) and aspirin (bottom) crystals, respectively.

Similar to pure drug nanocrystals, hybrid nanocrystals can be prepared using the anti-solvent method, where a concentrated drug solution (in organic solvent) is added rapidly to the anti-solvent, water, under intense stirring and sonication. Fluorophore(s), which is/are pre-mixed with water, can be entrapped as the crystals grow. Because nanocrystals are being formed rapidly due to the sudden drop in solubility, they have a large quantity of defects, where imaging agents can be integrated. It is important to note that the fluorophore is physically integrated, requiring no chemical conjugation. The tiny amount

of integrated-fluorophore can be detected in animals by optical imaging. Based on some preliminary results, hybrid nanocrystals of paclitaxel containing a near infrared fluorophore were able to accumulate in the tumor and exert efficacy in a breast cancer MCF-7 xenograft [169].

### **1.5. Statement of Problems**

Chemotherapy remains as the cornerstone of cancer therapy, specifically in inhibiting the growth of residual or metastasized cancer cells after the debulking surgery. Nonetheless, in clinical settings, the delivery of chemotherapeutics has been impeded by their poor aqueous solubility. Take paclitaxel (PTX) as an example. Over the past two decades, it has played a significant role in the treatment of various malignancies, including ovarian, lung, breast, and head and neck carcinomas [236]. After its discovery in the early 1960s, problems related to its solubility remain challenging. Early investigations led to the conclusion that the solubilization of PTX in a 1:1 ratio of Cremophor EL<sup>®</sup>, a polyoxyethylated castor oil vehicle, and dehydrated ethanol was the most viable option for commercial formulation of PTX (Taxol<sup>®</sup>). A high incidence of acute hypersensitivity reactions, nephrotoxicity, neurotoxicity, and neutropenia [3, 4] has been associated with the inherent toxicity of the delivery vehicle, Cremophor EL. Even with premedication of corticosteroids and a histamine antagonist, 40% of patients still developed minor reactions (e.g. flushing and rash) and nearly 3% of them experienced potentially life-threatening reactions [4, 237]. Overall, conventional chemotherapy, which utilizes small molecule drugs, suffers from toxicity due to the lack of tumor selectivity and the use of harsh solvents for solubilization.

Efforts in minimizing systemic toxicity by targeted anti-tumor therapy are underway. Specifically, chemotherapeutics have been encapsulated into nano-sized vehicles, which can selectively accumulate and be retained in the tumor due to the EPR effect [5-7]. The leakiness of the tumor blood vessel and decreased efficiency of tumor lymphatic drainage allow the accumulation of nanovehicles at the target site.

In the past two to three decades, numerous research efforts have been concentrated on creating nanoconstructs, including liposomes, micelles, solid lipid nanoparticles, polymeric nanoparticles, dendrimers, and core-shell structures, for the delivery of cancer therapy. Although some products are currently being investigated in clinical trials, only a few have been approved by the FDA [22, 23]. One of them is Abraxane<sup>®</sup> (nab paclitaxel; ABI-007), which is a novel formulation of PTX prepared by high-pressure homogenization in the presence of human serum albumin [238]. The resultant amorphous particles have a mean diameter of 130-150 nm, which can be injected intravenously without any further need of solubilization. Adverse side effects, albeit minimized, were still observed during the clinical trials [239]. However, the cost of Abraxane<sup>®</sup> is outrageously high, relative to the generic formulation, Taxol<sup>®</sup>. Depending on the dose needed, patient may need to spend between \$10,000 to 22,000 over the period of 12 weeks [240].

In general, the current approaches for solubilizing and encapsulating antineoplastic agents into nano-sized vehicles are still limited by low drug loading, drug leakage [24, 25], inherent toxicity of the encapsulating materials [27], and complex fabrication methods [28], which makes the manufacturing at large scale hard to achieve. Nano-sized drug crystals (nanocrystals) contain close to 100% drug, and it is feasible to produce

them at a large scale. Due to the absence of harsh solvents, nanocrystal formulations of anticancer drugs also were reported to have elevated maximum tolerated dose relative to conventionally delivered drug [201, 202]. Hence, nanocrystals possess appealing properties, which may be suitable for cancer therapy.

Indeed several antineoplastic active ingredients, including PTX, have been formulated as nanocrystals for intravenous administration. Most PTX nanocrystals were generated by top-down approaches, either via milling [201, 241] or high-pressure homogenization [219]. One study developed PTX nanocrystals via a novel bottom-up approach [242]. Most studies only reported the extent of efficacy and toxicity of the formulation in murine xenograft models. When administered at the same dose, 20 mg/kg, PTX nanocrystals were reported to exert a similar efficacy as Taxol [242]. Increased efficacy, with minimal toxicity, was observed when the dose was elevated to 60 mg/kg [242] and 100 mg/kg [129]. Pharmacokinetics and tissue distribution of PTX nanocrystals, prepared by high-pressure homogenization, were studied in the rats. Although PTX nanocrystals were rapidly cleared by the reticuloendothelial system (RES), it was postulated that the prolonged half-life of elimination was due to the slow release of PTX from macrophages. Yet, the degree of tumor accumulation has not been investigated thus far.

Furthermore, the advancement of *in vivo* imaging modalities, specifically optical imaging, has significantly benefited the development of novel cancer nanotechnologies, in terms of providing an early assessment of therapeutic response. The *in vivo* imaging devices have enabled the visualization of the temporal and spatial biodistribution as well as longitudinal imaging of nanotheranostics in the same animal at multiple time points. Novel hybrid nanocrystals were developed by entrapping near infrared fluorophore(s) in

drug nanocrystals in a simple, one-pot synthesis. Even with continuous advancement in technology, optical imaging has inherent limitations in terms of fluorescent probe localization, depth of detection, and quantification. Although *in vivo* fluorescence imaging is widely utilized in pre-clinical settings, minimum efforts have been expanded to investigate the correlation between drug concentration and fluorescence signal in *ex vivo* tissues.

## **1.6. Objectives**

The overall goal of this dissertation is to formulate both pure and hybrid nanocrystals, evaluate their performance *in vitro* and *in vivo*, and investigate the extent of tissue distribution and tumor accumulation in a murine model. Specifically, paclitaxel (PTX) will be used as a model drug.

Our central hypothesis is that solvent-free nanocrystals allow a safer delivery of poorly water soluble drugs and are able to accumulate in the tumor due of the EPR effect, releasing free drug molecules that exert comparable therapeutic effects to the conventional delivery method. As such, the following specific aims are pursued in order to test the hypothesis:

- 1). Fabricate pure nanocrystals of paclitaxel, fully characterize their physical properties, and determine their physical and chemical stability in different media and storage conditions.

PTX nanocrystals were produced by a combination approach. The nano-precipitates produced by the anti-solvent methods were further homogenized to obtain a narrow size

particle distribution. The particle size, size distribution, morphology, surface charge, crystallinity, and the crystal form of nanocrystals were determined. The alterations in particle size and morphology of paclitaxel nanocrystals in different media were evaluated by scanning electron microscopy and dynamic light scattering. The stability, in terms of maintaining particle size, morphology, surface charge, and chemical composition, of PTX nanocrystals in aqueous suspension stored at 4°C were compared to that in ambient temperature. The particle size and morphology of the freeze-dried product stored at 4°C, room temperature, and 40°C/75% relative humidity, were evaluated.

2). Evaluate the cellular cytotoxicity of pure PTX nanocrystals and mechanism of cellular internalization of hybrid PTX/FPR-648 nanocrystals.

PTX nanocrystal suspensions were tested for their inhibitory effect *in vitro*, particularly in human colon adenocarcinoma HT-29 cells. The IC<sub>50</sub>, the half maximum inhibitory concentration, of PTX nanocrystals were compared with Taxol at three different time points: 24, 48, and 72 hours, to elucidate any duration-dependent chemosensitivity. PTX/FPR-648 hybrid nanocrystals were produced by the combination approach, as previously mentioned. Particle size and morphology of the product were determined. The cellular internalization of PTX/FPR-648 nanocrystals in human breast cancer MCF-7 was investigated to elucidate higher cytotoxicity associated with PTX nanocrystals in human breast cancer MCF-7. Confocal microscopy was utilized to seek any evidence of nanocrystal internalization via non-phagocytic endocytosis pathways.

3). Evaluate the efficacy and toxicity of pure and hybrid PTX nanocrystals in xenograft murine models as well as the performance of hybrid PTX nanocrystals *in vivo*.

a. The efficacy and toxicity of pure PTX nanocrystals were assessed from the Kaplan-Meier plot and percent of body weight change generated through a survival study in colon cancer HT-29 xenograft. The PTX nanocrystals were compared against the negative control (saline) and positive control (Taxol) at the same dose, 20 mg/kg.

b. Pure and hybrid PTX nanocrystals were produced using the anti-solvent method. The ability of PTX hybrid nanocrystals to perform as a theranostic system was tested in the murine human breast cancer MCF-7 orthotopic xenograft. Two fluorophores were incorporated: MMPSense 750, a bioactivatable fluorophore to monitor the disease state, and FPR-648, a regular near infrared fluorophore to trace the distribution and accumulation in the tumor site. The efficacy and toxicity of PTX/MMPSense/FPR-648 were compared to untreated, Taxol, and pure PTX nanocrystals by evaluating the percent change in tumor volume and body weight, respectively, daily for a total of 7 days subsequent to a single injection of 20 mg/kg.

c. Pure and hybrid nanocrystals were produced by the anti-solvent method. Nicardipine, a calcium channel blocker, which may enhance the EPR effect via local blood vessel dilation, was incorporated into the PTX nanocrystals. The efficacy and toxicity of PTX/nicardipine hybrid nanocrystals were compared to Taxol and PTX pure nanocrystals by evaluating the percent change of tumor volume and body weight, respectively, for 7 days after a single dose of treatment at 20 mg/kg of PTX.

4). Compare the tissue distribution and tumor accumulation of  $^3\text{H}$ -PTX/FPI-749 nanocrystals and  $^3\text{H}$ -Taxol by radioactive analysis, and determine if the post-mortem

distribution of fluorescence signals from the optical imaging can be correlated to that of radiolabeled PTX.

<sup>3</sup>H-PTX/FPI-749 nanocrystals were produced by using the combination approach. The morphology and particle size of hybrid nanocrystals without the radioactive payload were determined. The tumor accumulation and tissue distribution of <sup>3</sup>H-PTX/FPI-749 nanocrystals were compared head-to-head with the conventional formulation, <sup>3</sup>H-Taxol. Furthermore, the *ex vivo* distribution of fluorescence signal detected under optical imaging and radiolabeled PTX were compared.

In the following chapters, the results from each specific aim will be presented and further discussed. The purpose is to provide a thorough evaluation of the physicochemical characterization and behavior *in vitro* and *in vivo* of paclitaxel nanocrystals.

## Chapter 2 - Preparation and Physicochemical Characterization of Paclitaxel

### Nanocrystals

#### 2.1 Introduction

Paclitaxel (PTX) is isolated from the bark of North American Pacific yew tree, *Taxus brevifolia* [243]. It exerts notable antineoplastic activity in clinical studies against various cancers, including ovarian, lung, breast, and head and neck carcinomas [236]. The efficacy of PTX in other human carcinomas is also actively being investigated. PTX prevents the ability of cells to perform normal mitosis (in G2 and M phases) by both promoting and stabilizing microtubule assembly [244]. It has a molecular weight of 853.9 g/mol and is highly lipophilic (Figure 2.1). The clinical application of PTX has been limited due to its low solubility in water ( $< 1 \mu\text{g/mL}$ ). Currently, Taxol and Abraxane are two commercially available formulations of PTX. In Taxol, PTX is dissolved in a mixture of Cremophor EL<sup>®</sup>, a polyoxyethylated castor oil vehicle, and dehydrated ethanol USP (1:1, v/v). Cremophor EL, however, is notably responsible for some adverse effects, including hypersensitivity reactions, nephrotoxicity, neurotoxicity, and neutropenia [3, 4]. To alleviate the reactions, corticosteroids and histamine antagonist are generally given prior to the infusion. Yet, 40% of the patients still develop minor reactions (e.g. flushing and rash) and nearly 3% of them experience potentially life-threatening reaction [4, 237]. Abraxane (nab paclitaxel; ABI-007) is a novel formulation prepared by high-pressure homogenization of PTX in the presence of human serum albumin at a concentration of 3-4%, similar to that found in the blood [238]. With its mean particle diameter of 130-150 nm, close to one-hundredth the size of a single red

blood cell, the colloidal suspension eliminates the need for solubilization. This novel formulation does hold some promise in cancer therapy. The preclinical and clinical studies of Abraxane have been reviewed [239]. Other alternative attempts to create Cremophor-free formulations, such as cosolvents, emulsions, micelles, liposomes, microsphere nanoparticles, cyclodextrins, paste, and implants, have been made to improve the solubility of PTX and minimize side effects associated with the delivery vehicle [245].

In recent years, PTX also has been formulated as nanocrystals (nanosuspension) [201, 210, 219, 241, 242]. Compared to Taxol and Abraxane, nanocrystals exhibit a high ratio of drug to excipient (drug loading). Thus, upon infiltration to the target cells, nanocrystals can potentially unload elevated drug concentration to the cells, resulting in an increase in therapeutic efficacy. Nanocrystals are also simple to formulate and feasible for scale up. Additionally, relative to human serum albumin utilized in the production of Abraxane, the excipients used, if any, for nanocrystal formulation are readily available and cost-effective [246]. Out of the five reported formulations of PTX nanocrystals (nanosuspension), three were produced solely by the size-reduction method, either by milling [201, 241] or high-pressure homogenization [219]. Patterkari and colleagues attempted to fabricate the nanocolloids by both top-down (ultrasonication) and bottom-up approaches (anti-solvent/evaporation) [210]. Meanwhile, Liu and others developed the PTX nanocrystals by a novel bottom-up approach known as three-phase nanoparticle engineering technology (3PNET), which requires at least a ratio of 1 to 5 of PTX and Pluronic F127<sup>®</sup> [242]. The nanocrystals generated by the aforementioned methods have particle sizes between 100 and 400 nm.

In this study, to obtain both narrow size distribution and approximate size of 200 nm, PTX nanocrystals were produced by combining the bottom-up (anti-solvent) and top-down (homogenization) methods. Since the nanocrystals are intended for intravenous administration of cancer therapy, it is necessary that the fabricated nanocrystals are below 400 nm, the suggested maximum value for particles to exploit the enhanced permeability and retention (EPR) effect [29]. The physical properties, crystallinity, and storage stability of the produced PTX nanocrystals were evaluated.

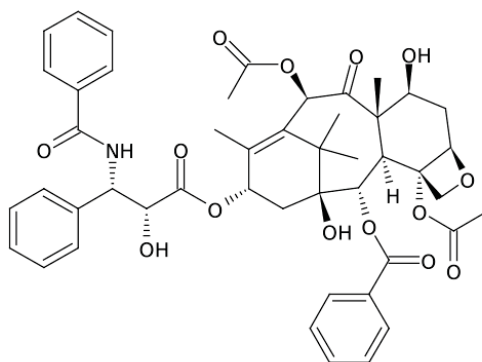


**Figure 2.1.** Chemical structure of Paclitaxel (PTX)

## 2.2 Materials and Methods

### 2.2.1 Materials

Paclitaxel (PTX, >99.5%, USP30) was purchased from 21CECPharm (United Kingdom). Ethanol (HPLC grade), acetonitrile (HPLC grade), phosphate buffered saline, and cell culture media were purchased from Fisher Scientific (Pittsburgh, PA). Sodium chloride was purchased from Sigma (St. Louis, MO). Saline (0.9% w/v sodium chloride) for injection was from Hospira (Lake Forrest, IL). PTX dihydrate was obtained by drying

PTX anhydrous (from manufacturer) that had been placed and stirred in DI water overnight. Deionized (DI) water (by Milli-Q<sup>®</sup>, filtered through 0.2 µm membrane) was used for all the experiments. 0.050 µm (50 nm) Whatman<sup>®</sup> nuclepore polycarbonate track-etched membranes used for filtration were purchased from Fisher Scientific (Pittsburgh, PA).

### **2.2.2 Preparation of Paclitaxel Nanocrystals**

Paclitaxel nanocrystals were produced by the combination approach as depicted in Figure 2.2. Specifically, the nanocrystals produced by a bottom up approach, anti-solvent method, were then subjected to homogenization (i.e. a top-down approach). In a typical experiment, 1 mL of 3 mg/mL of paclitaxel in ethanol was added rapidly to 20 mL deionized water in 3-neck round bottom flask (500 mL). The mixture was stirred at 1,100 rpm with stirrer shaft and under intense sonication (in sonication bath F20D, output of 70 W and 42±6 KHz, Fisher Scientific). Ice was added to the sonication bath to keep the temperature between 14-18°C. After 10 minutes of stirring time, the flask was removed from the stirring station and placed in a desiccator to remove bubbles generated due to rapid stirring. The mixture was then filtered through a 50 nm polycarbonate membrane. The retentate was re-suspended in 2 mL DI water placed in 20 mL scintillation vial and homogenized (Fisher Scientific<sup>®</sup> PowerGen<sup>®</sup> 125) for 6 minutes at 30,000 rpm. When needed, nanocrystal batches were combined to obtain the desired concentration. For solid-state characterization and storage stability studies, the concentrated suspension of PTX nanocrystals were freeze-dried (LabConco Freeze Dryer 4.5) overnight.

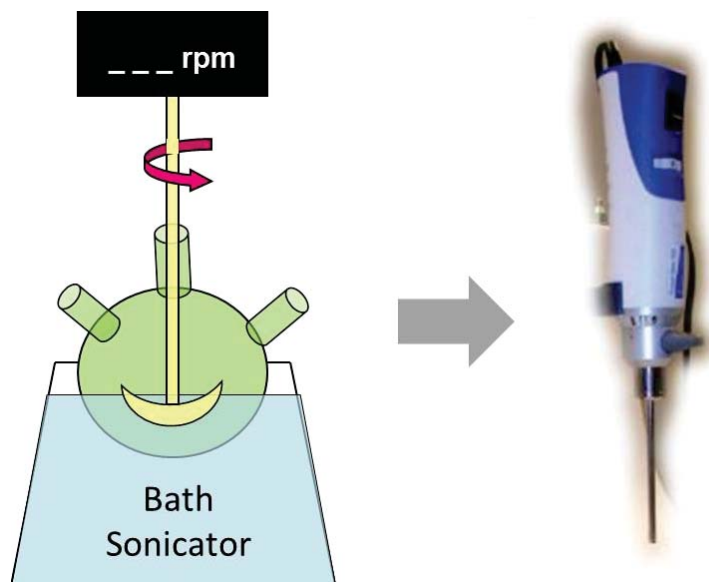


**Figure 2.2.** Schematic of nanocrystal preparation method by combination approach.

### 2.2.3 Particle Size and Surface Charge Measurements of Paclitaxel Nanocrystals

Scanning electron microscope (SEM) images were obtained using a Hitachi SEM 4300 at an accelerating voltage of 3 kV. All SEM samples were prepared similarly by the following method. A drop (10-20  $\mu\text{L}$ ) of nanocrystal suspension was placed on a 50 nm nuclepore filter membrane. After being vacuum-dried, the filter membrane was attached to the SEM sample holder by using PELCO Tabs™, Carbon Conductive Tabs, 9 mm OD (Ted Pella, Redding, CA). Prior to visualization, using a sputter coater, samples were coated with conductive layers of gold palladium (Au/Pd) for 1 minute with a current of 20 mA, resulting in an approximately 10-15 nm thick coating. Analysis of particle size from the SEM images was performed using SigmaScan (Systat software Inc, San Jose, CA). The mean size (i.e. longest dimension) and standard deviation from approximately one hundred particles are presented. In addition to SEM analysis, the hydrodynamic diameter of PTX nanocrystals was measured in deionized water (viscosity of 0.8872 cP

and refraction index of 1.330) at a concentration of 0.1 mg/ml using dynamic light scattering (DLS), Malvern Nano-ZS instrument (Malvern Instruments, UK). The zeta potential was measured using the same instrument in 10 mM sodium chloride (NaCl) at a concentration of 0.1 mg/ml. Both particle size and zeta potential measurements were performed in triplicate.

#### **2.2.4 Solid-state Characterization of Paclitaxel Nanocrystals**

The crystallinity of freeze-dried PTX nanocrystals was assessed by using a Rigaku X-ray diffractometer (Rigaku Americas Corp.) with Cu K $\alpha$  radiation (40 kV, 44 mA). Scans were obtained from 5 to 40 $^{\circ}$ 2 $\theta$ , with steps of 0.04 $^{\circ}$  and scan rate of 0.5 $^{\circ}$ 2 $\theta$ /min. Modulated differential scanning calorimetry (MDSC) analysis was performed on a TA Instruments Q2000 (TA Instruments, New Castle, DE). DSC thermograms for both PTX nanocrystals and dihydrate were obtained using a 3 $^{\circ}$ C/minute heating rate from 25 to 300 $^{\circ}$ C in pinhole pans. PTX nanocrystals and dihydrate were modulated at  $\pm$  1.5 $^{\circ}$ C / 60 seconds and  $\pm$  0.48 $^{\circ}$ C / 60 seconds, respectively. Thermogravimetric analysis (TGA) analysis was performed on TA Instruments Q50 (TA Instruments, New Castle, DE) at a heating rate of 10 $^{\circ}$ C/minute from 25 to 300 $^{\circ}$ C. The corresponding TA Instruments Universal Analysis software was used to analyze the DSC and TGA data.

#### **2.2.5 HPLC Analysis**

Quantification of paclitaxel was conducted by high liquid chromatography (HPLC, Waters Breeze) with a Waters' Symmetry C18 5  $\mu$ m column (4.6 x 150 mm); it was analyzed by a UV detector (Waters 2487 dual  $\lambda$  absorbance detector) at 227 nm with a

mobile phase of ethanol/acetonitrile (50:50) pumped at a rate of 2 mL/min (Waters 1525 binary pump). The column was equilibrated to 35°C prior to sample injection (20 µL).

### **2.2.6 Solubility of Paclitaxel Nanocrystals in PBS**

Excess amount of PTX anhydrous (from manufacturer), PTX dihydrate, and PTX nanocrystals were placed in 20 mL of scintillation vials (n=3) containing PBS, which had been equilibrated to 37°C. The vials were sealed, placed in rotator, and kept in a 37°C incubator (VWR Shel Lab Model 1525, Sheldon Manufacturing, Inc., Cornelius, OR) for the entire period of the study. At various sampling intervals, 1 mL of solution was removed from each vial and passed through a Millex LCR 0.45µm PTFE filter, 25 mm. The filtrate was appropriately diluted with ethanol and assayed by HPLC.

### **2.2.7 Particle Size Analysis of Paclitaxel Nanocrystals in Different Media**

Particle size of PTX nanocrystals was monitored after incubation in the following media (at 0.1 mg/mL) was monitored: (a) saline, (b) cell culture media (Dubelco's Modified Eagle Medium (DMEM) with no phenol red + 10% fetal bovine serum), and (c) nude mouse' whole blood/buffered sodium citrate (9:1 v/v, 0.109 M, 3.2%, to prevent coagulation). Specifically, PTX nanocrystals were suspended in the media at a concentration of 0.1 mg/ml and incubated at 37°C with a shaking speed of 100 rpm (Series 2.5 Incubator Shaker, New Brunswick Scientific Co., Inc, Edison, NJ). Prior to SEM analysis, the mixture was briefly mixed using a vortex mixer, and 10-20 µL of sample was withdrawn for SEM analysis. All SEM images were analyzed with SigmaScan as described

previously. The hydrodynamic size of the PTX nanocrystals in saline and cell culture media were also evaluated at 37°C by using a DLS Malver Nano-ZS.

### **2.2.8 Storage Stability of Paclitaxel Nanocrystals**

The storage stability of PTX nanocrystals was analyzed for both suspension and freeze-dried forms. The suspension of PTX nanocrystals was stored at 3 mg/ml in a refrigerator at 4°C and at room temperature. The freeze-dried form was stored in a refrigerator at 4°C, at room temperature, and in a stability chamber at 40°C/75% relative humidity. At various sampling intervals, key parameters were analyzed. For the suspension, particle size (DLS and SEM), zeta potential, and % PTX remaining were determined. The freeze-dried product was re-suspended in DI water and subjected to sonication prior to the SEM analysis.

## **2.3 Results and Discussion**

### **2.3.1 Particle Size and Surface Charge Measurements of Paclitaxel Nanocrystals**

PTX nanocrystals with average size of 200 nm can be produced by the combination approach. Figure 2.3 illustrates the typical morphology and size of the PTX nanocrystals. Particularly for the specific batch imaged, the hydrodynamic diameter ( $Z_D$ ) was  $176 \pm 1$  nm. Compared to the DLS result, the particle size measured from the SEM images using the SigmaScan,  $200 \pm 60$  nm, correlates fairly well. When measured in 10 mM NaCl at a concentration of 0.1 mg/mL, the surface charge was  $-6.3 \pm 0.2$  mV (pH:  $6.3 \pm 0.4$ ). Figure 2.4 and 2.5 show the graphs obtained from the Nano-ZS for particle size and zeta potential measurements, respectively. The DLS generated a polydispersity index (PI) of

$0.08 \pm 0.02$ . The measured PI, which was less than 0.25, suggested the presence of narrow particle size distribution.

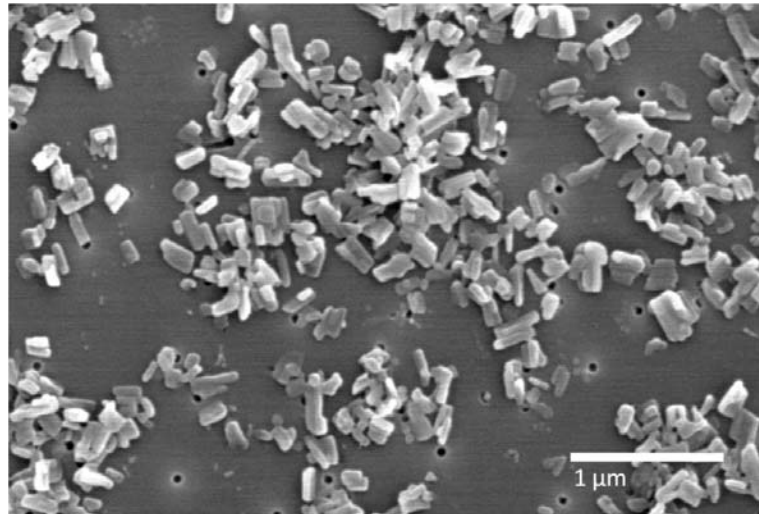


**Figure 2.3.** SEM image showing typical morphology and size of PTX nanocrystals produced with the combination approach.

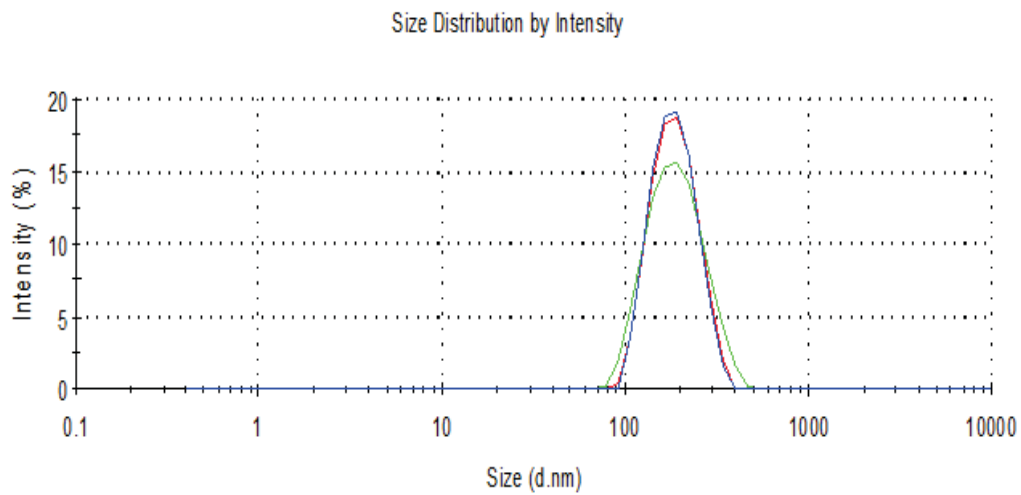


**Figure 2.4.** Particle size measurements of PTX nanocrystals suspended in DI water at 0.1 mg/mL by Nano-ZS. The three lines represent the triplicate measurements.

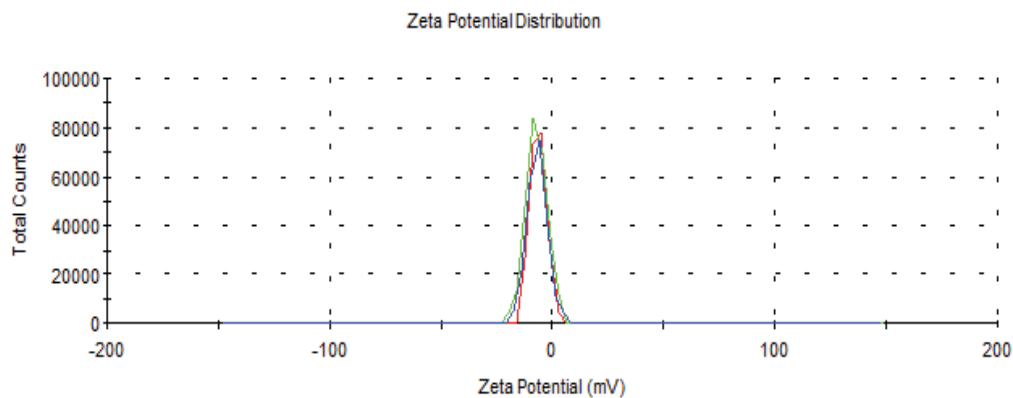


**Figure 2.5.** Zeta potential measurements of PTX nanocrystals suspended in 10 mM NaCl at 0.1 mg/mL by Nano ZS. The three lines represent the triplicate measurements.

The PTX nanocrystals produced by the combination approach had a well-defined, short rod-like morphology. Because the nanocrystals had an aspect ratio (i.e. length/width of particle) of approximately 2 and narrow size distribution (i.e. as indicated from the PI), DLS was able to provide a fairly good correlation and serve as a non-invasive technique to measure the particle size. The intensity-weighted average hydrodynamic size ( $Z_D$ ) of particles correlates to the number-weighted distribution generated by analysis from the SigmaScan.

Particle size is known to have an impact not only on biodistribution, but also clearance and tumor uptake [29]. The smaller particles (e.g. 50-300 nm) generally have a tendency to be slowly removed from the circulation [214, 216]. However, due to the tumor dynamic status and heterogeneity (e.g. vascular leakiness or cut-off [220, 221]) as well as specific characteristics (e.g. size, shape, charge) of the particle, it is difficult to predict the maximal value of particle size that can exploit EPR. Nonetheless, it has collectively been

suggested that particles up to 400 nm are able to take advantage of the EPR effect [29, 247]. To that end, with the particle size of approximately 200 nm, nanocrystals should be able to extravasate into the tumor site.

Acquired data on surface charge will provide some insight on stability and particle interactions with biological fluid *in vivo*. It is well-accepted that in order to obtain an electrostatically stabilized suspension, a surface charge of  $\pm 30$  mV or larger (absolute value) is desired [191]. However, studies have indicated that highly charged nanoparticles had a much higher opsonization rate than neutral or slightly charged nanoparticles of the same size [191, 192]. The zeta potential of our PTX nanocrystal product was generally around -15 to -22 mV when measured in DI water [169]. The observed negative surface charge might possibly be due to the surface adsorption of PTX degradation (i.e. hydrolysis) products [248]. The large fluctuations, which often observed during zeta potential measurements in water, may be due to the lack of pH control and low ionic strength. Because pH of the medium, conductivity of the fluid, and concentration of additive heavily affect the surface charge, it is imperative to note the specific parameters during measurement. When measured in 10 mM NaCl at 25°C and a concentration of 0.1 mg/mL, the zeta potential of PTX nanocrystals ranged between -6 to -9 mV. The zeta potential of the batch presented in Figure 2.3 was  $-6.3 \pm 0.2$  mV (pH:  $6.3 \pm 0.4$ ). A decrease of electrostatic stability, which was due to the decrease of double layer thickness, was expected with the increased in ionic strength [249].

### 2.3.2 Solid-state Characterization of Paclitaxel Nanocrystals

The PXRD diffractograms of PTX anhydrous, PTX dihydrate, and freeze-dried PTX nanocrystals are compiled in Figure 2.6. The PTX obtained from the manufacturer was in the anhydrous form. However, since PTX nanocrystals came in contact with water during the preparation process and storage prior to being freeze dried, they were found to be in the dihydrate form. The sharp diffraction peaks of PTX nanocrystals confirmed they were crystalline and therefore superior in chemical stability relative to the amorphous form. The PTX dihydrate was obtained by suspending and stirring the commercial PTX in water at ambient temperature for 24 hours [250]. Solid dihydrate product was then collected by filtration and vacuum drying.

Both freeze-dried PTX nanocrystals and dihydrate were also analyzed by modulated DSC (Figure 2.7). The MDSC reversible heat flow may give information regarding the existence of a glass transition temperature  $T_g$ , which could hardly be detected. It further confirmed that the PTX nanocrystals did not contain a significant amount of amorphous material. The endothermic peaks between 50-100°C and 160-170°C suggested the removal of water and a solid-solid transition from the dihydrate to the dehydrate (anhydrous) form, respectively [250]. Degradation was then observed between 210-230°C. TGA analysis was performed on PTX nanocrystals and presented in Figure 2.8. The weight loss of 4.4%, which corresponds to 2.01 mol of water/mol of PTX, further confirmed that PTX nanocrystals were indeed in the  $\text{PTX}\cdot 2\text{H}_2\text{O}$  (dihydrate) form.

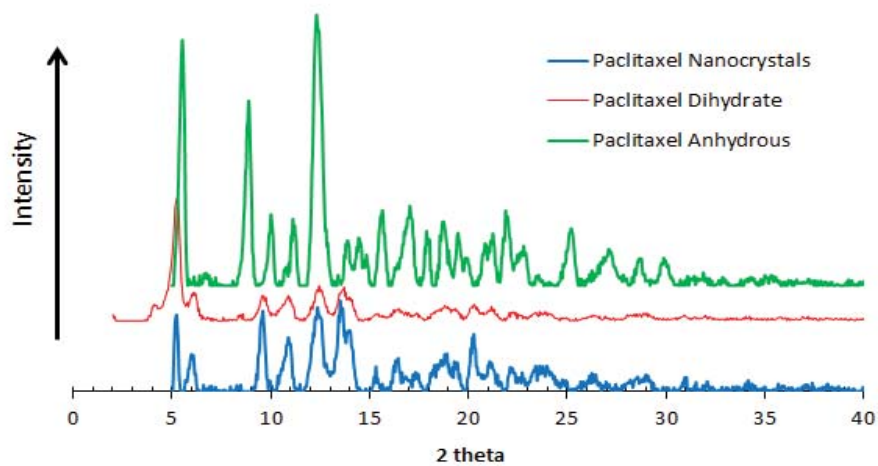


**Figure 2.6.** Powder X-ray diffractograms of PTX nanocrystals, dihydrate, and anhydrous.

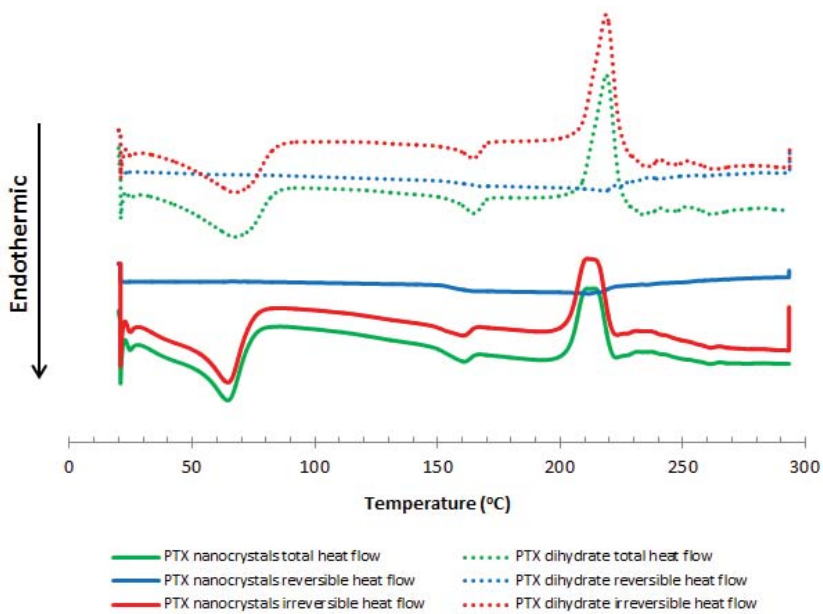


**Figure 2.7.** Modulated DSC thermograms of PTX nanocrystals and dihydrate.

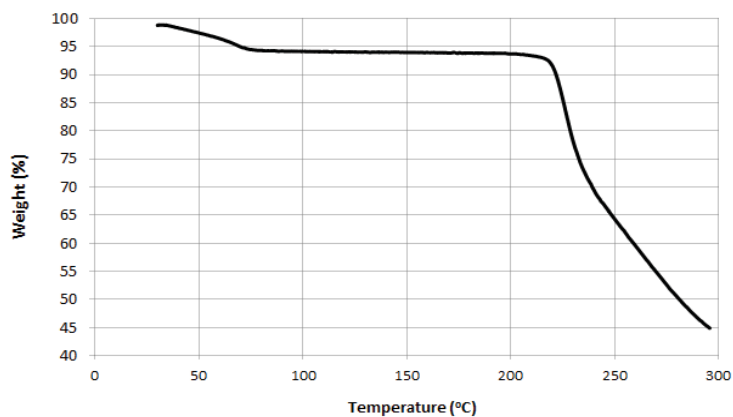


**Figure 2.8.** TGA analysis of PTX nanocrystals.

### 2.3.3 Solubility of Paclitaxel Nanocrystals in PBS

The kinetic and thermodynamic solubility of PTX nanocrystals were evaluated in comparison with the two forms of PTX, anhydrous and dihydrate. Their solubility profiles in 37°C PBS were plotted against time (Figure 2.9). The kinetic solubility of PTX nanocrystals ( $2.00 \pm 0.11 \mu\text{g/ml}$ ) was significantly higher ( $p < 0.05$ ) than that of PTX dihydrate ( $1.78 \pm 0.11 \mu\text{g/ml}$ ) in the first hour. In addition to an increase in dissolution rate, an increase in saturation solubility is often associated with nanocrystal formulation. The increase in saturation solubility can be related to the particle radius (curvature) [251] by the Ostwald-Freundlich equation as follows:

$$\ln \frac{C_{s,r}}{C_{s,\infty}} = \frac{2\gamma V_m}{rRT}$$

with  $C_{s,r}$  and  $C_{s,\infty}$  the solubilities of particle with radius  $r$  and of a very large particle, respectively,  $\gamma$  the interfacial surface between the solid surface and surrounding medium,  $V_m$  the molar volume of the compound,  $R$  the gas constant, and  $T$  the absolute temperature. Nonetheless, nanocrystals were not able to maintain the high energy

supersaturation state. It transformed to a lower energy state as observed by the decrease in the solubility. PTX anhydrous behaved similarly. Typically, the anhydrous form had an elevated kinetic solubility (dissolution) in aqueous media. The solubility concentration decreased as the anhydrous form transformed to the dihydrate after 24 hours of equilibration time. The solid PTX dihydrate, which was obtained from suspending commercial PTX (anhydrous) for 24 hours, may still contain a small percentage of PTX anhydrous as it had a similar solubility pattern as the anhydrous form during the first day of study. After equilibrating for 72 hours, the solubilities of the PTX anhydrous, dihydrate, and nanocrystals in PBS at 37°C were  $1.38 \pm 0.08$ ,  $1.15 \pm 0.09$ ,  $1.20 \pm 0.03$   $\mu\text{g/ml}$ , respectively. No significant solubility change was observed after 96 hours of equilibration time.

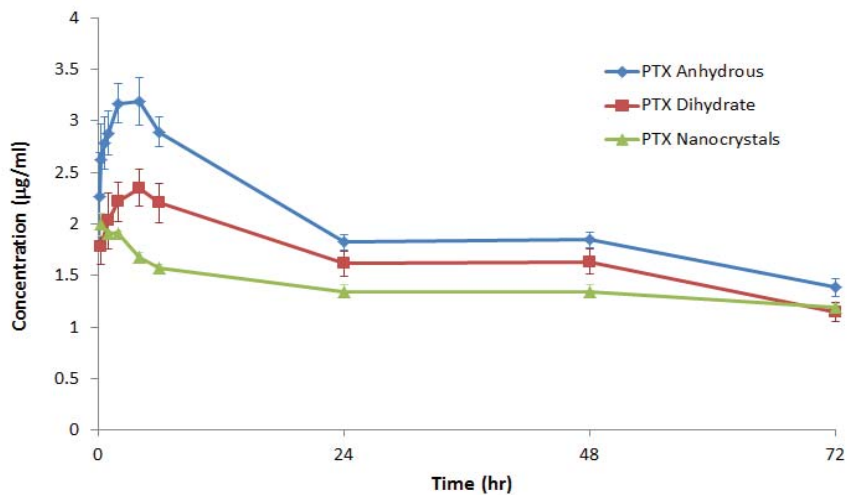


**Figure 2.9.** Solubility profiles of PTX anhydrous, dihydrate and nanocrystals in PBS at 37°C.

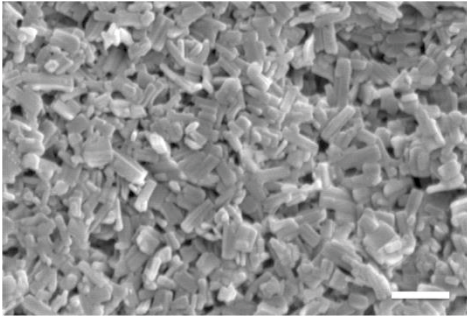
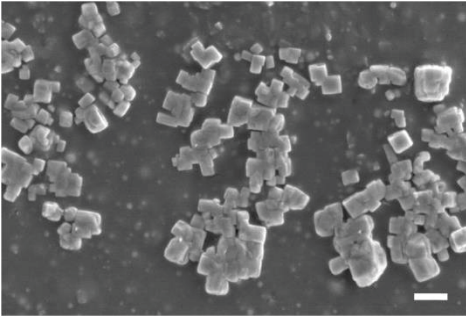
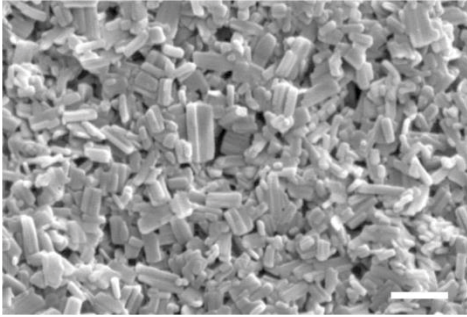
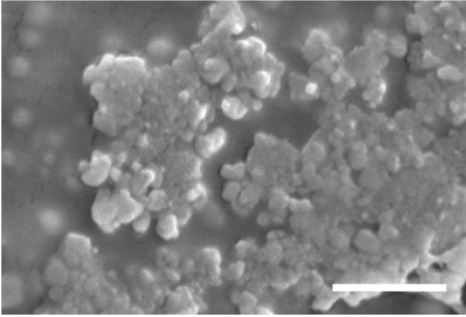
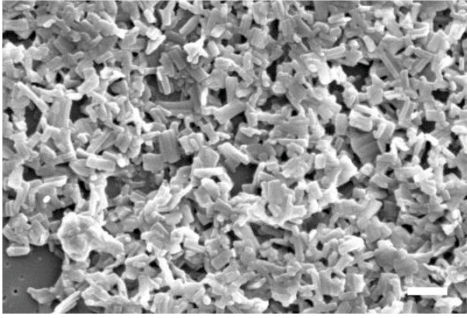
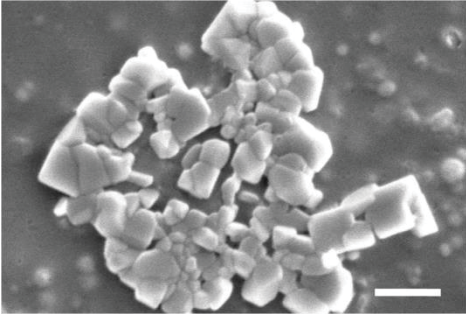
#### **2.3.4 Particle Size Analysis of Paclitaxel Nanocrystals in Different Media**

The stability of PTX nanocrystals in saline and cell culture media was evaluated. The SEM images and analysis were compiled in Table 2.1 and 2.2. The hydrodynamic diameters were plotted in Figure 2.10. The studies were carried out to further understand any change in size and/or morphology when PTX nanocrystals interacted with: (a) saline prior to the intravenous injection (Chapter 4), (b) cell culture media during cell cytotoxicity studies (Chapter 3). When incubated in 37°C saline, there seemed to be no significant alteration of the individual particle morphology (Table 2.1) or size (Table 2.2). However, some degree of flocculation of PTX nanocrystals might have occurred in undisturbed saline as suggested by the increase in the hydrodynamic size (Figure 2.10). The reduced stability of PTX nanocrystals in higher ionic strength solution is discussed in Section 2.3.1. With this knowledge, PTX nanocrystals, which were suspended in saline, were subjected to vigorous sonication prior to their intravenous administration of treatment.

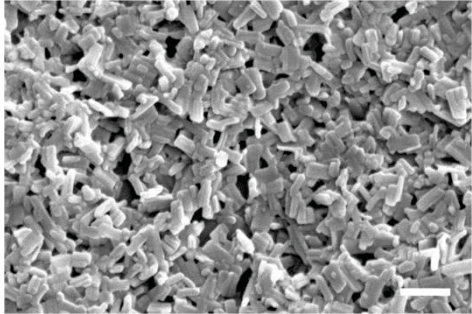
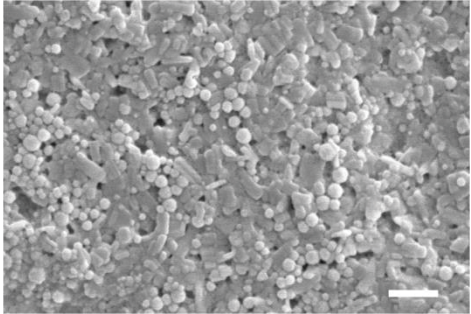
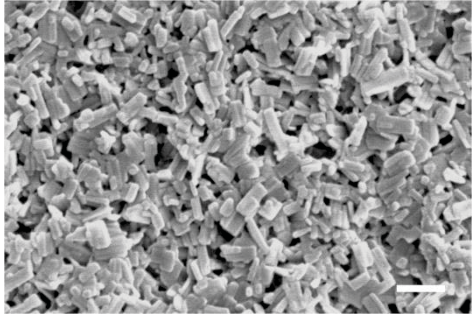
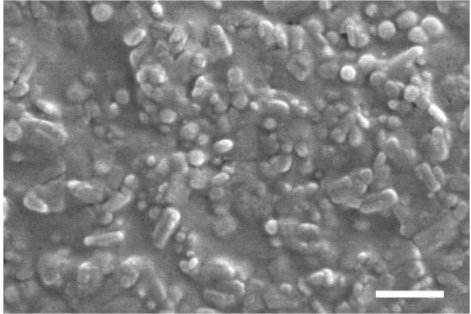
The SEM images (Table 2.1) and particle size analysis (Table 2.2) of PTX nanocrystals incubated in 37°C complete cell culture media (+10% fetal bovine serum (FBS) + 1% penicillin streptomycin) suggested the following observations: (a) some PTX nanocrystals aggregated due to temperature elevation, and (b) some interaction between PTX nanocrystals and cell culture media occurred. Typically, FBS contains approximately 15 mg of bovine serum albumin (BSA). When 0.1 mL of 0.1 mg/mL (~11.7  $\mu$ M) PTX nanocrystals was incubated in 0.1 mL of medium containing 10% FBS (~2.3  $\mu$ M), there was a ratio of approximately 1 to 5 PTX to BSA. Strong interactions between PTX and albumin have been reported. One study reported that in the presence of

3  $\mu\text{M}$  of HSA and 1% ethanol, PTX bound both non-specifically and specifically to albumin at more than six sites with different, yet non-independent, affinities [252]. Assuming a similar interaction between PTX and BSA, then at the concentration studied, albumin was not saturated with PTX. Albumin might have encouraged dissolution of PTX from PTX nanocrystals. The plotted hydrodynamic diameters of PTX nanocrystals in cell culture media (Figure 2.10) showed that there was no observable change, which may suggest that the rate at which PTX nanocrystals aggregated may be similar to that of dissolution (i.e. due to interaction of free PTX with albumin). Inaccuracy in the instrument measurements due to these dynamic phenomena was also probable. Aggregation due to albumin molecules can be minimized by stabilizing the nanocrystals with poly(ethylene glycol) (PEG). A study reported that dipalmitoylphosphatidylcholine (DPPC) vesicles became physically unstable, aggregating within minutes upon mixing with BSA [253]. Yet, upon modifying the lipid vesicle with PEG, which was able to provide steric repulsion, the vesicles showed no tendency to aggregate with albumin molecules for days.

**Table 2.1.** SEM images of PTX nanocrystals incubated in 37°C saline and cell culture media (DMEM + 10% fetal bovine serum (FBS)) at concentration of 0.1 mg/ml. Two images were presented for each time point. Scale bars represent 500 nm.

Time	Saline	DMEM + 10% FBS
20 minutes		
40 minutes		
1 hour		

**Table 2.1** (continued). SEM images of PTX nanocrystals incubated in 37°C saline and cell culture media (DMEM + 10% fetal bovine serum (FBS)) at concentration of 0.1 mg/ml. Two images were captured and presented for each time point. Scale bars represent 500 nm.

<b>Time</b>	<b>Saline</b>	<b>DMEM + 10% FBS</b>
<b>2 hours</b>		
<b>3 hours</b>		

**Table 2.2.** Particle size analysis of SEM images presented in Table 2.1 by SigmaScan.

Data represents mean  $\pm$  S.D.

<b>Media</b>	PTX nanocrystal particle size (nm) after the following incubation times:				
	<b>20 minutes</b>	<b>40 minutes</b>	<b>1 hour</b>	<b>2 hours</b>	<b>3 hours</b>
<b>Saline</b>	210 $\pm$ 70	240 $\pm$ 90	280 $\pm$ 90	240 $\pm$ 80	240 $\pm$ 90
<b>Cell culture</b>	350 $\pm$ 130	90 $\pm$ 30	280 $\pm$ 130	170 $\pm$ 80	150 $\pm$ 70

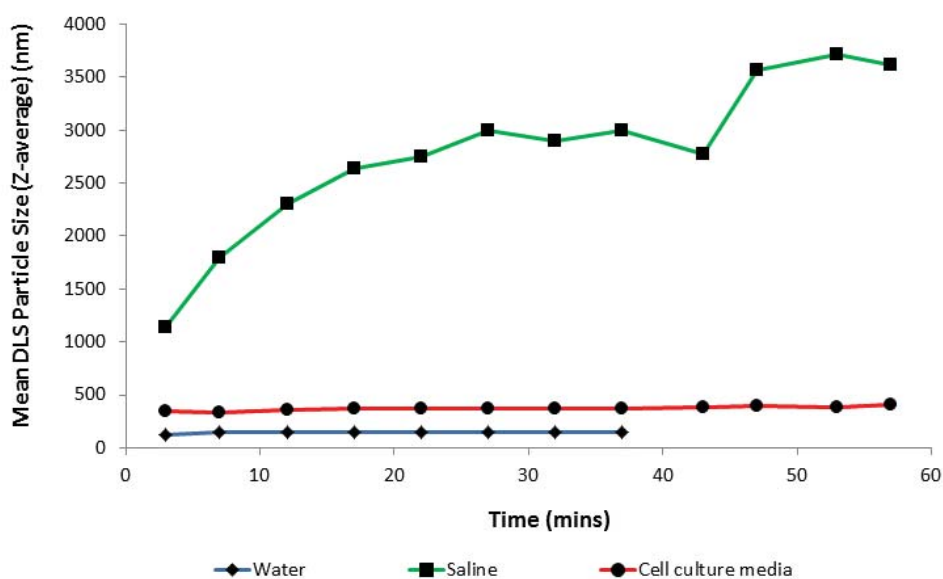


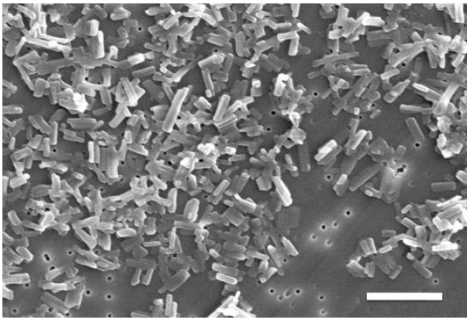
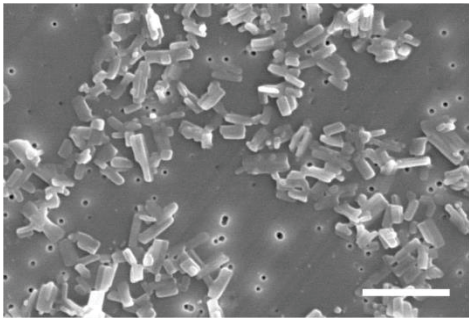
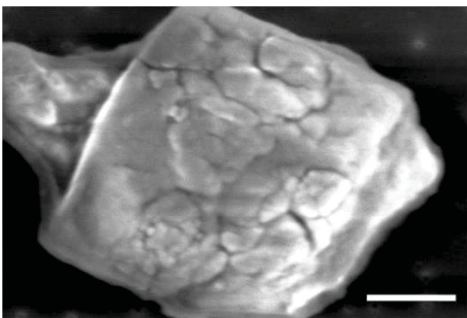
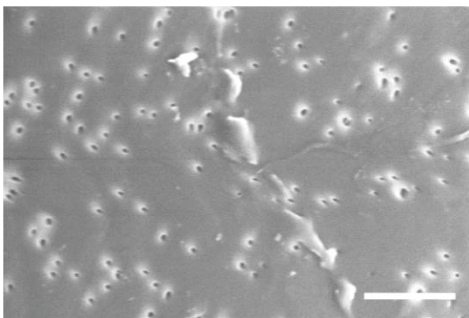
**Figure 2.10.** Particle size analysis of PTX nanocrystals incubated in different media at 37°C by DLS.

To study the interaction between PTX nanocrystals and blood subsequent to intravenous administration, PTX nanocrystals were incubated in 37°C whole nude mouse blood/buffered sodium citrate (9:1 v/v, 0.109 M, 3.2%, to prevent coagulation) at concentration of 0.1 mg/mL. The visualization of the particle morphology was attempted by imaging a small portion of the mixture under SEM. However, obtaining SEM images representing the PTX nanocrystals in blood sample was rather difficult, especially at longer incubation times (Table 2.3). In most samples, PTX nanocrystals were rather embedded in a thick layer of blood as observed at the 2 hour incubation time (Table 2.3 right panel). Some captured images that may resemble PTX nanocrystals were presented in the table. After 45 minutes of incubation, some particles that bore a resemblance to

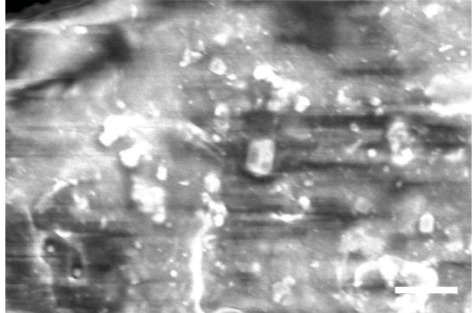
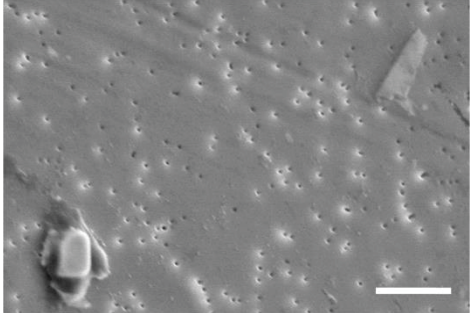
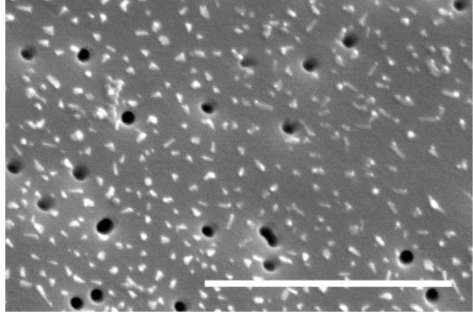
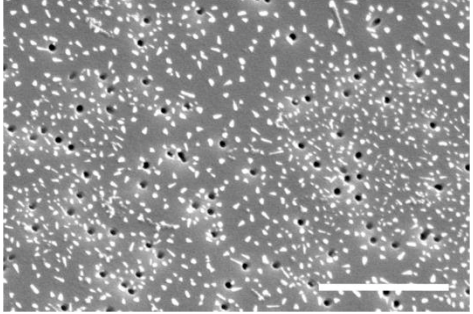
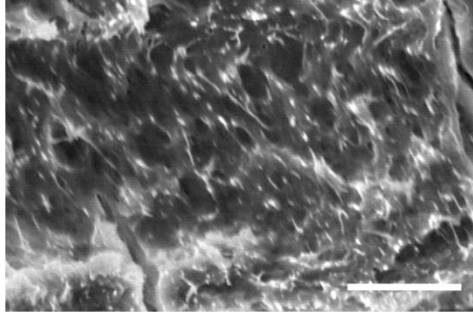
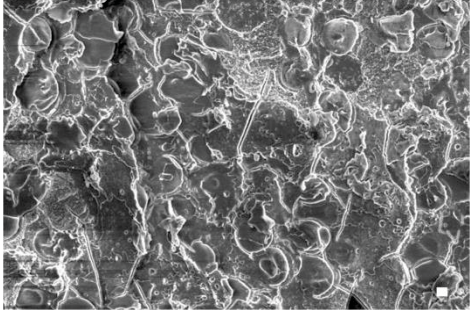
PTX nanocrystals were imaged. Analyzed by SigmaScan, the longest dimension of the particles was determined to be  $50 \pm 15$  nm. Although the morphology of particles observed at that time point shared a rod-like morphology with PTX nanocrystals, it is difficult to accurately confirm. If the assumption was correct, then images from 45 minutes (Table 2.3) suggested that roughly 75% of the particles had dissolved.

Based on Hixson-Crowell cubic root law, assuming that particles are spherical and under sink condition, equation (2) (Section 1.3.4.4) can be used to calculate the time to reach a complete dissolution. With PTX having approximate diffusion coefficient and solubility of  $2 \times 10^{-7}$  cm<sup>2</sup>/s and 1 µg/ml, respectively, the calculation presented in Table 1.1 suggests that complete dissolution for particles with 100 nm radius could be reached within 4.2 minutes. Here, the concentration of PTX nanocrystals in blood was 0.1 mg/mL, which is approximately half of the initial concentration in the mouse body subsequent to a typical intravenous injection at a PTX dose of 20 mg/kg. At concentration of 0.1 mg/mL, which is 100 times higher than aqueous solubility (c.a. 1 µg/ml [250]), the sample may not have been under sink condition. In addition, aggregation of nanocrystals may decrease the surface area exposed to the blood, hence delaying the time to reach complete dissolution. Thus, although some nanocrystals may have dissolved, a good portion may still remain even after 45 minutes of immersion in blood, as observed in the SEM images (Table 2.3).

**Table 2.3.** SEM images of PTX nanocrystals incubated in nude mouse whole blood/ buffered sodium citrate (9:1 v/v, 0.109 M, 3.2%, to prevent coagulation) at a concentration of 0.1 mg/ml. At each pre-determined incubation time, two SEM images were presented. Scale bars represent 1  $\mu\text{m}$ .

Time	SEM Images of PTX Nanocrystals in Nude Mouse Whole Blood	
<b>5 minutes</b>		
<b>15 minutes</b>		

**Table 2.3** (continued). SEM images of PTX nanocrystals incubated in nude mouse whole blood/ buffered sodium citrate (9:1 v/v, 0.109 M, 3.2%, to prevent coagulation) at a concentration of 0.1 mg/ml. At each pre-determined incubation time, two SEM images were presented. Scale bars represent 1  $\mu$ m.

<b>30 minutes</b>	 Scanning electron micrograph showing PTX nanocrystals at 30 minutes. The image displays a surface with irregular, bright, crystalline structures. A white scale bar is located in the bottom right corner.	 Scanning electron micrograph showing PTX nanocrystals at 30 minutes. The image shows a surface with numerous small, dark, circular features and a few larger, bright, irregular structures. A white scale bar is located in the bottom right corner.
<b>45 minutes</b>	 Scanning electron micrograph showing PTX nanocrystals at 45 minutes. The image shows a surface with many small, dark, circular features and some larger, bright, irregular structures. A white scale bar is located in the bottom right corner.	 Scanning electron micrograph showing PTX nanocrystals at 45 minutes. The image shows a surface with many small, dark, circular features and some larger, bright, irregular structures. A white scale bar is located in the bottom right corner.
<b>2 hours</b>	 Scanning electron micrograph showing PTX nanocrystals at 2 hours. The image shows a surface with a complex, interconnected network of bright, fibrous structures. A white scale bar is located in the bottom right corner.	 Scanning electron micrograph showing PTX nanocrystals at 2 hours. The image shows a surface with a complex, interconnected network of bright, fibrous structures. A white scale bar is located in the bottom right corner.

### **2.3.5 Storage Stability of Aqueous Suspensions of Paclitaxel Nanocrystals**

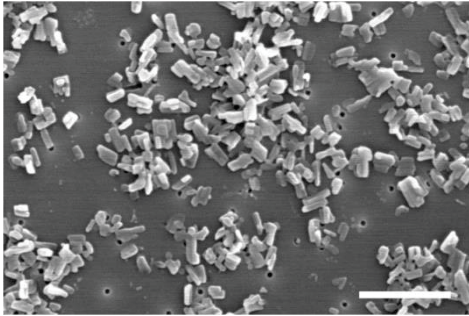
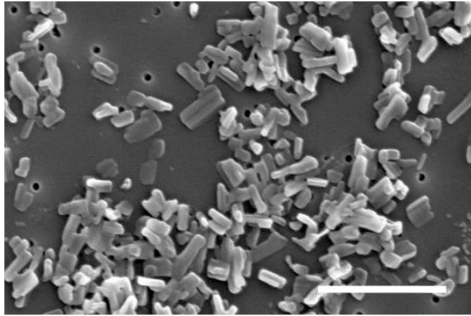
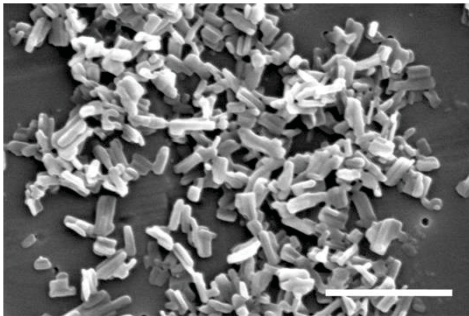
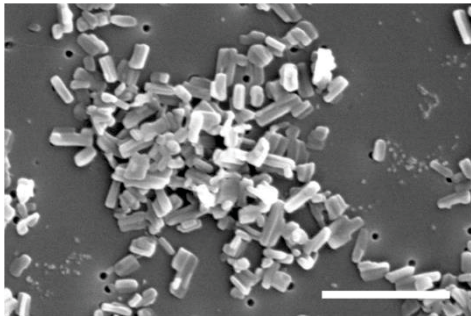
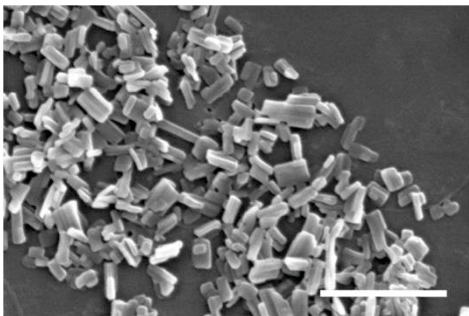
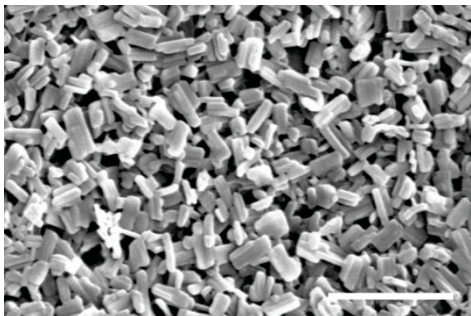
The stability of PTX nanocrystal suspensions in DI water was evaluated over a period of 3 months at either 4°C or room (ambient) temperature. The concentration of the stock solution was 3 mg/mL, and prior to parameter measurements, they were diluted to 0.1 mg/mL. The SEM images to show the morphology of the particles are presented in Table 2.4. The change in nanocrystals' properties (size, polydispersity index, percent drug remaining, zeta potential, and pH) were summarized in Table 2.5 (4°C) and 2.6 (room temperature). When stored at 4°C, there was no significant change in the particle size, measured either from SEM images (SigmaScan) or analyzed by DLS. When stored at room temperature, the particle size and polydispersity index (PI) drifted as the time elapsed. The increase in PI value may suggest that PTX nanocrystals might experience some flocculation that may shift the particle size distribution.

The percent drug remaining suggested that the shelf life (i.e. when concentration decreased by 10%) was less than 1 month. In both storage conditions, approximately 5% of drug degraded after 2 weeks of storage. Since the suspension stock was kept at high concentration, 3 mg/mL, the amount of dissolved (free) molecules that were prevalent for aqueous degradation was minimal. The kinetics and products of PTX degradation have been thoroughly studied by Tian and Stella [248, 254, 255], with maximal stability obtained near pH 4-5. Dordunoo and Burt [256] also observed a U-shaped pH-profile suggesting that the hydrolytic reaction would involve neutral species of PTX catalyzed by  $H^+$ ,  $H_2O$ , or  $OH^-$ . If PTX was in the dissolved state, the degradation would have occurred rapidly. However, since the stock suspension was supersaturated (i.e. 3 mg/mL), the rate of degradation was limited by the dissolution rates governed by the solubility. Since the

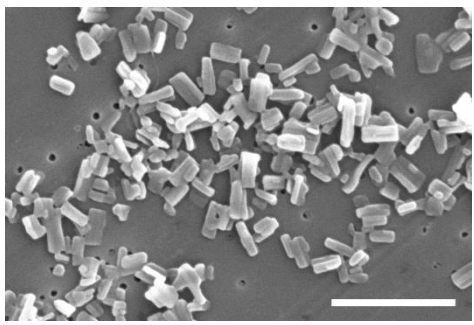
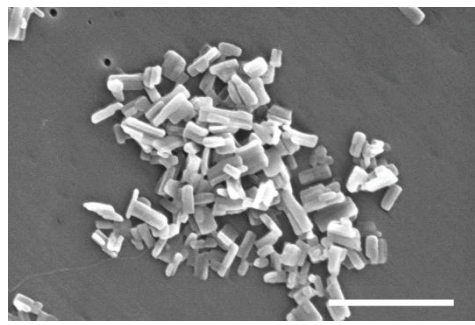
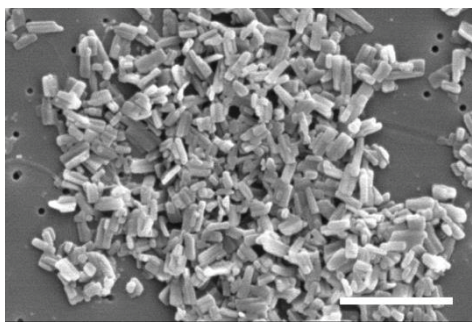
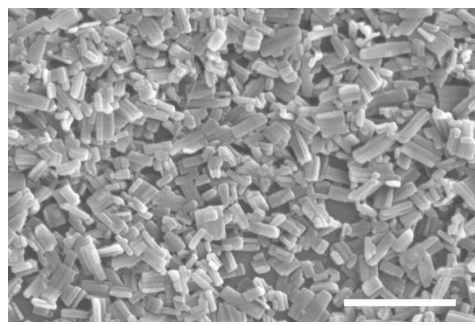
solubility is higher at room temperature, it was not surprising to find that the percent of drug remaining, when stored at room temperature, was less.

The zeta potential data for PTX nanocrystals stored in 4°C could be logically correlated to the change in pH. During storage, dissolved PTX may undergo hydrolysis [248], which caused the decline in pH. In more acidic condition, the numbers of OH<sup>-</sup> ions decreased, causing the zeta potential to become more positive and vice versa. Meanwhile, there was lack of correlation between zeta potential and pH measurements of suspensions stored in room temperature. Errors in measurements and uncleanliness of zeta potential cells (folded capillary cells) could contribute to the discrepancies observed.

**Table 2.4.** SEM images of PTX nanocrystals suspension in water (at concentration of 1 mg/ml) stored at 4°C and room temperature. Two images were presented for each time point. Scale bars represent 1  $\mu$ m.

Storage Duration	SEM images of PTX nanocrystals during storage	
	4°C	Room temperature
0 day		
0.5 month		
1 month		

**Table 2.4** (continued). SEM images of PTX nanocrystals suspension in water (at concentration of 1 mg/ml) stored at 4°C and room temperature. Two images were presented for each time point. Scale bars represent 1  $\mu$ m.

2 months	 SEM image showing PTX nanocrystals after 2 months of storage at 4°C. The crystals appear as small, irregular, light-colored particles. A white scale bar is located in the bottom right corner.	 SEM image showing PTX nanocrystals after 2 months of storage at room temperature. The crystals appear as small, irregular, light-colored particles. A white scale bar is located in the bottom right corner.
3 months	 SEM image showing PTX nanocrystals after 3 months of storage at 4°C. The crystals appear as small, irregular, light-colored particles. A white scale bar is located in the bottom right corner.	 SEM image showing PTX nanocrystals after 3 months of storage at room temperature. The crystals appear as small, irregular, light-colored particles. A white scale bar is located in the bottom right corner.

**Table 2.5.** Summary of the key parameters of PTX nanocrystals during storage at 4°C.

Data represents mean  $\pm$  S.D.

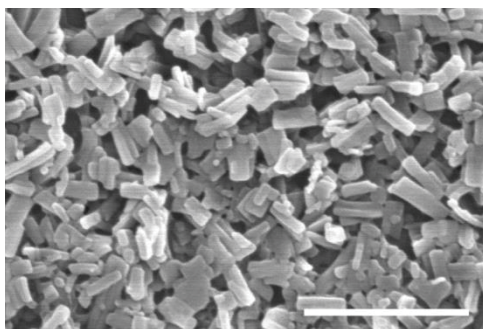
<b>Time (mo.)</b>	<b>Size (nm) (SigmaScan)</b>	<b>Size (nm) (DLS)</b>	<b>PI (DLS)</b>	<b>% Drug Remaining</b>	<b>Zeta Potential (mV)</b>	<b>pH</b>
<b>0</b>	200 $\pm$ 60	176 $\pm$ 1	0.08 $\pm$ 0.02	100.0	-9.0 $\pm$ 0.3	6.7 $\pm$ 0.1
<b>0.5</b>	200 $\pm$ 60	167 $\pm$ 3	0.10 $\pm$ 0.05	96.2 $\pm$ 2.2	-7.3 $\pm$ 0.1	5.5 $\pm$ 0.1
<b>1</b>	210 $\pm$ 70	158 $\pm$ 1	0.07 $\pm$ 0.01	88.9 $\pm$ 0.8	-6.8 $\pm$ 0.4	5.3 $\pm$ 0.1
<b>2</b>	200 $\pm$ 70	169 $\pm$ 2	0.06 $\pm$ 0.04	91.4 $\pm$ 2.2	-7.0 $\pm$ 0.9	5.7 $\pm$ 0.1
<b>3</b>	200 $\pm$ 70	179 $\pm$ 6	0.03 $\pm$ 0.01	85.4 $\pm$ 4.9	-7.8 $\pm$ 0.9	7.0 $\pm$ 0.1

**Table 2.6.** Summary of the key parameters of PTX nanocrystals during storage at room temperature. Data represents mean  $\pm$  S.D.

<b>Time (mo.)</b>	<b>Size (nm) (SigmaScan)</b>	<b>Size (nm) (DLS)</b>	<b>PI (DLS)</b>	<b>% Drug Remaining</b>	<b>Zeta Potential (mV)</b>	<b>pH</b>
<b>0</b>	200 $\pm$ 60	176 $\pm$ 1	0.08 $\pm$ 0.02	100.0	-9.0 $\pm$ 0.3	6.7 $\pm$ 0.1
<b>0.5</b>	200 $\pm$ 70	181 $\pm$ 2	0.10 $\pm$ 0.01	96.6 $\pm$ 3.9	-11.6 $\pm$ 0.7	6.4 $\pm$ 0.1
<b>1</b>	210 $\pm$ 70	207 $\pm$ 5	0.15 $\pm$ 0.01	88.0 $\pm$ 0.7	-7.3 $\pm$ 1.0	6.2 $\pm$ 0.1
<b>2</b>	200 $\pm$ 70	233 $\pm$ 4	0.22 $\pm$ 0.02	88.2 $\pm$ 5.7	-9.4 $\pm$ 1.0	5.8 $\pm$ 0.1
<b>3</b>	290 $\pm$ 70	235 $\pm$ 20	0.24 $\pm$ 0.17	84.8 $\pm$ 2.5	-6.9 $\pm$ 1.0	5.8 $\pm$ 0.1

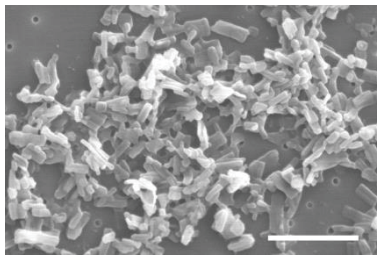
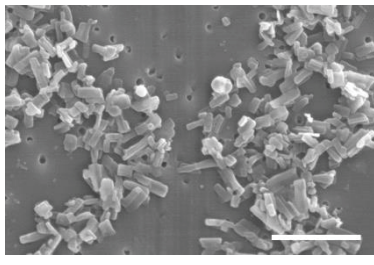
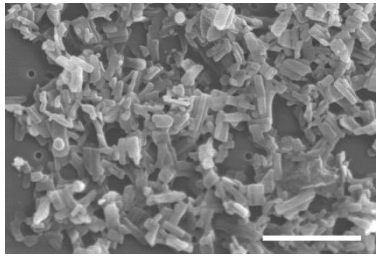
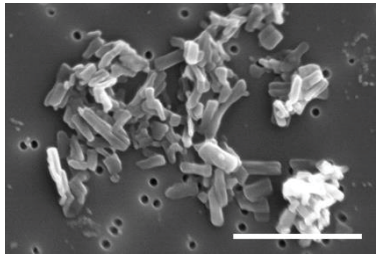
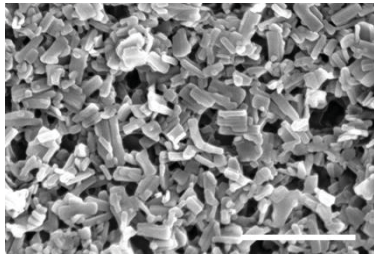
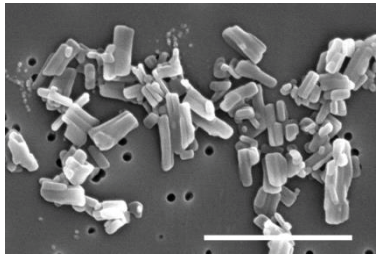
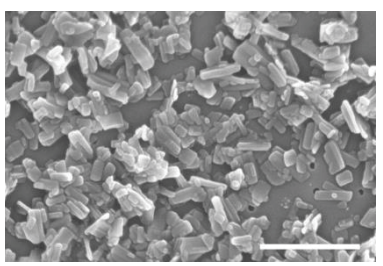
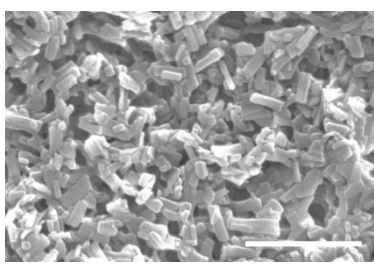
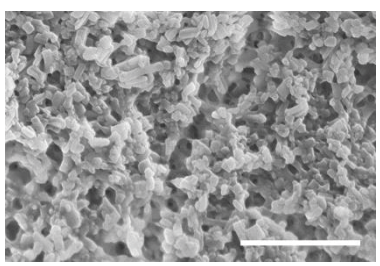
### 2.3.6 Storage Stability of Freeze Dried Paclitaxel Nanocrystals

The stability of freeze-dried PTX nanocrystals was monitored to assess the possibility of storing nanocrystals for the long term. Figure 2.11 represents the fresh freeze-dried of PTX nanocrystals. The SEM images and subsequent analysis of reconstituted freeze-dried product in DI water are shown in Table 2.7 and 2.8. It is worth noting that it was difficult to image the dry form of the freeze dried product by SEM due to the significant charging effect (i.e. caused by poor electrical conductivity of the specimen). SEM images (Table 2.7) and particle size analysis (Table 2.8) suggested that 200 nm-PTX nanocrystals maintained their physical integrity well when stored at 4°C but might be prone to degradation when stored at room temperature. However, after 2 months of storage in an accelerated stability chamber at 40°C/75%RH, particle size decreased significantly (up to 50%), which suggested the likelihood of product degradation upon long-term storage. Particle size measurements by DLS were not carried out because some portion of PTX nanocrystals were still aggregated even though they were sonicated upon reconstitution in DI water. Ease in reconstitution could be achieved by stabilizing nanocrystals with surfactant(s) or polymer(s).



**Figure 2.11.** SEM image of fresh freeze-dried PTX nanocrystals re-suspended in DI water. Scale bar represents 1  $\mu\text{m}$ .

**Table 2.7.** SEM images of freeze-dried PTX nanocrystals re-suspended in DI water at various time points. Scale bars: 1  $\mu\text{m}$ .

4°C	Room Temperature	40°C / 75%RH
<b>- 0.5 month -</b>		
		
<b>- 1 month -</b>		
		
<b>- 2 month -</b>		
		

**Table 2.8.** Particle size analysis of SEM images presented in Table 2.7 by SigmaScan.

Data represents mean  $\pm$  S.D.

Time	Particle Size (nm) Measurements		
	4°C	Room Temperature	40°C / 75% RH
0 day	190 $\pm$ 60		
0.5 month	220 $\pm$ 80	230 $\pm$ 70	210 $\pm$ 60
1 month	210 $\pm$ 70	190 $\pm$ 60	180 $\pm$ 80
2 months	210 $\pm$ 90	180 $\pm$ 70	120 $\pm$ 50

#### 2.4 Conclusion

PTX nanocrystals were successfully produced by an anti-solvent method and further homogenized to achieve an average particle size of approximately 200 nm. The freeze-dried product was confirmed to be the crystalline dihydrate form. The slight negative charge in DI water, about -15 mV, suggested that small portion of dissolved PTX has been hydrolyzed and adsorbed to the surface. The suspension, however, became less stable (i.e. increased in zeta potential) at lower ionic strength. PTX nanocrystals were stable when incubated in DI water, but interactions with components of cell culture media and blood were observed. At size of 200 nm, the physical integrity of PTX nanocrystals in stability chamber was compromised after 2 months of storage. When kept at 4°C, aqueous suspensions should be stable enough to be used for up to 1 month of storage.

## Chapter 3 - Cellular Toxicity and Uptake of Paclitaxel Nanocrystals

### 3.1 Introduction

In order to reach the tumor tissues, intravenously an administered drug nanoparticle has to be able to cross various biological membranes (e.g. walls of blood cells, tissue matrix surrounding the target cells), and eventually penetrate through the cell membrane barrier, either by passive diffusion or active transport, to access the biological target. Efficient internalization of the nanovehicles, via non-phagocytic endocytosis pathways, is often better than simple free diffusion, which may admit a low concentration of therapeutics. Thus, it is necessary to evaluate the performance of PTX nanocrystals at the cellular level, prior to conducting any *in vivo* study. Two *in vitro* studies were conducted:

(1) PTX nanocrystal suspensions were tested for their inhibitory effect on cell growth *in vitro*, particularly in human colon adenocarcinoma HT-29 cells. The  $IC_{50}$ , the half maximum inhibitory concentration, of PTX nanocrystals was compared with Taxol at three different time points: 24, 48, and 72 hours, to elucidate any duration-dependent differences.

(2) The cellular internalization of PTX nanocrystals in human breast cancer MCF-7 was investigated to rationalize the higher potency associated with PTX nanocrystals in human breast cancer MCF-7. Confocal microscopy was utilized to seek any evidence of nanocrystal internalization via non-phagocytic endocytosis pathways.

Unlike phagocytosis, which is mostly restricted to specialized cells (professional phagocytes: macrophages, monocytes, neutrophils, dendritic cells [257]; nonprofessional phagocytes: fibroblasts, epithelial and endothelial cells [258]), endocytosis pathways

occur in all cells. Overall, endocytosis is classified into four main mechanisms, which have been extensively reviewed [259-261]: clathrin-dependent, caveolae-dependent, other clathrin- and caveolae-independent, and macropinocytosis.

(i) Clathrin-mediated endocytosis (CME) generally serves as the main mechanism of internalization of macromolecules. Via this pathway, endocytosed material accumulates in degradative lysosomes, where drug content can be released intracellularly as a result of lysosomal biodegradation.

(ii) Depending on the properties, particles can be alternatively endocytosed via caveolae-mediated endocytosis (CvME). Unlike CME, caveolae from the membrane generates a distinctive cytosolic caveolar vesicle (caveosome), which does not contain any degradation enzyme. When enzyme-sensitive therapeutics (e.g. peptides, proteins, nucleic acids) are encapsulated in the nanocarrier, it is best to tailor the properties of the vehicle to by-pass the lysosomal degradation via the caveolae-mediated endocytosis.

(iii) Macropinocytosis occurs in many cells, including macrophages. It refers to the formation of large endocytic vesicles of random shape and size created by actin-driven invagination of the plasma membrane [262]. Unlike phagocytosis, however, the protrusions do not zipper up (to form U shape) along the ligand-coated particles. Instead, they collapse onto and fuse with plasma membranes [263], forming a macropinosomes. Intracellularly, macropinosomes either: (a) acidify and shrink, or (b) fuse with lysosomal compartments.

(iv) Nanoparticles can alternatively be taken up by clathrin- and caveolae- independent pathways [264], but the understanding of their interactions is still at a preliminary stage.

The pathway by which a particle can be endocytosed depends heavily on both particle properties (e.g. size, geometric shape, surface charge and characteristics) and cell type [261]. A study on size-dependent endocytosis showed that when 50-1000 nm fluorescent polystyrene beads were tested in non-phagocytic murine melanoma B16 cells, particles with diameters of less than 200 nm were found to be taken up via the CME, while those with approximate size of 500 nm were internalized via the CvME pathway [211]. Although each study could be particle- and cell-dependent, it is generally accepted that smaller sized particles gain faster cellular entry, but large particles with sizes up to 5  $\mu\text{m}$  could still be engulfed through pinocytosis [260]. Since cell plasma membranes are negatively charged, nanoconstructs possessing a positively charged surface typically have stronger association and thus more rapid internalization. As for shape, no general trend has been identified yet due to other predominant factors, including size, nature, and the surface charge of the particles. Some indicated that spherical nanoparticles had a higher efficiency and faster rate of endocytosis compared to rod- or disc- [265, 266] shape particles, while others suggested the preferential uptake of cylindrical [267] or rod-shape [268] particles. In this study, we attempted to unveil the cellular uptake of PTX nanocrystals, particularly in the human breast adenocarcinoma MCF-7 cells. A weakly basic amine probe, LysoTracker Red<sup>®</sup>, was used to identify the cell's endo-lysosomal compartment, the accumulation point of either the CME or macropinocytosis pathway. Since PTX does not fluoresce, hybrid PTX nanocrystals were synthesized by entrapping the near-infrared fluorophore FPR-648 (dye number 71, synthesized by Park *et al.* [269]). Cell internalization of the fixed cells was visualized by confocal microscopy, which arguably generates the least artifacts [260].

The idea of preparing hybrid nanocrystals was inspired by a common phenomenon in nature, colored diamonds and gems. Crystals are hardly perfect – most if not all, have defects. When a minute amount of impurities or guest molecules get entrapped in the defect sites of the host crystal lattice, the structural integrity of the hosting crystal is barely altered but the optical properties changes dramatically. Kahr and coworkers have demonstrated numerous organic crystals that are ‘dyed’ by guests [235].

Hybrid nanocrystals can be prepared using the same precipitation method, except that a fluorophore was mixed in water prior to the addition of the drug solution. Because nanocrystals are being formed rapidly due to the sudden drop of solubility, they have a large quantity of defects, where imaging agents can be integrated. It is important to note that the fluorophore is physically integrated, requiring no chemical conjugation. The tiny amount integrated-fluorophore can be detected by optical imaging (e.g. confocal microscope and *in vivo* imaging system).

## **3.2 Materials and Methods**

### **3.2.1 Materials**

Paclitaxel (>99.5%, USP30) was purchased from 21CECPharm (United Kingdom); FPR-648 fluorophore (maximum excitation wavelength,  $\lambda_{ex}$ =648 nm; maximum emission,  $\lambda_{em}$ =671 nm) was obtained from Polysciotech (West Lafayette, IN). Ethanol (HPLC grade), acetonitrile (HPLC grade), DMSO (dimethyl sulfoxide, ACS grade), Dulbecco’s Modified Eagle’s Medium (DMEM), penicillin streptomycin, and 0.25% trypsin-EDTA were purchased from Fisher Scientific (Pittsburgh, PA). McCoy’s 5A medium, HT-29 human colon adenocarcinoma and MCF-7 human breast adenocarcinoma cells were

purchased from American Type Culture Collection (ATCC) (Manassas, VA). Prolong<sup>®</sup> Gold Antifade Reagent with DAPI was obtained from Invitrogen (Grand Island, NY). All chemicals and solvents were utilized without further purification. Deionized water (by Milli-Q<sup>®</sup>, filtered through 0.2 µm membrane) was used for all the experiments. 0.050 µm (50 nm) Whatman<sup>®</sup> nuclepore polycarbonate track-etched membranes used for filtration were purchased from Fisher Scientific (Pittsburgh, PA).

### **3.2.2 Preparation of Pure and Hybrid Paclitaxel Nanocrystals**

Paclitaxel nanocrystals were produced by the combination approach as previously described in Section 2.2.2. For the pure PTX nanocrystals, 1 mL of 3 mg/mL paclitaxel in ethanol was added rapidly to 20 mL deionized water in a 3-neck round bottom flask (500 mL). The mixture was stirred at 1,100 rpm with a stirrer shaft and under intense sonication (in sonication bath F20D, output of 70 W and 42±6 KHz, Fisher Scientific). Ice was added to the sonication bath to keep the temperature between 14-18°C. After 10 minutes of stirring time, the flask was removed from the stirring station and placed in desiccator to remove bubbles generated due to rapid stirring. The mixture was then filtered through a 50 nm polycarbonate membrane. The retentate was re-suspended in 2 mL DI water, placed in a 20 mL scintillation vial, and homogenized (Fisher Scientific<sup>®</sup> PowerGen<sup>®</sup> 125) for 6 minutes at 30,000 rpm. PTX/FPR-648 hybrid nanocrystals were produced in a similar manner, except that 0.25 mL of 1 mg/mL FPR-648 was added to DI water prior to the addition of 5 mg/mL PTX/ethanol solution.

### 3.2.3 Cytotoxicity Study of Paclitaxel Nanocrystals in HT-29 Cells

The cellular cytotoxicity of PTX nanocrystals and dissolved PTX in DMSO (PTX/DMSO) in colon cancer HT-29 cells were compared using the sulforhodamine B (SRB) assay. The SRB assay relies on the ability of the SRB dye to bind to the cell's protein basic amino acid residue subsequent to cell fixation with trichloroacetic acid (TCA). The assay of SRB fluorescence was found to be linearly proportional to the number of cells and cellular proteins when measured at cellular density of 1 to 200% confluence [270]. Specifically, cells were cultured in McCoy's 5A medium supplemented with 10% fetal bovine serum and 1% penicillin streptomycin in a 37°C humidified incubator containing 5% CO<sub>2</sub>. After reaching 80% confluence, cells were trypsinized and seeded in 96-well plates at a density of 1x10<sup>4</sup> cells/well for the 24- and 48-hour incubation times or 0.8x10<sup>4</sup> cells/well for the 72-hour incubation time. Samples were prepared in duplicates, and cells were allowed to attach to the bottom of the wells by incubating them overnight. For the treatment with dissolved PTX/DMSO, 200 µg/mL stock of PTX in DMSO was diluted to a total of 9 stock solutions with targeted concentrations between 50 ng/mL to 2000 ng/mL. Prior to adding the treatment to the cells, the PTX/DMSO solution was further diluted 200 times (0.5% v/v) with complete cell culture media, to obtain targeted concentrations between 0.25 and 100 ng/mL. PTX nanocrystals were diluted in a similar manner, except that they were suspended in DI water. The actual concentration of each stock solution was determined by HPLC.

The HT-29 cells were incubated with either PTX/DMSO solutions or aqueous suspension of PTX nanocrystals for 24, 48, or 72 hours. The schematic of the cytotoxicity study is depicted in Table 3.1. Wells in column 1 only contained complete culture media without

any cells seeded. In column 2, the seeded cells were incubated with complete culture media that had been added with either 1% of DMSO or DI water for control. Either PTX/DMSO or PTX nanocrystals were added in column 3 to 11. Column 12 was intentionally left as blank. Plates were briefly shaken subsequent to the addition of media and treatments.

**Table 3.1.** The 96-well setup for the cellular toxicity study of PTX nanocrystals and dissolved PTX in HT-29 cells.

	1	2	3	4	5	6	7	8	9	10	11	12
A	no cell, culture media only	cells in control medium	0.25 ng/mL	0.5 ng/mL	1 ng/mL	2.5 ng/mL	5 ng/mL	10 ng/mL	25 ng/mL	50 ng/mL	100 ng/mL	blank
B												
C												
D												
E												
F												
G												
H												

After cells had been incubated for the appointed time (24, 48, or 72 hours), the media were aspirated from the wells. Cells were subsequently fixed with 100  $\mu$ L/well of cold 10% trichloroacetic acid (TCA) and stored at 4°C for one hour. The 96-well plates were washed 5 times with deionized water and sharply flicked to remove excess water. Plates were left to air-dry overnight.

100  $\mu$ L of 0.4% Sulforhodamine B (SRB) dissolved in 1% acetic acid, was added to every column except #12 in the 96 well plate. Plates were incubated for 30 minutes at room temperature and covered with aluminum foil to minimize light exposure. To remove excess SRB, plates were washed with a multichannel pipetter by layering 200  $\mu$ L of 1% acetic acid over the fixed cells and flipped to remove the wash. This process was repeated five times. Plates were air dried in the biological safety hood overnight, covered with foil.

The bound-protein dye was solubilized by adding 100  $\mu$ L of 10 mM Tris Base (pH 10.0). Plates were wrapped in aluminum foil and gently shaken on a gyrator for 30 minutes. The optical density was determined by an automatic plate reader, SpectraMax M5 (Molecular Devices) at a wavelength of 560 nm.

The optical density was recorded and correlated to the percent of protein for each respective well. The average of absorbance in each column was taken. The average values of column 2 to 11 were first subtracted from that of column 1, the background. The cell numbers (i.e. linear to the SRB absorbance) in treated wells (e.g. column 3 (C3) to 11 (C11)) were then compared to that of column 2 (C2), the positive control. The % cell viable was calculated with the following equation:

$$\% \text{ cell viable} = 100\% - \left( \frac{\text{absorbance of treated cells (C3 to C11)}}{\text{absorbance of positive control (C2)}} \times 100\% \right)$$

The concentration of drug was graphed versus the percent cell viable on a log scale, and the IC<sub>50</sub>, the half maximal inhibitory concentration, was determined.

### **3.2.4 Characterization of Paclitaxel Hybrid Nanocrystals**

The morphology and size of the PTX hybrid nanocrystals were observed by SEM as previously described in Section 2.2.3. Analysis of particle size from the SEM images was performed using SigmaScan (Systat software Inc, San Jose, CA). The mean size (i.e. longest dimension) and standard deviation from approximately one hundred particles are presented.

### **3.2.5 Analysis of the Fluorophore Entrapment**

Quantification of paclitaxel was conducted by high liquid chromatography (HPLC, Waters Breeze) with a Waters Symmetry C18 5  $\mu\text{m}$  column (4.6 x 150 mm); it was analyzed by a UV detector (Waters 2487 dual  $\lambda$  absorbance detector) at 227 nm with a mobile phase of ethanol/acetonitrile (50:50) pumped at a rate of 2 mL/min (Waters 1525 binary pump). The column was equilibrated to 35°C prior to sample injection (20  $\mu\text{L}$ ).

The measurement of FPR-648 entrapment was done using a fluorescence (96-well) plate reader. Standard solutions of FPR-648 fluorophore with concentrations ranging from 0.1  $\mu\text{g/ml}$  to 2  $\mu\text{g/ml}$  were prepared in DMSO and measured at excitation and emission wavelengths of 650 and 670 nm, respectively, by SpectraMax M5 (Molecular devices). Similar to the standard solution, PTX/FPR-648 hybrid nanocrystals were dissolved in DMSO prior to the fluorescence analysis. Standards and samples were prepared in triplicate. Wells were filled with 150  $\mu\text{L}$  solution.

### **3.2.6 Cellular Uptake Study of Paclitaxel Hybrid Nanocrystals in MCF-7 Cells**

Breast cancer MCF-7 cells were cultured in Dulbecco's Modified Eagle Medium (DMEM) medium supplemented with 10% fetal bovine serum (FBS) in a humidified atmosphere containing 5% CO<sub>2</sub> at 37 °C. For the cellular uptake study, cells were seeded on 22x22 mm<sup>2</sup> glass cover slips in a 6-well plate at a density of 200,000 cells/well. To allow attachment to the cover slips, cells were incubated overnight prior to treatment. PTX/FPR-648 hybrid nanocrystals suspension was mixed with complete culture media (10% v/v) to a final concentration of 80 µg/mL. The mixture was added to the cells, and they were incubated for 0.5, 1, and 2 hours. At the end of the incubation time, the media were aspirated, and LysoTracker Red (Invitrogen, Grand Island, NY), which was dissolved in PBS, was added at a concentration of 100 nM. The cells continued to be incubated at 37°C for 30 minutes. After staining the lysosomal compartment with LysoTracker, wells were washed gently three times with cold PBS. Subsequently, cells were fixed by adding 1 mL of 4% paraformaldehyde (Boston Bioproducts, Ashland, MA). The plates were placed in a 4°C refrigerator for 10 minutes during fixation. Cells were then washed carefully with PBS for three additional times. To prevent the fluorescence to fade (photobleach), approximately 20 µL Prolong Gold with DAPI was mounted to the microscope glass slide. The individual glass cover slip was then flipped onto microscope glass slide and sealed with nail polish on the edge. Slides were stored at 4°C prior to viewing to preserve the integrity of the fluorescence.

Slides were viewed under a Leica AOBs TCS SP5 inverted laser scanning confocal microscope equipped with Leica Application Suite Advanced Fluorescence 2.3.1 build 5196 software. The DAPI, used to stain the cell nucleus, was excited with Argon 405

laser and observed at emission window of 415-485 nm. The LysoTracker Red, which stained the lysosomal compartment, was excited with HeNe 543 laser and viewed in the emission window of 555-583 nm. Meanwhile, the FPR-648, which was incorporated into the hybrid nanocrystals, was excited with a HeNe 633 laser and observed using an emission window of 695-740 nm.

### **3.3 Results and Discussion**

#### **3.3.1 Cytotoxicity Study of Paclitaxel Nanocrystals in HT-29 Cells**

The results of the cellular cytotoxicity study of PTX nanocrystals versus dissolved PTX by the SRB assay in HT-29 human colon adenocarcinoma cells are shown in Figure 3.1. The calculated  $IC_{50}$  values for different incubation times are presented in Table 3.2. Both PTX nanocrystals and dissolved PTX exerted similar toxicity at all the three time points (i.e. 24, 48, and 72 hours), indicating that there was no duration-dependent chemosensitivity during those particular periods. We also learned that relative to the PTX nanocrystals, dissolved PTX in DMSO was approximately two to three times more potent, which is most likely due to the following reasons: (a) dissolved PTX (PTX/DMSO) was able to rapidly and freely diffuse through the cell membrane due to its concentration gradient; or (b) some PTX nanocrystals may aggregate during the incubation period, which might cause a heterogeneous PTX size distribution that led to reduced exposure to some cells. It is worth noting that cells were 100% viable when incubated with 0.5% v/v DMSO/cell culture media (in the control column, C2, described in section 3.2.3); thus, the cytotoxicity observed was due to the PTX and not due to the addition of DMSO.

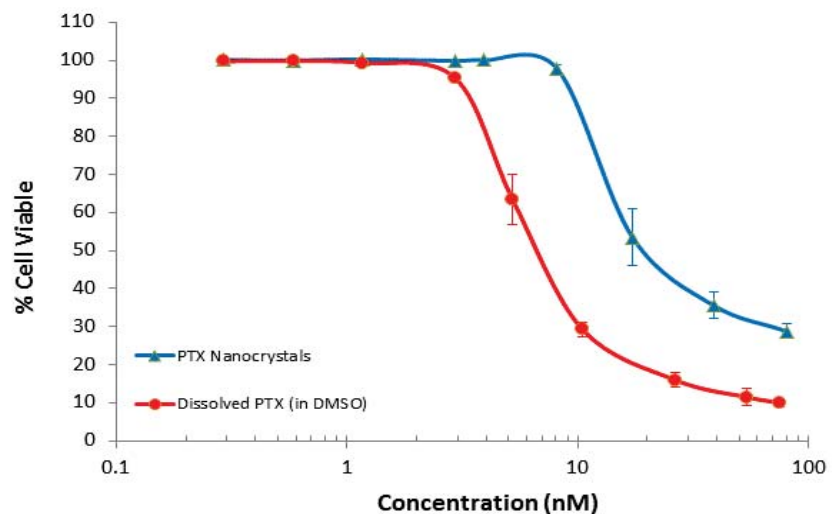


**Figure 3.1.** The cytotoxicity curve of PTX nanocrystals and dissolved PTX in human colon cancer HT-29 by SRB assay.

**Table 3.2.** The  $IC_{50}$  values of PTX nanocrystals and dissolved PTX in HT-29 cells at different incubation times.

Incubation time	$IC_{50}$ (nM) in HT-29 Cells	
	PTX nanocrystals	Dissolved PTX (PTX/DMSO)
24 hours	$22.3 \pm 1.7$	$9.6 \pm 0.4$
48 hours	$18.1 \pm 0.3$	$9.2 \pm 0.3$
72 hours	$24.1 \pm 2.7$	$7.1 \pm 0.4$

### 3.3.2 Particle Size Measurement

The PTX/FPR-648 hybrid nanocrystals were imaged under a scanning electron microscope (SEM), and the individual particle sizes (Figure 3.2) were analyzed by Sigma Scan. The average longest dimension of the hybrid PTX nanocrystals was  $190 \pm 70$  nm, which was similar to that of pure PTX nanocrystals, as discussed in section 2.3.1. The maximum size of nanoparticles that can be internalized by cells was reported to be about 500 nm [213]. Thus, the produced nanocrystals, unless aggregated, should be able to infiltrate the cell membrane.

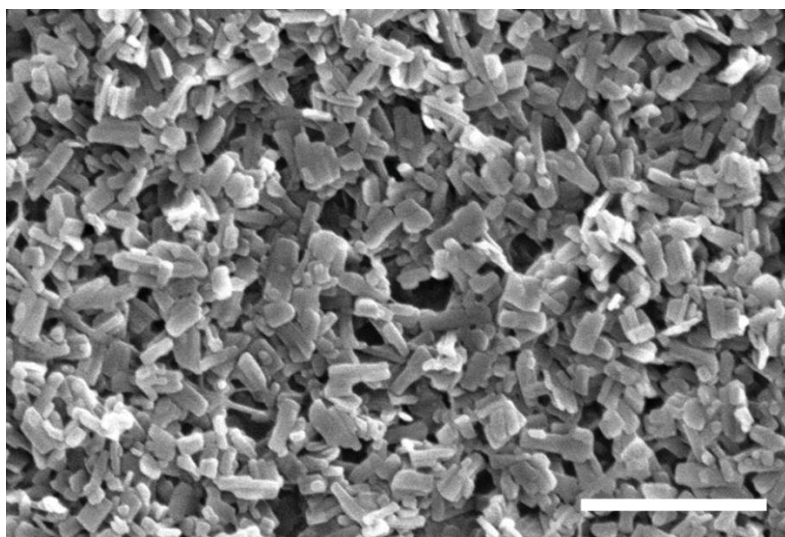


**Figure 3.2.** SEM image of PTX/FPR-648 hybrid nanocrystals for cellular uptake in breast cancer MCF-7. Scale bar represents 1  $\mu$ m.

### 3.3.3 Analysis of the FPR-648 Fluorophore Entrapment

There was a linear correlation between the concentration of FPR-648 and absorbance unit when measured between 0.1 and 2  $\mu$ g/mL (Figure 3.3). The concentration of the entrapped FPR-648 in PTX hybrid nanocrystals can be determined by dissolving the

hybrid nanocrystals in DMSO. The dilution factor was 1:5 (v/v). Using the standard curve, it was determined that the FPR-648 concentration was 5.6  $\mu\text{g/mL}$ , which corresponds to 0.13% (w/w) entrapment. Due to the dye sensitivity, PTX hybrid nanocrystals could still be visualized in confocal microscopy even at very low concentration. These PTX/FPR-648 hybrid nanocrystals were particularly used to study the cellular uptake of PTX nanocrystals in human breast cancer MCF-7, which will be discussed in the following section.

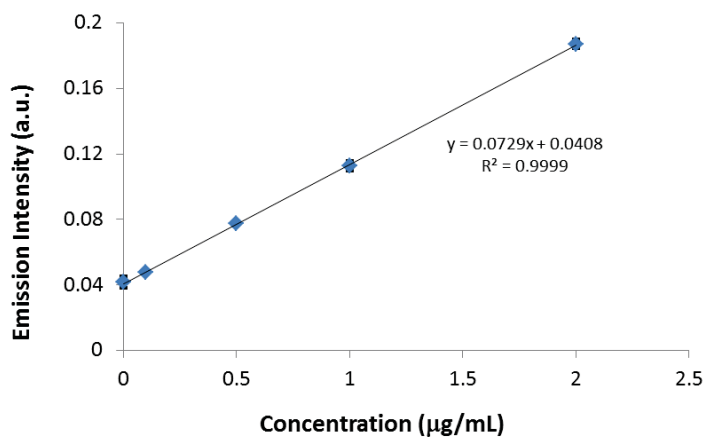


**Figure 3.3.** The standard curve of FPR-648 in DMSO measured at  $\lambda_{\text{ex}}$ : 650 nm and  $\lambda_{\text{em}}$ : 670 nm.

### 3.3.4 Cellular Uptake Study of Paclitaxel Nanocrystals in MCF-7 Cells

The cellular toxicities of PTX nanocrystals versus dissolved PTX in DMSO were also compared in breast cancer cells MCF-7 by previous laboratory members (unpublished data). For the dissolved PTX, with  $\text{IC}_{50}$  value of  $37.4 \pm 1.3$  nM, MCF-7 cells were found to be less sensitive relative to the HT-29 cells. Even though tested by using different

cytotoxicity assays, XTT (2,3-bis (2-methoxy-4-nitro-5-sulfophenyl)-5-carboxanilide)-2H terazodium), Chou and colleagues observed a similar trend [271]. Interestingly, the cytotoxicity of PTX nanocrystals after 72 hours post-incubation in both cells, MCF-7 ( $IC_{50}$ :  $21.7 \pm 0.3$  nM) and HT-29 ( $IC_{50}$ :  $24.1 \pm 2.7$  nM), were not significantly different. Yet, PTX nanocrystals and dissolved PTX induced cytotoxicities with an opposite trend in the two cells. Relative to dissolved PTX, the nanocrystals were more toxic to the MCF-7 (had lower  $IC_{50}$ ) than HT-29 cells. Differences in particle size, size distribution, cell properties, cell-specific particulate uptake, and operator could affect the observed outcome. However, it is also possible that MCF-7 cells were able to internalize PTX nanocrystals via the endocytosis pathway, which could result in a higher payload delivered to the cytosol subsequent to lysosomal biodegradation. Meng *et al.* reported that rod-shaped mesoporous silica nanoparticles (MSNP) loaded with taxol and camptothecin were able to induce more toxicity relative to the spherical drug loaded-MSNP and dissolved drug [272]. The rod-shape MSNPs had different longest dimension of approximately 120, 175, and 280 nm with corresponding aspect ratios of about 1.6, 2.3, and 4.3. When tested in HeLa cells, all the rod-shape particles were internalized by macropinocytosis, which then transferred to acidifying endosomal compartment that specializes in particle degradation. The ones with a dimension of approximately 175 nm and aspect ratio (AR) of 2.1 to 2.5 were taken up the most.

The following cellular uptake studies were carried out to investigate the intracellular pathways of PTX nanocrystals in MCF-7. Figure 3.4 shows a set of confocal images of breast cancer MCF-7 cells that had been incubated with PTX/FPR-648 hybrid nanocrystals for 0.5, 1, and 2 hours. Each image set was taken at the same z-level,

approximately in the middle of the cells (i.e. signals were not generated from the surface of the cells). The cell nucleus and endo-lysosomal compartment were stained with DAPI (blue) and Lysotracker Red, respectively. Hybrid PTX/FPR-648 nanocrystals (cyan) were utilized for this purpose. FPR-648 has a longer emission wavelength, where its fluorescence signal can be separated from other probes (e.g. DAPI and Lysotracker Red) in the visible range.

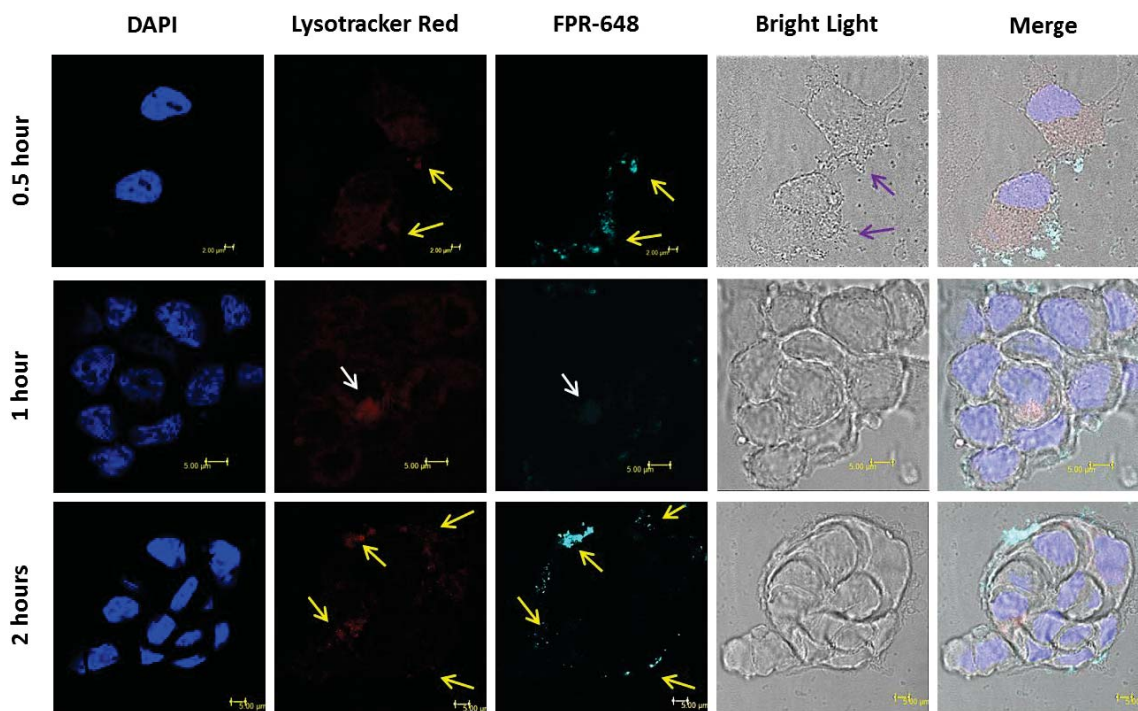


**Figure 3.4.** Compilation of confocal microscopy images of MCF-7 cells incubated with PTX/FPR-648 hybrid nanocrystals (cyan) for 0.5, 1, and 2 hours. The cell nucleus and lysosome were stained with DAPI (blue) and Lysotracker Red, respectively. Scale bars in the top panel indicate 2  $\mu\text{m}$  while those in middle and bottom panels indicate 5  $\mu\text{m}$ . The purple, yellow, and white arrows might suggest the formation of membrane ruffles, macropinocytosis, and clathrin-mediated endocytosis, respectively.

The top panel (30 minutes) of Figure 3.4 shows that PTX/FPR-648 (cyan) nanocrystals started to accumulate on the surface of the membrane. MCF-7 might internalize some of the particles via macropinocytosis as formations of membrane ruffles (purple arrows) were observed. Macropinocytosis formation heavily relies on the movement of actin cytoskeleton and actin-driven membrane, which results in the membrane ruffling and the formation of filopodia for the closure of macropinocytotic vesicles [262]. The images may suggest that the actin-driven membrane ruffles protruded to engulf the nanocrystals in the extracellular matrix, melt with the cell membrane, formed intracellular vacuole (macropinosome), and fused with lysosome (red signal) [262, 273]. The macropinosomes generally have size between 0.5-10  $\mu\text{m}$  [260].

At 1 hour post-incubation time (Figure 3.4), it was observed that the cyan and red signals were co-localized in the middle of group of cells. This may suggest that some of the PTX hybrid nanocrystals (*c.a.* 200 nm) that were stable and did not aggregate were taken up by the CME. Similar to macropinocytosis, endocytosed nanocrystals ended up to accumulate in lysosome (red), where drug cargo could be released intracellularly subsequent to lysosomal biodegradation. Fluorescently-labeled polystyrene beads with size of 200 nm were taken up intracellularly by CME in non-phagocytic murine melanoma B16 cells [211].

After 2 hours of incubation, PTX hybrid nanocrystals started to aggregate to greater extent. Due to their large size, internalization via macropinocytosis was more preferable than the CME. Clusters of hybrid nanocrystals were found to merge with the LysoTracker Red signals on the cell peripheral. Though the significance is still uncertain, unlike the lysosomes that were responsible for degrading the endocytosed nanocrystals by CME (1

hour incubation), those that merged with nanocrystal-loaded macropinocytosis changed their localization from random to clustered arrangement in the cell [272]. Overall, the confocal images suggested that MCF-7 cells were able to internalize the PTX hybrid nanocrystals via macropinocytosis and/or CME. The rate and efficiency of these internalizations had not been studied. Beyond 2 hours of incubation, most of the PTX hybrid nanocrystals aggregated, which was likely due to their decreased stability in elevated temperature and interaction with albumin as described in Section 2.3.4.

It is worth noting that there were only a portion of cells that were left during the fixation process (i.e. with 4% paraformaldehyde) and thus for viewing under the microscope. The nanocrystal suspension concentration at which cells were incubated was 80  $\mu\text{g}/\text{mL}$  (93.6 nM), approximately four times higher than its  $\text{IC}_{50}$  value. Sufficient addition of hybrid nanocrystals to the cells was necessary in order to have large numbers of nanocrystals for microscope visualization. Yet, since the  $\text{IC}_{50}$  of PTX in the cell is well below the solubility, the dissolved drug was able to promote rapid cell death, thus minimizing the number of cells left on the cover slip.

To ensure that the cyan signal observed was coming from the dissolved dye, MCF-7 cells were also incubated with free FPR-648 at concentration of 0.1  $\mu\text{g}/\text{ml}$  (Figure 3.5). This concentration was equivalent to the amount of entrapped dye, 0.13% (w/w), in 80  $\mu\text{g}/\text{mL}$  of PTX/FPR-648 hybrid nanocrystals used for the cellular uptake studies (Figure 3.4). Although cells were incubated with same concentration of dye, hardly any cyan signal was observed in those exposed with the free dye (Figure 3.5). This observation suggested that the cyan signals in Figure 3.4 were from the PTX/FPR-648 hybrid nanocrystals. In the case where dye might leach out prematurely from the hybrid nanocrystals, it would be

rapidly dissolved to the cell culture media due to its high aqueous solubility (i.e. more than 1 mg/mL).

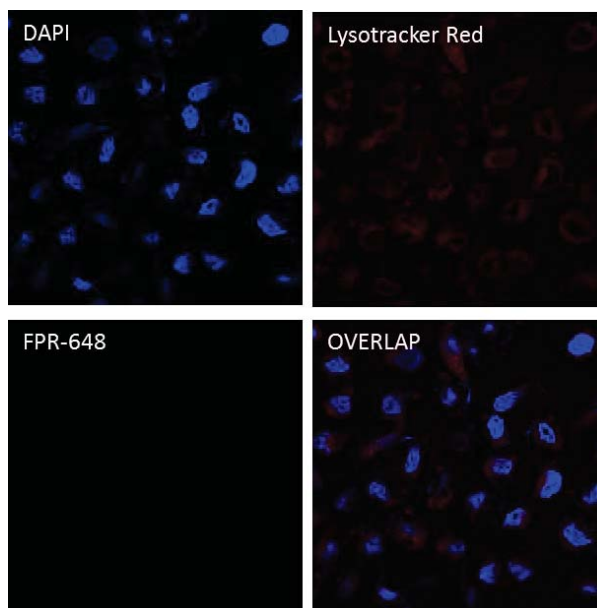


**Figure 3.5.** The confocal images of MCF-7 cells incubated with free FPR-648 dye at concentration of 0.1  $\mu\text{g/ml}$  for 2 hours.

Unlike in MCF-7 cells, PTX nanocrystals induced less toxicity in HT-29. Two working hypotheses are proposed: (a) PTX nanocrystals may not preferably be internalized in HT-29 cells (e.g. due to particle size), (b) the amount of available dissolved PTX, which can passively diffuse to cell membrane, was reduced due to the decreased exposed surface area of aggregated PTX nanocrystals. The internalization of PTX nanocrystals may be cell-specific. Similar to the case of polystyrene nanoparticles (size from 20 -1000nm), due to their size, they were not preferably endocytosed by HUVEC endothelial, the EVC 304 bladder carcinoma, and the HNX 14C squamous carcinoma cell lines. Meanwhile,

the 20-100 nm particles were internalized by Hepa 1-6 hepatoma and the HepG2 human hepatocyte cell lines, and the 20-600 nm particles by the KLN 205 squamous carcinoma cells [274]. HT-29 has been reported to internalize some nanoconstructs by endocytosis pathways. Third-generation (G3) polyamidoamine (PAMAM) dendrimers having a size of approximately between 5 and 12 nm were shown to colocalize with the lysosome compartment of HT-29 [275]. Folic acid-targeted chitosan-modified gold nanorods, with a size of 85 nm, were observed to be internalized via receptor-mediated endocytosis [276]. To rationalize for the discrepancy, the evaluation of cell internalization of PTX nanocrystals in HT-29 cells needs to be conducted in the future.

### **3.4 Conclusion**

In HT-29 cells, PTX nanocrystals were found to be less toxic compared to the dissolved PTX. However, there was no duration-dependent chemosensitivity observed during the period of 24, 48, and 72 hours. Although further studies are needed to investigate the difference in the cytotoxicity, PTX nanocrystals may have aggregated during the incubation, decreasing the rate of dissolution and thus diffusion to the cell membrane. In contrast, PTX nanocrystals exerted more antitumor activity in MCF-7 cells. The ability of MCF-7 cells to internalize PTX nanocrystals either via macropinocytosis or clathrin-mediated endocytosis may result in the delivery of higher drug concentration into the cell cytosol subsequent to the lysosomal biodegradation.

## Chapter 4 - *In Vivo* Studies of Paclitaxel Pure and Hybrid Nanocrystals

### 4.1 Survival Study in HT-29 Xenograft Model

#### 4.1.1 Introduction

The work presented in this section was aimed at evaluating the efficacy and toxicity of PTX nanocrystals produced by the combination approach, as described in Chapter 2. The treatment was evaluated in a human colorectal adenocarcinoma HT-29 xenograft model in immunodeficient mice. The survival of these mice was compared against the negative (saline) and positive (Taxol) control groups to evaluate the antitumor activity of the PTX nanocrystals. In parallel, the toxicity was assessed by comparing the percent body weight change of the treatment groups. Due to the absence of Cremophor EL/ethanol, PTX nanocrystals were expected to induce less toxicity relative to Taxol.

Since PTX nanocrystals are intended for intravenous administration, a small particle size is desired to avoid embolization. The optimum size of targeting tumor's leaky vasculature is still debatable because other particle properties, including the shape, nature, and surface charge, also dictate the pharmacokinetics and distribution of the particles *in vivo*. However, collectively it has been proposed that in order to exploit the EPR effect, the particle size should be below 400 nm [29]. While high absolute surface charge ( $\pm 30$  mV) is needed to obtain stability, it has also been shown that highly charged nanoparticles had a much higher opsonization rate than neutral or slightly charged nanoparticles of the same size [191, 192]. Generally, due to the strong electrostatic interaction between the particles and anionic erythrocyte membrane, cationic particles caused higher hemolytic activity while anionic particles are not hemolytic [191]. Many have reported that

conjugation of poly-ethylene glycol (PEG) onto the surface of nanovehicles could produce stealth properties and decrease the phagocytic clearance by the reticuloendothelial system. Yet, PEGylated particles had also been reported to have slower uptake into tumor cells compared to bare ones – creating the PEG dilemma [277, 278]. For the evaluation of efficacy and toxicity, a neutral and non-stabilized PTX nanocrystal suspension with a particle size of approximately 200 nm was produced and administered weekly for a total of four intravenous injections.

## **4.1.2 Materials and Methods**

### **4.1.2.1 Materials**

Paclitaxel (>99.5%, USP30) was purchased from 21CECPharm (United Kingdom). Ethanol (HPLC grade), acetonitrile (HPLC grade), DMSO (dimethyl sulfoxide, ACS grade), penicillin streptomycin, and 0.25% trypsin-EDTA were purchased from Fisher Scientific (Pittsburgh, PA). Saline (0.9% w/v sodium chloride) for injection was obtained from Hospira (Lake Forrest, IL). HT-29 human colon adenocarcinoma cells and McCoy's 5A medium were purchased from ATCC (Manassas, VA). All chemicals and solvents were utilized without further purification. Deionized water (by Milli-Q<sup>®</sup>, filtered through 0.2 µm membrane) was used for all the experiments. 0.050 µm (50 nm) Whatman<sup>®</sup> nuclepore polycarbonate track-etched membranes used for filtration were purchased from Fisher Scientific (Pittsburgh, PA).

#### **4.1.2.2 Preparation of Pure PTX Nanocrystals and Taxol**

Paclitaxel pure nanocrystals were produced by the combination approach as previously described in Section 2.2.2. PTX nanocrystals were kept as a concentrated suspension in DI water and stored at 4°C. Prior to each intravenous injection, the PTX nanosuspension was diluted with saline to achieve a concentration of 3 mg/mL. The dilution factor was between 1:3 and 1:4 (v/v). Mixture was sonicated before intravenous administration to minimize any flocculation. Taxol was prepared by dissolving PTX into a 50:50 mixture of ethanol and Cremophor EL® at a concentration of 30 mg/mL. For the intravenous injection, 10% v/v of the concentrated stock was diluted with saline to obtain a concentration of 3 mg/mL.

#### **4.1.2.3 Characterization and Analysis of PTX Nanocrystals**

The particle size and surface charge of PTX nanocrystals were measured using the same methods as described in Section 2.2.3. Chemical quantification of PTX was conducted by high liquid chromatography (HPLC, Waters Breeze) with a Waters Symmetry C18 5 µm column (4.6 x 150 mm) at 227 nm. Acetonitrile and water (50:50) were pumped at a total flow rate of 2 mL/min (Waters 1525 binary pump). The column was equilibrated to 35°C prior to sample injection (20 µL).

#### **4.1.2.4 HT-29 Cell Cultures**

HT-29 human colon adenocarcinoma cells were cultured in McCoy's 5A medium supplemented with 10% fetal bovine serum and 1% penicillin streptomycin in a 37°C humidified incubator containing 5% CO<sub>2</sub>. To establish HT-29 xenografts in nude mice,

HT-29 cells were harvested (by using 0.25% trypsin-EDTA) when they were 70-90% confluent. After being counted, cells were suspended in a 50:50 mixture of sterile phosphate buffered saline (PBS) and Matrigel (BD Biosciences, San Jose, CA) at concentration of  $3 \times 10^7$  cells/mL. Cell suspensions were kept in ice prior to their inoculation.

#### **4.1.2.5 Animal Study**

The animal study was conducted under a protocol approved for using nude mice by the University's Institutional Animal Care and Use Committee (IACUC). Female nude outbred mice (Tac:Cr: (NCr)-Foxn1 Nu) were obtained from Taconic at 4 weeks of age (14.5-20 g). Mice were acclimated for one week after arrival. Subsequently, mice were anesthetized by isoflurane inhalation for placing an ear identification tag and cell inoculation. HT-29 xenografts were established by injecting 100  $\mu$ L HT-29 cells ( $3 \times 10^6$ ) subcutaneously to each flank. Animals were monitored three times weekly for their weight and tumor volume. The tumor dimension was measured by digital calipers, and the volume was calculated by using the following equation:

$$Tumor\ volume = \frac{1}{2} \times longest\ dimension \times (shortest\ dimension)^2$$

Tumors became palpable (100-300 mm<sup>3</sup>) after nine days of inoculation. A total of 36 mice were randomized into 3 groups to receive one out of the following injections: saline (control), Taxol, or PTX nanocrystals. Intravenous injection of Taxol and PTX nanocrystals were administered via tail vein weekly on day 10, 17, 24, and 31 after inoculation at concentration of 20 mg/kg. 150  $\mu$ L of saline was administered to the control group. Body weight and tumor volume were measured three times weekly.

During the survival study, animals had to be euthanized as soon as the following criteria occurred: (i) they became moribund, (ii) their tumor reached 1500 mm<sup>3</sup> in size, became ulcerated, or impeded their ability to attain food or water, (iii) they lost 20% of their body weight, or (iv) they developed a severe medical condition or adverse effects. Those conditions are the typical humane endpoints recommended by the Institutional Animal Care and Use Committee (IACUC). The study was ended on day 32 after cell inoculation as all the mice in the control group had been euthanized.

The percent body weight change (BWC) was calculated based on the following equation:

$$\% BWC = \frac{(BW \text{ on day } n - BW \text{ on day 9 after inoculation})}{BW \text{ on day 9 after inoculation}} \times 100\%$$

#### **4.1.2.6 Statistical Analysis**

The statistical analysis was performed by Dr. Heidi Weiss' group in the Biostatistics Shared Resource Facility (Markey Cancer Center, University of Kentucky). Descriptive statistics were calculated and graphical display of percent of change in body weight from the baseline levels were generated for each group. Pairwise comparison at each time point of follow-up was performed using the non-parametric Wilcoxon rank-sum test to account for non-normality of data. Kaplan-Meier curves for overall survival were estimated for each treatment group and comparison of overall survival across treatment groups were performed based on the log-rank test. Median times as well as proportion surviving at specific time points were estimated from the Kaplan-Meier curve. Tumor volume was summarized descriptively and the percent change of tumor volume from baseline was plotted. The percent change in tumor volume at specific time points was

compared between groups using an analysis of variance model with pairwise comparisons between groups generated from the model.

### **4.1.3 Results and Discussion**

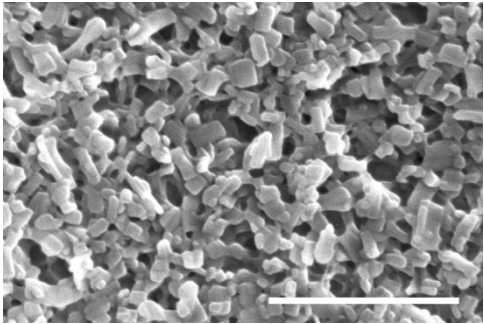
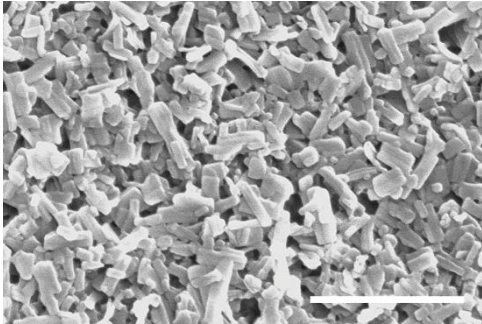
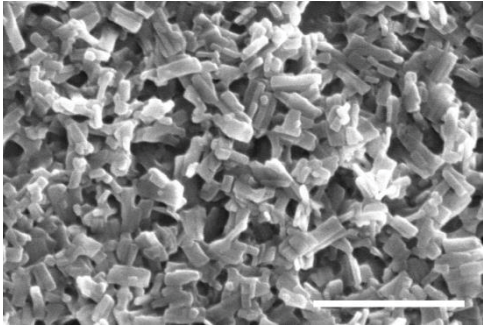
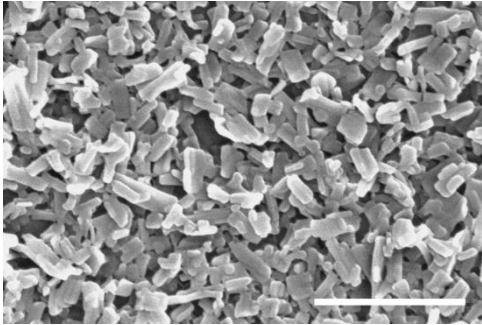
#### **4.1.3.1 Characterization of PTX Nanocrystals**

PTX nanocrystals used for this particular animal study were produced by using the combination approaches as described in Section 2.2.2. With this approach, nanocrystals with approximate size of 200 nm can be produced. The SEM images of intravenously administered PTX nanocrystals are presented in Table 4.1. The mean and standard deviation of the particle size were analyzed by using the SigmaScan (Systat Software, San Jose, CA) and summarized in Table 4.2. Additionally, the hydrodynamic diameters, polydispersity index, and zeta potential of the four PTX nanocrystal batches administered during the survival study were determined (Table 4.2).

Except for PTX nanocrystals used for the first injection, the particle size measurements analyzed by SigmaScan (from the SEM images) and DLS were comparable. Due to more heterogeneous size distribution, as indicated by the PI value (*c.a.* 0.25), the particle size measurement by DLS was higher. Other injections had narrower size distribution as their PI values were less than 0.25. As discussed in Section 2.3.1, the zeta potential of PTX nanocrystals measured in DI water was approximately between -15 and -22 mV, but it was increased (i.e. more positive) as it was dispersed in 10 mM NaCl. The understanding of this destabilization is important because the PTX nanocrystal stock suspension was diluted with saline in order to achieve isotonic intravenous injection. Any flocculation

that might occur due to the increase in the ionic strength could be minimized by mixing the stock just a few minutes before injection and subjecting the mixture to sonication.

**Table 4.1.** SEM images of PTX nanocrystals utilized for four weekly treatments during the survival study. Scale bars represent 1  $\mu\text{m}$ .

<b>Injection 1</b>	<b>Injection 2</b>
	
<b>Injection 3</b>	<b>Injection 4</b>
	

**Table 4.2.** The physical characterizations (mean  $\pm$  S.D.) of PTX nanocrystals used during the survival study.

Properties	Paclitaxel Nanocrystals			
	Injection 1	Injection 2	Injection 3	Injection 4
Particle size (SigmaScan)	149 $\pm$ 44	198 $\pm$ 63	193 $\pm$ 63	195 $\pm$ 62
Hydrodynamic diameter (DLS)	179 $\pm$ 1	200 $\pm$ 4	197 $\pm$ 3	198 $\pm$ 2
Polydispersity Index	0.25 $\pm$ 0.01	0.16 $\pm$ 0.02	0.15 $\pm$ 0.04	0.17 $\pm$ 0.04
Surface charge (in 10 mM NaCl)	Not measured	Not measured	Not measured	-9.85 $\pm$ 0.52

#### 4.1.3.2 Animal Study

The colon cancer HT-29 tumor xenografts were palpable nine days subsequent to the subcutaneous implantation of the cells. A total of 36 mice were randomized into three groups (n=12): saline, 20 mg/kg Taxol, and 20 mg/kg PTX nanocrystals. They were scheduled to receive four weekly injections (i.e. day 10, 17, 24, and 31 after inoculation). The mean and standard deviation (error bar) of the tumor volume from each group are summarized in Figure 4.1. After body weight and tumor volume measurements at day 23, some mice in the control and Taxol groups had to be euthanized due to the large tumor volume or rapid body weight decrease (see explanation in the following paragraph). Since the number of mice in the control and Taxol groups decreased, the percent change

of the tumor volume was no longer graphed starting on day 23 after inoculation. Due to the absence of PTX treatment, the tumors of mice in the saline group grew rapidly. Conversely, compared to the control group, there was a trend of tumor suppression ( $p < 0.001$ ) in both Taxol and PTX nanocrystal groups starting on day 16 after inoculation, although the difference between the treatments was marginally significant ( $p = 0.1$ ). There was no significant difference ( $p = 0.49$ ) between the change in the tumor volume of mice in the Taxol and PTX nanocrystal groups at day 23.

On day 23 after inoculation, 2 mice in the control (saline) group and Taxol were euthanized because the sum of their tumor volume had exceeded  $1500 \text{ mm}^3$ . Large tumor size generally impedes the ability of mouse to walk and obtain enough food to support its normal body function and tumors. On the same day, another mouse in the Taxol group was sacrificed due to significant weight loss (i.e. more than 20%). For this particular mouse, the decrease in body weight was most likely due to the toxicities that are associated with the utilization of Cremophore EL and ethanol as 3-5% of the body loss was observed subsequent to each intravenous injection. By day 32 after inoculation, all the mice in the control group had to be sacrificed due to their large tumor size. Thus, following the established animal protocol, which was based on the recommended humane endpoint, the survival study was ended. The survival of treatments groups was plotted with Kaplan-Meier curves as presented in Figure 4.2. Out of the 12 mice in the Taxol group, 2 mice had to be euthanized due to significant body weight loss, while 2 others had uncontrollable tumor growth. All the 4 mice in the PTX nanocrystal group were sacrificed due to large tumor volume (i.e. larger than  $1500 \text{ mm}^3$ ). The survival probabilities at day 30 after inoculation for control, Taxol, and PTX nanocrystal group

were 16.7%, 66.7%, and 83.3%, respectively. The mice in the control group reached the median survival time by day 25 after inoculation, while the median survival time was not reached for the Taxol and PTX nanocrystal group. Overall, the log-rank analysis revealed that there were significant differences between the control and Taxol ( $p = 0.0032$ ) as well as the control and PTX nanocrystals ( $p = 0.001$ ), indicating the treatments' efficacy. However, there was no significant difference between the two treatments ( $p > 0.5$ ). Liu *et al.* also reported that when administered with the same dose, 20 mg/kg, PTX in Cremophore-EL and their PTX nanocrystal formulation exhibited similar tumor inhibition activity (i.e. there was no significant difference between the two treatments) [242]. The low toxicity of the nanocrystals prompted them to increase the dose of administration. Significant tumor inhibition ( $p < 0.001$ ) was achieved when the PTX nanocrystal dose was increased to 60 mg/kg.

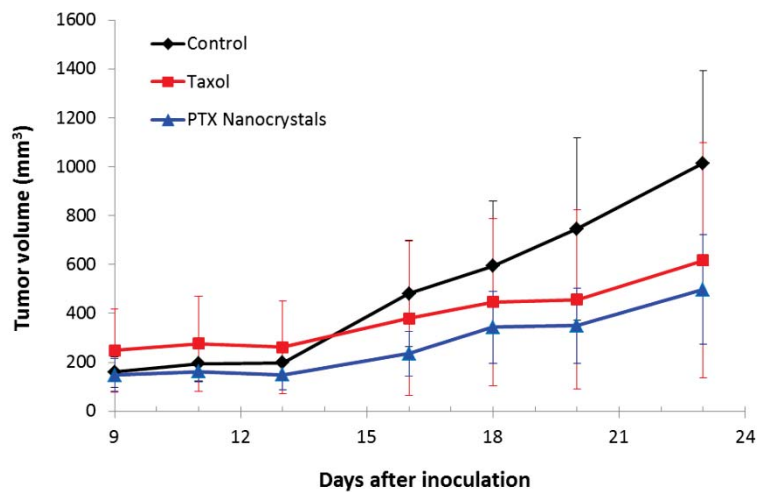


**Figure 4.1.** The tumor volume chart from the three different groups: control (saline), 20 mg/kg Taxol, 20 mg/kg PTX nanocrystals up to day 23 after inoculation (prior to euthanization, n=12 for all the groups).

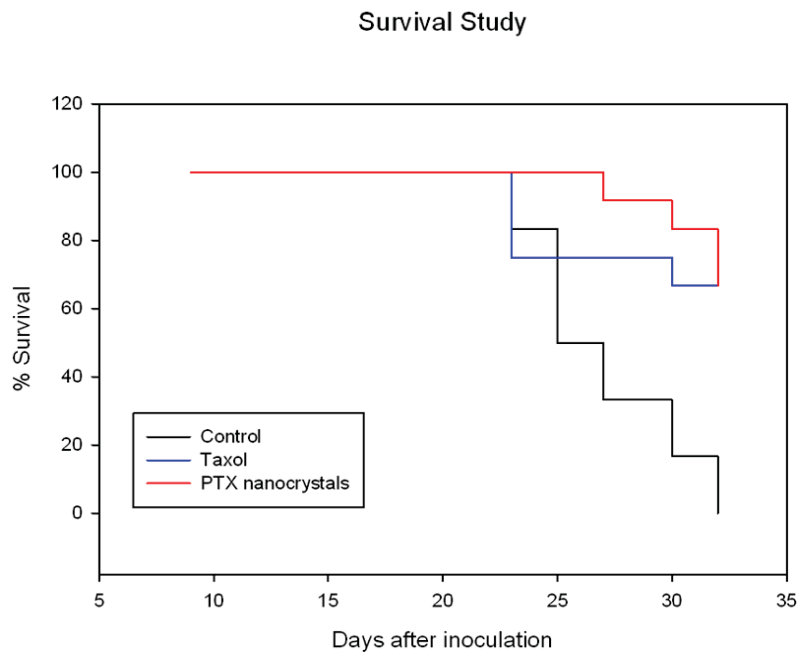


**Figure 4.2.** The percent of animal survival versus time. Animals were administered either with saline, 20 mg/kg Taxol or PTX nanocrystals at day 10, 16, 24, and 31 after inoculation (n=12 on day 0).

PTX nanocrystals were formulated with an objective to offer a safer delivery of PTX. The chart signifying the mean and standard deviation (i.e. the error bars) of the percent body weight change during the course of the survival study is depicted in Figure 4.3. Upon statistical analysis, the differences in the percent body weight change of the Taxol and PTX nanocrystals groups on day 16 and 23 after inoculation (i.e. 6<sup>th</sup> day after weekly injections) were significant ( $p < 0.05$ ). In the Taxol group, out of the 8 mice that survived on day 32 after inoculation, half of them had more than 5% loss of their body weight. In contrast, only 1 of the 8 mice left in the PTX nanocrystal group had body weight loss of more than 5%.

It is important to note that similar to previous animal studies conducted in our lab, mice in the Taxol group had a tendency to lose their body weight during the course of the study. A decrease in body weight could be associated with cancer cachexia, loss of body weight that hardly can be reversed nutritionally, and/or treatment. Yet, the repetitious observed trends suggested that it was likely due to the solvent-associated toxicity. Therefore, in spite of the similarity in the efficacy effect when administered at 20 mg/kg, PTX nanocrystals potentially could offer safer delivery of PTX relative to Taxol.

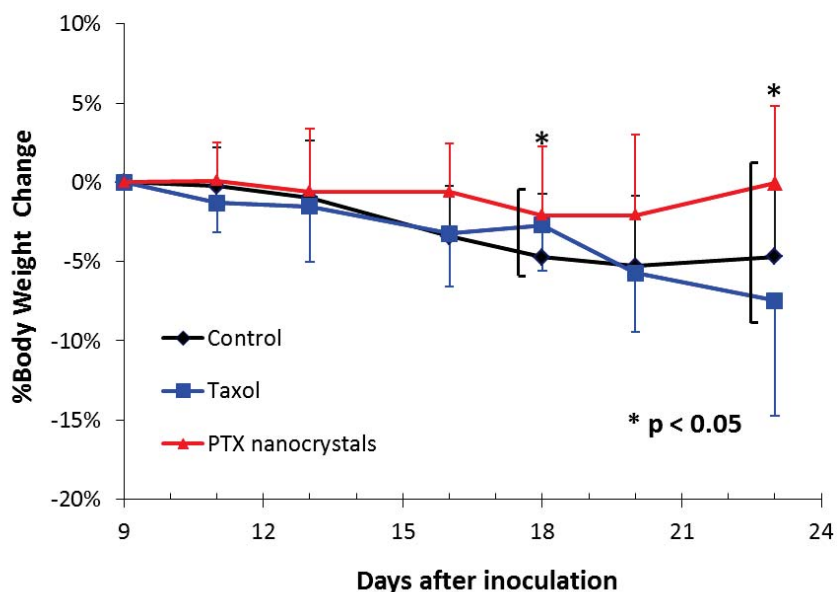


**Figure 4.3.** Percent body weight change of animals in three treatment groups up to day 23 after inoculation (prior to euthanization, n=12 for all the groups).

#### 4.1.4 Conclusion

PTX nanocrystals for intravenous injection were produced by the combination approach. The efficacy and toxicity of PTX nanocrystals were compared to control (saline) and Taxol in a human colorectal adenocarcinoma HT-29 xenograft model in immunodeficient mice. Subsequent to four weekly treatments, the result of the survival study revealed that there was no significant difference in the efficacy of Taxol and PTX nanocrystals at 20 mg/kg dose. However, relative to Taxol, the solvent-free PTX nanocrystal suspension was able to offer less toxic, thus safer delivery of PTX.

## **4.2 Evaluation of PTX/MMPSense/FPR-648 Nanocrystals in MCF-7 Xenograft**

### **4.2.1 Introduction**

“Theranostics” is defined as a material that is designed to have combination of therapeutic and diagnostic modalities. In (pre)clinical settings, theranostic nanomedicines can be utilized to validate and optimize the properties of drug delivery systems and enable personalized medicine, as opposed to adopting a “one size fits all” approach. The inclusion of the diagnostic probe(s) in theranostics allows one to longitudinally monitor the therapeutic efficacy and possibly predict a potential treatment response. For the therapy and diagnosis of cancer, theranostic nanomedicines are aimed to have the ability to accumulate in the tumor efficiently, exert treatment efficacy with minimal toxicity, and simultaneously provide real-time, non-invasive information about the distribution and the diseased tissue. In the past few years, vast numbers of theranostic nanomedicines have been reported and reviewed [31, 32, 68, 72, 279]. Most theranostic systems are constructed from lipid bilayer vesicles, polymers, and inorganic materials, which may generate additional toxicity. By utilizing hybrid nanocrystals, which are composed mostly of the drug molecules, the extraneous hazards could be minimized. Additionally, high drug-loaded hybrid nanocrystals can be produced using a “one-pot” synthesis, permitting simple formulation.

The ability of PTX hybrid nanocrystal system to perform as a theranostic system was tested in the murine human breast cancer MCF-7 orthotopic xenograft (inoculated in the mammary fat pads). The tumor growth and metastatic potential rely heavily on the site of inoculation [280-283]. Orthotopic implantation, where cells are re-inoculated into the site of the original tumor, produce metastatic lesions more frequently than those inoculated

elsewhere [281]. Two imaging moieties, bioactivatable MMPSense 750 FAST and near-infrared fluorophore FPR-648, were concurrently incorporated into the nanocrystals. MMPSense 750 was expected to give a feedback of the disease state (e.g. metastasis), while the entrapped FPR-648 could assist in non-invasively tracing the distribution of the nanocrystal system. Because their emission wavelengths are separated by 100 nm (MMPSense  $\lambda_{em}$ : 775 nm, FPR-648  $\lambda_{em}$ : 672 nm), the fluorescent signals can be observed in two separate excitation/emission windows by the *in vivo* imaging system IVIS<sup>®</sup>.

MMPSense 750 FAST is a bioactivatable dye, which is optically silent in its native (quenched) state but becomes highly fluorescent as the peptide bond portions are cleaved by matrix metalloproteinases (MMPs). Matrix-metalloproteinases (MMPs), a large family of zinc –dependent proteolytic enzyme, particularly MMP-2 (gelatinase-A) and MMP-9 (gelatinase-B) are involved in the progression of breast cancer [284]. While MMP-2 is expressed in very early stage breast cancer and believed to play role in the first events leading to the tumor formation [285], MMP-9 appears to be associated with lymph-node metastasis [286]. MCF-7 human breast adenocarcinoma expressed both MMP-2 and MMP-9 only when co-cultured with tumor-derived fibroblasts [284]. Clapper *et al.* have reported the successful use of bioactivatable molecular imaging probes, MMPSense, to correlate the positive fluorescence signal and the presence of pathologically confirmed colonic adenocarcinoma [287]. The ability of entrapped MMPSense (i.e. in hybrid nanocrystals) to monitor the disease state (e.g. metastasis) was non-invasively evaluated by using the IVIS Spectrum system ( $\lambda_{ex}$ : 745 nm and  $\lambda_{em}$ : 800 nm). The signals detected from hybrid nanocrystals suggested that subsequent to tumor and tissue accumulation, the quenched MMPSense was able to be released from the crystal lattice and undergo

cleavage by MMPs in the site where their activity is elevated. The co-entrapment of bioactivatable probe and therapeutic agents can be beneficial, in that response to therapy can be monitored longitudinally subsequent to each treatment, which may take a few weeks. Since the bioactivatable probe is highly sensitive, it should be able to detect a very small number of precancerous or cancerous cells with elevated protease activity [287].

## **4.2.2 Materials and Methods**

### **4.2.2.1 Materials**

Paclitaxel (>99.5%, USP30) was purchased from 21CECPharm (United Kingdom); FPR-648 fluorophore ( $\lambda_{ex}$ =648 nm;  $\lambda_{em}$ =672 nm) was obtained from Akina (West Lafayette, IN); MMPSense 750 Fluorescent Activatable Sensor Technology (FAST) ( $\lambda_{ex}$ =745 nm;  $\lambda_{em}$ =800 nm) was purchased from Perkin Elmer (Waltham, MA). Ethanol (HPLC grade), acetonitrile (HPLC grade), and DMSO (dimethyl sulfoxide, ACS grade) were purchased from Fisher Scientific (Pittsburgh, PA). All chemicals and solvents were utilized without further purification. Deionized water (by Milli-Q<sup>®</sup>, filtered through 0.2  $\mu$ m membrane) was used for all the experiments. 0.050  $\mu$ m (50 nm) Whatman<sup>®</sup> nuclepore polycarbonate track-etched membranes used for filtration were purchased from Fisher Scientific (Pittsburgh, PA). MCF-7 human breast adenocarcinoma cells were obtained from ATCC (Manassas, VA).

#### **4.2.2.2 Preparation of Pure and PTX/MMPSense/FPR-648 Hybrid Nanocrystals**

Pure and hybrid paclitaxel nanocrystals were produced by using an anti-solvent method. For the pure nanocrystal, 1 mL of 5 mg/mL of paclitaxel in ethanol was added to 20 mL deionized water in round-bottom flask. The mixture was subjected to stirring at 800 rpm and sonication (sonication bath, F20D, Fisher Scientific) for 10 minutes. To make hybrid PTX/MMPSense/FPR-648 nanocrystals, 6.48 nmol (in 0.27 ml) of MMPSense 750 FAST and 0.635 mg (in 0.127 ml) of FPR-648 were added to deionized water prior to the addition of PTX solution. After stirring at 800 rpm for 10 minutes, the speed was adjusted to 300 rpm (for 15 minutes) and 150 rpm (for another 15 minutes) in order to minimize bubbles formed and encourage entrapment of the imaging agents. After crystallization, the solution was filtered through a 50-nm polycarbonate membrane, and the retentate was re-suspended in water for additional filtration-re-suspension cycles to remove imaging agents that may potentially adhere to the surface of the crystals.

#### **4.2.2.3 Physical Characterization and Chemical Analysis of Nanocrystal Systems**

SEM images were obtained using the Hitachi SEM 4300 at accelerating voltage of 3 kV. Using a sputter coater, samples were coated with conductive layers of gold palladium (Au/Pd) for 1 minute with a current of 20 mA. Particle size and zeta potential were measured in deionized water using Malvern Zetasizer (Nano-ZS).

PTX concentrations were analyzed by a high-performance liquid chromatography (HPLC) system (Waters Breeze with a dual wavelength absorbance detector, Waters 2487) at an absorbance wavelength of 227 nm. A reverse-phase C-18 column (5  $\mu$ m, 150 mm  $\times$  4.6 mm, Waters) was used. The mobile phase composed of 50% acetonitrile and

50% deionized water was pumped at a total flow rate of 2 mL/min. The column was equilibrated to 35 °C prior to sample injection (20 µl).

IVIS<sup>®</sup> Spectrum was utilized to measure the percent entrapment of fluorophores (MMPSense 750 and FPR-648) in the hybrid nanocrystals. When tested with near-infrared dye Cy5.5, small animal optical imaging system, such as IVIS<sup>®</sup>, was capable of producing high linear correlation between fluorescence intensity and concentration for more than 3 log orders of magnitude (i.e. 1 to 1000 nM) with R<sup>2</sup> of 0.996 [288]. Standard solutions of MMPSense 750 and FPR-648 were prepared in DMSO. MMPSense 750 standards were prepared at concentrations of 0.2, 0.5, 1, and 2 nmol/mL, while those of FPR-648 were at concentrations of 0.25, 0.5, 0.75, and 1 µg/mL. MMPSense 750 was analyzed at excitation and emission wavelengths of 745 and 800 nm, respectively, while, FPR-648 was analyzed at lower wavelengths ( $\lambda_{\text{excitation}}$ : 640 nm,  $\lambda_{\text{emission}}$ : 700 nm).

#### **4.2.2.4 Cell Culture of MCF-7**

The MCF-7 human breast adenocarcinoma cells were cultured with DMEM (Dulbecco's Modified Eagle Medium, Hyclone) with 10% fetal bovine serum (Hyclone) and 1% penicillin/streptomycin (Hyclone). Trypsin-EDTA (ethylenediaminetetraacetic acid, Mediatech) was used to dissociate cells from the dish. All the cell culture reagents were purchased from Fisher Scientific (Pittsburgh, PA). Cells were cultured at 37 °C in a humidified atmosphere with 5% CO<sub>2</sub>. To establish the MCF-7 xenograft in nude mice, cells were harvested (by using 0.25% trypsin-EDTA) when they were 70-90% confluent. After being counted, cells were suspended in serum-free DMEM at a concentration of 5x10<sup>7</sup> cells/ml. Cell suspensions were kept in ice bucket prior to their inoculation.

#### 4.2.2.5 Animal Study

Female nude outbred mice (Tac:Cr: (NCr)-Foxn1 Nu) were obtained from Taconic at 4 weeks of age (14.5-20 g). All of the animal experiments complied with the principles of care and use of laboratory animals and were approved by the University of Kentucky Institutional Animal Care and Use Committee (IACUC). Seven days after arrival, one  $17\beta$ -estradiol pellet (1.7 mg, 60-day release; Innovative Research of America, Inc.) was implanted under the skin between the ears of each mouse. Two days later,  $5 \times 10^6$  MCF-7 cells (100  $\mu$ L) were inoculated subcutaneously into each side of the mammary fat pad. All experimental procedures were performed under general anesthesia by isoflurane inhalation. Subsequent to the treatment injections, animals were monitored daily for their body weight and tumor volume using a digital caliper. The tumor volume was calculated by using the following equation:

$$Tumor\ volume = \frac{1}{2} \times longest\ dimension \times (shortest\ dimension)^2$$

Approximately 8 weeks after tumor inoculation, a total of 24 mice were randomized into 4 groups (n=6): untreated (control), Taxol, PTX nanocrystals, and PTX/MMPSense/FPR-648 hybrid nanocrystals. Taxol formulation (3 mg/ml) was prepared by diluting 300  $\mu$ l of 30 mg/ml of paclitaxel in Cremophore EL/ethanol (50:50) solution with 2.7 mL of saline (0.9% sodium chloride). The intravenous injections that were administered to the mice via tail veins were summarized in Table 4.3. Concurrently, 0.1 nmol of the bioactivatable dye, MMPSense 750, diluted in PBS was also injected into all mice, except those in the PTX/MMPSense/FPR-648 hybrid nanocrystal group. The *in vivo* performance of free and entrapped (i.e. in hybrid nanocrystals) MMPSense 750 were monitored by IVIS<sup>®</sup> Spectrum ( $\lambda_{ex}$ : 745 nm,  $\lambda_{em}$ : 800 nm). The fluorescence signal of entrapped FPR-648 in

PTX/MMPSense/FPR-648 hybrid nanocrystals was also longitudinally monitored by IVIS<sup>®</sup> at  $\lambda_{\text{ex}}$ : 640 nm,  $\lambda_{\text{em}}$ : 700 nm. All mice were euthanized at day 7.

**Table 4.3.** The details of injections for evaluating MMPSense performance *in vivo*.

Groups	Number of mice	Paclitaxel	MMPSense
No xenograft	5	-	0.1 nmol
Untreated	6	-	0.1 nmol
Taxol	6	20 mg/kg	0.1 nmol
PTX nanocrystals	6	20 mg/kg	0.1 nmol
PTX/MMPS/FPR-648 nanocrystals	6	20 mg/kg	0.2 nmol (1.83 % w/w entrapment)

#### 4.2.2.6 IVIS<sup>®</sup> Imaging

Prior to and during the IVIS<sup>®</sup> imaging, mice were anesthetized by isoflurane inhalation. To monitor the MMPSense 750 fluorescence signals, mice were imaged at excitation and emission wavelengths of 745 nm and 800 nm, respectively. Images were all taken with the same parameters as follows: (a) exposure time: 4 seconds, (b) F/Stop: 2, (c) binning: 8 (medium), (d) field of view (FOV): 13. To monitor the FPR-648 fluorescence signals, excitation wavelength of 640 nm and emission wavelength of 700 nm were utilized. Images were taken with 0.25 second exposure time, but the remaining parameters were kept constant.

#### **4.2.2.7 Statistical Analysis**

The statistical analysis was performed by Dr. Heidi Weiss' group in Biostatistics Shared Resource Facility (Markey Cancer Center, University of Kentucky). Graphical display of percent of change in body weight from the baseline levels were generated for each group. Pairwise comparisons at each time point of follow-up were performed using the non-parametric Wilcoxon rank-sum test to account for non-normality of data. The percent change in tumor volume at specific time points was compared between groups using an analysis of variance model with pairwise comparisons between groups generated from the model.

#### **4.2.3 Results and Discussion**

##### **4.2.3.1 Characterization and Analysis of PTX Pure and PTX/MMPSense/FPR-648 Hybrid Nanocrystals**

The PTX nanocrystals, both pure and hybrid, used for this particular animal study were produced by the anti-solvent method. The harvested nanocrystals were not subjected to any homogenization, as aforementioned in Section 2.2.2. The SEM images, size analysis (by SigmaScan), polydispersity index, and zeta potential of both products are presented in Table 4.4 and Table 4.5, respectively. For PTX pure nanocrystals, the hydrodynamic diameter determined from DLS was similar to the particle size analyzed from the SEM image (by SigmaScan). In contrast, the particle size of the PTX/MMPSense/FPR-648 nanocrystals determined by DLS was underestimated possibly because of their elongated shape and particle size heterogeneity. The polydispersity indices suggest that the size distribution of the pure PTX nanocrystals was narrower than that of the PTX hybrid

nanocrystals. In addition, the more negative value of zeta potential of the hybrid nanocrystals is suspected due to the adsorption of MMPSense molecules, which are negatively charged in the aqueous environment [289]. Although the exact molecular structure of MMPSense is undisclosed, the technology was based on the bioactivatable probes previously reported [290]. The polymer backbone, which supports the cleavable site (proline-leucine-glycine-valine-arginine peptide) and unquenched fluorophores [291], could promote higher adsorption of MMPSense to the surface of the nanocrystals, in addition to being integrated in the crystal lattice.

**Table 4.4.** SEM images of PTX and PTX/MMPSense/FPR-648 nanocrystals. Scale bars represent 1  $\mu\text{m}$ .

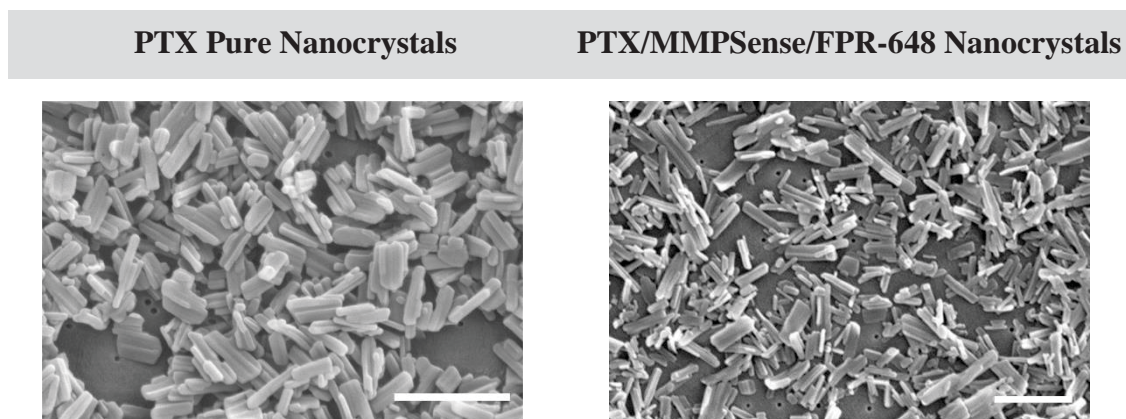


**Table 4.5.** Physical properties of PTX pure and hybrid nanocrystals (mean  $\pm$  S.D.).

Properties	PTX Nanocrystals	PTX/MMPSense/FPR-648 Nanocrystals
Particle size (SigmaScan)	300 $\pm$ 140 nm	380 $\pm$ 140 nm
Hydrodynamic diameter (DLS)	270 $\pm$ 5 nm	280 $\pm$ 20 nm
Polydispersity Index	0.10 $\pm$ 0.03	0.19 $\pm$ 0.05
Surface charge (in DI water)	-14.9 $\pm$ 0.1 mV	-20.6 $\pm$ 0.6 mV

The amount of fluorophores entrapped was analyzed by using the IVIS<sup>®</sup> Spectrum. The standard solutions and samples were placed in a 96-well plate, and the fluorescence intensity from the wells was analyzed by Living Image<sup>®</sup> software (Caliper Life Science, Hopkinton, MA) specifically written for the analysis of IVIS<sup>®</sup> images. The IVIS<sup>®</sup> image of a portion of the 96-well plate that was filled with the standard solutions of MMPSense 750 and FPR-648 is shown in Figure 4.4. The MMPSense 750 and FPR-648 standard

solutions were placed in the top and bottom portion, respectively. When imaged at  $\lambda_{\text{ex}}$ : 640 nm and  $\lambda_{\text{em}}$ : 700 nm, only the FPR-648 standard solutions fluoresced. Meanwhile, MMPSense solutions were detected when excitation and emission wavelengths of 745 nm and 800 nm, respectively, were utilized. This image shows the specificity of the instrument, which is equipped with narrow bandwidth (30 nm) excitation filters and narrow bandwidth (20 nm) emission filters. Additionally, the IVIS<sup>®</sup> spectral un-mixing algorithm allows researchers to separate signals from multiple fluorescent reporters within the same animal or source.

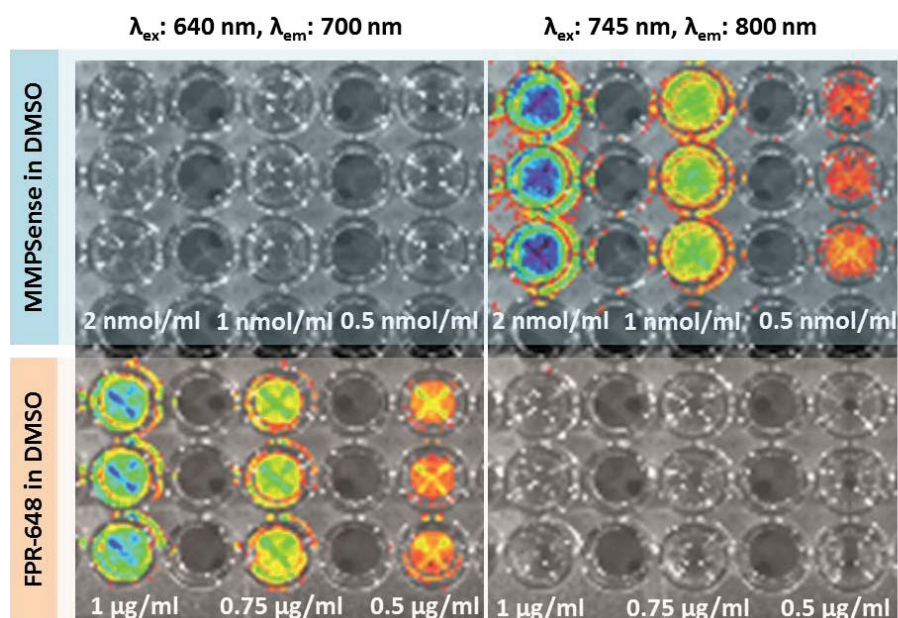


**Figure 4.4.** IVIS<sup>®</sup> images of wells that were filled with standard solutions prepared in DMSO and imaged either with  $\lambda_{\text{ex}}$ : 640 nm and  $\lambda_{\text{em}}$ : 700 nm or  $\lambda_{\text{ex}}$ : 745 nm and  $\lambda_{\text{em}}$ : 800. Only the bottom part, FPR-648 solutions, fluoresced at the former excitation/emission window, while the top part, MMPSense 750 solutions, fluoresced at the latter.

The standard curves generated from triplicate standard solutions of MMPSense 750 and FPR-648 are presented in Figure 4.5 and 4.6, respectively. IVIS<sup>®</sup> was capable of producing high linear correlation between fluorescence intensity and concentration for more than 3 log orders of magnitude (i.e. 1 to 1000 nM) with  $R^2$  of 0.996 when tested with near infrared dye Cy5.5 [288]. From the standard curves, it was determined that there was 1.6 nmol/mL of MMPSense 750 (MW: ~43,000 g/mol) in 3.76 mg/mL of PTX nanocrystals, giving a percent entrapment of 1.83% (w/w). Meanwhile, there was 0.5  $\mu$ g/mL (0.01% w/w) of FPR-648 entrapped. Due to its high sensitivity, the IVIS<sup>®</sup> optical imaging modality, is able to detect fluorophore(s) even at nanomolar concentrations.

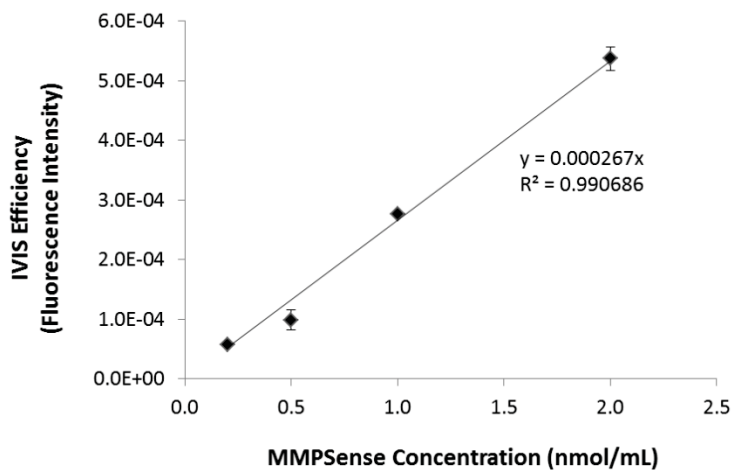


**Figure 4.5.** The standard curve of MMPSense 750 obtained from the IVIS<sup>®</sup> Spectrum

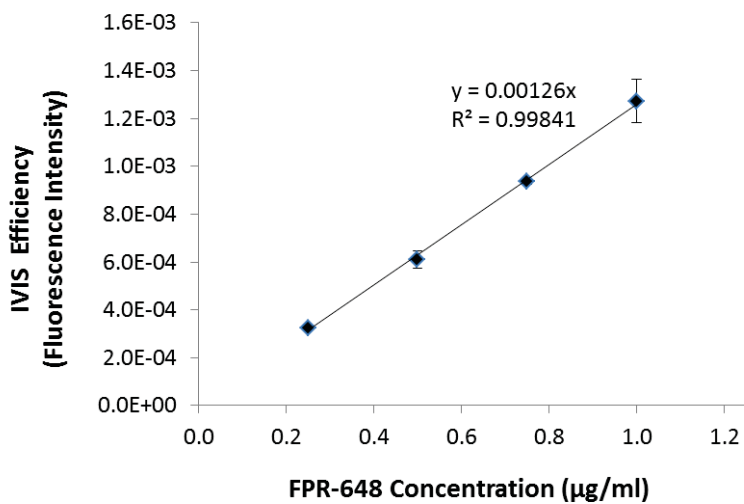


**Figure 4.6.** The standard curve of FPR-648 obtained from the IVIS<sup>®</sup> Spectrum

#### 4.2.3.2 Animal Study

The MMPSense molecules are optically silent (quenched) in their native state, but they become highly fluorescent as the peptide bond portion gets cleaved by matrix metalloproteinases (MMPs), which facilitate tumor cell invasion and metastasis [292]. Specifically, MMP-2 and MMP-9 are overexpressed in MCF-7 cell lines [284]. To test the robustness of MMPSense 750 performance in an animal model, first, 0.1 nmol of the MMPSense 750 dissolved in phosphate buffered saline (PBS) was first injected into athymic mice without any tumor burden, and the animals were imaged by IVIS<sup>®</sup> (Figure 4.7). Because tumor was not initiated in the animals and MMPs were minimally expressed, little fluorescent signal should be observed. Nonetheless, fluorescent signals were detected up to day 2 after injection. Later, it was confirmed with the supplier (Perkin Elmer) that the dye was not 100% quenched (or conjugated), i.e. mixed with a small percentage of unquenched fluorophores due to the synthesis process. At day 2, most of the unquenched dye was renally cleared from the body.

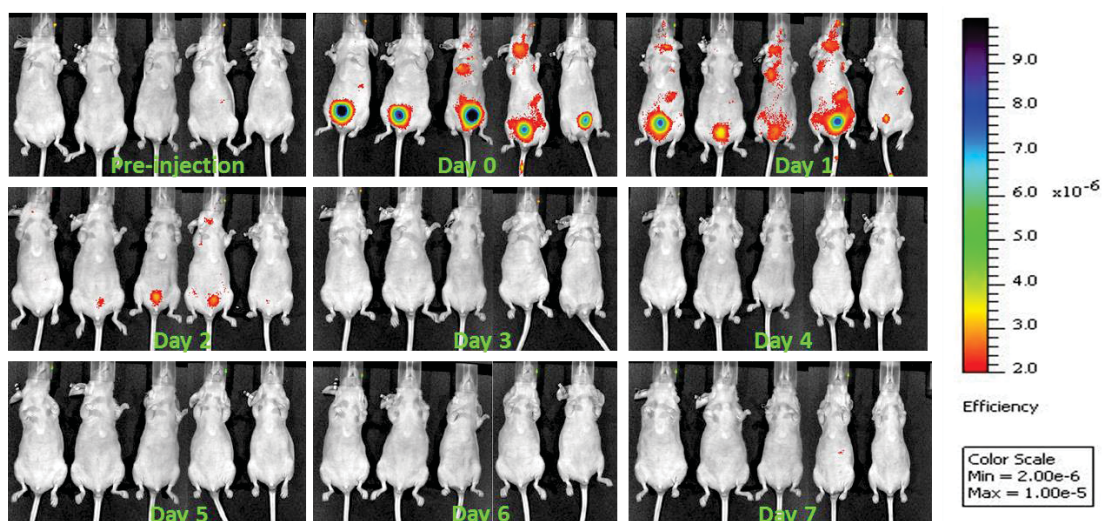


**Figure 4.7.** IVIS<sup>®</sup> images of non-xenograft mice (n=5) injected with 0.1 nmol MMPSense 750.

From the fluorescence analysis, it was determined that there was 1.83% w/w entrapment of MMPSense 750 in the PTX hybrid nanocrystal. In a single intravenous injection of PTX hybrid nanocrystals at 20 mg/kg, the total amount of entrapped MMPSense was approximately equivalent to 0.2 nmol per animal. To validate and compare the ability of the entrapped versus free MMPSense to monitor the cancer state, 0.1 nmol (half concentration of the entrapped dye) of the free MMPSense/PBS was injected simultaneously with Taxol, pure PTX nanocrystals, or by itself in the case of the untreated group. The IVIS<sup>®</sup> images from the four groups were compared at day 2, when the majority of the pre-existing unquenched MMPSense had been cleared (Figure 4.8).

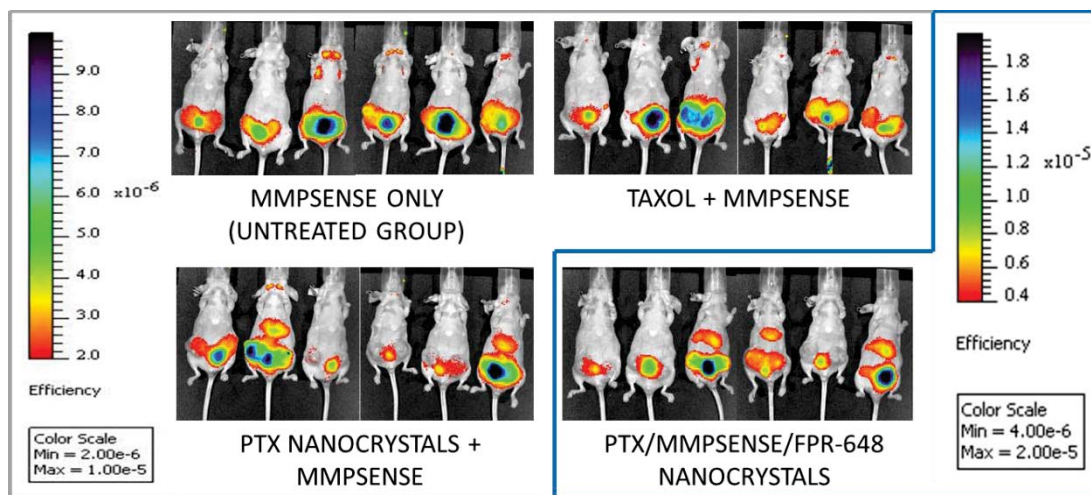


**Figure 4.8.** IVIS images of mice from different treatment groups at day 2 after injection. MMPSense solution (0.1 nmol) was given to the first three groups with or without the treatment, while approximately 0.2 nmol of MMPSense were entrapped in the injected hybrid nanocrystals given to the last group. The color intensity scale was doubled ( $4 \times 10^{-6}$  to  $2 \times 10^{-5}$ ) of the last group in order to match the half amount of the dyes used in the first three groups ( $2 \times 10^{-6}$  to  $1 \times 10^{-5}$ ).

The apparent fluorescent signals at day 2, hence, should signify the intensities that were due to MMPsense activation. The cleaved fluorophores, which are hydrophilic, were then cleared renally. Due to the difference in the chemical makeup, the clearance of the paclitaxel may differ from the fluorophores. The images also showed that entrapped MMPsense in the PTX nanocrystals was capable of exerting the same functionality to respond to the elevation of MMPs as that by the unbound MMPsense. This suggests that the entrapped MMPsense dye were released out of the nanocrystals and cleaved by MMPs in the main tumor and metastasis sites.

The IVIS images of mice from all the treatment groups from day 0 to 5 are summarized in Figure 4.9.A. The mean and standard deviation of fluorescent signal intensities are shown in Figure 4.9.B. Based on Figure 4.9.A (day 0 to 3 images), the stronger fluorescent signals observed in some mice of the pure and hybrid nanocrystals groups may rise from the variation in the amount of MMPsense in the intravenous injection. The mice showing stronger signals in later time points had higher initial intensities on day 0. Furthermore, although some degrees of variation were observed, the mean values of the photonic efficiency from all of the xenografted mice were almost doubled at 19 hours after the injection (Figure 4.9.B). Compared with the signal attenuation over time observed in the mice with no xenograft, the signal amplification in the xenografted mice signified that the MMPsense probe was activated by the MMPs. It is also worth noting that the MMPsense incorporated in the hybrid nanocrystals were able to perform similarly to the free MMPsense, which was injected by itself (for the untreated group) or along with other treatments (Taxol and pure paclitaxel nanocrystals). The large standard deviation in the hybrid nanocrystal group was caused by the variability on the amount of

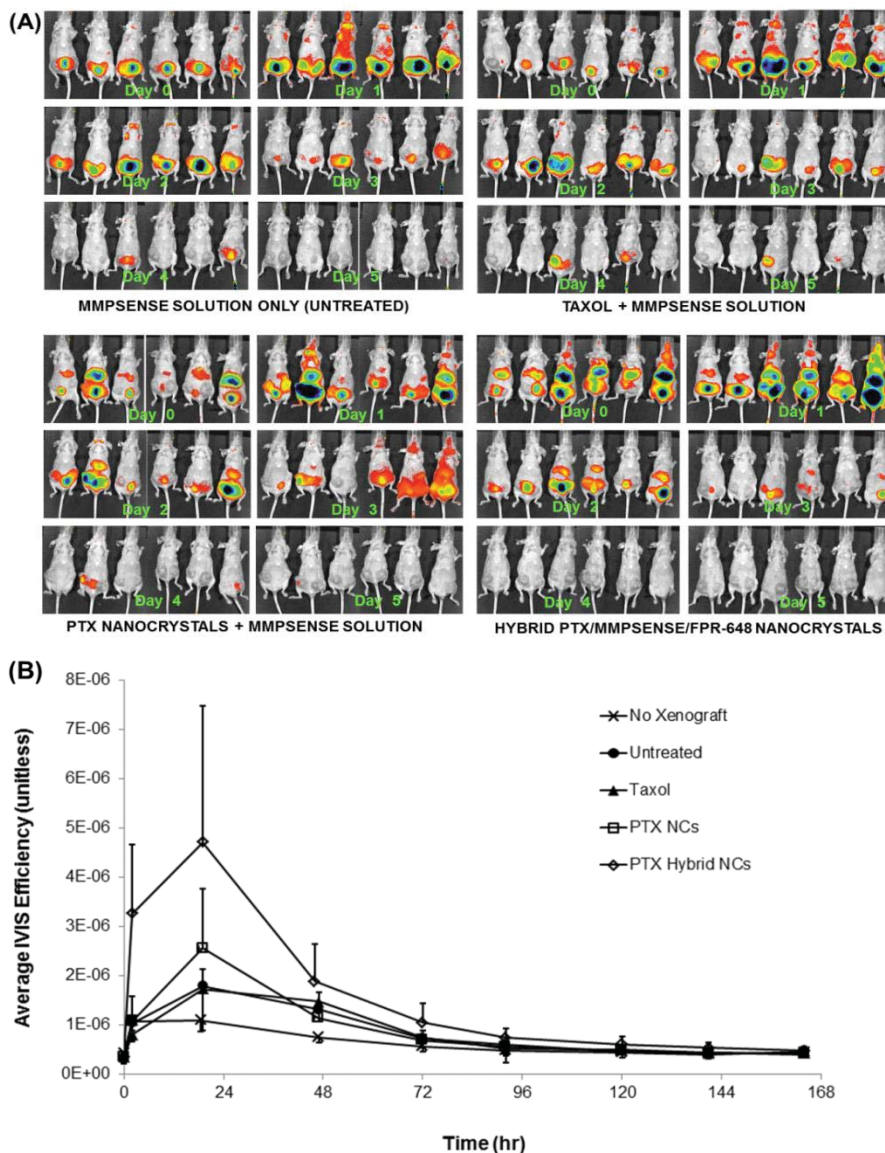


**Figure 4.9.** (A) IVIS images of mice from untreated, Taxol, PTX pure, and PTX hybrid nanocrystal groups from day 0 to day 5. Day 0 images were taken 2 hours post-injection. The color scale from the PTX hybrid nanocrystal group (left) was doubled compared to the other groups (as in Figure 3). (B) The average IVIS efficiency (i.e., IVIS efficiency ( $\text{cm}^2$ ) divided by the area of each mouse ( $\text{cm}^2$ )) was plotted against the time. The data points indicate mean  $\pm$  S.D.  $n=6$  for the xenografted mice (Figure 4.8) and  $n=5$  for no-xenograft group (Figure 4.7).

MMPSense, both integrated and on the surface of the nanocrystals, in each injection. Figure 4.9.A further suggests that there were more unquenched dyes integrated with the nanocrystals, likely resulting from the integrity of MMPsense being compromised due to the exposure to ethanol, rapid stirring, and intense sonication during the process of nanocrystal production. The unquenched dyes were mostly cleared before day 2 through the kidney and urinary bladder, and most of the fluorescence imaging observed on day 2 should have arisen from the quenched dyes that were released from the nanocrystals and cleaved by the MMPs. In all groups, the fluorescence signals died down significantly after day 3. The similarity in the fluorescence imaging of the pure and hybrid nanocrystal groups did imply the possibility that MMPSense molecules were mostly adsorbed to the surface of the hybrid nanocrystals, detached quickly upon the injection of the nanocrystals. Moreover, given the relatively large entrapment ratio (1.83% w/w), a majority of the dyes were more likely not integrated throughout the nanocrystals, differing from FPR-648 discussed below.

In order to non-invasively trace the distribution of the hybrid nanocrystal *in vivo*, it was intended to incorporate the NIR dye FPR-648 in the crystal lattice of the nanocrystals. IVIS<sup>®</sup> images of mice treated by the PTX/MMPSense/FPR nanocrystals were obtained at the lower emission wavelength (Figure 4.10). The weak fluorescent spots observed in the images prior to the injection were due to the autofluorescence. Post-injection IVIS<sup>®</sup> images indicate that the majority of the hybrid nanocrystals were accumulated in the liver. Because of their size range, 250-600 nm, the hybrid nanocrystals were prone to be sequestered by the Kupffer cells in the mononuclear phagocyte system (MPS). It is important to note that the observed fluorescence arose from the combination of both

entrapped and dissolved dye molecules. In a previous animal study, the solution of FPR-749 dye, which has similar chemical structure to FPR-648, were cleared approximately 72 hours subsequent to the injection [169]. Thus, given the fact that the fluorescent remains up to day 7, it is highly plausible that the nanocrystals were not completely dissolved, continuously releasing the dye molecules. Figure 4.10 may suggest that the hybrid nanocrystals, which accumulated in the liver, may slowly be released to the blood circulation and passively to the tumor site. Small amounts of fluorescence were observed in the excised tumor and liver (bottom of Figure 4.10). The imaging results differ from our earlier data, where tumor showed the strongest intensity [169]. Note that only one NIR dye was integrated in the PTX nanocrystals in the earlier study [169]; the integration and possibly surface adsorption of the large, negatively charged molecules, MMPsense, altered the surface properties (e.g., surface charge and wettability) and possibly the biodistribution of the hybrid nanocrystals, compared with the PTX/FPR-749 nanocrystals [169]. From the theranostic point of view, the bioimaging results do support a great potential of the hybrid nanocrystals whose distribution can be traced in the real-time. Still, it is worth pointing out that the live fluorescence imaging that is contributed by both integrated and unbound dye molecules. More importantly, the biodistribution of free dyes may be significantly different from that of drug molecules and/or nanocrystals.

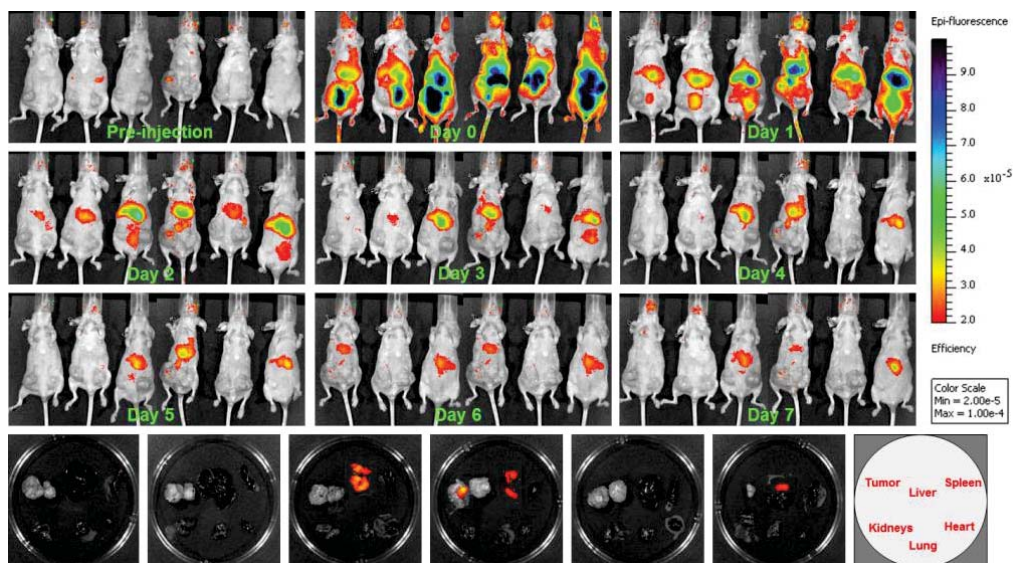


**Figure 4.10.** IVIS<sup>®</sup> images of mice in the hybrid nanocrystal group viewed at  $\lambda_{ex}$ : 640 nm and  $\lambda_{em}$ : 700 nm signifying the fluorescence signal detected from the near-infrared dye, FPR-648, incorporated in the hybrid nanocrystals. The excised tumors and major organs (liver, spleen, kidneys, lung, and heart) were imaged on day 7 with the same imaging parameters.

The amount of drug accumulated in the tumor was sufficient to induce some degree of tumor volume suppression, as seen in Figure 4.11. Compared to the control group, the treatments (Taxol, PTX nanocrystals, and PTX hybrid nanocrystals) induced tumor suppression ( $p < 0.05$ ) starting on day 3 after injection and continuing to day 7. On day 7, the treatments significantly suppressed the tumor growth compared to the control group ( $p$ -values  $< 0.01$  for all treatments). There was no significant difference in the percent of tumor volume change between the treatments ( $p > 0.1$ ) throughout the study. Clearly, without any solubilization means, the nanocrystals were capable of inducing similar degree of tumor growth suppression as the solubilized formulation (e.g. Taxol).

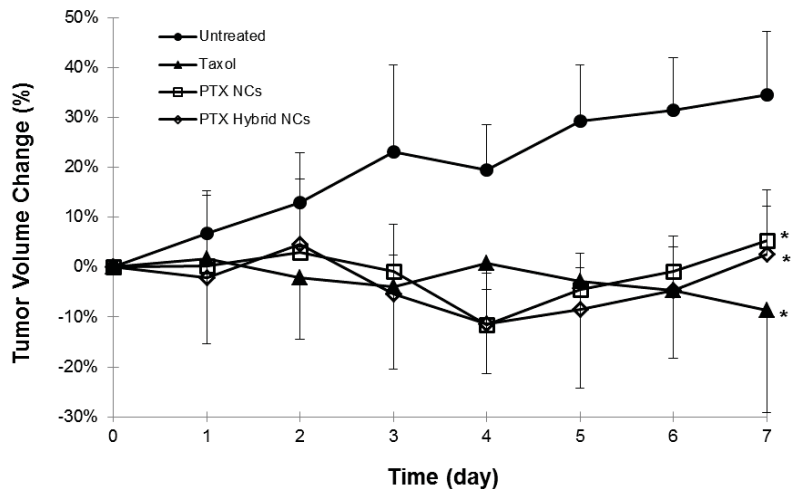


**Figure 4.11.** Percent change in tumor volume measured daily after single injection of treatments on day 0. Each point indicates the mean  $\pm$  S.D. (n=6). \*P<0.01 compared to the untreated group on day 7. All treatments induced tumor suppression (P<0.05) on days 3, 4, 5, and 6.

Furthermore, the treatment toxicity was evaluated by the percent body weight change during the course of the study (Figure 4.12). Note that all of the mice, including ones with no tumor (MCF-7 xenograft), experienced some extent of body weight loss due to the induced stress from daily transportation and exposure of anesthesia during the (IVIS<sup>®</sup>) imaging process. Compared to the control (untreated), the percent of body weight of the Taxol group was significantly different ( $p < 0.05$ ) on days 2, 3, 4, and 6, and trends towards significance were observed on day 5 ( $p = 0.07$ ) and 7 ( $p = 0.16$ ). The mice in the Taxol group were likely able to recoup their body weight back by day 7 because most of the treatments might have been cleared. Conversely, the body weights of mice in the pure and hybrid nanocrystals group were not significantly different ( $p > 0.1$ ) from the control (untreated). This result suggested that nanocrystals were able to offer

safer and less toxic delivery than the solubilized formulation. As such, it is possible to increase the dose of nanocrystals to achieve more efficient treatment.

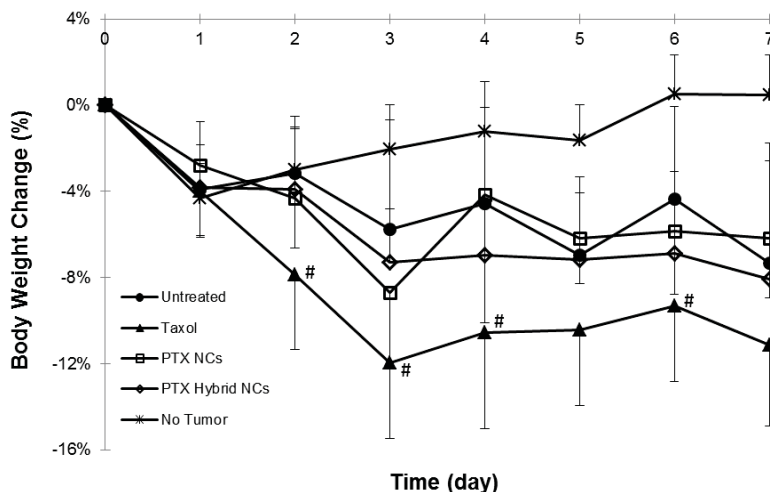


**Figure 4.12.** Percent change in body weight measured daily. Each point indicates the mean  $\pm$  S.D. (n= 6). #  $P < 0.05$  compared to the untreated group on days 2, 3, 4, and 6.

#### 4.2.4 Conclusion

In this study, the potential of paclitaxel hybrid nanocrystals as a cancer theranostic system was evaluated. Two imaging probes, MMPSense 750 and FPR-648, were intended to be physically incorporated in the drug nanocrystals that were formulated by crystallization. Both dyes were imaged at different excitation and emission wavelengths. While MMPSense reported the degree of metastasis, the integrated FPR-648 served as a tracer for the biodistribution of the nanocrystals in the animals. At a dose level of 20 mg/kg, PTX pure and hybrid nanocrystals were as efficacious as Taxol in suppressing the growth of MCF-7 xenograft. Yet, the nanocrystals induced less toxicity than the conventional solubilized formulation. The bioimaging capability of the hybrid

nanocrystals was limited by the size and impurities of MMPSense. Despite the likelihood that MMPSense molecules may mostly adsorb to the crystal surface, the study demonstrates that hybrid nanocrystals have a great potential to be utilized as a simple, versatile, and enabling platform for cancer theranostics. Studies are under way to explore other types of bioimaging modalities, using smaller and purer dyes, which are compatible with crystal integration. Furthermore, to have a better understanding of the optical imaging and the release of the optical dyes from nanocrystals, the biodistribution of nanocrystals, free drug, and dye molecules will be further investigated.

### 4.3 Evaluation of PTX/Nicardipine Nanocrystals in MCF-7 Xenograft

#### 4.3.1 Introduction

Solid tumors generally possess distinctive anatomical and pathophysiological characteristics, including extensive angiogenesis, hypervascularity, defective vascular architecture, ineffective lymphatic drainage, and increased production of vasculature permeability mediators [5, 7, 293]. This phenomenon is known as the enhanced permeability and retention (EPR) effect, which has become the basis of modern anticancer drug design and strategies. Despite its popularity, limitations associated with the EPR strategy still exist: (a) absence of EPR effect in the central area of metastatic cancers [294, 295], (b) necrotic tissues or large hypovascular areas in larger tumors (e.g. 1-2 cm in diameter) [5], and (c) low vascular densities (hypovascularity) in certain tumors (e.g. metastatic liver and prostate cancers) [296]. Efforts to intensify the EPR effect and achieve more homogenous drug delivery to tumors have been pursued. One is through angiotensin II (ATII)-induced hypersensitivity (hydrodynamic enhancement) and another is by applying a nitric oxide (NO)-releasing agent.

(i) By hydrodynamic enhancement of drug delivery. Suzuki [297] and Hori [298, 299] demonstrated the irregularity of tumor blood flow. Unlike normal blood flow, that of tumor was only seen once within 15 to 20 minutes time frame. It often stopped temporarily or flowed in the opposite direction. Maeda *et al.* employed this knowledge to increase the tumor uptake of macromolecular drugs, SMANCS (styrene-maleic/anhydride-neocarzinostatin), [294, 300] by using ATII infusion. Upon slow intravenous administration of ATII, normal blood vessels experienced systemic hypertension as a result of vasoconstriction. In addition, the endothelial cell-cell junctions

became tighter, which results in less extravasation of drug into normal tissue. In solid tumor, due to defective smooth muscle cells and ATII receptors and large endothelial cell gaps, the opposite effect was observed. As a result of increased systemic blood pressure, tumor blood vessels dilated and blood flow increased. Overall, the induced systemic hypertension resulted in a markedly increased tumor blood flow while that of normal tissue remained constant [297]. The positive increment in blood flow was frequently accompanied by extravasation of macromolecules. SMANCS, when given with slow infusion of ATII, tended to leak out more easily from vessels to tumor tissue, demonstrating the enhanced EPR effect [30, 294].

(ii) By applying nitric oxide (NO)-releasing agent. Nitroglycerin (NG) has been used to treat angina pectoris (i.e. painful heart condition due to an imbalance of blood and oxygen supply). In cardiology, NG liberates nitrite ( $\text{NO}_2^-$ ), which is then reduced to  $\text{NO}^*$  under hypoxic conditions [301]. Similar to hypoxia in cardiac infarct tissue, the tissue oxygen tension ( $\text{pO}_2$ ) of hypovascular tumor tissues is low, resulting in a decrease in pH (more acidic) [302]. Since NO is one of the mediators of vascular permeability, the enhancement of the EPR effect could be obtained by applying NG, a NO-releasing agent. When NG ( $\geq 1.0 \mu\text{g}/\text{mouse}$ , up to  $1.0 \text{ mg}/\text{mouse}$ ) was applied topically over the tumor or skin opposite or distal to the tumor site, a dose-dependent increase in the EPR effect was produced [303].

In this study, we aimed to enhance the EPR effect by entrapping a vasodilation agent, which potentially can be released locally near the tumor site, in PTX nanocrystals. We shied away from incorporating ATII into the nanocrystals due to its potential to affect the entire systemic circulation subsequent to intravenous injection. Additionally, due to the

low solubility and stability of nitrates, a calcium channel blocker was chosen to locally induce vasodilation instead. Among the class of calcium channel blockers (e.g. nifedipine, felodipine, amlodipine), nicardipine has the highest solubility in aqueous solution (i.e. adjusted with acetic acid). The molecular structure of nicardipine is presented in Figure 4.13. The efficacy and toxicity of PTX/nicardipine hybrid nanocrystals were compared to Taxol and PTX pure nanocrystals by evaluating the percent change of tumor volume and body weight, respectively, for 7 days after a single dose of treatment at 20 mg/kg of PTX.

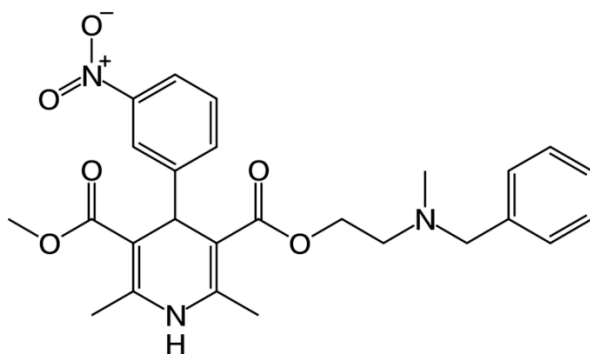


**Figure 4.13.** The chemical structure of nicardipine.

## 4.3.2 Materials and Methods

### 4.3.2.1 Materials

Paclitaxel (>99.5%, USP30) was purchased from 21CECPharm (United Kingdom). Ethanol (HPLC grade), acetonitrile (HPLC grade), DMSO (dimethyl sulfoxide, ACS grade), penicillin streptomycin, and 0.25% trypsin-EDTA were purchased from Fisher Scientific (Pittsburgh, PA). Nicardipine was purchased from Sigma (St. Louis, MO). All chemicals and solvents were utilized without further purification. Deionized water (by

Milli-Q<sup>®</sup>, filtered through 0.2  $\mu\text{m}$  membrane) was used for all the experiments. 0.050  $\mu\text{m}$  (50 nm) Whatman<sup>®</sup> Nuclepore polycarbonate track-etched membranes used for filtration were purchased from Fisher Scientific (Pittsburgh, PA). MCF-7 human breast adenocarcinoma cells were obtained from American Type Culture Collection (Manassas, VA).

#### **4.3.2.2 Preparation of Pure and PTX/Nicardipine Hybrid Nanocrystals**

Pure and hybrid paclitaxel nanocrystals were produced by using an anti-solvent method. For the pure nanocrystal, 1 mL of 5 mg/mL of paclitaxel in ethanol was added to 20 mL deionized water in a round-bottom flask (500 mL). The mixture was subjected to stirring at 1000 rpm and sonication (sonication bath, F20D, Fisher Scientific) for 10 minutes. The stirring rate was changed to 300 rpm for 30 minutes and subsequently to 150 rpm for 30 minutes. To make hybrid PTX/Nicardipine nanocrystals, 1 mL of 5 mg/mL of PTX/ethanol solution were added to 20 mL of 10% aqueous acetic acid containing 5 mg/mL of nicardipine. After stirring at 1000 rpm for 10 minutes, the speed was adjusted to 300 rpm (for 30 minutes) and 150 rpm (for another 30 minutes) in order to minimize bubbles formed and encourage entrapment of nicardipine. After crystallization, the solution was filtered through 50-nm polycarbonate membrane, and the retentate was re-suspended in water for additional filtration-re-suspension cycles to remove nicardipine that may potentially adhere to the surface of the crystals.

#### **4.3.2.3 Characterization of Nanocrystal Systems**

SEM images were obtained using a Hitachi SEM 4300 at an accelerating voltage of 3 kV. Using a sputter coater, samples were coated with conductive layers of gold palladium (Au/Pd) for 1 minute with a current of 20 mA.

#### **4.3.2.4 Chemical Analysis**

PTX concentrations were analyzed by high-performance liquid chromatographic (HPLC) system (Waters Breeze with a dual wavelength absorbance detector, Waters 2487, and multi  $\lambda$  fluorescence detector, Waters 2475) at an absorbance wavelength of 227 nm. A reverse-phase C-18 column (5 $\mu$ m, 150mm $\times$ 4.6mm, Waters) was used. The mobile phase composed of 50% acetonitrile and 50% deionized water was pumped at a total flow rate of 1 mL/min. The column was equilibrated to 35°C prior to sample injection (10  $\mu$ L). Nicardipine was separated by using a 30:70 mixture of acetonitrile and 0.015M KH<sub>2</sub>PO<sub>4</sub> aqueous buffer (pH 3.95) at a flow rate of 1 mL/min. The column temperature was equilibrated to 40°C. The percent of entrapped nicardipine was determined by dissolving the hybrid nanocrystals in ethanol. Standard solutions were prepared by solubilizing nicardipine in ethanol.

#### **4.3.2.5 Cell Culture**

The MCF-7 human breast adenocarcinoma cells were cultured with DMEM (Dulbecco's Modified Eagle Medium, Hyclone) with 10% fetal bovine serum (Hyclone) and 1% penicillin/streptomycin (Hyclone). Trypsin-EDTA (ethylenediaminetetraacetic acid, Mediatech) was used to dissociate cells from the dish. All the cell culture reagents were

purchased from Fisher Scientific (Pittsburgh, PA). Cells were cultured at 37 °C in a humidified atmosphere with 5% CO<sub>2</sub>. To establish the MCF-7 xenograft in nude mice, cells were harvested (by using 0.25% trypsin-EDTA) when they were 70-90% confluent. After being counted, cells were suspended in serum-free DMEM at a concentration of 5×10<sup>7</sup> cells/mL. Cell suspensions were kept in ice until their inoculation.

#### **4.3.2.6 Animal Study**

Female nude outbred mice (Tac:Cr: (NCr)-Foxn1 Nu) were obtained from Taconic at 4 weeks of age (14.5-20 g). All of the animal experiments comply with the principles of care and use of laboratory animals and were approved by the University of Kentucky Institutional Animal Care and Use Committee (IACUC). Seven days after arrival, one 17β-estradiol pellet (1.7 mg, 60-day release; Innovative Research of America, Inc.) was implanted under the skin between the ears of each mouse. Two days later, 5×10<sup>6</sup> MCF-7 cells (100 μL) were inoculated subcutaneously to each side of the flank. All experimental procedures were performed under general anesthesia by isoflurane inhalation. Animals were monitored daily for their body weight and tumor volume using a digital caliper. The tumor volume was calculated by using the following equation:

$$Tumor\ volume = \frac{1}{2} \times longest\ dimension \times (shortest\ dimension)^2$$

A total of 18 mice were randomized into 3 groups (n=6): Taxol, PTX nanocrystals, and PTX/nicardipine hybrid nanocrystals. Taxol formulation (3 mg/ml) was prepared by diluting 300 μL of 30 mg/ml of paclitaxel in Cremophore EL/ethanol (50:50) solution with 2700 μL of saline (0.9% sodium chloride). Treatments were administered at day 0 with a single PTX dose of 20 mg/kg. All animals were euthanized at day 7.

#### **4.3.2.7 Statistical Analysis**

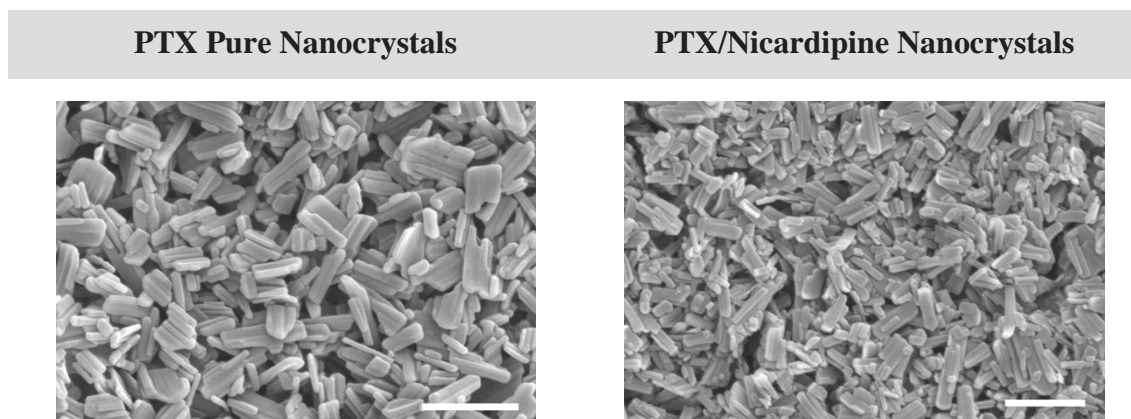
The statistical analysis was performed by Dr. Heidi Weiss' group in Biostatistics Shared Resource Facility (Markey Cancer Center, University of Kentucky). Graphical display of percent of change in body weight from the baseline levels were generated for each group. Pairwise comparisons at each time point of follow-up were performed using the non-parametric Wilcoxon rank-sum test to account for non-normality of data. The percent change in tumor volume at specific time points was compared between groups using an analysis of variance.

### **4.3.3 Result and Discussion**

#### **4.3.3.1 Characterization and Analysis of Nanocrystals**

The mean particle size of the pure PTX and hybrid PTX/nicardipine nanocrystals (Table 4.6) analyzed by SigmaScan were  $360 \pm 120$  nm and  $370 \pm 130$  nm, respectively. The incorporation of nicardipine did not seem to alter the morphology of the crystal significantly. Based on the HPLC analysis, there was 1.18% (w/w) of nicardipine entrapped in the hybrid nanocrystals.

**Table 4.6.** SEM images of PTX and PTX/Nicardipine nanocrystals. Scale bars represent 1  $\mu\text{m}$ .



#### 4.3.3.2 Animal Studies

The percent change of tumor volume (Figure 4.14) of PTX pure and PTX/nicardipine hybrid nanocrystals were compared to the positive control, Taxol, at the same dose of 20 mg/kg. Statistically, there was no significant difference ( $p > 0.05$ ) in the percent tumor volume change between the groups. In a 20 mg/kg paclitaxel dose, the 1.18% (w/w) entrapment of nicardipine would be equivalent to 0.24 mg/kg, which is approximately 20 times lower than the typical intravenous dose, 4 mg/kg, administered in murine model [304]. The amount of nicardipine entrapped in the hybrid nanocrystals might have been too minute, in that it did not alter any therapeutic significance. Additionally, the nicardipine that was able to be released from the hybrid nanocrystals may have been extensively metabolized hepatically since it is known as a substrate for CYP3A4 and P-gp [304]. Across the treatment groups, the tumor volume suppression was minimally observed, which may be due the fact that the treatments were administered when the tumors were rather large (i.e. with an average size of larger than 900  $\text{mm}^3$  / flank). A

single dose of injection administered during this study may not be sufficient to suppress the exponentially-growing tumor xenograft.

Figure 4.15 depicts the percent change in body weight of the mice in the three groups, Taxol, pure PTX nanocrystals, and PTX/nicardipine nanocrystals, monitored 7 days subsequent to a bolus treatment on day 0. Although the average body weight change of the Taxol group was shifted downwards (i.e. weight loss), there was no significant difference ( $p > 0.05$ ) in the body weight change between the groups. The largest body weight difference between the PTX nanocrystals and Taxol groups was at day 6 ( $p = 0.17$ ). The toxicity associated with Taxol was most likely due to the exposure of solvents (e.g. ethanol and Cremophor EL), which were utilized for solubilization prior to the intravenous injection. The percentages of body weight change of PTX nanocrystals and PTX/nicardipine nanocrystals were similar. This observation suggested that the minute amount of nicardipine incorporated in the nanocrystals did not induce additional toxicity.

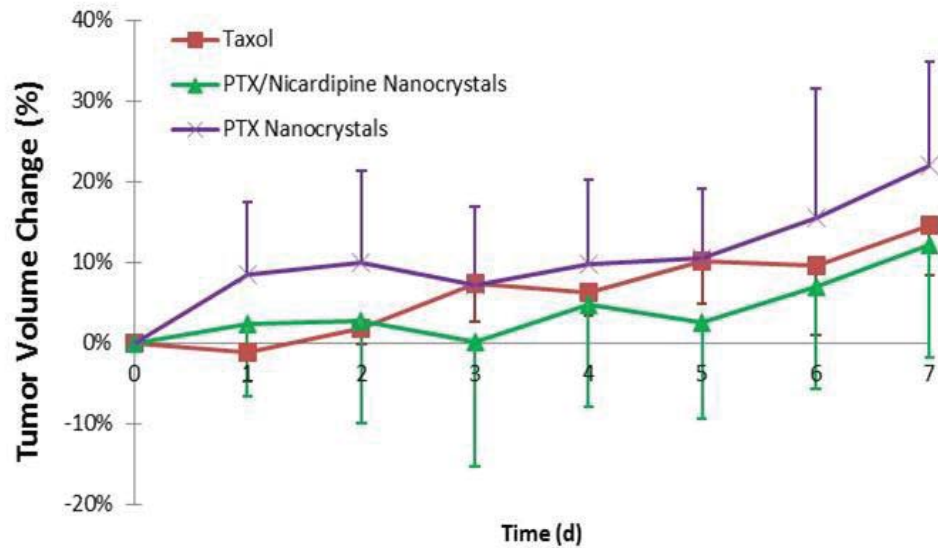


**Figure 4.14.** The percent of tumor volume change of animals administered with Taxol, PTX nanocrystals, and PTX/Nicardipine nanocrystals (n=6).

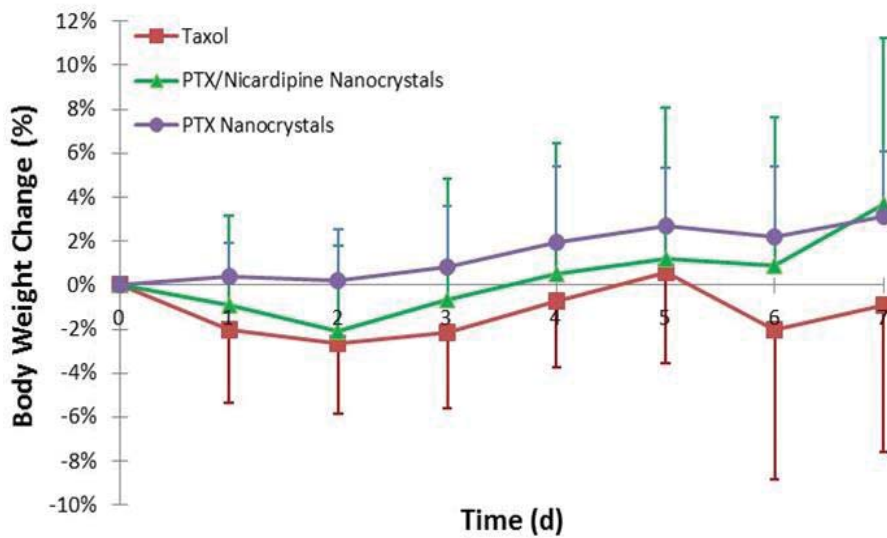


**Figure 4.15.** The percent of body weight change of animals administered with Taxol, PTX nanocrystals, and PTX/Nicardipine nanocrystals (n=6).

#### **4.3.4 Conclusion**

This study was aimed to incorporate a calcium channel blocker, nicardipine, which can serve as a vasodilation agent, in the crystal lattice of PTX nanocrystals. Both PTX pure and PTX/nicardipine nanocrystals were produced with anti-solvent method, having a rectangular prism-shaped morphology, with an average longest dimension of about 350 nm. The incorporated amount of nicardipine was equivalent to 1.18% w/w with respect to the PTX. Mice bearing MCF-7 xenograft were divided into three groups, receiving a single intravenous 20 mg/kg dose of Taxol, PTX nanocrystals, or PTX/nicardipine nanocrystals on day 0. Statistical results suggested that there were no significant differences ( $p > 0.5$ ) in the percent change of tumor volume and body weight. The amount of nicardipine that was entrapped in the nanocrystals was most likely too minute to exert enhanced macromolecules permeability surrounding tumor and ultimately the therapeutic significance. In order to understand the influence of vasodilation agent to the EPR effect, it may need to be pre-administered intratumorally prior to the treatment injections.

## **Chapter 5 - Tumor Accumulation and Tissue Distribution of <sup>3</sup>H-Taxol versus <sup>3</sup>H-Paclitaxel/FPI-749 Hybrid Nanocrystals**

### **5.1 Introduction**

In cancer therapy, nanomedicines have been designed to increase the tumor targeting efficiency, facilitate controlled drug release, and minimize toxicity, which stems from the delivery vehicle(s) and/or lack of target selectivity. In order to reach the target (i.e. tumor), the nanomedicines must circumvent a vast number of biological barriers [305], which protect the body from the entry of “foreign” materials. Thus, in order to understand the behavior and performance of a nanoconstruct in the biological system, an assessment of the pharmacokinetics and biodistribution is essential.

Nanoconstructs, virtually irrespective of the particle composition [261], may be rapidly cleared from the bloodstream by macrophages of the MPS shortly after intravenous injection. Macrophages, which are known as professional phagocytes, generate pathways of entry of particles into cells by: (a) recognition of opsonization in the bloodstream, (b) adhesion to the opsonized particles, and (c) ingestion of the material. During the opsonization, foreign materials are tagged by proteins (opsonins) and become visible to macrophages. The opsonized particles are then attached to the surface of macrophage via distinctive receptor-ligand interaction. At the cellular level, phagosomes are being formed, and the cargo is being unloaded throughout the cytoplasm. Eventually, phagosomes will emerge with lysosomes to form phagolysosomes, the rate of which relies heavily on the combination of particle properties (e.g. size, geometric shape, rigidity, and surface properties) [261]. The minimization of opsonization via PEGylation

has been mentioned previously in Chapter 4. Particles, which are able to escape from the macrophages, are circulated in the blood and ultimately can reach the tumor via the EPR effect.

In order to effectively exert the anticancer therapy, nanovehicles have to release the active ingredient into the tumor at an optimum rate (e.g. 3-10% per day [5]). If the release rate is too slow then insufficient concentrations of the drug can reach the tumor site. Similarly, a fast release rate would lead to a high free drug in the circulation, which could generate systemic toxicity, but minimum tumor accumulation [5].

Relative to normal tissue, tumors are known to lack effective lymphatic drainage [30, 306-308]. Under normal conditions, the lymphatic system can effectively recover macromolecules (e.g. proteins, nanosize drug delivery vehicle) from the interstitial space back into the blood circulation. The impaired lymphatic system in tumors, hence, leads to lower clearance of macromolecules from the tumor interstitium and longer retention. Lipiodol (iodinated poppyseed oil)-solubilized SMANCS (drug) selectively accumulated and remained in tumor tissue [306, 307]. Similarly, intravenously administered Evans blue/albumin extravasated to the tumor but did not disappear for 1 to 2 weeks [30]. Unfortunately, the ineffective lymphatic drainage also leads to an increased interstitial fluid pressure (IFP), which limits the convective extravasation of the nanovehicle despite the presence of a leaky vasculature. To that end, the tumor's impaired lymphatic drainage could either amplify the 'retention' effect or hinder therapy due to the IFP.

Preclinical pharmacokinetics and biodistribution studies are generally conducted in order to understand the behavior and assess the ability of investigational agents to target the site of action *in vivo*. Routinely, the data are obtained from the chemical and/or radioactivity

analysis of excised organs and tissues. As an alternative, the use of near infrared fluorescence imaging to carry out the aforementioned studies has gained popularity in recent years. Optical imaging can provide a convenient, easy, and rapid means of assessing the agent's biodistribution in the excised organs [229, 231, 233, 309]. Furthermore, a quantitative, non-invasive whole body biodistribution of fluorescent-labeled agents has recently been attempted by employing fluorescence molecular tomography (FMT) [234].

Optical imaging in small animals can be generally categorized into two approaches [310-314]:

(a) Planar imaging also called fluorescence reflectance imaging (FRI), is based on a simple two-dimensional photographic method. Here, the light source is being excited, and the reflectance is being detected from the same side of the imaged animals. A laser (e.g. light emitting diode or white light source with appropriate low-pass filter), which offers high power yet narrow excitation bandwidth, is generally employed as the light source to illuminate a large part of the animal or the whole animal. The fluorescent light from the tissues is then detected by a highly sensitive charged-couple device (CCD) camera using an appropriate emission filter. The detection depth is restricted to a few millimeters due to: (i) the constant background noise caused by unattenuated autofluorescence from the superficial layer, and (ii) the photon attenuation in the deep tissue due to scattering and absorption, specifically by protein, blood (oxy- (HbO<sub>2</sub>) and deoxyhemoglobin (Hb)), and water. For topographical registration, the fluorescence image is typically superimposed with the animal photographic image acquired with white light illumination.

Reflectance imaging is widely used and can offer a high-throughput imaging and screening of surface fluorescence events *in vivo* or in excised tissue. Besides the fast acquisition time, the instrument is safe (no ionizing radiation) and simple to operate, relatively inexpensive, and space efficient [313]. However, planar imaging suffers from inherent limitations in terms of fluorescent probe localization, accurate quantitation, and depth of detection. The fluorescent probe depth and concentration cannot be decoupled, in that a strong signal from a deep lesion may appear similar to a weak one generated from the surface.

(b) Tomography imaging offers deeper detection, better quantification and sensitivity, and accurate localization. Currently, there are three approaches for generating images in optical tomography: continuous wave (CW), time domain (TD), and frequency domain (FD) [310, 311]. In CW, the subject's surface is illuminated by the light source at multiple points. The transmitted light measurements collected from various projections are then combined with an inverse mathematical model to reconstruct the fluorophore volumetric distribution [315, 316]. In TD, a spot on the object of interest is illuminated with a sub-nanosecond duration of a laser pulse, and the arrival distribution of photons is measured by a fast detector as a function of time at different locations. Besides providing spatial intensity distribution, TD system can offer temporal information on the fluorescence lifetime [317, 318]. In FD, the subject is illuminated by a radio frequency modulated light source. The tomography is reconstructed based on the measurement of amplitude attenuation and phase delay of emitted fluorescence light as it propagates to tissue [319]. Overall, CW and FD systems are relatively inexpensive, easy to develop, and acquire data in a shorter time. The TD, albeit slower, is highly sensitive.

The hyper-sensitivity due to modeling errors and statistical noise is one of the current limitations of fluorescent tomography [312]. Spatial resolution can also be improved by combining with other modalities, such as CT, MRI, or ultrasound, but it shifts the cost markedly. Most fluorescence tomography systems can only image one animal at a time, which may not permit a high throughput screening for accelerated research.

The *in vivo* optical imaging has enabled the visualization of the temporal and spatial biodistribution as well as longitudinal imaging of the same animal at multiple time points for nanotheranostics. Although *in vivo* fluorescence imaging is widely utilized in the pre-clinical setting, minimum effort has been made to investigate the correlation between drug concentration and detected fluorescence signals in *ex vivo* tissues.

In this chapter, the tumor accumulation and tissue distribution of tritium-labeled PTX/FPI-749 hybrid nanocrystals were compared head-to-head with the conventional formulation, (tritium-labeled) Taxol. Detailed studies on Taxol's pharmacokinetics [320, 321], biodistribution, metabolism and excretion [322, 323] in murine models have been reported in the past. One study also had recently reported the pharmacokinetics and tissue distribution of Taxol and a paclitaxel nanosuspension (*c.a.* 200 nm), produced by high-pressure homogenization, at a dose level of 10 mg/kg in male Sprague Dawley (SD) rats [219]. However, the extent of tumor accumulation of nanocrystals composed of chemotherapeutics has not been reported yet. Furthermore, the *ex vivo* distribution of the fluorescence signal detected under optical imaging and radiolabeled PTX were compared.

## 5.2 Materials and Methods

### 5.2.1 Materials

Paclitaxel (>99.5%, USP30) was purchased from 21CECPharm (United Kingdom). <sup>3</sup>H-Paclitaxel in ethanol ( $\geq 97\%$  chemical purity, 4 mCi/mmol, 0.145 mCi/mL) was purchased from Moravek Biochemicals and Radiochemicals (Brea, CA). FPI-749 fluorophore (maximum excitation wavelength,  $\lambda_{ex}=750$  nm; maximum emission,  $\lambda_{em}=782$  nm) was obtained from Polysciotech (West Lafayette, IN). Ethanol (HPLC grade) and acetonitrile (HPLC grade) were purchased from Fisher Scientific (Pittsburgh, PA). All chemicals and solvents were utilized without further purification. Deionized water (by Milli-Q<sup>®</sup>, filtered through 0.2  $\mu$ m membrane) was used for all the experiments. 0.050  $\mu$ m (50 nm) Whatman<sup>®</sup> Nuclepore polycarbonate track-etched membranes used for filtration were purchased from Fisher Scientific (Pittsburgh, PA). HT-29 human colon adenocarcinoma cells were purchased from American Type Culture Collection (ATCC) (Manassas, VA).

### 5.2.2 Preparation and Analysis of <sup>3</sup>H-Taxol and <sup>3</sup>H-PTX/FPI-749 Nanocrystals

The majority of the tritium in the <sup>3</sup>H-PTX was distributed in the p- and m- positions of the aromatic rings. <sup>3</sup>H-Taxol was prepared by spiking the Taxol injection concentrate containing PTX at 30 mg/mL in a 50:50 (v/v) mixture of Cremophor EL and ethanol, with <sup>3</sup>H-PTX to achieve a specific activity of 2.058 mCi/mmol. Prior to intravenous injection, the stock was diluted with saline (1:9 v/v) to obtain an equivalent concentration of 3 mg/mL. <sup>3</sup>H-PTX/FPI-749 hybrid nanocrystals were produced by the combination approach as previously described in Section 2.2.2. Specifically, 0.7 mL of 1 mg/mL FPI-

749 was added to 20 mL deionized water in 3-neck round bottom flask (500 mL). Then, 1 mL of 5 mg/mL (2.058 mCi/mol) of <sup>3</sup>H-paclitaxel in ethanol was added rapidly to the flask. The mixture was stirred at 1,100 rpm with a stirrer shaft and under intense sonication (in sonication bath F20D, output of 70 W and 42±6 KHz, Fisher Scientific). Ice was added to the sonication bath to keep the temperature between 14-18°C. After 10 minutes of stirring time, the stirring speed was reduced to 600 rpm (10 minutes) and 300 rpm (10 minutes) to encourage further crystal growth and fluorophore entrapment. The sonication bath was turned on for the entire period of the stirring. The flask was removed from the stirring station and placed in a vacuum desiccator to remove bubbles generated due to rapid stirring. The mixture was then filtered through 50 nm polycarbonate membrane. The retentate was re-suspended in water for additional filtration-re-suspension cycles to remove imaging agents that may potentially adhere to the surface of the crystals. The combination of washed retentate (from 16 batches) was re-suspended in 2.8 mL of DI water and homogenized (Fisher Scientific® PowerGen® 125) for 6 minutes at 30,000 rpm. A trial batch of PTX hybrid nanocrystals without any radioactivity was produced using a similar method. The sample was analyzed under scanning electron microscope (SEM) for size measurement (by SigmaScan). The preparation of the SEM sample was similar to that described in Section 2.2.3.

To quantitate the radioactivity in the dosing preparations, three 10 µL aliquots of injection solutions was added into liquid scintillation cocktail and analyzed by a liquid scintillation counter, Tri-Carb 2910TR (Perkin Elmer).

### **5.2.3 Cell Culture**

HT-29 human colon adenocarcinoma cells were cultured in McCoy's 5A medium supplemented with 10% fetal bovine serum and 1% penicillin streptomycin in 37°C humidified incubator containing 5% CO<sub>2</sub>. To establish the HT-29 xenograft in nude mice, HT-29 cells were harvested (by using 0.25% trypsin-EDTA) when they were 70-90% confluent. After being counted, cells were suspended in 50:50 mixture of sterile phosphate buffered saline (PBS) and Matrigel (BD Biosciences, San Jose, CA) at a concentration of  $3 \times 10^7$  cells/mL. Cell suspensions were kept in ice until their inoculation.

### **5.2.4 Animal Study**

The animal study was conducted under a protocol approved for using nude mice by the University's Institutional Animal Care and Use Committee (IACUC). Female nude outbred mice (Tac:Cr: (NCr)-Foxn1 Nu) were obtained from Taconic at 4 weeks of age (14.5-20 g). Mice were acclimated for one week after arrival. Subsequently, mice were anesthetized by isoflurane inhalation for placing ear identification tag and cell inoculation. HT-29 xenograft was established by injecting 100  $\mu$ L HT-29 cells ( $3 \times 10^6$ ) subcutaneously to each flank. When tumors became palpable, a total of 111 athymic mice were randomized into different groups. Three mice were allocated to receive no treatment (control). For the Taxol group, 48 mice were divided into 12 time points (n=4): 5, 15, 30 minutes, 1, 2, 4, 6, 8, 24 hours, 2, 3, and 4 days. For the PTX hybrid nanocrystals, 60 mice were divided into group of 4 for 15 time points: 11, 15, 30 minutes, 1, 2, 4, 6, 8, 24 hours, 2, 3, 4, 5, 6, and 7 days. <sup>3</sup>H-Taxol and <sup>3</sup>H-PTX nanocrystals were administered intravenously once at a concentration of 20 mg/kg via the tail vein. <sup>3</sup>H-Taxol and <sup>3</sup>H-

PTX/FPI-749 nanocrystal formulations were diluted in saline prior to injection. Each mouse received approximately 1  $\mu\text{Ci}$  of tritium dose per injection. Mice in the PTX hybrid nanocrystal group were imaged under IVIS<sup>®</sup> prior to euthanization. Due to transportation and imaging time, the first time point at which animals could be euthanized was 11 minutes. Mice were euthanized at pre-determined time points by CO<sub>2</sub> asphyxiation. After performing cervical dislocation, blood, tumor, and major organs (e.g. liver, spleen, heart, lungs, and kidneys) were collected and weighed in pre-weighed scintillation vials.

### **5.2.5 Tritium Analysis in Blood and Tissue**

Blood and tissue were prepared according to the protocol established by Perkin Elmer for “liquid scintillation counter sample preparation by solubilization”. Blood (0.1-0.4 mL) was digested with 1 mL of a mixture of tissue solubilizer Soluene<sup>®</sup> 350 (Perkin Elmer, Waltham, MA) and ethanol (1:1 ratio) and placed in a 50-60°C oven (Fisher Scientific Isotemp) for at least 2 hours. After cooling to room temperature, sample was decolorized by adding 500  $\mu\text{L}$  (in 100-200  $\mu\text{L}$  aliquots) of 30% hydrogen peroxide solution. Once the reaction subsided, samples were placed back in the oven for another 30 minutes. 15 mL of liquid scintillation cocktail (Perkin Elmer) was added to the blood samples, and the mixture was vortexed. Samples were allowed to quench for 1 hour in the dark before measurement was carried out with a Tri-Carb 2910TR liquid scintillation counter (Perkin Elmer). The counting efficiency for blood samples was low, and therefore was subject to greater measurement error.

Prior to tissue homogenization, 3 mL of deionized water was added to the tumor and liver samples while 1 mL water was added to the spleen, heart, lungs, and kidneys. To obtain complete tissue digestion, only 50-200 mg of tissue sample was utilized. Thus, homogenate (0.5 mL for tumor and lungs, 0.2 mL for liver and kidneys, 1 mL for spleen and heart) was digested with Soluene® 350 and placed in 50-60°C oven for at least 4 hours. After cooling the digested homogenates, 200 µL of 30% hydrogen peroxide was added to decolorize them. Once the reaction subsided, vials were placed back in the 50-60°C oven for another 30 minutes. Prior to analysis, 10 mL of Hionic-Fluor was added to the sample. Samples were allowed to quench for 1 hour in the dark before measurement was carried out with a Tri-Carb 2910TR liquid scintillation counter.

### **5.2.6 IVIS® Imaging**

Prior to euthanization, mice were subjected to IVIS® imaging to potentially visualize the extent of PTX/FPI-749 hybrid nanocrystal biodistribution at pre-determined time points. Mice were imaged both from the dorsal and ventral side. The following were the parameters used for the imaging:  $\lambda_{excitation}$ : 745 nm,  $\lambda_{emission}$ : 800 nm, exposure time: 4 seconds, F stop: 2, binning: medium (8), and field of view (FOV): 13. After being euthanized, tumor and major organs were imaged by using the same set of parameters.

### **5.2.7 Statistical Analysis**

Tumor accumulation measured at specific time points between groups was analyzed using analysis of variance, which includes treatment group, time and interaction between these two factors in the model.

### 5.3 Results and Discussion

#### 5.3.1 Characterization of Hybrid PTX /FPI-749 Nanocrystals

The SEM image of the PTX hybrid nanocrystals is presented in Figure 5.1. Measured by SigmaScan (Systat software, San Jose, CA), the averaged longest dimension of the crystals was 200 nm. The size of the hybrid nanocrystals was comparable to that of the pure PTX nanocrystals, described in Section 2.3.1. Although particle accumulation in the tumor depends on various parameters, including size, shape, surface charge, and leakiness of the tumor vasculature, collectively it has been suggested that nanoparticles less than 400 nm should be able to take advantage of the enhanced permeability and retention (EPR) effect [29]. To that end, these hybrid PTX nanocrystals having a size of approximately 200 nm were expected to be able to extravasate into the tumor site.

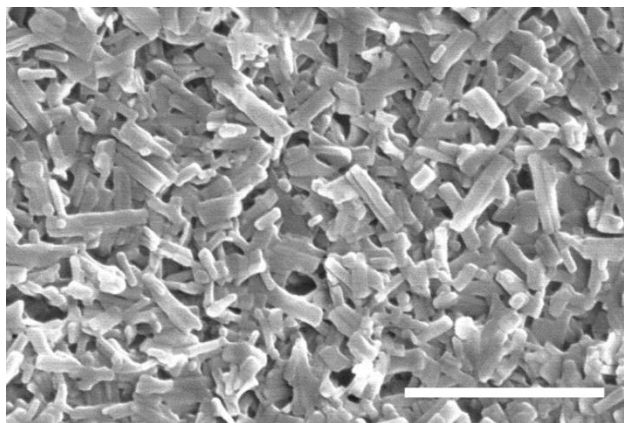


**Figure 5.1.** SEM image of PTX hybrid nanocrystals without any radioactive payload.

Scale bar represents 1  $\mu\text{m}$ .

### 5.3.2 Tissue Distribution by Tritium Analysis

The normalized tissue distribution of  $^3\text{H}$ -Taxol ( $^3\text{H}$ -Tax) and  $^3\text{H}$ -PTX/FPI-749 nanocrystals ( $^3\text{H}$ -PTX NCs) are presented in Figure 5.2 and 5.3, respectively. Similar to previous studies [322, 323],  $^3\text{H}$ -Tax was distributed extensively to all the major organs and exhibited a non-linear, two compartmental, pharmacokinetic profile. The extensive tissue distribution of PTX and solubilizing agents can potentially induce profound toxic effects, as suggested by the body weight change (Chapter 4). Compared to  $^3\text{H}$ -Tax,  $^3\text{H}$ -PTX NCs were cleared rapidly from the blood circulation. By 15 minutes post-injection, only  $0.42 \pm 0.12\%$  of injected dose/gram of blood was detected in the  $^3\text{H}$ -PTX NCs group as opposed to  $2.89 \pm 0.24\%$  in  $^3\text{H}$ -Tax. The significant decrease in blood level and high drug concentration in the liver, spleen, and lungs suggested that PTX nanocrystals were sequestered by the macrophages of the reticuloendothelial system (RES) most likely within seconds of intravenous administration [324]. Despite the fact that close to 40% of the injected dose accumulated in the liver, it has been demonstrated repeatedly that the engulfment of nanoparticles by Kupffer cells (specialized macrophages) does not adversely affect the safety profile of the drug [129]. Histological analysis of rat spleen revealed that intravenously administered itraconazole nanocrystals were engulfed by macrophages and resided within the cytoplasm; the number of resident macrophages was increased with dose elevation to accommodate the particle burden [325]. Specifically for PTX nanocrystals, the MPS deposition also did not seem to expose any significant toxicity to the animals. As observed in Figure 4.3 (Section 4.1.3.2), the animals treated with PTX nanocrystals experienced the least body weight loss relative to Taxol and even control during the survival study in HT-29 xenograft. Similar trends were

also noted in Section 4.2.3.2 and 4.3.3.2 (performance evaluation in MCF-7 xenograft).

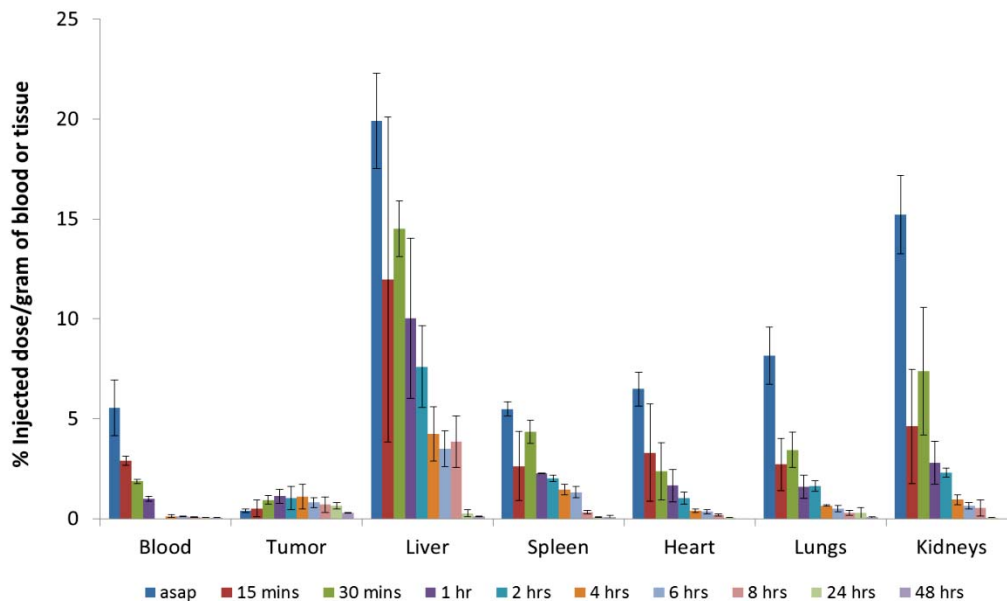


**Figure 5.2.** The distribution (% injected dose/gram of blood or tissue) of 20 mg/kg <sup>3</sup>H-Taxol. The term “asap” refers to 5 minutes post-injection time.

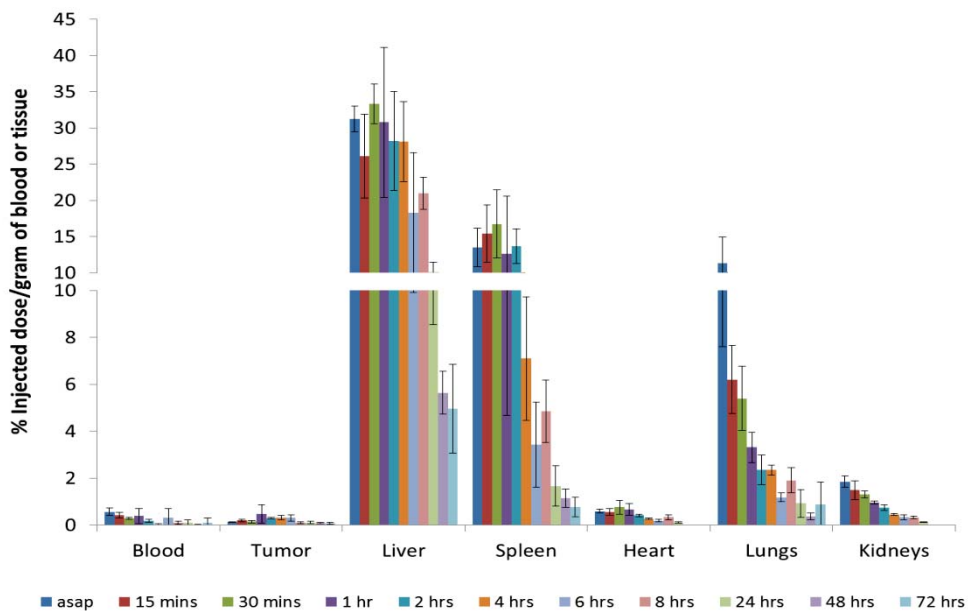


**Figure 5.3.** The distribution (% injected dose/gram of blood or tissue) of 20 mg/kg <sup>3</sup>H-PTX/FPI-749 nanocrystals. The term “asap” refers to 11 minutes post-injection time.

Administration of higher dose may be possible, and liver may temporarily act as a depot site to release the drug back into the circulation.

Compared with the  $^3\text{H}$ -Taxol distribution (Figure 5.4.A),  $^3\text{H}$ -PTX/FPI-749 nanocrystals were distributed rapidly to the major organs within the first 11 minutes (Figure 5.4.B). Nonetheless, Figure 5.4.B suggested the free  $^3\text{H}$ -PTX was redistributed from the clearing organ (i.e., liver) back to the systemic circulation, especially at the 1- and 6-hour time points. The decreased mean concentration of  $^3\text{H}$ -PTX in the liver was accompanied with an increased mean concentration in the blood. This observation suggests that there was higher concentration of  $^3\text{H}$ -PTX that was redistributed than being cleared. Conversely, subsequent to the intravenous injection of  $^3\text{H}$ -Taxol,  $^3\text{H}$ -PTX concentration in the blood circulation continually decreased. The difference in the blood concentrations observed in the  $^3\text{H}$ -Tax and  $^3\text{H}$ -PTX NCs was also generated due to the micellar entrapment of PTX by Cremophor EL in plasma [239]. In Taxol, the free paclitaxel is able to partition reversibly into circulating Cremophor EL, which serves as a circulating PK compartment in the blood and alters the blood PK. This reversible partitioning also reduces the fraction of unbound drug, the form that penetrates into tumor [320].

The relative amounts of the drug out of every injection in the major organs and tumor were also analyzed for both  $^3\text{H}$ -Taxol and  $^3\text{H}$ -PTX nanocrystals (Figure 5.5.A and B). Within the first 10-15 minutes, the total percentage of PTX in the major organs and tumor was only summed up to approximately 50%. The remainder of the injected dose was largely distributed in other tissues, likely due to the lipophilic nature of the drug. A previous study indicated that within 0.5 hour post-injection of Taxol, PTX was found mostly in the liver, kidney, lung, spleen, heart, gall bladder (bile), and small intestine

[323]. A good portion was also found in the stomach, dorsal fat, colon, cecum, breast, and lymph nodes. It is striking to see that less than 1% of the drug accumulated in the tumor. The comparison of tumor accumulation between the two formulations will be further discussed later.

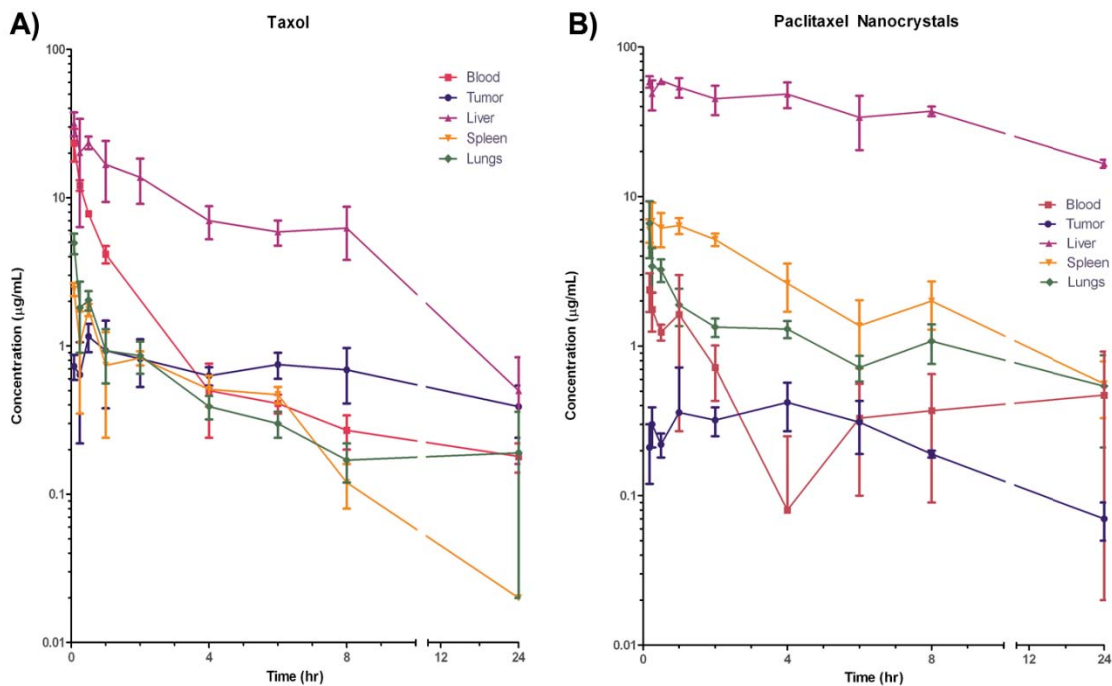


**Figure 5.4.** The distribution (mean  $\pm$  S.D.) of  $^3\text{H}$ -PTX in female nude mice after a bolus intravenous injection of (A)  $^3\text{H}$ -Taxol and (B)  $^3\text{H}$ -PTX/FPI-749 nanocrystals at 20 mg/kg.

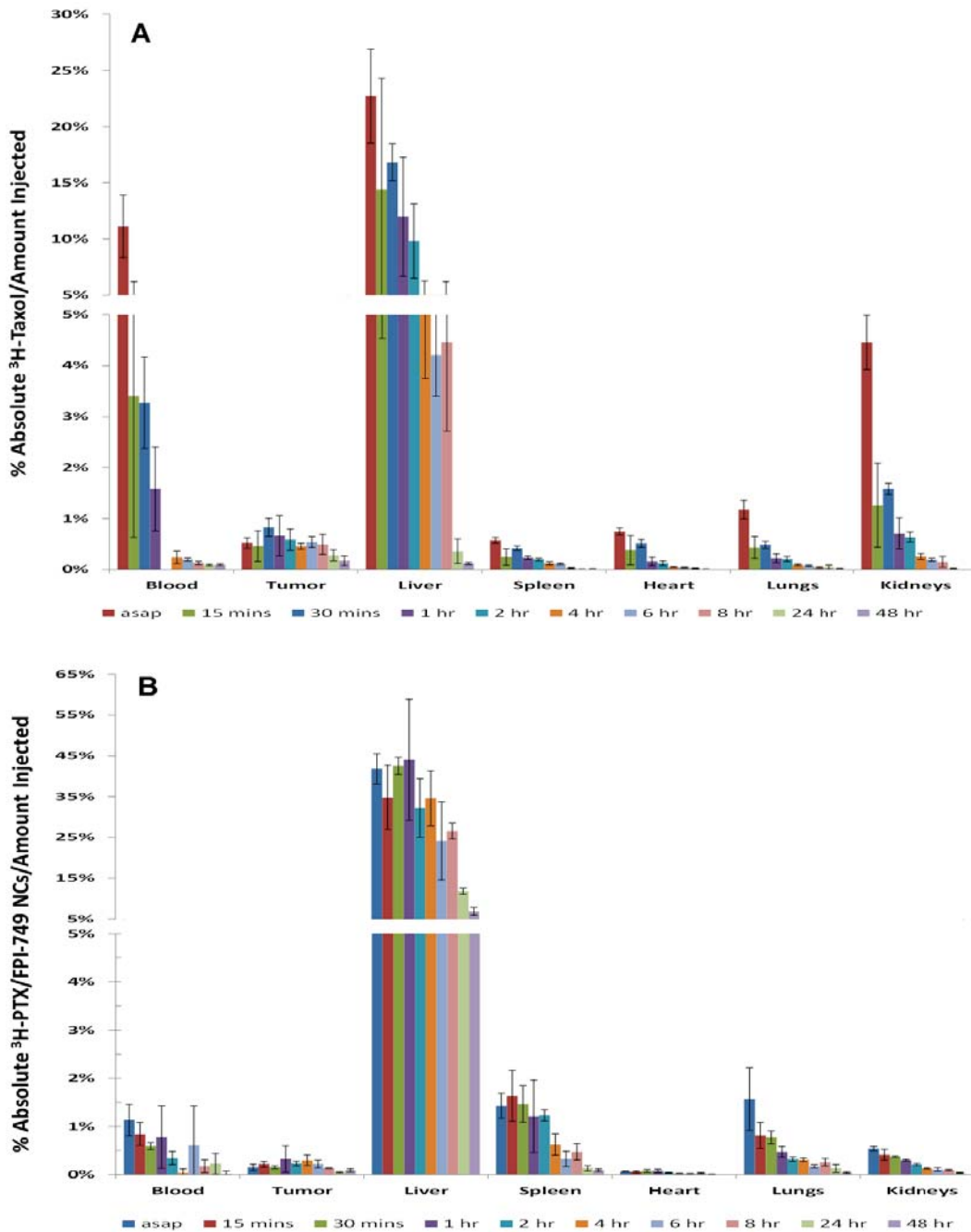


**Figure 5.5.** The distribution (% absolute amount in blood or tissue/amount injected, mean  $\pm$  S.D.) of 20 mg/kg (A)  $^3\text{H}$ -Taxol and (B)  $^3\text{H}$ -PTX/FPI-749 nanocrystals. The term “asap” refers to 5 and 11 minutes post-injection time of  $^3\text{H}$ -Taxol and  $^3\text{H}$ -PTX/FPI-749 nanocrystals, respectively.

Generally, the macrophages are unable to necessarily identify the nanocrystals, but rather recognize specific opsonin proteins bound to the surface of the particles. Opsonins are broadly defined as any component of blood serum that assists the process of phagocytic recognition [326]. To temporarily circumvent the recognition by the RES, nanovehicles are often camouflaged by “PEGylation” (i.e. coating the surface with poly-ethylene glycol (PEG) [327]. Though the mechanisms are still controversial, it is believed that the ability of PEG to decrease surface charge and/or hydrophobicity, wet the particle surface, squeeze out water molecules, and create a repulsive force to inhibit opsonin protein binding, play a significant role in prolonging circulation time [326, 328].

The nanocrystals used in the study were bare, without any functionalization or adsorption by surfactants or polymers. PEGylation is a common practice to circumvent or delay the recognition by the MPS, possibly due to the hydrophilic polymer shell that prevents opsonins from attaching to the surface and subsequent phagocytosis [329, 330]. Because nanocrystals undergo consistent dissolution no matter how low the solubility is, surface decoration by PEGs may not be as effective as other nanosystems (e.g., covalently conjugated by the polymers). There are a few studies where drug nanocrystals were stabilized by PEG or PEG block polymers but they were still sequestered in MPS significantly [331-333]. Clearly, it is a challenging task to secure surfactants to the surface of nanocrystals, especially during the administration and blood circulation stages.

### 5.3.3 Tumor Accumulation

Figure 5.6 depicts the comparison between the normalized tumor accumulation subsequent to intravenous injection of  $^3\text{H}$ -Tax or  $^3\text{H}$ -PTX NCs to athymic mice. The maximum tumor accumulation in both treatments was observed during 1 to 6 hours post-injection. Statistically analyzed by analysis of variance at all time points, the tumor accumulation of  $^3\text{H}$ -Tax was significantly different from  $^3\text{H}$ -PTX NCs across all time points ( $p < 0.0001$ ). Furthermore, the analysis from group\*time interaction was not significant ( $p = 0.182$ ), which indicated that there was a consistent difference between the treatments across all time points. A major reason for the low tumor accumulation by the nanocrystals obviously lies in the short duration in the blood circulation and the quick sequestration by MPS. Elevated tumor interstitial pressure and unique vasculatures of HT-29 xenograft may also be responsible. HT-29 tumors were reported to be less vascular, for example, than the human colon adenocarcinoma LS174T [334]. The result could be attributed to the following factors:

- (1) Elevated tumor interstitial fluid pressure, which is often associated with solid tumors, could deter the therapy.
- (2) Less severity and abnormalities in the tumor vessels of HT-29. The pore cut-off size of the tumor vasculature has been reported to be dependent on the tumor type and histological grade [220-222]. As evidenced by a functional pore size of 1200 to 2000 nm, blood vessels of MCa-IV mouse mammary carcinoma are on the high end of the range of leakiness for tumors [221]. Three pathways, including openings between the vessel lining cells, holes through the lining cells, and endothelial fenestrae, were reported to be responsible for the unusual leakiness of MCa-IV tumor vessels [220]. HT-29, in contrast,

has been reported to be less vascular than LS174T [335], which has pore size of 400-600 nm [221].

(3) Short distribution half-life ( $t_{1/2\alpha}$ ) [219] only allowed low concentrations of PTX nanocrystals available in the blood circulation and reduced the probability of nanocrystal infiltration into the tumor.

(4) The high intratumoral accumulation of  $^3\text{H}$ -Tax could be ascribed to the fact that Cremophor EL encapsulates PTX as micelles [239]. Thus, the Taxol formulation is not necessarily the same as a drug solution (in organic solvent). Our laboratory recently compared the tumor accumulation of camptothecin nanocrystals, produced by the anti-solvent method, with a camptothecin salt solution. The result revealed that camptothecin nanocrystals, even with a particle size between 200 and 700 nm (needle-like), were able to accumulate significantly in the tumor relative to the salt solution [168].

Nonetheless, as observed in Figure 5.6, the tumor accumulation of  $^3\text{H}$ -Tax continued to decrease after 6 hours, which corresponded well to the blood concentration.  $^3\text{H}$ -Tax was rapidly cleared from the tumor due to the reversible partitioning of PTX into the circulating Cremophor EL, which reduces the free drug amount [320]. Interestingly, the tumor accumulation of  $^3\text{H}$ -PTX nanocrystals after 6 hours was steadily maintained. It is likely that, once the nanocrystals successfully accumulated in the tumor site, they would not be cleared easily due to relatively large particle size and ineffective lymphatic drainage surrounding the tumor. Also as pointed out earlier, the sequestered nanocrystals in MPS continued to dissolve releasing PTX molecules back to the blood stream and maintaining the drug concentration in the tumor. The finding of initial sequestration of nanoparticles by phagocytosis followed by slow release is commonly observed [336].

Relative to solubilized formulation, nanocrystals are shown to have prolonged half-lives of elimination in murine models [331-333, 337, 338]. Thus, it is highly possible that, upon multiple injections, drug accumulation in the tumor will become significant, as demonstrated by the treatment regimen in the survival study discussed above.

Needless to say, the EPR effect as observed in this study was minimal. If the Taxol formulation may be regarded as a nanoparticle delivery system because of the possible micellar encapsulation of PTX, both nanosystems extravasated to the tumor less than 1% of the total injected dose.

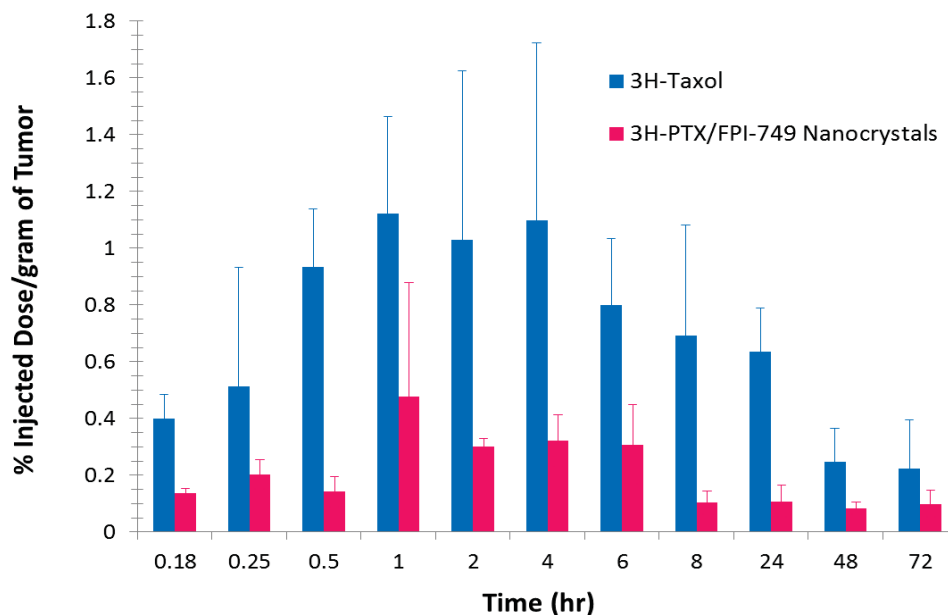


**Figure 5.6.** The tumor accumulation (% injected dose/gram of tumor) comparison between <sup>3</sup>H-Taxol and <sup>3</sup>H-PTX/FPI-749 nanocrystals. The “asap” refers to 5 minutes for <sup>3</sup>H-Taxol and 11 minutes for <sup>3</sup>H-PTX/FPI-749 nanocrystals.

### 5.3.4 IVIS<sup>®</sup> Imaging for Non-Invasive Tissue Distribution

The performance of optical imaging (e.g. IVIS<sup>®</sup>) as a tool to non-invasively trace the tumor accumulation and tissue distribution of hybrid PTX nanocrystals (<sup>3</sup>H-PTX/FPI-749 nanocrystals) was evaluated. Prior to euthanization at pre-determined time points, mice injected with <sup>3</sup>H-PTX/FPI-749 nanocrystals were imaged with the IVIS<sup>®</sup> Spectrum both from the dorsal and ventral sides. The IVIS images obtained from the dorsal and ventral sides were compiled in Figure 5.7 and 5.8, respectively. Three mice were allocated as controls (no treatment). The near infrared fluorophore FPI-749 ( $\lambda_{ex}=750$  nm,  $\lambda_{em}=782$ ) was chosen as the optical probe because the contamination with autofluorescence decreases for longer wavelengths (i.e. between 650-900 nm) and is significantly lower once excitation is longer than 750 nm [312].

As shown in Figure 5.7, strong peripheral fluorescence signals were detected within the first few hours after injection. There was also an increase in the fluorescence ratio between the tumor and peripheral areas starting after 1 hour (Figure 5.8). This seems to be supported by the tumor accumulation data of the tritium-labeled drug that was maximized at 1 hour (Figure 5.5.B). The signal in the tumor site was significant after 1 day and decreased after 5 days. From the ventral side, the strongest intensity came from the liver area within a few minutes of intravenous injection and remained as the site with the strongest fluorescent signal throughout the observation period (Figure 5.8). After 30 minutes, the intensity in the bladder area was increased steadily for about 4 hours, indicating urinary clearance of the dye. The signals in the flank areas were also noticeable particularly after 8 hours, but significantly weakened after 5 days.

Nonetheless, discrepancies existed between the biodistribution results determined by tritium labeling and what the whole-body fluorescence imaging indicated. This is particularly pertinent for the tumor sites. While only less than 1% of the injected dose was extravasated to the tumor, the IVIS® images (Figure 5.7 and 5.8) indicated strong apparent fluorescent signals in the tumor sites. The discrepancies could be caused by several reasons. First, the fluorescent signal is a summation of the contributions by both entrapped and freely dissolved dyes. When most nanocrystals remained un-dissolved, a fluorescent image corresponds closely to where nanocrystals reside. However, when hybrid nanocrystals dissolved, both free drug and dye molecules were released; consequently, the difference in biodistribution between PTX as measured by scintillation counting and fluorescence images is expected to become larger. It was observed that the majority of the hybrid nanocrystals had been distributed to the liver, spleen, and lungs, with only about 1% of the injection remained in blood by 11 minutes. Hence, the concentration of nanocrystals that were circulated in the blood was rapidly depleted, which might promote a shift in the concentration gradient towards the sink condition. From the calculation of complete dissolution for spherical particles under sink condition based on Hixson-Crowell presented in Table 1.1, a particle composed of paclitaxel (i.e. assumed to have diffusion coefficient of  $2 \times 10^{-7} \text{ cm}^2/\text{s}$ , solubility of  $1 \text{ } \mu\text{g}/\text{ml}$ , and  $100 \text{ nm}$  radius) would have been dissolved within 4.2 minutes. If aggregation did occur upon injection, then the time to reach complete dissolution would be longer. Significant numbers of nanocrystals that remained in blood circulation may have dissolved within a few minutes, but the sequestered ones may remain in the organs for much longer period. Second, because PTX is hydrophobic and the dye is hydrophilic, the two different

molecules are expected to have drastically different biodistribution preferences and clearance pathways. At 30 minutes after injection, strong fluorescent signal started to appear in the urinary bladder area, indicating that free FPI-749 molecules were renally cleared and excreted through the bladder. Meanwhile, the percent of  $^3\text{H}$ -PTX NCs found in the kidney was considerably lower (i.e. more than 50-fold lower than that in the liver). Third, planar optical images were collected by superimposing the photographic image acquired with white light illumination and emitted fluorescent light detected by highly sensitive and low noise charged-couple device (CCD) [311]. The epi-fluorescence signal detected by the photographic method can hardly be quantified accurately since the fluorophore depth and concentration cannot be clearly differentiated. Light scattering and absorption by blood (oxyhemoglobin and deoxyhemoglobin) and water further attenuate the signal particularly emitted from internal organs (e.g. liver, spleen, lungs, heart) [339]. Conversely, accumulation of dye in the xenografted tumor (flank) sites, which are within surface proximity, appeared to be very strong. This pitfall can be partially avoided by using systems that rely on fluorescence tomography-based-imaging methods [234], where light-transport models are used as part of the reconstruction process aiming at recovering the position of the fluorescence source [312].

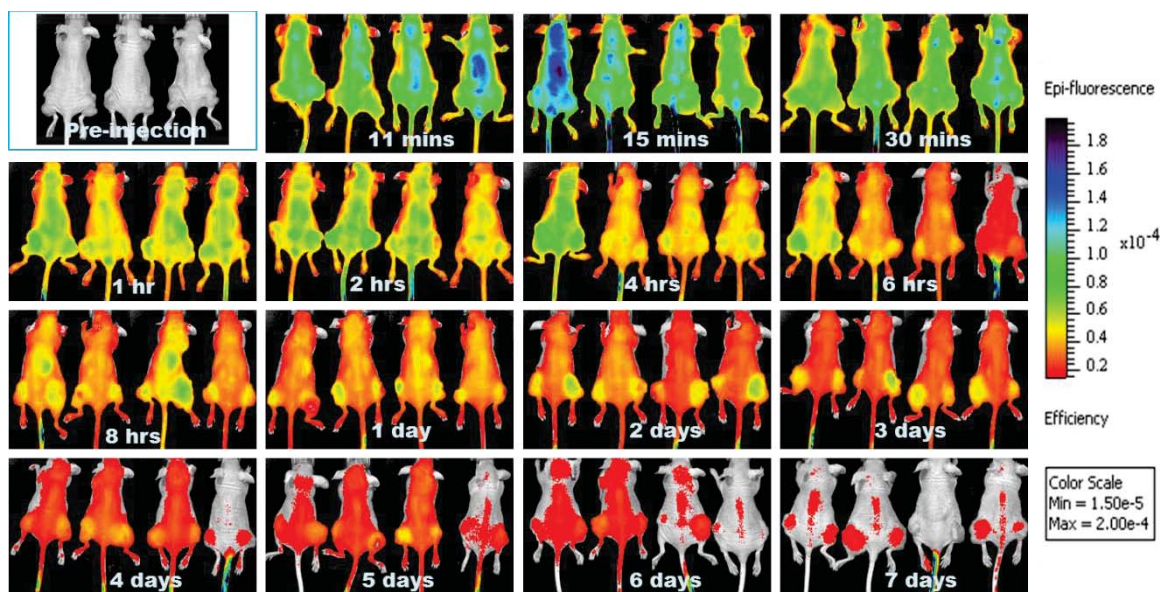


**Figure 5.7.** IVIS® images of the dorsal view of athymic mice injected with  $^3\text{H}$ -PTX/FPI-749 nanocrystals.

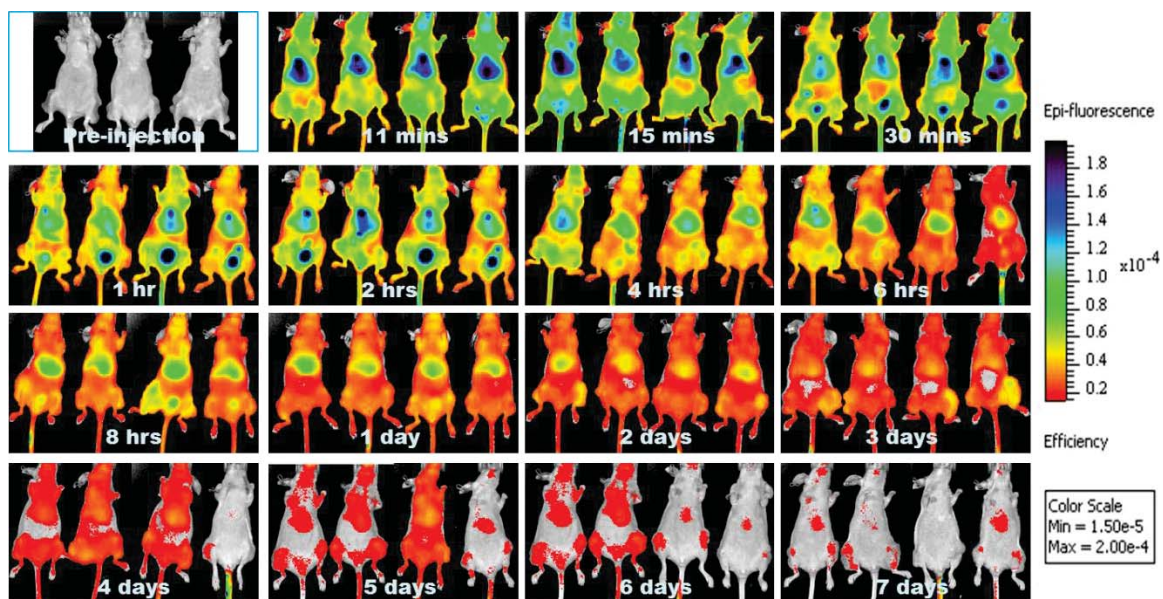


**Figure 5.8.** IVIS® images of the ventral view of athymic mice injected with  $^3\text{H}$ -PTX/FPI-749 nanocrystals.

### 5.3.5 *Ex vivo* IVIS® Imaging

Subsequent to euthanization by CO<sub>2</sub> asphyxiation, harvested tumor and major organs of mice administered with <sup>3</sup>H-PTX NCs were imaged under IVIS® (Figure 5.9). In order to compare with the normalized tissue distribution of <sup>3</sup>H-PTX (Figure 5.3), the total fluorescence intensities from individual organs and tumors were normalized by the weight of a tissue (Figure 5.10). While the trends in the liver and spleen between the drug distribution and bioimaging were comparable, the fluorescent intensities in the tumor, heart, lungs, and kidneys were much elevated. It is important to note that the fluorescence in heart, lungs, and kidneys dissipated rapidly – indicated by the steep slopes – implying that the dye molecules were cleared out of the system. In contrast, a temporal delay of clearance in tumor was observed.

The results further illustrate the limitation of using fluorescence imaging for biodistribution detections of drug delivery systems. When the dye is released from the nanocrystals, discrepancy exists. Still, coherence does exist, particularly in the liver in which 40-50% of the hybrid nanocrystals were sequestered by macrophages. Strong fluorescent signals observed also in the spleen and lungs were most likely contributed by entrapped FPI-749 from nanocrystals. The strong intensity in the tumor, nevertheless, likely came from released, free dye molecules – for example, from phagocytized nanocrystals – that re-entered the blood circulation. Hybrid nanocrystals or dye molecules that were trapped on the peripheral blood vasculatures of tumor gave off apparent strong fluorescent signals, which are heavily surface-weighted. Moreover, light absorption by hemoglobin in the NIR range can present an interference factor as well [340, 341]. Blood-rich organs (e.g., liver, spleen, and lungs) are known to attenuate the reflected

fluorescent signal the most [339], while tumor tissues, which contain much less hemoglobin, do not attenuate as much. Divergences in the result of tissue distribution analyzed by radiolabeled material and optical imaging of excised tissues, especially in tumor, have been observed previously [229, 231, 309] . Thus, extra caution should be taken when evaluating the tumor-targeting efficiency of novel therapies by using optical imaging. The apparent high fluorescence signal observed in tumors may not necessarily mean that the treatment targets the tumor efficiently.

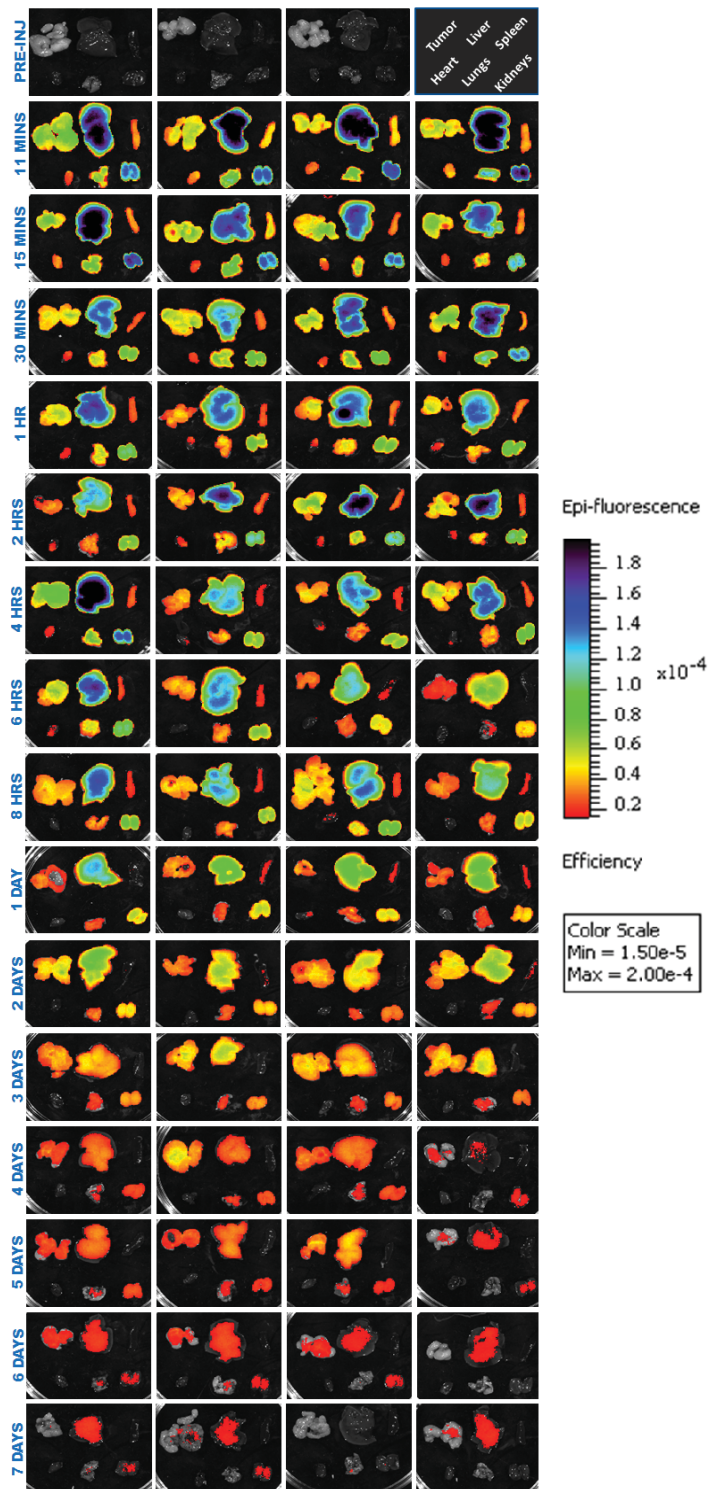


**Figure 5.9.** IVIS® images of ex-vivo tissues of animals administered with <sup>3</sup>H-PTX/FPI-749 nanocrystals

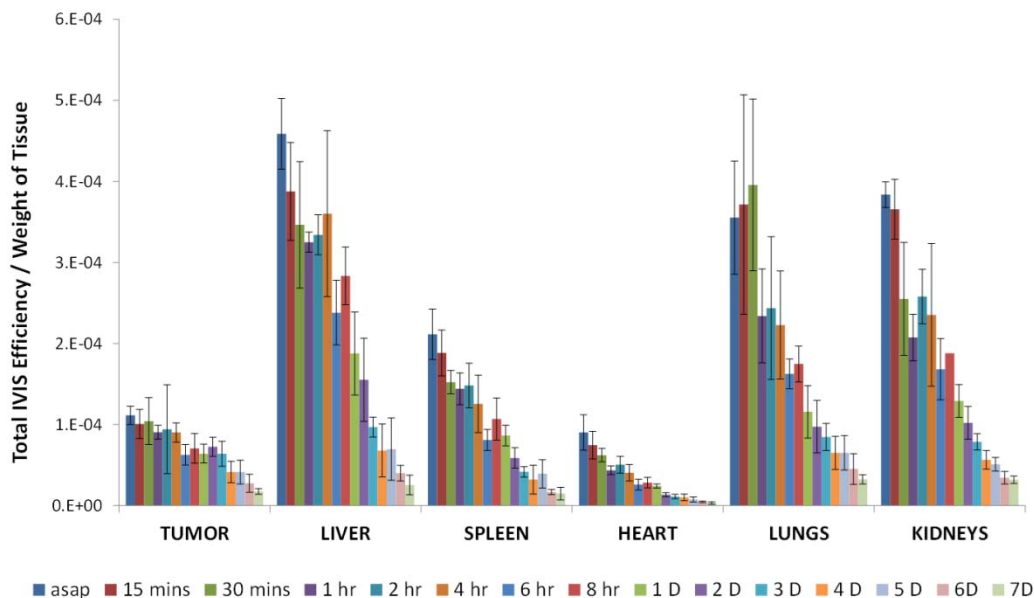


**Figure 5.10.** The fluorescence distribution (% total efficiency/gram of blood or tissue) of 20 mg/kg  $^3\text{H}$ -PTX/FPI-749 nanocrystals. The term “asap” refers to 11 minutes post-injection time.

#### 5.4 Conclusion

The tissue distribution study showed that  $^3\text{H}$ -Taxol was extensively distributed to the major organs, which could impose systemic toxicity, as observed in the decrease of percent body weight change during the survival study (Chapter 4). The  $^3\text{H}$ -Taxol was extensively distributed to major organs, while  $^3\text{H}$ -PTX/FPI-749 nanocrystals were rapidly cleared from the blood circulation by the MPS with more than 40% of the injected dose found in the liver.  $^3\text{H}$ -Taxol was maintained in plasma longer and accumulated in the tumor at higher concentrations than  $^3\text{H}$ -PTX/FPI-749 nanocrystals. Yet, the concentration of  $^3\text{H}$ -PTX in tumor was maintained quite steadily from 8 to 72 hours, suggesting the

prolonged retention and possible release of  $^3\text{H}$ -PTX from engulfed nanocrystals in the macrophages. Still, less than 1% of the injected dose by either Taxol or PTX nanocrystals was present in the tumor at any given time point.

Discrepancies were found between the biodistribution of the drug and the fluorescent imaging of the whole body and excised tumor and tissues. Since tissues inherit different molecular compositions and structures, they are optically distinctive in light attenuation, which translated in consequential divergence in quantitative results. In addition, the observed strong fluorescent intensity in the tumor was likely contributed by dissolved free dyes that were accumulated in the region. The clearance of fluorescent molecules from the tumor was reduced, possibly resulting from the impaired lymphatic drainage.

There are a few lessons that may be learned from this study regarding further development of nanocrystal-based delivery systems, and other systems in general, for cancer therapy and diagnosis. First, the EPR effect for both the solubilized formulation and nanocrystals was similar and insignificant with regard to drug accumulation. If the tumor can be regarded as an organ of its own, the drug concentration was much less than the concentration in other major organs, especially liver, lungs, spleen, and kidneys. Obviously, the results were affected by not just the delivery system, but also by the tumor type and its biology. Still, such a low accumulation (less than 1%) could lead to tumor suppression and antitumor efficacy. Therefore, for cancer therapy, the most critical is perhaps not to get more drugs to the tumor, but to reduce drug accumulation in major organs or at least to steer the biodistribution away from key organs (e.g., heart and brain) to reduce toxic effects. Drug accumulation in heart following nanocrystal administration was significantly less than that achieved with the free Taxol formulation. On the other

hand, the liver appeared to tolerate high accumulation of nanocrystals, and such accumulation acted as a depot of the drug and permitted the re-distribution of the drug to the plasma and consequently the tumor.

Second, the difference in the biodistribution between the fluorescent dye and the drug indicates that using the optical imaging for the indication of drug distribution can be limited and misleading. This is not only because of the limitation of light penetration by the IVIS<sup>®</sup> system, but also due to the variation in the physicochemical properties of the two molecules such as lipophilicity, which likely lead to the differences in biodistribution. As the hybrid nanocrystals started to dissolve and release the dye, the observed optical signal was a contribution of both hybrid nanocrystals and free dye molecules. The imaging probe could become more and more diverged from drug location as they further distributed.

Consequently, future development of pure and hybrid nanocrystals for cancer theranostics will focus on the control of the biodistribution in major organs. This may be achieved by chemical modification of the surface of nanocrystals. Furthermore, when using hybrid nanocrystals for theranostic purposes, the biodistribution of the nanocrystals, free drug, and free probes need to be resolved and differentiated.

## Chapter 6 - Conclusion and Future Outlook

Nanocrystals have shown promising potentials for drug delivery, particularly for delivering poorly soluble anticancer drugs. Major challenges still remain and must be overcome before nanocrystal-based formulation can reach the bench side. Through the advancements in formulation development, nanocrystals with uniform particle size and morphology can be produced either via diminution or precipitation approach. However, there seems to be a lack of feasible means to minimize opsonization by MPS subsequent to intravenous injection. Due to the dynamic process of dissolution (refer to Section 1.3.4.4), any stabilizer attached to the surface can be detached from the surface during blood circulation and extravasation. Also, the physical entrapment of stabilizer in the crystal lattice has not yielded significant progress in the past as the addition of stabilizer tends to reduce the product yield. The idea of creating a non-sheddable stabilizer for nanocrystals [342] could be adapted to the future development of drug nanocrystals.

When compared to the conventional delivery, Taxol, at the same administration dose, 20 mg/kg, paclitaxel nanocrystals exerted similar efficacy, but yet with much reduced toxicity. Although results of the biodistribution study showed that Taxol, due to the micellar encapsulation by Cremophor [320], had better tumor accumulation over PTX nanocrystals, the clearance of the latter was temporally delayed. When tested in colon cancer HT-29 xenograft, only less than 1% of the intravenously administered dose of either Taxol or PTX nanocrystals was recovered in the tumor, indicating limitation of the EPR effect [29]. Yet, at such a low drug concentration, treatment led to tumor suppression and antitumor efficacy. More than 40% of the injected nanocrystals were

being sequestered by the macrophages within the first 10 to 15 minutes and found in the liver. Interestingly, the engulfed nanocrystals were able to be re-distributed back to the systemic circulation. It is worth noting that the sequestration of intravenously injected nanocrystals remains in the specialized macrophages and does not affect the safety profile of the drug [129]. Hence, due to its low inherent toxicity, nanocrystal suspension can be administered at much higher doses to achieve better therapeutic efficacy. Yet, additional studies on various dosing scheme should be explored because frequent injections and/or high concentration dosing may not lead to the increase in drug concentration in the tumor but in healthy tissues and organs as well.

In order to obtain an improved theranostic nanocrystals, imaging probes also need to be tightly secured, which may be achieved through means chemical modification of the surface of nanocrystals. Due to its practicality, optical imaging has been increasingly utilized as a tool to trace the distribution of administered nanotheranostics. When a fluorophore is being used as an imaging probe, it is crucial that the selected dye either stays encapsulated or conjugated with the main component of the particles (e.g. drug molecule) for an extended period of time – at least until the theranostic system reaches the target (e.g. tumor). If the probe started to dissociate from the carrier, then the observed optical signal may not fully reflect the true biodistribution of the system, as the physicochemical properties of the carrier and probe may differ. In the case of hybrid nanocrystals that were studied, as they started to dissolve and release the dye, the observed optical signal was contributed from both entrapped and free dye molecules.

Although optical imaging can provide a convenient, easy, and rapid means of assessing the agent's biodistribution in the excised organs [229, 231, 233, 309], complications and

discrepancies may arise due to the inherent tissue properties. Because different tissues inherit distinctive molecular compositions and structures, they are optically distinctive in attenuating the light source. Consequently, this translates to divergence in quantitative results [339]. One of the determining factors in this deviation is the light interference due to absorption by hemoglobin in the NIR range. Blood-rich organs (e.g. liver, spleen, lungs, and heart) are known to attenuate the reflected fluorescent signal the most, while tumor tissues, which contain much less hemoglobin, do not attenuate light as much. Additionally, further complications arise because the spatial resolution of planar imaging is limited as the produced imaging information from this system is surface-weighted, in that anything closer to the surface will appear brighter [37]. When using hybrid nanocrystals for theranostic purposes in the future studies, the biodistribution of the nanocrystals, free drug, and free probes need to be resolved and differentiated.

\

## APPENDICES

### A.1 Hybrid Camptothecin/Gold Nanocrystals

#### A.1.1 Introduction

The development of multifunctional nanomedicine, which combines the therapeutic and diagnostic capabilities, has tremendous potential to revolutionize the future of cancer therapy. By incorporating bio-imaging agent molecules, the delivery of therapeutic agent can be potentially monitored and traced *in vivo*. Over the past decade, the application of fluorescent markers, both organic- and inorganic-based material, has been vastly explored [343, 344]. While organic dyes may suffer from limitations, such as photobleaching, biodegradation, and narrow excitation/broad emission spectra, the lack of biocompatibility and high toxicity hinders the utilization of the inorganic markers [345]. In addition, fluorescence imaging is still limited to *in vivo* studies due to low sensitivity and shallow optical path. Current imaging modalities, including positron emission tomography (PET), computed tomography (CT), magnetic resonance imaging (MRI), and ultrasound, can provide anatomical patterns and basic information regarding tumor location, size, and progression and are still the standard clinical tools [346, 347].

Attributed to its availability, efficiency, and cost, X-ray based CT is among the most convenient imaging/diagnostic tools in hospitals today [65, 348]. Iodinated aromatic molecules are the most commonly contrast agent used in clinics and dominate the X-ray contrast media markets [349, 350]. Due to its rapid renal clearance, however, approximately 100 to 200 mL of highly concentrated iodinated contrast medium solution (*ca.* 600 mg/mL) are administered intravenously to achieve adequate contrast [349].

Adverse reactions caused by excessive amount of chemicals have also been reported [349, 351, 352]. In the past few years, the feasibility of using gold nanoparticles as a CT contrasting agent has been tested *in vivo*, both through passive [353, 354] or active [65, 353] targeting. Within a CT image, one can distinguish the difference between tissues based on the degrees of the X-ray attenuation; more X-rays are attenuated in denser tissues. The contrast of structure or fluid within the body can be enhanced by utilizing contrast agent, where its attenuation coefficient is determined by the atomic number and electron density. Because gold's atomic number and electron density (79 and 19.32 g/cm<sup>3</sup>, respectively) are higher than iodine (53 and 4.9 g/cm<sup>3</sup>, respectively), gold gives a higher mass attenuation coefficient. For instance, at 100 keV (a standard X-ray energy for diagnostic imaging), gold and iodine have attenuation coefficient of 5.16 and 1.94 cm<sup>2</sup>/g, respectively; thus, gold provides about 2.7 times stronger contrast per unit weight than iodine. In addition, the low toxicity and good biocompatibility [64] make gold (clusters and nanoparticles) an ideal contrast agent. More importantly, regardless the shape of gold nanoparticles, the only important parameter in CT imaging is the total amount of gold per unit volume [65]. The utilization of gold as contrast agent *in vivo* was first reported in 2006 [353], and it is being continually explored.

In the past two decades, colloidal drug delivery systems (CCDS), including liposomes, solid lipid nanoparticles, polymeric nanoparticles, and micelles, have been used to formulate highly insoluble antic drugs. Despite the fact that these systems have been extensively studied, various inherent limitations remain. They generally have limited drug loading capacity [16, 355]. Phospholipid-based structures, such as liposomes, may also suffer from drug leakage and instability during the preparation, storage, and

administration process that can compromise the therapeutic outcomes [24, 25]. As such, more physically stable and solvent-free nanocrystals-based formulation may be used for delivering antineoplastic drugs and reach the tumor site in the solid form. This multifunctional design may lead to cancer theranostic systems, which can be passively targeted to tumor site via enhanced permeation and retention (EPR) effect [6]. The fundamental concept of such an integrated crystalline system lies in physical inclusion of a bioimaging substance in the crystal lattice of a host drug compound; no chemical conjugation is thereby needed. Herein, the purpose of this report is to demonstrate successful incorporation of gold ions or atoms and their clusters in the crystal lattice of a chemotherapeutic drug, camptothecin (CPT). The idea of this novel hybrid nanocrystal was inspired by the studies of “dyeing crystals” [235], where organic dyes are imbedded in organic crystals. To the best of our knowledge, purported incorporation of an inorganic material into organic nanocrystal lattice for biomedical applications has not been previously reported.

CPT was selected as the model drug because it has a broad spectrum of therapeutic activity against various cancer types [356, 357]. Similar to other chemotherapeutic agents, CPT has a low solubility in water (*ca.* 1.2 µg/mL at 25 °C). It also has a well-established clinical and been the focus of numerous drug delivery studies since its discovery in 1966 [358]. Specifically, the antitumor activity of CPT results from its ability to actively target and inhibit the DNA enzyme topoisomerase I (TOP1). Unfortunately, the clinical application of the drug remains greatly limited, largely due to its inherent instability in solution as well as protein binding in the plasma. The native, biologically active compound may undergo hydrolysis and produce an inactive form

(Figure A.1.1). The ring-open reaction, which converts the lactone to carboxylate, occurs above pH 7. Despite the chemical instability of the molecule, pure CPT nanocrystals showed to accumulate in tumor and inflict the antitumor effect, as demonstrated in our recent study [168]. In our experiments reported here, preparation and storage of hybrid CPT nanocrystals were conducted in pH 4-water to maintain its active lactone form.

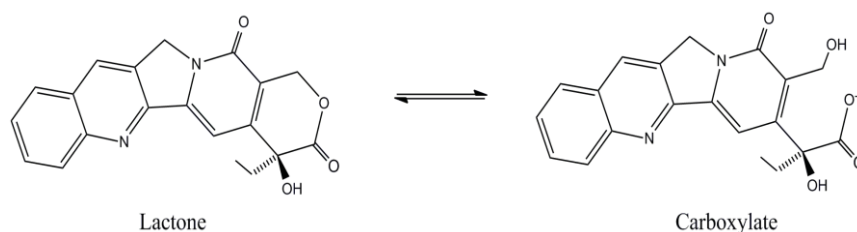


**Figure A.1.1.** The two forms of camptothecin (CPT)

## A.1.2 Materials and Method

### A.1.2.1 Materials

Camptothecin (>99%) was purchased from 21CECPharm (United Kingdom); all other chemicals and solvents were obtained from Sigma (St. Louis, MO) and Fisher Scientific (Pittsburgh, PA). 200-mesh-lacey carbon grids were from Electron Microscopy Sciences (Hatfield, PA).

### A.1.2.2 Preparation of Hybrid Camptothecin Nanocrystals

Hybrid of gold nanoparticles and/or gold ions in camptothecin nanocrystals were produced by an anti-solvent precipitation method with a simultaneous reducing reaction. In detail, to produce hybrid camptothecin/gold nanoparticle nanocrystals, 40 ml of boiled

pH 4 water (adjusted with 0.25 M HCl), 3 mL of 1 mM hydrogen tetrachloroaurate,  $\text{HAuCl}_4$ , were added in a three-neck-flask. The mixture was stirred at 500 rpm with a stirrer shaft and under intense sonication. The stirring speed was subsequently decreased in order to minimize bubbles formed and to encourage crystal growth. Next, 0.3 ml of 1% trisodium citrate dehydrate aqueous solution was added to the system. While the gold salt solution was being reduced, 2 ml of 1 mg/ml camptothecin/dimethyl sulfoxide (CPT/DMSO) was added. The system continued to be sonicated and stirred to encourage crystal growth and formation of gold nanoparticles. The suspension's color changed from clear to pinkish. To produce hybrid camptothecin/gold ions nanocrystals, the same method was performed without the addition of 0.3 ml of 1% trisodium citrate dehydrate aqueous solution. In this case, the gold remained as a salt solution, not reduced, and may be entrapped to the crystal lattice more homogeneously. In contrast to the hybrid gold nanoparticles suspension, the solution and retentate for the gold salt solution remains colorless. Once hybrid nanocrystals formed, the crystals were harvested by vacuum filtering with a 50 nm polycarbonate nuclepore filter. With vacuum filtration system still intact, approximately 5 to 10 ml of pH 4 water was added to wash any gold nanoparticles that were not incorporated or attached to the crystals. The product harvested on the filter was then re-suspended in pH 4 water by sonicating the filter paper. For further removal of gold nanoparticles or ions that were not associated with the crystals, the filtration, washing and re-suspension by sonication were repeated three times. Following the final filtration process, the product collected on the filter paper was re-suspended in 1 ml of pH 4 water and diluted with aqua regia mixtures for gold analysis with inductively coupled plasma (ICP). Filtrate from each filtration process was also collected for mass balance

calculation. Only trace amount of camptothecin and gold nanoparticles were present in the second and third filtrate; thus, only the first filtrate was analyzed by ICP. Before mixing with the digestion solution, filtrate was concentrated by boiling the water, leaving a total volume of 5 ml. The filtration and analysis process are depicted in Figure A.1.2.

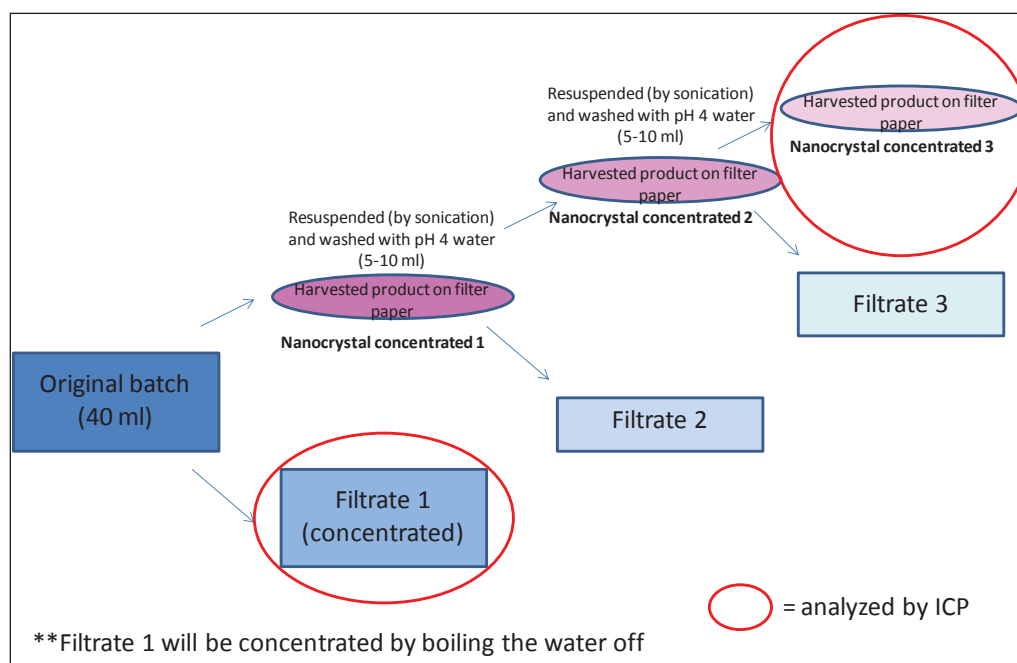


**Figure A.1.2** The schematic of filtration and harvesting hybrid nanocrystals

### A.1.2.3 Chemical Analysis of Hybrid Camptothecin Nanocrystals

Varian Vista-Pro ICP-OES was utilized to quantify the amount of the gold incorporated. 1 ml of either the concentrated product or filtrate was digested with 1 ml of freshly mixed aqua regia (i.e. a mixture of concentrated nitric acid and hydrochloric acid (1:3 molar ratio)) and diluted with 3 ml of deionized water. Standard solutions were prepared by using ICP standard for gold (Fisher Scientific, Pittsburgh, PA) diluted with aqua regia at concentrations of 0.010, 0.050, 0.1, 0.5, 1, 5, 10, and 50 ppm. Analysis was performed at wavelength of 267.594 nm. Quantification of camptothecin was conducted by high-

performance liquid chromatography (HPLC, Waters Breeze) with UV detection (Waters 2487 dual  $\lambda$  absorbance detector) at 256 nm. A Waters' Symmetry C18 5  $\mu$ m column (4.6 x 150 mm) was used at 33°C with a mobile phase of acetonitrile : 2% triethylamine aqueous solution adjusted to pH 5.5 with acetic acid (36:64) pumped at a rate of 0.5 mL/min (Waters 1525 binary pump).

#### **A.1.2.4 Electron Microscopy Imaging and Energy Dispersive X-ray Spectroscopy (EDS)**

SEM images were obtained using Hitachi SEM 4300 at an accelerating voltage of 3 kV. Prior to visualization, samples were coated with conductive layers of gold palladium (Au/Pd) for 1 minute with current of 20 mA in a sputter coater, resulting in approximately 15 nm thick coating. The coating helped to reduce sample charging. The freeze-dried hybrid nanocrystal suspension was imaged by using JEOL 2010F TEM, which is equipped with the Oxford EDS detector. TEM was operated at 200 KeV. Scanning Transmission Electron Microscopy (STEM) was performed at high angle conditions of approximately 50 mrad, using a 1.7 angstrom high resolution probe. EDS was performed under STEM conditions using a 1 nm analytic probe. A small amount of the freeze dried hybrid nanocrystals were rubbed on the carbon lacey grid and placed in the sample holder for imaging. Samples obtained from one-time cycle of washing and re-suspension was compared to that washed and re-suspended three times.

### A.1.3 Result and Discussion

Incorporation of gold in CPT nanocrystals was attempted in two forms, either as gold atoms or gold ions. Both preparations were conducted in a single, physical step, eliminating typical multi-step chemical treatment of conjugating bio-imaging agents [359, 360]. For the hybrid nanocrystals of camptothecin and gold atoms (e.g. gold nanoparticles), chloroauric acid was being reduced at the same time when the nucleation of camptothecin nanocrystals started via the anti-solvent method. The redox was based on a simple route developed by McFarland, *et al.* [361], where citrate aqueous solution was added to reduce the chloroauric acid. Reduced gold was believed to be integrated into CPT nanocrystals as individual atoms and/or clusters. As the reduction progressed, the solution changed from clear to pinkish. Concurrently, a high concentration of dissolved CPT in dimethyl sulfoxide (DMSO) nucleated and crystallized as the DMSO solution was quickly added to the pH 4 water. In the case of incorporating gold ions, citrate solution was not added. Thus, without the reduction step, individual or clusters of chloroauric acid could be freely entrapped in the crystal lattice of the camptothecin nanocrystals. At the end of each batch process, product was filtered and freeze-dried either with (Figure A.1.3) or without (Figure A.1.4) extra washing and resuspension step. The hybrid camptothecin nanocrystals had morphology of rectangular thin sheet, with the length ranged from approximately 300 nm to 1.5  $\mu\text{m}$  (Figure A.1.3). The TEM and STEM images (Figure A.1.3) clearly showed that gold clusters were incorporated and/or attached to the organic nanocrystals with high affinity, even after vigorous washing and sonicating (Figure A.1.4). Visually, the hybrid nanocrystals seem to be aggregated, possibly due to the freeze drying process. The size of the embedded gold atom clusters

was approximately 10 nm (Figure A.1.3 and A.1.4), consistent with the size reported by McFarland, *et al* [361]. EDS analysis of the gold clusters in the CPT nanocrystals revealed that the expected characteristic peaks of oxygen (O), carbon (C), gold (Au), and copper (Cu) were present. The oxygen and carbon peaks were due to the organic material, CPT, and the copper peak was present because it was the material of the sample holder and grid.

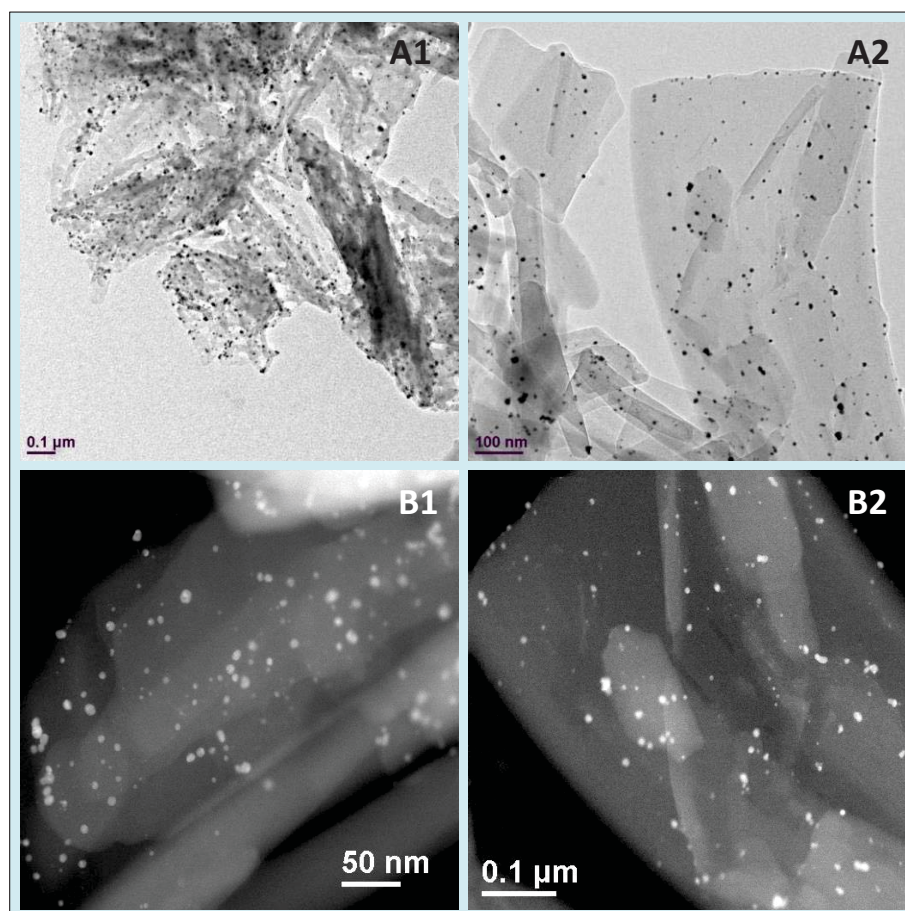


**Figure A.1.3.** CPT/gold hybrid nanocrystals without vigorous washing and filtering: (A) TEM images, (B) STEM images.

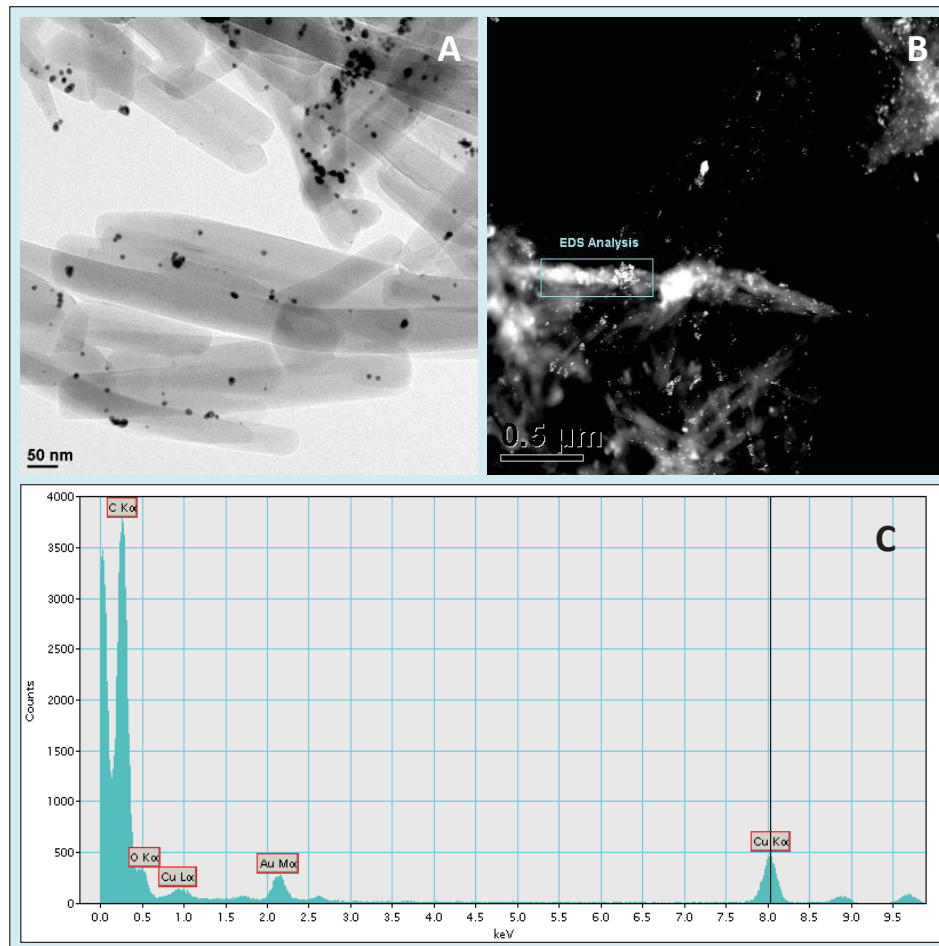


**Figure A.1.4.** CPT/gold hybrid nanocrystals with vigorous washing and filtering: (A) TEM image, (B) STEM image, (C) EDS analysis.

In the absence of reduction of chloroauric acid during the nanocrystal preparation, individual or clusters of gold ions (chloroaurate) were incorporated in the camptothecin nanocrystals. The clusters of these ions were approximately 1.4 nm in size (Figure A.1.5 B and B\*), and the individual gold ions seen as white spots were approximately 2Å in diameter (Figure A.1.5 C and C\*) with a narrow size distribution. The white spots are believed to be individual gold ions incorporated in the lattice of the camptothecin nanocrystals. If these ions were not imbedded in the lattice, they would have been

washed off. The gold ions were also shown to be more homogenously distributed relative to that of the reduced gold atoms/clusters (Figure A.1.3 and A.1.4).

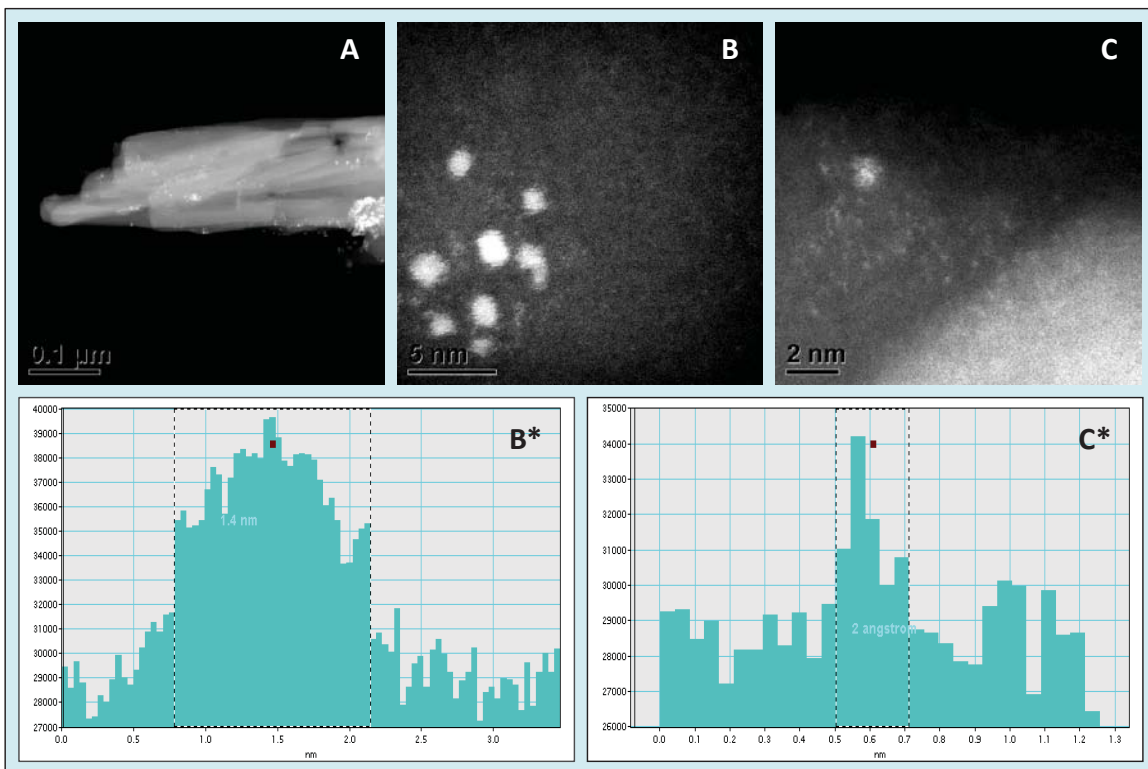


**Figure A.1.5.** CPT/chloroaurate hybrid nanocrystals with vigorous washing and filtering: (A) STEM image of overall structure, (B) high resolution STEM image of imbedded gold clusters, (B\*) particle analysis of gold cluster, (C) high resolution STEM image of imbedded gold ions, (C\*) particle analysis of gold ion.

Fast Fourier Transform (FFT) image processing was utilized to get more a detailed and optimized structure image of the hybrid CPT nanocrystal (Figure A.1.6.). In this analysis a Fourier transform was applied to Figure A.1.6.(A) producing the diffractogram, Figure A.1.6.(C) The diffraction spots were then filtered as in Figure A.1.6.(D), and an inverse

Fourier transform applied producing image 5b. This brings out the CPT lattice planes giving a lattice spacing of approximately 4 Å.

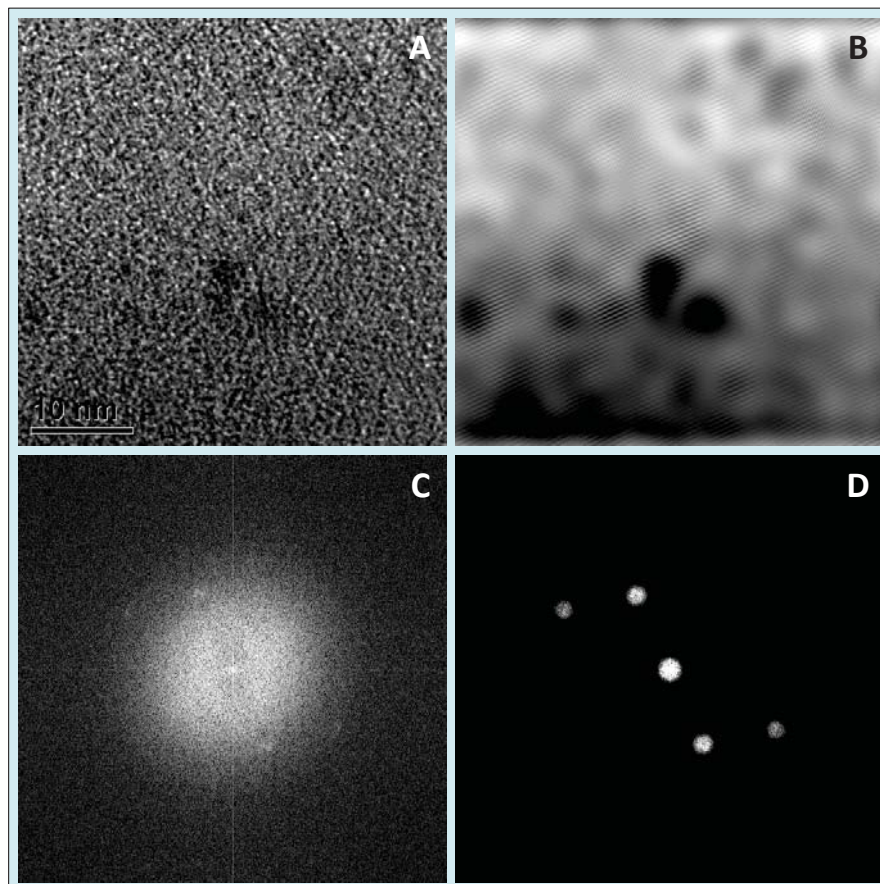


**Figure A.1.6.** (A) HR-TEM of hybrid CPT nanocrystals, (B) FFT filtered image using diffraction patterns (C and D) of a TEM image of hybrid camptothecin nanocrystals

Moreover, the percent entrapment of gold in the CPT nanocrystals was quantified by inductively coupled plasma-optically emission spectrometry (ICP-OES) [362]. Relative to the amount of the starting material, 8.11 and 1.31% of gold atoms and chloroauric acid, respectively, were present in the hybrid nanocrystals. The reduction process allows neutral gold clusters to form quickly and to be entrapped to the camptothecin

nanocrystals. On the other hand, chloroaurate incorporation may be relatively limited due to its ionized state in the solution and the need to bind a counter ion (most likely, proton) prior to the entrapment. As such, more gold atoms were integrated in the CPT nanocrystals. It is important to note that these nanocrystals were vigorously washed under sonication for multiple times so the majority of gold atoms or ions that were quantified were embedded inside the nanocrystals as defects.

#### **A.1.4 Conclusion**

Nanocrystal composites of a therapeutic and inorganic contrast agent may have multifunctional application even at relatively low loadings of gold. Because of the sensitivity of CT imaging and the high attenuation coefficient of gold, a good contrast-to-noise images can be obtained at gold concentrations of 100  $\mu\text{g/ml}$  [363, 364], which is approximately a hundred times lower than the cytotoxicity of gold nanoparticles. When operated at standard X-ray energy of 100 keV, same contrast obtained from iodine-based-contrast agent can be achieved with one-third-less-dose of gold. It is also important to note that even at its low dosing, gold can exhibit longer blood retention (i.e. allowing prolonged imaging time) due to its inherent physical property of high molecular weight [353]. Additional advantages of maximizing integrity and minimizing clearance of gold may be established by its entrapment in nanocrystal structure.

## **A.2 Nanocrystals of ZSTK474**

### **A.2.1 Introduction**

Certain protein associated with the PI3K/Akt/mTOR signaling, which plays critical role in cell proliferation, angiogenesis, and metastasis, is substantially overexpressed in CRCs relative to the normal colonic tissue [365, 366]. The findings suggested a new therapeutic strategy to specifically target the PI3K/Akt/mTOR signaling pathway. A novel PI3K inhibitor, ZSTK474 [2-(2-Difluoromethylbenzimidazol-1-yl)-4,6-dimorpholino-1,3,5-triazine] (Figure A.2.1), is more potent and stable compared to the two known precedent inhibitors, LY294002 and wortmannin [367]. When tested using the COMPARE analysis on a panel of 39 human cancer cell lines (termed JFCR39 [368]), ZSTK474 exhibited substantially lower mean GI<sub>50</sub> (50% growth inhibition) of 0.32 μM than LY294002 and wortmannin with GI<sub>50</sub> of 7.4 μM and 10 μM, respectively. Nonetheless, ZSTK474 is a poorly water soluble compound. Its solubility in water is approximately 1-5 μM (MW: 417.41 g/mol). Thus, in order to achieve sufficient bioavailability, oral dosage form of ZSTK474 was administered at high dose (> 100 mg/kg). When ZSTK474 was given daily at 100 mg/kg from days 0 to 13 in mouse B16F10 melanomas, tumor growth suppression was observe. Further tumor growth inhibition in B16F10 melanomas, A549, PC-3, and WiDr xenografts was observed at 400 mg/kg oral administration [367].

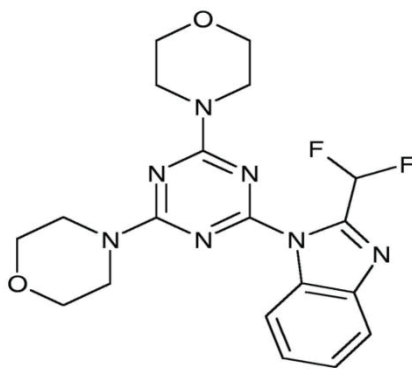


**Figure A.2.1.** The chemical structure of ZSTK474.

Although no noticeable toxicity was observed at 400 mg/kg oral dose, mice with WiDr colon cancer xenograft experienced significant body weight loss ( $p:0.009$ ) from day 7 to 14 during treatments [367]. The drug exposure can potentially be minimized by giving intravenous injection at much lower dose. However, the current approach of solubilizing poorly water soluble chemotherapeutics in solvents may also yield adverse side effects, due to solvent toxicity and non-specific distribution of dissolved molecules to rapidly growing cells. Various nano-encapsulation designs, such as liposomes [14, 15], micelles [16], solid lipid nanoparticles [17, 18], polymeric nanoparticles [19, 20], and dendrimers [21], have been developed to improve tumor-targeting efficiency. They do so by taking advantage of the tumor's enhanced permeation and retention (EPR) effect [7], which signifies the poorly constructed blood vessel and ineffective drainage of the lymphatic system. However, the design of the aforementioned nanoconstructs can become overly complex, resulting in poor carrier stability [24, 25], low drug loading [26], and difficult scale-up production.

With nanocrystal formulation, drug molecules are directly administered as solid, crystalline nanoparticles. There are no solubilizing chemicals, nor encapsulating carriers.

The drug loading is nearly 100%; at times, a few percent of surfactants are used. The physical integrity is also superior to other nanoparticle-based systems. For a poorly soluble drug, it is expected that free drug molecules will be slowly dissolved from the nanocrystals. All these properties make nanocrystal extremely appealing for delivering poorly soluble anticancer drugs. In addition, hybrid nanocrystals [169] can be constructed from this nanotemplate by physically entrapping near infrared fluorophore in the crystal lattice, offering not only treatment but also non-invasive monitoring of the biodistribution *in vivo*. Thus, the objective of this research is to formulate and characterize both pure and hybrid nanocrystals of ZSTK474 nanocrystals. Further studies to evaluate the efficacy and performance both *in vitro* and *in vivo* models of colorectal cancer were conducted in collaboration with Dr. Mark Evers' (Markey Cancer Center, University of Kentucky) laboratory.

## **A.2.2 Materials and Method**

### **A.2.2.1 Materials**

ZSTK474 (MW: 417.41 g/mol) was purchased from LC Laboratories (Woburn, MA). FPR-648 fluorophore (maximum excitation wavelength,  $\lambda_{ex}$ =648 nm; maximum emission,  $\lambda_{em}$ =671 nm) was obtained from Polysciotech (West Lafayette, IN). Dimethyl sulfoxide (DMSO, HPLC grade) and acetonitrile (HPLC grade) were purchased from Fisher Scientific (Pittsburgh, PA). Saline (0.9% w/v sodium chloride) for injection was from Hospira (Lake Forrest, IL). Deionized (DI) water (by Milli-Q<sup>®</sup>, filtered through 0.2  $\mu$ m membrane) was used for all the experiments. 0.050  $\mu$ m (50 nm) Whatman<sup>®</sup> nuclepore

polycarbonate track-etched membranes used for filtration were purchased from Fisher Scientific (Pittsburgh, PA).

#### **A.2.2.2 Preparation of ZSTK474 Nanocrystals**

The pure and hybrid ZSTK474 nanocrystals were prepared by using the combination approach. Briefly, 1 mL of 2.5 mg/mL ZSTK474 (LC Laboratory, Woburn, MA) dissolved in dimethyl sulfoxide (DMSO, ACS grade, Fisher Scientific, Pittsburgh, PA) was added rapidly to 20 mL of deionized water in a three-neck round bottom flask. The mixture was being stirred at 1000 rpm and sonicated for 10 minutes. Ice was added to the sonication bath to maintain the water temperature between 12-18°C. The product was collected by using 0.05  $\mu\text{m}$  Whatman<sup>®</sup> nuclepore polycarbonate paper (Fisher Scientific, Pittsburgh, PA) in vacuum filtration flask. The retentate was re-suspended in 2-3 mL deionized water by utilizing bath sonicator. To further minimize the particle size, re-suspended product of ZSTK474 pure nanocrystals was homogenized (Powergen 125, Fisher Scientific) for 10 minutes. Homogenized products from multiple batches were collected on using 0.05  $\mu\text{m}$  Whatman<sup>®</sup> nuclepore polycarbonate paper. The retentate was resuspended in small volume of deionized water to create a concentrated stock and stored in 4°C. Some part of the batch was freeze-dried (LabConco Freeze Dryer 4.5) for further solid-state characterization.

The procedure to prepare the hybrid nanocrystals was the same as that of the pure, except that Flamma Fluor FPR-648 (maximum excitation wavelength,  $\lambda_{ex}$ =648 nm; maximum emission,  $\lambda_{em}$ =672 nm) was added to deionized water prior to the addition of ZSTK474/DMSO solution. Fluorophore (FPR-648) that might adhere to the nanocrystal's

surfaces was removed by subjecting the sample to filtration-resuspension-filtration cycle until observed filtrate was clear.

#### **A.2.2.3 Physical Characterization and Chemical Analysis of ZSTK474 Nanocrystals**

Scanning electron microscope (SEM) images were obtained using Hitachi SEM 4300 at accelerating voltage of 3 kV. Sample was sputter coated with gold palladium (Au/Pd) at 20 mA for 1 minute prior to analysis. SigmaScan (Systat Software Inc.) software was used to obtain an estimate on the longest dimension of the nanocrystals. The average and standard deviation was derived from manual measurements of particle size from approximately one hundred particles. Particle size of the nanosuspension in deionized water was also measured using dynamic light scattering (DLS) Malvern Zetasizer Nano ZS. Zeta potential of nanocrystals in 10 mM sodium chloride was also obtained from the same instrument. Accumet pH meter 915 (Fisher Scientific) was utilized to measure the pH. To assess the crystallinity, X-ray power diffraction was collected on a powder X-ray diffractometer (Multiplex, Rigaku) with Cu KR radiation (40 kV, 44 mA). Scans were obtained from 5 to 40  $2\theta$  with step size of 0.02 and scan rate of 0.5°/min.

Quantitative analysis of ZSTK474 was conducted by high liquid chromatography (HPLC, Waters Breeze) with Waters' Symmetry C18 5  $\mu\text{m}$  column (4.6 x 150 mm) at 254 nm. Acetonitrile and water (65:35) were pumped at a total flow rate of 2 mL/min (Waters 1525 binary pump).

The entrapment of FPR-648 in hybrid nanocrystals was quantified using IVIS<sup>®</sup>. Triplicate of FPR-648 standard solutions in PBS (i.e. 1, 2, and 5  $\mu\text{g/mL}$ ) were placed in 96-well

plate. The fluorescence intensity was plotted against concentration to obtain standard curve, and the amount of FPR-648 in hybrid nanocrystals was determined from the linear correlation.

### **A.2.3 Result and Discussion**

#### **A.2.3.1 Characterization and Analysis of ZSTK474 Nanocrystals**

Nanocrystals of ZSTK474, with average size of 400 nm, were produced by the combination approach. Nucleation process was initiated when the high concentration of the drug solution added to water, where drug was practically insoluble. Although ZSTK474 nanocrystals were produced with the same method as the PTX nanocrystals (Section 2.3.1), their crystal growth subsequent to nucleation were more substantial. Scanning electron microscope (SEM) was utilized to visualize the morphology and measure the size of ZSTK474 nanocrystals (Figure A.2.2). The mean of particles' longest dimension in Figure A.2.2 was  $395.45 \pm 135.97$  nm. Due to the elongated shape, DLS underestimated the hydrodynamic diameter of the particles,  $304.0 \pm 10.50$  nm. The polydispersity index obtained from DLS measurement,  $0.153 \pm 0.026$ , was between 0.1-0.25, indicating that the particle size distribution was narrow [134] and the degree of flocculation or aggregation, if any, was minimal. When measured in 10 mM NaCl (concentration of 0.1 mg/mL, pH=5.33), the surface charge (zeta potential) of the ZSTK474 nanocrystals were slightly negative,  $-9.57 \pm 0.75$  mV. Although higher absolute value may be more desirable to resist flocculation, the negative surface charge is favorable because it has lower probability in inducing hemolytic reaction compared to one with positive charge [191]. The sharp peaks in the PXRD diffractogram (Figure

A.2.3) indicated that the ZSTK474 nanocrystals were crystalline, which is the most stable form relative to that of amorphous.

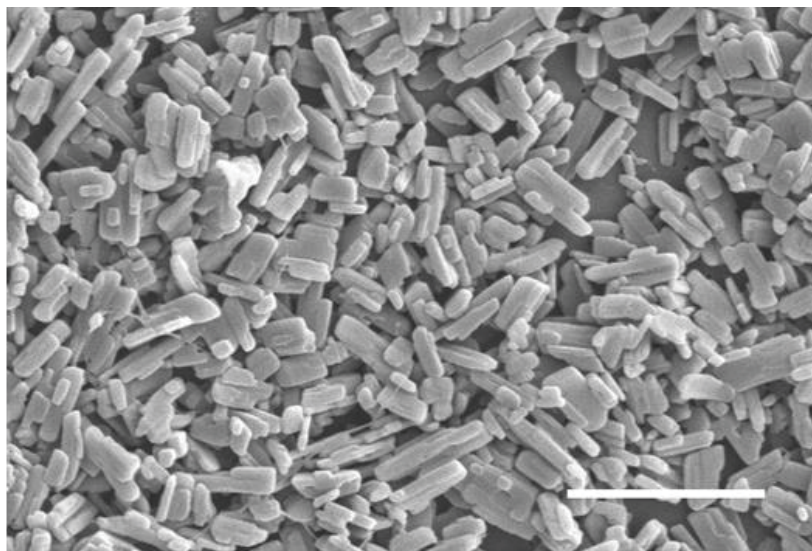


**Figure A.2.2.** SEM image of ZSTK nanocrystals. Scale bar represents 2  $\mu\text{m}$ .

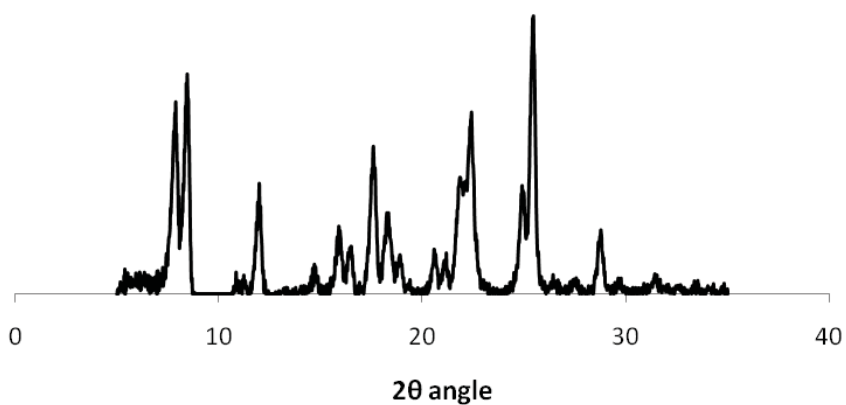


**Figure A.2.3.** Powder x-ray diffractogram of freeze-dried ZSTK474 nanocrystals.

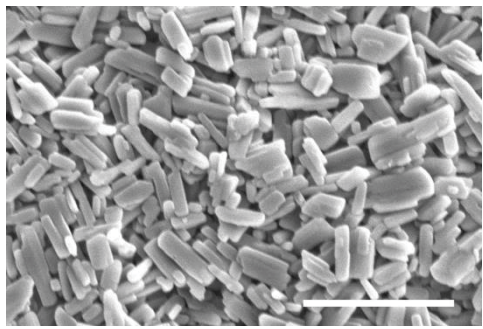
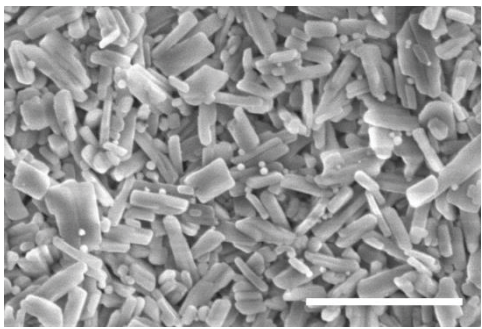
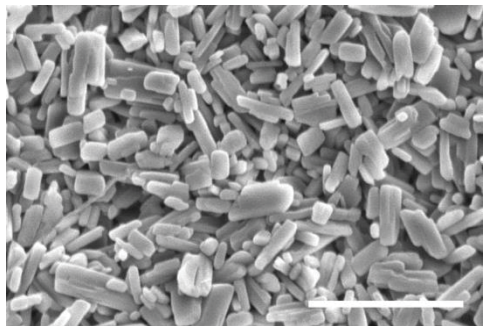
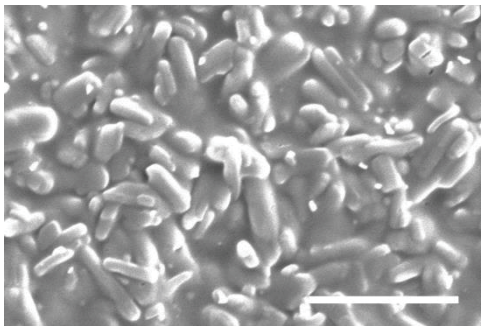
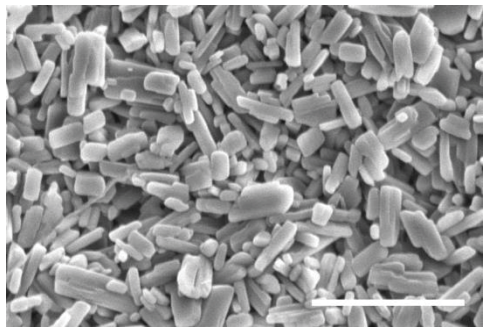
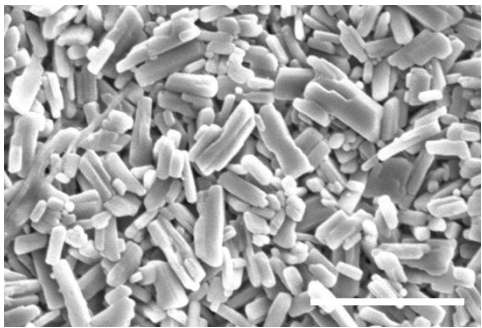
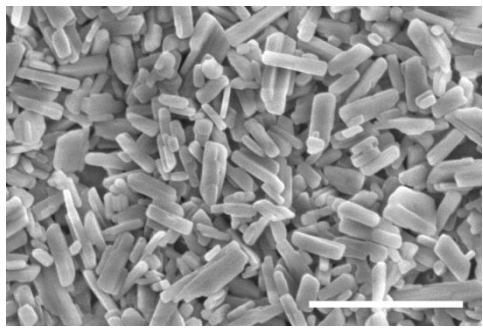
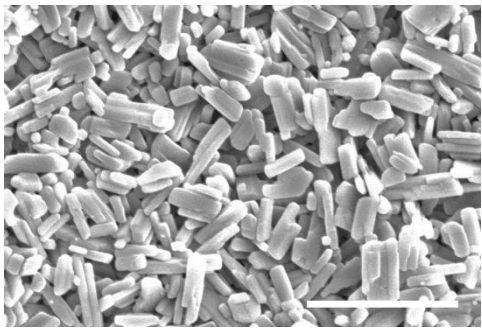
As for the hybrid ZSTK474/FPR-648 nanocrystals, the mean longest dimension analyzed by SigmaScan was  $492.4 \pm 269.30$  nm. There was 0.035% (w/w) entrapment of FPR-648 in the crystal lattice of ZSTK474. Despite the minute percent of entrapment, the fluorescence signal should still be able to be detected by *in vivo* optical modality (e.g.

IVIS<sup>®</sup>). The hybrid nanocrystals were tested *in vivo*, in collaboration with Dr. Evers' group.

#### **A.2.3.2 Stability of ZSTK474 Nanocrystals in Different Media**

The stability of ZSTK474 nanocrystals in different media was investigated. To achieve similar isotonicity, nanocrystals have to be re-suspended in saline prior to intravenous injection. Thus, the change in the particle size of nanocrystals suspension in saline at room temperature was evaluated (Table A.2.1 and A.2.2). Results revealed that there was no significant difference in the particle size during the three hour suspension period. This window should be sufficient as the amount of time taken for intravenous injection is far less than this. Based on the SEM images (Table A.2.1), there seem to be a minor interaction between nanocrystals and the components of cell culture media in the first hour when they were incubated at 37°C. However, compared to PTX nanocrystals (Section 2.3.4), ZSTK474 nanocrystals were more stable as the particle size and morphology were not significantly altered during this period. Since there may not be strong interaction between ZSTK474 and the components of cell culture media, such as albumin, ZSTK474 molecules may be released at slower rate compared to PTX nanocrystals.

**Table A.2.1.** SEM images of ZSTK474 nanocrystals suspended in saline (at room temperature) and cell culture media (McCoy's 5A + 10% fetal bovine serum + 1% penicillin streptomycin) at 37°C. Scale bars represent 2  $\mu\text{m}$ .

Time	Saline (Room Temperature)	Cell Culture Media (37°C)
30 minutes		
1 hour		
2 hours		
3 hours		

**Table A.2.2.** The stability study of ZSTK474 nanocrystals in different media. The particle size of the nanocrystals were analyzed from the SEM images by SigmaScan. Data represents means  $\pm$  S.D.

Time	Particle Size (nm) Measurement		
	DI Water (Room Temperature)	Saline (Room Temperature)	Cell Culture Media (37°C)
0.5 hour	450 $\pm$ 180	450 $\pm$ 190	490 $\pm$ 160
1 hour	460 $\pm$ 180	460 $\pm$ 220	540 $\pm$ 180
2 hours	430 $\pm$ 180	450 $\pm$ 170	490 $\pm$ 210
3 hours	430 $\pm$ 200	450 $\pm$ 170	460 $\pm$ 180

#### A.2.4 Conclusion

Colorectal cancer (CRC) overexpresses proteins that are associated with the PI3K/Akt/mTOR signaling. The administration of PI3K inhibitor, such as ZSTK474, can target more specifically the CRC site. Due to its low aqueous solubility and oral bioavailability, ZSTK474 has to be administered at high dose to achieve sufficient efficacy for tumor growth suppression. Here, a stable nanosuspension of pure and hybrid ZSTK474 was produced by the combination approach. The nanocrystals are expected to exert efficacy at much lower dose *in vivo* xenograft model.

## REFERENCES

1. Mullin JW, *Crystallization*, Butterworth-Heinemann. Oxford, 2001.
2. Rowinsky EK, Cazenave LA, Donehower RC (1990). Taxol - A novel investigational antimicrotubule agent. *Journal of the National Cancer Institute*, 82, 1247-1259.
3. Singla AK, Garg A, Aggarwal D (2002). Paclitaxel and its formulations. *International Journal of Pharmaceutics*, 235, 179-192.
4. Rowinsky EK, Eisenhauer EA, Chaudhry V, Arbuck SG, Donehower RC (1993). Clinical toxicities encountered with paclitaxel (Taxol(R)). *Seminars in Oncology*, 20, 1-15.
5. Fang J, Nakamura H, Maeda H (2011). The EPR effect: Unique features of tumor blood vessels for drug delivery, factors involved, and limitations and augmentation of the effect. *Advanced Drug Delivery Reviews*, 63, 136-151.
6. Maeda H, The enhanced permeability and retention (EPR) effect in tumor vasculature: The key role of tumor-selective macromolecular drug targeting, In *Advances in Enzyme Regulation, Vol 41*, ed. Weber, G, 2001, 189-207.
7. Maeda H, Wu J, Sawa T, Matsumura Y, Hori K (2000). Tumor vascular permeability and the EPR effect in macromolecular therapeutics: a review. *Journal of Controlled Release*, 65, 271-284.
8. Jain RK (2003). Molecular regulation of vessel maturation. *Nat Med*, 9, 685-693.
9. Less JR, Skalak TC, Sevick EM, Jain RK (1991). Microvascular architecture in a mammary-carcinoma - branching patterns and vessel dimensions *Cancer Research*, 51, 265-273.

10. Neri D, Bicknell R (2005). Tumour vascular targeting. *Nature Reviews Cancer*, 5, 436-446.
11. Mikhail AS, Allen C (2009). Block copolymer micelles for delivery of cancer therapy: Transport at the whole body, tissue and cellular levels. *Journal of Controlled Release*, 138, 214-223.
12. Kirpotin DB, Drummond DC, Shao Y, Shalaby MR, Hong K, Nielsen UB, Marks JD, Benz CC, Park JW (2006). Antibody targeting of long-circulating lipidic nanoparticles does not increase tumor localization but does increase internalization in animal models. *Cancer Research*, 66, 6732-6740.
13. Pirolo KF, Chang EH (2008). Does a targeting ligand influence nanoparticle tumor localization or uptake? *Trends in Biotechnology*, 26, 552-558.
14. Maruyama K (2011). Intracellular targeting delivery of liposomal drugs to solid tumors based on EPR effects. *Advanced Drug Delivery Reviews*, 63, 161-169.
15. Andresen TL, Jensen SS, Jorgensen K (2005). Advanced strategies in liposomal cancer therapy: Problems and prospects of active and tumor specific drug release. *Progress in Lipid Research*, 44, 68-97.
16. Torchilin VP (2007). Micellar nanocarriers: Pharmaceutical perspectives. *Pharmaceutical Research*, 24, 1-16.
17. Wong HL, Bendayan R, Rauth AM, Li YQ, Wu XY (2007). Chemotherapy with anticancer drugs encapsulated in solid lipid nanoparticles. *Advanced Drug Delivery Reviews*, 59, 491-504.

18. Bummer PM (2004). Physical chemical considerations of lipid-based oral drug delivery - Solid lipid nanoparticles. *Critical Reviews in Therapeutic Drug Carrier Systems*, 21, 1-19.
19. Tong R, Cheng JJ (2007). Anticancer polymeric nanomedicines. *Polymer Reviews*, 47, 345-381.
20. Pridgen EM, Langer R, Farokhzad OC (2007). Biodegradable, polymeric nanoparticle delivery systems for cancer therapy. *Nanomedicine*, 2, 669-680.
21. Wolinsky JB, Grinstaff MW (2008). Therapeutic and diagnostic applications of dendrimers for cancer treatment. *Advanced Drug Delivery Reviews*, 60, 1037-1055.
22. Peer D, Karp JM, Hong S, Farokhzad OC, Margalit R, Langer R (2007). Nanocarriers as an emerging platform for cancer therapy. *Nature Nanotechnology*, 2, 751-760.
23. Wei A, Mehtala JG, Patri AK (2012). Challenges and opportunities in the advancement of nanomedicines. *Journal of Controlled Release*, 164, 236-246.
24. Gulati M, Grover M, Singh S, Singh M (1998). Lipophilic drug derivatives in liposomes. *International Journal of Pharmaceutics*, 165, 129-168.
25. Mayer LD, Krishna R, Webb M, Bally M (2000). Designing liposomal anticancer drug formulations for specific therapeutic applications. *Journal of Liposome Research*, 10, 99-115.
26. Kataoka K, Harada A, Nagasaki Y (2001). Block copolymer micelles for drug delivery: design, characterization and biological significance. *Advanced Drug Delivery Reviews*, 47, 113-131.

27. Moghimi SM, Hunter AC, Murray JC (2005). Nanomedicine: current status and future prospects. *Faseb Journal*, 19, 311-330.
28. Bae Y, Nishiyama N, Fukushima S, Koyama H, Yasuhiro M, Kataoka K (2005). Preparation and biological characterization of polymeric micelle drug carriers with intracellular pH-triggered drug release property: Tumor permeability, controlled subcellular drug distribution, and enhanced in vivo antitumor efficacy. *Bioconjugate Chemistry*, 16, 122-130.
29. Bae YH, Park K (2011). Targeted drug delivery to tumors: Myths, reality and possibility. *Journal of Controlled Release*, 153, 198-205.
30. Matsumura Y, Maeda H (1986). A new concept for macromolecular therapeutics in cancer-chemotherapy - mechanism of tumoritropic accumulation of proteins and the antitumor agent SMANCS *Cancer Research*, 46, 6387-6392.
31. Lammers T, Aime S, Hennink WE, Storm G, Kiessling F (2011). Theranostic Nanomedicine. *Accounts of Chemical Research*, 44, 1029-1038.
32. Janib SM, Moses AS, MacKay JA (2010). Imaging and drug delivery using theranostic nanoparticles. *Advanced Drug Delivery Reviews*, 62, 1052-1063.
33. Kherlopian AR, Song T, Duan Q, Neimark MA, Po MJ, Gohagan JK, Laine AF (2008). A review of imaging techniques for systems biology. *Bmc Systems Biology*, 2.
34. Lyons SK (2005). Advances in imaging mouse tumour models in vivo. *Journal of Pathology*, 205, 194-205.

35. Massoud TF, Gambhir SS (2003). Molecular imaging in living subjects: seeing fundamental biological processes in a new light. *Genes & Development*, 17, 545-580.
36. Weissleder R (2002). Scaling down imaging: Molecular mapping of cancer in mice. *Nature Reviews Cancer*, 2, 11-18.
37. Weissleder R (2001). A clearer vision for in vivo imaging. *Nature Biotechnology*, 19, 316-317.
38. Vooijs M, Jonkers J, Lyons S, Berns A (2002). Noninvasive imaging of spontaneous retinoblastoma pathway-dependent tumors in mice. *Cancer Research*, 62, 1862-1867.
39. Ntziachristos V, Tung CH, Bremer C, Weissleder R (2002). Fluorescence molecular tomography resolves protease activity in vivo. *Nat Med*, 8, 757-760.
40. Ntziachristos V, Weissleder R (2002). Charge-coupled-device based scanner for tomography of fluorescent near-infrared probes in turbid media. *Med Phys*, 29, 803-809.
41. Bardhan R, Lal S, Joshi A, Halas NJ (2011). Theranostic nanoshells: From probe design to imaging and treatment of cancer. *Accounts of Chemical Research*, 44, 936-946.
42. Luo SL, Zhang EL, Su YP, Cheng TM, Shi CM (2011). A review of NIR dyes in cancer targeting and imaging. *Biomaterials*, 32, 7127-7138.
43. Merian J, Gravier J, Navarro F, Texier I (2012). Fluorescent nanoprobe dedicated to *in vivo* imaging: From preclinical validations to clinical translation. *Molecules*, 17, 5564-5591.

44. Frangioni JV (2003). In vivo near-infrared fluorescence imaging. *Current Opinion in Chemical Biology*, 7, 626-634.
45. Hilderbrand SA, Weissleder R (2010). Near-infrared fluorescence: application to in vivo molecular imaging. *Current Opinion in Chemical Biology*, 14, 71-79.
46. Pham W, Medarova Z, Moore A (2005). Synthesis and application of a water-soluble near-infrared dye for cancer detection using optical imaging. *Bioconjugate Chemistry*, 16, 735-740.
47. Miyashiro I, Miyoshi N, Hiratsuka M, Kishi K, Yamada T, Ohue M, Ohigashi H, Yano M, Ishikawa O, Imaoka S (2008). Detection of sentinel node in gastric cancer surgery by indocyanine green fluorescence imaging: Comparison with infrared imaging. *Annals of Surgical Oncology*, 15, 1640-1643.
48. Ogasawara Y, Ikeda H, Takahashi M, Kawasaki K, Doihara H (2008). Evaluation of breast lymphatic pathways with indocyanine green fluorescence imaging in patients with breast cancer. *World Journal of Surgery*, 32, 1924-1929.
49. Sevick-Muraca EM, Sharma R, Rasmussen JC, Marshall MV, Wendt JA, Pham HQ, Bonefas E, Houston JP, Sampath L, Adams KE, Blanchard DK, Fisher RE, Chiang SB, Elledge R, Mawad ME (2008). Imaging of lymph flow in breast cancer patients after microdose administration of a near-infrared fluorophore: Feasibility study. *Radiology*, 246, 734-741.
50. Tagaya N, Yamazaki R, Nakagawa A, Abe A, Hamada K, Kubota K, Oyama T (2008). Intraoperative identification of sentinel lymph nodes by near-infrared fluorescence imaging in patients with breast cancer. *American Journal of Surgery*, 195, 850-853.

51. Troyan SL, Kianzad V, Gibbs-Strauss SL, Gioux S, Matsui A, Oketokoun R, Ngo L, Khamene A, Azar F, Frangioni JV (2009). The FLARE(TM) intraoperative near-infrared fluorescence imaging system: A first-in-human clinical trial in breast cancer sentinel lymph node mapping. *Annals of Surgical Oncology*, *16*, 2943-2952.
52. Sameiro M, Goncalves T (2009). Fluorescent labeling of biomolecules with organic probes. *Chemical Reviews*, *109*, 190-212.
53. Reiss P, Protiere M, Li L (2009). Core/shell semiconductor nanocrystals. *Small*, *5*, 154-168.
54. Choi HS, Nasr K, Alyabyev S, Feith D, Lee JH, Kim SH, Ashitate Y, Hyun H, Patonay G, Strekowski L, Henary M, Frangioni JV (2011). Synthesis and *in vivo* fate of zwitterionic near-infrared fluorophores. *Angewandte Chemie-International Edition*, *50*, 6258-6263.
55. Ye YP, Bloch S, Kao J, Achilefu S (2005). Multivalent carbocyanine molecular probes: Synthesis and applications. *Bioconjugate Chemistry*, *16*, 51-61.
56. Zhang ZR, Achilefu S (2004). Synthesis and evaluation of polyhydroxylated near-infrared carbocyanine molecular probes. *Organic Letters*, *6*, 2067-2070.
57. Gao XH, Cui YY, Levenson RM, Chung LWK, Nie SM (2004). *In vivo* cancer targeting and imaging with semiconductor quantum dots. *Nature Biotechnology*, *22*, 969-976.
58. Xing Y, Chaudry Q, Shen C, Kong KY, Zhau HE, Wchung L, Petros JA, O'Regan RM, Yezhelyev MV, Simons JW, Wang MD, Nie S (2007). Bioconjugated

- quantum dots for multiplexed and quantitative immunohistochemistry. *Nature Protocols*, 2, 1152-1165.
59. Hardman R (2006). A toxicologic review of quantum dots: Toxicity depends on physicochemical and environmental factors. *Environmental Health Perspectives*, 114, 165-172.
  60. Smith AM, Duan HW, Mohs AM, Nie SM (2008). Bioconjugated quantum dots for in vivo molecular and cellular imaging. *Advanced Drug Delivery Reviews*, 60, 1226-1240.
  61. Smith AM, Nie SM (2010). Semiconductor nanocrystals: Structure, properties, and band gap engineering. *Accounts of Chemical Research*, 43, 190-200.
  62. Bulte JW, Kraitchman DL (2004). Iron oxide MR contrast agents for molecular and cellular imaging. *NMR Biomed*, 17, 484-499.
  63. Christiansen C (2005). X-ray contrast media--an overview. *Toxicology*, 209, 185-187.
  64. Connor EE, Mwamuka J, Gole A, Murphy CJ, Wyatt MD (2005). Gold nanoparticles are taken up by human cells but do not cause acute cytotoxicity. *Small*, 1, 325-327.
  65. Popovtzer R, Agrawal A, Kotov NA, Popovtzer A, Balter J, Carey TE, Kopelman R (2008). Targeted gold nanoparticles enable molecular CT imaging of cancer. *Nano Letters*, 8, 4593-4596.
  66. Hainfeld JF, Slatkin DN, Focella TM, Smilowitz HM (2006). Gold nanoparticles: a new X-ray contrast agent. *Br J Radiol*, 79, 248-253.

67. Jensen JA (2007). Medical ultrasound imaging. *Prog Biophys Mol Biol*, 93, 153-165.
68. Lammers T, Kiessling F, Hennink WE, Storm G (2010). Nanotheranostics and Image-Guided Drug Delivery: Current Concepts and Future Directions. *Molecular Pharmaceutics*, 7, 1899-1912.
69. Torchilin VP (2007). Targeted pharmaceutical nanocarriers for cancer therapy and Imaging. *Aaps Journal*, 9, E128-E147.
70. Torchilin VP (2005). Recent advances with liposomes as pharmaceutical carriers. *Nature Reviews Drug Discovery*, 4, 145-160.
71. Davis ME, Chen Z, Shin DM (2008). Nanoparticle therapeutics: an emerging treatment modality for cancer. *Nature Reviews Drug Discovery*, 7, 771-782.
72. Al-Jamal WT, Kostarelos K (2011). Liposomes: from a clinically established drug delivery system to a nanoparticle platform for theranostic nanomedicine. *Acc Chem Res*, 44, 1094-1104.
73. Weng KC, Noble CO, Papahadjopoulos-Sternberg B, Chen FF, Drummond DC, Kirpotin DB, Wang D, Hom YK, Hann B, Park JW (2008). Targeted Tumor Cell Internalization and Imaging of Multifunctional Quantum Dot-Conjugated Immunoliposomes in Vitro and in Vivo. *Nano Letters*, 8, 2851-2857.
74. Li S, Goins B, Zhang L, Bao A (2012). Novel Multifunctional Theranostic Liposome Drug Delivery System: Construction, Characterization, and Multimodality MR, Near-Infrared Fluorescent, and Nuclear Imaging. *Bioconjugate Chemistry*, 23, 1322-1332.

75. Levine DH, Ghoroghchian PP, Freudenberg J, Zhang G, Therien MJ, Greene MI, Hammer DA, Murali R (2008). Polymersomes: A new multi-functional tool for cancer diagnosis and therapy. *Methods*, 46, 25-32.
76. Sanson C, Diou O, Thévenot J, Ibarboure E, Soum A, Brûlet A, Miraux S, Thiaudière E, Tan S, Brisson A, Dupuis V, Sandre O, Lecommandoux Sb (2011). Doxorubicin loaded magnetic polymersomes: Theranostic nanocarriers for MR imaging and magneto-chemotherapy. *Acs Nano*, 5, 1122-1140.
77. Abeylath SC, Ganta S, Iyer AK, Amiji M (2011). Combinatorial-designed multifunctional polymeric nanosystems for tumor-targeted therapeutic delivery. *Accounts of Chemical Research*, 44, 1009-1017.
78. Maeng JH, Lee D-H, Jung KH, Bae Y-H, Park I-S, Jeong S, Jeon Y-S, Shim C-K, Kim W, Kim J, Lee J, Lee Y-M, Kim J-H, Kim W-H, Hong S-S (2010). Multifunctional doxorubicin loaded superparamagnetic iron oxide nanoparticles for chemotherapy and magnetic resonance imaging in liver cancer. *Biomaterials*, 31, 4995-5006.
79. Caldorera-Moore ME, Liechty WB, Peppas NA (2011). Responsive theranostic systems: Integration of diagnostic imaging agents and responsive controlled release drug delivery carriers. *Accounts of Chemical Research*, 44, 1061-1070.
80. Liu J, Lee H, Allen C (2006). Formulation of drugs in block copolymer micelles: Drug loading and release. *Current Pharmaceutical Design*, 12, 4685-4701.
81. Kwon GS, Okano T (1996). Polymeric micelles as new drug carriers. *Advanced Drug Delivery Reviews*, 21, 107-116.

82. Lai JR, Chang YW, Yen HC, Yuan NY, Liao MY, Hsu CY, Tsai JL, Lai PS (2010). Multifunctional doxorubicin/superparamagnetic iron oxide-encapsulated Pluronic F127 micelles used for chemotherapy/magnetic resonance imaging. *Journal of Applied Physics*, 107.
83. Li XJ, Qian YF, Liu T, Hu XL, Zhang GY, You YZ, Liu SY (2011). Amphiphilic multiarm star block copolymer-based multifunctional unimolecular micelles for cancer targeted drug delivery and MR imaging. *Biomaterials*, 32, 6595-6605.
84. Xie J, Lee S, Chen XY (2010). Nanoparticle-based theranostic agents. *Advanced Drug Delivery Reviews*, 62, 1064-1079.
85. Chouly C, Pouliquen D, Lucet I, Jeune JJ, Jallet P (1996). Development of superparamagnetic nanoparticles for MRI: Effect of particle size, charge and surface nature on biodistribution. *Journal of Microencapsulation*, 13, 245-255.
86. Duguet E, Vasseur S, Mornet S, Devoisselle JM (2006). Magnetic nanoparticles and their applications in medicine. *Nanomedicine*, 1, 157-168.
87. Grancharov SG, Zeng H, Sun S, Wang SX, O'Brien S, Murray CB, Kirtley JR, Held GA (2005). Bio-functionalization of monodisperse magnetic nanoparticles and their use as biomolecular labels in a magnetic tunnel junction based sensor. *J Phys Chem B*, 109, 13030-13035.
88. Ito A, Shinkai M, Honda H, Kobayashi T (2005). Medical application of functionalized magnetic nanoparticles. *Journal of Bioscience and Bioengineering*, 100, 1-11.

89. Mornet S, Vasseur S, Grasset F, Duguet E (2004). Magnetic nanoparticle design for medical diagnosis and therapy. *Journal of Materials Chemistry*, *14*, 2161-2175.
90. Kohler N, Fryxell GE, Zhang MQ (2004). A bifunctional poly(ethylene glycol) silane immobilized on metallic oxide-based nanoparticles for conjugation with cell targeting agents. *Journal of the American Chemical Society*, *126*, 7206-7211.
91. Kohler N, Sun C, Fichtenholtz A, Gunn J, Fang C, Zhang MQ (2006). Methotrexate-immobilized poly(ethylene glycol) magnetic nanoparticles for MR imaging and drug delivery. *Small*, *2*, 785-792.
92. Kohler N, Sun C, Wang J, Zhang MQ (2005). Methotrexate-modified superparamagnetic nanoparticles and their intracellular uptake into human cancer cells. *Langmuir*, *21*, 8858-8864.
93. Jain TK, Richey J, Strand M, Leslie-Pelecky DL, Flask CA, Labhasetwar V (2008). Magnetic nanoparticles with dual functional properties: Drug delivery and magnetic resonance imaging. *Biomaterials*, *29*, 4012-4021.
94. Xie J, Chen K, Huang J, Lee S, Wang JH, Gao J, Li XG, Chen XY (2010). PET/NIRF/MRI triple functional iron oxide nanoparticles. *Biomaterials*, *31*, 3016-3022.
95. Yu CC, Wang JJ, Lee CL, Lee SH, Pan TM (2008). Safety and mutagenicity evaluation of nanoparticulate red mold rice. *Journal of Agricultural and Food Chemistry*, *56*, 11038-11048.
96. Piao Y, Kim J, Bin Na H, Kim D, Baek JS, Ko MK, Lee JH, Shokouhimehr M, Hyeon T (2008). Wrap-bake-peel process for nanostructural transformation from

- beta-FeOOH nanorods to biocompatible iron oxide nanocapsules. *Nature Materials*, 7, 242-247.
97. Bailey RE, Smith AM, Nie SM (2004). Quantum dots in biology and medicine. *Physica E-Low-Dimensional Systems & Nanostructures*, 25, 1-12.
98. Kim SW, Zimmer JP, Ohnishi S, Tracy JB, Frangioni JV, Bawendi MG (2005). Engineering InAs<sub>x</sub>P<sub>1-x</sub>/InP/ZnSe III-V alloyed core/shell quantum dots for the near-infrared. *Journal of the American Chemical Society*, 127, 10526-10532.
99. Xie RG, Chen K, Chen XY, Peng XG (2008). InAs/InP/ZnSe Core/Shell/Shell quantum dots as near-infrared emitters: Bright, narrow-band, non-cadmium containing, and biocompatible. *Nano Research*, 1, 457-464.
100. Zimmer JP, Kim SW, Ohnishi S, Tanaka E, Frangioni JV, Bawendi MG (2006). Size series of small indium arsenide-zinc selenide core-shell nanocrystals and their application to in vivo imaging. *Journal of the American Chemical Society*, 128, 2526-2527.
101. Dixit V, Van den Bossche J, Sherman DM, Thompson DH, Andres RP (2006). Synthesis and grafting of thioctic acid-PEG-folate conjugates onto Au nanoparticles for selective targeting of folate receptor-positive tumor cells. *Bioconjugate Chemistry*, 17, 603-609.
102. Oyelere AK, Chen PC, Huang XH, El-Sayed IH, El-Sayed MA (2007). Peptide-conjugated gold nanorods for nuclear targeting. *Bioconjugate Chemistry*, 18, 1490-1497.

103. Ow H, Larson DR, Srivastava M, Baird BA, Webb WW, Wiesner U (2005). Bright and stable core-shell fluorescent silica nanoparticles. *Nano Letters*, 5, 113-117.
104. Roy I, Ohulchanskyy TY, Pudavar HE, Bergey EJ, Oseroff AR, Morgan J, Dougherty TJ, Prasad PN (2003). Ceramic-based nanoparticles entrapping water-insoluble photosensitizing anticancer drugs: A novel drug-carrier system for photodynamic therapy. *Journal of the American Chemical Society*, 125, 7860-7865.
105. Kang K, Choi J, Nam JH, Lee SC, Kim KJ, Lee SW, Chang JH (2009). Preparation and characterization of chemically functionalized silica-coated magnetic nanoparticles as a DNA separator. *Journal of Physical Chemistry B*, 113, 536-543.
106. Wang CG, Chen Y, Wang TT, Ma ZF, Su ZM (2008). Monodispersed gold nanorod-embedded silica particles as novel raman labels for biosensing. *Advanced Functional Materials*, 18, 355-361.
107. Wolcott A, Gerion D, Visconte M, Sun J, Schwartzberg A, Chen SW, Zhang JZ (2006). Silica-coated CdTe quantum dots functionalized with thiols for bioconjugation to IgG proteins. *Journal of Physical Chemistry B*, 110, 5779-5789.
108. Slowing II, Vivero-Escoto JL, Wu CW, Lin VSY (2008). Mesoporous silica nanoparticles as controlled release drug delivery and gene transfection carriers. *Advanced Drug Delivery Reviews*, 60, 1278-1288.

109. Park JH, Gu L, von Maltzahn G, Ruoslahti E, Bhatia SN, Sailor MJ (2009). Biodegradable luminescent porous silicon nanoparticles for in vivo applications. *Nature Materials*, 8, 331-336.
110. Pan BF, Cui DX, Sheng Y, Ozkan CG, Gao F, He R, Li Q, Xu P, Huang T (2007). Dendrimer-modified magnetic nanoparticles enhance efficiency of gene delivery system. *Cancer Research*, 67, 8156-8163.
111. Majoros IJ, Myc A, Thomas T, Mehta CB, Baker JR (2006). PAMAM dendrimer-based multifunctional conjugate for cancer therapy: Synthesis, characterization, and functionality. *Biomacromolecules*, 7, 572-579.
112. Majoros IJ, Thomas TP, Mehta CB, Baker JR (2005). Poly(amidoamine) dendrimer-based multifunctional engineered nanodevice for cancer therapy. *Journal of Medicinal Chemistry*, 48, 5892-5899.
113. Ornelas C, Pennell R, Liebes LF, Weck M (2011). Construction of a well-defined multifunctional dendrimer for theranostics. *Organic Letters*, 13, 976-979.
114. Balasubramanian K, Burghard M (2006). Biosensors based on carbon nanotubes. *Analytical and Bioanalytical Chemistry*, 385, 452-468.
115. Dhar S, Liu Z, Thomale J, Dai HJ, Lippard SJ (2008). Targeted single-wall carbon nanotube-mediated Pt(IV) prodrug delivery using folate as a homing device. *Journal of the American Chemical Society*, 130, 11467-11476.
116. Liu Z, Tabakman SM, Chen Z, Dai HJ (2009). Preparation of carbon nanotube bioconjugates for biomedical applications. *Nature Protocols*, 4, 1372-1382.

117. Lu YJ, Wei KC, Ma CCM, Yang SY, Chen JP (2012). Dual targeted delivery of doxorubicin to cancer cells using folate-conjugated magnetic multi-walled carbon nanotubes. *Colloids and Surfaces B-Biointerfaces*, 89, 1-9.
118. Kam NWS, O'Connell M, Wisdom JA, Dai HJ (2005). Carbon nanotubes as multifunctional biological transporters and near-infrared agents for selective cancer cell destruction. *Proceedings of the National Academy of Sciences of the United States of America*, 102, 11600-11605.
119. Schipper ML, Nakayama-Ratchford N, Davis CR, Kam NWS, Chu P, Liu Z, Sun XM, Dai HJ, Gambhir SS (2008). A pilot toxicology study of single-walled carbon nanotubes in a small sample of mice. *Nature Nanotechnology*, 3, 216-221.
120. Zhou FF, Wu S, Song S, Chen WR, Resasco DE, Xing D (2012). Antitumor immunologically modified carbon nanotubes for photothermal therapy. *Biomaterials*, 33, 3235-3242.
121. Duncan R, Gaspar R (2011). Nanomedicine(s) under the microscope. *Molecular Pharmaceutics*, 8, 2101-2141.
122. Shegokar R, Müller RH (2010). Nanocrystals: Industrially feasible multifunctional formulation technology for poorly soluble actives. *International Journal of Pharmaceutics*, 399, 129-139.
123. Müller RH, Jacobs C, Kayser O (2001). Nanosuspensions as particulate drug formulations in therapy Rationale for development and what we can expect for the future. *Advanced Drug Delivery Reviews*, 47, 3-19.
124. Müller RH, Moschwitz J, Bushrab FN, Manufacturing of nanoparticles by milling and homogenization techniques., In *Nanoparticle Technology for Drug*

- Delivery, Drugs, and Pharmaceutical Sciences*, eds. Gupta, RB, Kompella, UB, Taylor & Francis Group, LLC, New York, 2006, 21-51.
125. Chan HK, Kwok PCL (2011). Production methods for nanodrug particles using the bottom-up approach. *Advanced Drug Delivery Reviews*, 63, 406-416.
  126. Rabinow BE (2004). Nanosuspensions in drug delivery. *Nature Reviews Drug Discovery*, 3, 785-796.
  127. Liversidge GG, Cundy KC, Bishop JF, Czekai DA. Surface modified drug nanoparticles. US Patent 5,145,684. 1991.
  128. Junghanns J, Müller RH (2008). Nanocrystal technology, drug delivery and clinical applications. *International Journal of Nanomedicine*, 3, 295-309.
  129. Merisko-Liversidge E, Liversidge GG, Cooper ER (2003). Nanosizing: a formulation approach for poorly-water-soluble compounds. *European Journal of Pharmaceutical Sciences*, 18, 113-120.
  130. Haynes DH. Phospholipid-coated microcrystals: injectable formulations of water insoluble drugs. US Patent 5,091,187. 1992.
  131. Keck CM, Müller RH (2006). Drug nanocrystals of poorly soluble drugs produced by high pressure homogenisation. *European Journal of Pharmaceutics and Biopharmaceutics*, 62, 3-16.
  132. Müller RH, Becker R, Kruss KP, Peters K. Pharmaceutical nanosuspensions for medicament administration as systems with increased saturation solubility and rate of solution. US Patent 5,858,410. 1999.

133. Illig KJ, Mueller RL, Ostrander KD, Swanson JR (1996). Use of microfluidizer processing for preparation of pharmaceutical suspensions. *Pharmaceutical Technology*, 20, 78-88.
134. Patravale VB, Date AA, Kulkarni RM (2004). Nanosuspensions: a promising drug delivery strategy. *Journal of Pharmacy and Pharmacology*, 56, 827-840.
135. Begat P, Young PM, Edge S, Kaerger JS, Price R (2003). The effect of mechanical processing on surface stability of pharmaceutical powders: Visualization by atomic force microscopy. *Journal of Pharmaceutical Sciences*, 92, 611-620.
136. Panagiotou T, Fisher RJ (2008). Form nanoparticles via controlled crystallization. *Chemical Engineering Progress*, 104, 33-39.
137. Becker R, Döring W (1935). Kinetische behandlung der keimbildung in übersättigten dämpfen. *Annals of Physics*, 24, 719-752.
138. Kashchiev D, van Rosmalen GM (2003). Review: Nucleation in solutions revisited. *Crystal Research and Technology*, 38, 555-574.
139. Volmer M, *Kinetik der phasenbildung*, Steinkopf. Dresden, 1939.
140. Horn D, Rieger J (2001). Organic nanoparticles in the aqueous phase - theory, experiment, and use. *Angewandte Chemie-International Edition*, 40, 4331-4361.
141. Oxtoby DW (1998). Nucleation of first-order phase transitions. *Accounts of Chemical Research*, 31, 91-97.
142. Dirksen JA, Ring TA (1991). Fundamentals of crystallization - kinetic effects on particle-size distributions and morphology. *Chemical Engineering Science*, 46, 2389-2427.

143. Chen JF, Wang YH, Guo F, Wang XM, Zheng C (2000). Synthesis of nanoparticles with novel technology: High-gravity reactive precipitation. *Industrial & Engineering Chemistry Research*, 39, 948-954.
144. Hu TT, Wang JX, Shen ZG, Chen JF (2008). Engineering of drug nanoparticles by HGCP for pharmaceutical applications. *Particuology*, 6, 239-251.
145. Panagiotou T, Mesite SV, Fisher RJ (2009). Production of norfloxacin nanosuspensions using microfluidics reaction technology through solvent/antisolvent crystallization. *Industrial & Engineering Chemistry Research*, 48, 1761-1771.
146. Byrappa K, Ohara S, Adschiri T (2008). Nanoparticles synthesis using supercritical fluid technology - towards biomedical applications. *Advanced Drug Delivery Reviews*, 60, 299-327.
147. Luque de Castro MD, Priego-Capote F (2007). Ultrasound-assisted crystallization (sonocrystallization). *Ultrasonics Sonochemistry*, 14, 717-724.
148. List M, Sucker H. Pharmaceutical colloidal hydrosols for injection. GB Patent 2,200,048. 1988.
149. Gassmann P, Sucker H. Improvements in pharmaceutical compositions. WO 018105. 1992.
150. List M, Sucker H. Hydrosols of pharmacologically active agents and their pharmaceutical compositions comprising them. US Patent 5,389,382. 1995.
151. Gassmann PS, H. Pharmaceutical compositions comprised of stabilized peptide particles. US Patent 6,447,806. 2002.

152. Zhong J, Shen ZG, Yang Y, Chen JF (2005). Preparation and characterization of uniform nanosized cephadrine by combination of reactive precipitation and liquid anti-solvent precipitation under high gravity environment. *International Journal of Pharmaceutics*, 301, 286-293.
153. Zhao H, Wang JX, Wang QA, Chen JF, Yun J (2007). Controlled liquid antisolvent precipitation of hydrophobic pharmaceutical nanoparticles in a microchannel reactor. *Industrial & Engineering Chemistry Research*, 46, 8229-8235.
154. Chiou H, Li L, Hu TT, Chan HK, Chen JF, Yun J (2007). Production of salbutamol sulfate for inhalation by high-gravity controlled antisolvent precipitation. *International Journal of Pharmaceutics*, 331, 93-98.
155. Hu T, Chiou H, Chan HK, Chen JF, Yun J (2008). Preparation of inhalable salbutamol sulphate using reactive high gravity controlled precipitation. *Journal of Pharmaceutical Sciences*, 97, 944-949.
156. Chiou H, Chan HK, Heng D, Prud'homme RK, Raper JA (2008). A novel production method for inhalable cyclosporine A powders by confined liquid impinging jet precipitation. *Journal of Aerosol Science*, 39, 500-509.
157. Chiou H, Chan HK, Prud'homme RK, Raper JA (2008). Evaluation on the use of confined liquid impinging jets for the synthesis of nanodrug particles. *Drug Development and Industrial Pharmacy*, 34, 59-64.
158. Kumar V, Adamson DH, Prud'homme RK (2010). Fluorescent Polymeric Nanoparticles: Aggregation and Phase Behavior of Pyrene and Amphotericin B Molecules in Nanoparticle Cores. *Small*, 6, 2907-2914.

159. Rogers TL, Johnston KP, Williams RO (2001). Solution-based particle formation of pharmaceutical powders by supercritical or compressed fluid CO<sub>2</sub> and cryogenic spray-freezing technologies. *Drug Development and Industrial Pharmacy*, 27, 1003-1015.
160. Reverchon E, De Marco I, Torino E (2007). Nanoparticles production by supercritical antisolvent precipitation: A general interpretation. *Journal of Supercritical Fluids*, 43, 126-138.
161. Bustami RT, Chan HK, Dehghani F, Foster NR (2000). Generation of micro-particles of proteins for aerosol delivery using high pressure modified carbon dioxide. *Pharmaceutical Research*, 17, 1360-1366.
162. Lancaster RW, Singh H, Theophilus AL. Apparatus and process for preparing crystalline particles. WO 0038811. 2000.
163. Abbas A, Srour M, Tang P, Chiouc H, Chan HK, Romagnoli JA (2007). Sonocrystallisation of sodium chloride particles for inhalation. *Chemical Engineering Science*, 62, 2445-2453.
164. Dhumal RS, Biradar SV, Paradkar AR, York P (2009). Particle engineering using sonocrystallization: Salbutamol sulphate for pulmonary delivery. *International Journal of Pharmaceutics*, 368, 129-137.
165. Kaerger JS, Price R (2004). Processing of spherical crystalline particles via a novel solution atomization and crystallization by sonication (SAXS) technique. *Pharmaceutical Research*, 21, 372-381.
166. Dhumal RS, Biradar SV, Yamamura S, Paradkar AR, York P (2008). Preparation of amorphous cefuroxime axetil nanoparticles by sonoprecipitation for

- enhancement of bioavailability. *European Journal of Pharmaceutics and Biopharmaceutics*, 70, 109-115.
167. Kipp JE, Wong JCT, Doty MJ, Rebbeck CL. Microprecipitation method for preparing submicron suspensions. US Patent 6,869,617. 2001.
168. Zhang H, Hollis CP, Zhang Q, Li TL (2011). Preparation and antitumor study of camptothecin nanocrystals. *International Journal of Pharmaceutics*, 415, 293-300.
169. Zhao RS, Hollis CP, Zhang H, Sun LL, Gemeinhart RA, Li TL (2011). Hybrid nanocrystals: achieving concurrent therapeutic and bioimaging functionalities toward solid tumors. *Molecular Pharmaceutics*, 8, 1985-1991.
170. Van Eerdenbrugh B, Van den Mooter G, Augustijns P (2008). Top-down production of drug nanocrystals: Nanosuspension stabilization, miniaturization and transformation into solid products. *International Journal of Pharmaceutics*, 364, 64-75.
171. Kocbek P, Baumgartner S, Kristl J (2006). Preparation and evaluation of nanosuspensions for enhancing the dissolution of poorly soluble drugs. *International Journal of Pharmaceutics*, 312, 179-186.
172. Lee J, Lee SJ, Choi JY, Yoo JY, Ahn CH (2005). Amphiphilic amino acid copolymers as stabilizers for the preparation of nanocrystal dispersion. *European Journal of Pharmaceutical Sciences*, 24, 441-449.
173. Deng Z, Xu S, Li S (2008). Understanding a relaxation behavior in a nanoparticle suspension for drug delivery applications. *International Journal of Pharmaceutics*, 351, 236-243.

174. Gao L, Zhang DR, Chen MH, Zheng TT, Wang SM (2007). Preparation and characterization of an oridonin nanosuspension for solubility and dissolution velocity enhancement. *Drug Development and Industrial Pharmacy*, 33, 1332-1339.
175. Van Eerdenbrugh B, Vermant J, Martens JA, Froyen L, Van Humbeeck J, Augustijns P, Van Den Mooter G (2009). A screening study of surface stabilization during the production of drug nanocrystals. *Journal of Pharmaceutical Sciences*, 98, 2091-2103.
176. Kesisoglou F, Panmai S, Wu YH (2007). Nanosizing - Oral formulation development and biopharmaceutical evaluation. *Advanced Drug Delivery Reviews*, 59, 631-644.
177. Na GC, Stevens HJ, Yuan BO, Rajagopalan N (1999). Physical stability of ethyl diatrizoate nanocrystalline suspension in steam sterilization. *Pharmaceutical Research*, 16, 569-574.
178. Zheng JY, Bosch HW (1997). Sterile filtration of NanoCrystal(TM) drug formulations. *Drug Development and Industrial Pharmacy*, 23, 1087-1093.
179. Wu LB, Zhang J, Watanabe W (2011). Physical and chemical stability of drug nanoparticles. *Advanced Drug Delivery Reviews*, 63, 456-469.
180. Malvern Instruments Limited (2011). Dynamic light scattering - common terms defined. [http://www.biophysics.bioc.cam.ac.uk/wp-content/uploads/2011/02/DLS\\_Terms\\_defined\\_Malvern.pdf](http://www.biophysics.bioc.cam.ac.uk/wp-content/uploads/2011/02/DLS_Terms_defined_Malvern.pdf) (last accessed March 29, 2013).

181. Matsuyama T, Yamamoto H (2004). Particle shape and laser diffraction: A discussion of the particle shape problem. *Journal of Dispersion Science and Technology*, 25, 409-416.
182. Muhlenweg H, Hirleman ED (1998). Laser diffraction spectroscopy: Influence of particle shape and a shape adaptation technique. *Particle & Particle Systems Characterization*, 15, 163-169.
183. Endoh S, Kuga Y, Ohya H, Ikeda C, Iwata H (1998). Shape estimation of anisometric particles using size measurement techniques. *Particle & Particle Systems Characterization*, 15, 145-149.
184. Stevens N, Shrimpton J, Palmer M, Prime D, Johal B (2007). Accuracy assessments for laser diffraction measurements of pharmaceutical lactose. *Measurement Science & Technology*, 18, 3697-3706.
185. Buckton G, *Interfacial Phenomena in Drug Delivery and Targeting*, Harwood Academic Publishers. Switzerland, 1995, 133-134.
186. Jacobs C, Müller RH (2002). Production and characterization of a budesonide nanosuspension for pulmonary administration. *Pharmaceutical Research*, 19, 189-194.
187. Chung TH, Wu SH, Yao M, Lu CW, Lin YS, Hung Y, Mou CY, Chen YC, Huang DM (2007). The effect of surface charge on the uptake and biological function of mesoporous silica nanoparticles 3T3-L1 cells and human mesenchymal stem cells. *Biomaterials*, 28, 2959-2966.

188. Harush-Frenkel O, Rozentur E, Benita S, Altschuler Y (2008). Surface charge of nanoparticles determines their endocytic and transcytotic pathway in polarized MDCK cells. *Biomacromolecules*, 9, 435-443.
189. He CB, Hu YP, Yin LC, Tang C, Yin CH (2010). Effects of particle size and surface charge on cellular uptake and biodistribution of polymeric nanoparticles. *Biomaterials*, 31, 3657-3666.
190. Juliano RL, Stamp D (1975). Effect of particle-size and charge on clearance rates of liposomes and liposome encapsulated drugs. *Biochemical and Biophysical Research Communications*, 63, 651-658.
191. Xiao K, Li YP, Luo JT, Lee JS, Xiao WW, Gonik AM, Agarwal RG, Lam KS (2011). The effect of surface charge on *in vivo* biodistribution of PEG-oligocholeic acid based micellar nanoparticles. *Biomaterials*, 32, 3435-3446.
192. Dobrovolskaia MA, Aggarwal P, Hall JB, McNeil SE (2008). Preclinical studies to understand nanoparticle interaction with the immune system and its potential effects on nanoparticle biodistribution. *Molecular Pharmaceutics*, 5, 487-495.
193. Sharma P, Zujovic ZD, Bowmaker GA, Denny WA, Garg S (2011). Evaluation of a crystalline nanosuspension: Polymorphism, process induced transformation and *in vivo* studies. *International Journal of Pharmaceutics*, 408, 138-151.
194. Van Eerdenbrugh B, Vermant J, Martens JA, Froyen L, Van Humbeeck J, Van den Montre G, Augustijns P (2010). Solubility increases associated with crystalline drug nanoparticles: Methodologies and significance. *Molecular Pharmaceutics*, 7, 1858-1870.

195. Martin A, *Physical Pharmacy*, Lippincott Williams & Wilkins. Baltimore, MA, 1993.
196. Liu JH, Li L (2005). SDS-aided immobilization and controlled release of camptothecin from agarose hydrogel. *European Journal of Pharmaceutical Sciences*, 25, 237-244.
197. Cremasco MA, Wang LNH (2012). Estimation of partition, free and specific diffusion coefficients of paclitaxel and taxanes in a fixed bed by moment analysis: experimental, modeling and simulation studies. *Acta Scientiarum-Technology*, 34, 33-40.
198. Gardner CR, Walsh CT, Almarsson O (2004). Drugs as materials: Valuing physical form in drug discovery. *Nature Reviews Drug Discovery*, 3, 926-934.
199. Lipinski CA (2000). Drug-like properties and the causes of poor solubility and poor permeability. *Journal of Pharmacological and Toxicological Methods*, 44, 235-249.
200. Lipinski CA, Lombardo F, Dominy BW, Feeney PJ (1997). Experimental and computational approaches to estimate solubility and permeability in drug discovery and development settings. *Advanced Drug Delivery Reviews*, 23, 3-25.
201. MeriskoLiversidge E, Sarpotdar P, Bruno J, Hajj S, Wei L, Peltier N, Rake J, Shaw JM, Pugh S, Polin L, Jones J, Corbett T, Cooper E, Liversidge GG (1996). Formulation and antitumor activity evaluation of nanocrystalline suspensions of poorly soluble anticancer drugs. *Pharmaceutical Research*, 13, 272-278.

202. Liu F, Park JY, Zhang Y, Conwell C, Liu Y, Bathula SR, Huang L (2010). Targeted Cancer Therapy With Novel High Drug-Loading Nanocrystals. *Journal of Pharmaceutical Sciences*, 99, 3542-3551.
203. De Jong WH, Borm PJA (2008). Drug delivery and nanoparticles: Applications and hazards. *International Journal of Nanomedicine*, 3, 133-149.
204. Ganta S, Paxton JW, Baguley BC, Garg S (2009). Formulation and pharmacokinetic evaluation of an asulacrine nanocrystalline suspension for intravenous delivery. *International Journal of Pharmaceutics*, 367, 179-186.
205. Deng JX, Huang L, Liu F (2010). Understanding the structure and stability of paclitaxel nanocrystals. *International Journal of Pharmaceutics*, 390, 242-249.
206. Gao L, Zhang DR, Chen MH, Duan CX, Dai WT, Jia LJ, Zhao WF (2008). Studies on pharmacokinetics and tissue distribution of oridonin nanosuspensions. *International Journal of Pharmaceutics*, 355, 321-327.
207. Zhang Z, Zhang XM, Xue W, YangYang YN, Xu DR, Zhao YX, Lou HY (2010). Effects of oridonin nanosuspension on cell proliferation and apoptosis of human prostatic carcinoma PC-3 cell line. *International Journal of Nanomedicine*, 5, 735-742.
208. Wang YC, Liu ZP, Zhang DR, Gao XH, Zhang XY, Duan CX, Jia LJ, Feng FF, Huang YJ, Shen YM, Zhang QA (2011). Development and *in vitro* evaluation of deacety mycoepoxydiene nanosuspension. *Colloids and Surfaces B-Biointerfaces*, 83, 189-197.

209. Gao L, Liu GY, Wang XQ, Liu F, Xu YF, Ma J (2011). Preparation of a chemically stable quercetin formulation using nanosuspension technology. *International Journal of Pharmaceutics*, 404, 231-237.
210. Pattekari P, Zheng Z, Zhang X, Levchenko T, Torchilin V, Lvov Y (2011). Top-down and bottom-up approaches in production of aqueous nanocolloids of low solubility drug paclitaxel. *Physical Chemistry Chemical Physics*, 13, 9014-9019.
211. Rejman J, Oberle V, Zuhorn IS, Hoekstra D (2004). Size-dependent internalization of particles via the pathways of clathrin- and caveolae-mediated endocytosis. *Biochemical Journal*, 377, 159-169.
212. Zuhorn IS, Kalicharan R, Hoekstra D (2002). Lipoplex-mediated transfection of mammalian cells occurs through the cholesterol-dependent clathrin-mediated pathway of endocytosis. *Journal of Biological Chemistry*, 277, 18021-18028.
213. Yu X, Valmikinathan CM, Rogers A, Wang J, Nanotechnology and drug delivery, In *Biomedical Nanostructures*, eds. Gonsalves, KE, Halberstadt, CR, Laurencin, CT, Wiley-Interscience, Hoboken, NJ, 2007, 93-113.
214. Moghimi SM, Hunter AC, Murray JC (2001). Long-circulating and target-specific nanoparticles: Theory to practice. *Pharmacological Reviews*, 53, 283-318.
215. Shenoy D, Little S, Langer R, Amiji M (2005). Poly(ethylene oxide)-modified poly(beta-amino ester) nanoparticles as a pH-sensitive system for tumor-targeted delivery of hydrophobic drugs: Part 2. In vivo distribution and tumor localization studies. *Pharmaceutical Research*, 22, 2107-2114.

216. Barbe C, Bartlett J, Kong LG, Finnie K, Lin HQ, Larkin M, Calleja S, Bush A, Calleja G (2004). Silica particles: A novel drug-delivery system. *Advanced Materials*, 16, 1959-1966.
217. Alexis F, Pridgen E, Molnar LK, Farokhzad OC (2008). Factors affecting the clearance and biodistribution of polymeric nanoparticles. *Molecular Pharmaceutics*, 5, 505-515.
218. Li SD, Huang L (2008). Pharmacokinetics and biodistribution of nanoparticles. *Molecular Pharmaceutics*, 5, 496-504.
219. Wang YL, Li XM, Wang LY, Xu YL, Cheng XD, Wei P (2011). Formulation and pharmacokinetic evaluation of a paclitaxel nanosuspension for intravenous delivery. *International Journal of Nanomedicine*, 6, 1497-1507.
220. Hashizume H, Baluk P, Morikawa S, McLean JW, Thurston G, Roberge S, Jain RK, McDonald DM (2000). Openings between defective endothelial cells explain tumor vessel leakiness. *American Journal of Pathology*, 156, 1363-1380.
221. Hobbs SK, Monsky WL, Yuan F, Roberts WG, Griffith L, Torchilin VP, Jain RK (1998). Regulation of transport pathways in tumor vessels: Role of tumor type and microenvironment. *Proceedings of the National Academy of Sciences of the United States of America*, 95, 4607-4612.
222. Daldrup H, Shames DM, Wendland M, Okuhata Y, Link TM, Rosenau W, Lu Y, Brasch RC (1998). Correlation of dynamic contrast-enhanced MR imaging with histologic tumor grade: Comparison of macromolecular and small-molecular contrast media. *American Journal of Roentgenology*, 171, 941-949.

223. Fadeel B, Garcia-Bennett AE (2010). Better safe than sorry: Understanding the toxicological properties of inorganic nanoparticles manufactured for biomedical applications. *Advanced Drug Delivery Reviews*, 62, 362-374.
224. Tevaarwerk AJ, Holen KD, Alberti DB, Sidor C, Arnott J, Quon C, Wilding G, Liu G (2009). Phase I trial of 2-methoxyestradiol nanocrystal dispersion in advanced solid malignancies. *Clinical Cancer Research*, 15, 1460-1465.
225. Harrison MR, Hahn NM, Pili R, Oh WK, Hammers H, Sweeney C, Kim K, Perlman S, Arnott J, Sidor C, Wilding G, Liu G (2011). A phase II study of 2-methoxyestradiol (2ME2) NanoCrystalA (R) dispersion (NCD) in patients with taxane-refractory, metastatic castrate-resistant prostate cancer (CRPC). *Investigational New Drugs*, 29, 1465-1474.
226. Phair RD, Misteli T (2001). Kinetic modelling approaches to in vivo imaging. *Nature Reviews Molecular Cell Biology*, 2, 898-907.
227. Montet X, Ntziachristos V, Grimm J, Weissleder R (2005). Tomographic fluorescence mapping of tumor targets. *Cancer Research*, 65, 6330-6336.
228. Koo AN, Min KH, Lee HJ, Lee S-U, Kim K, Kwon IC, Cho SH, Jeong SY, Lee SC (2012). Tumor accumulation and antitumor efficacy of docetaxel-loaded core-shell-corona micelles with shell-specific redox-responsive cross-links. *Biomaterials*, 33, 1489-1499.
229. Lee BS, Park K, Park S, Kim GC, Kim HJ, Lee S, Kil H, Oh SJ, Chi DY, Kim K, Choi K, Kwon IC, Kim SY (2010). Tumor targeting efficiency of bare nanoparticles does not mean the efficacy of loaded anticancer drugs: Importance of radionuclide imaging for optimization of highly selective tumor targeting

- polymeric nanoparticles with or without drug. *Journal of Controlled Release*, 147, 253-260.
230. Lee M-S, Kim YH, Kim YJ, Kwon S-H, Bang J-K, Lee S-M, Song YS, Hahm D-H, Shim I, Han D, Her S (2011). Pharmacokinetics and Biodistribution of Human Serum Albumin-TIMP-2 Fusion Protein Using Near-Infrared Optical Imaging. *Journal of Pharmacy and Pharmaceutical Sciences*, 14, 368-377.
231. Li C, Xia JA, Wei XB, Yan HH, Si Z, Ju SH (2010). pH-Activated Near-Infrared Fluorescence Nanoprobe Imaging Tumors by Sensing the Acidic Microenvironment. *Advanced Functional Materials*, 20, 2222-2230.
232. Min KH, Lee HJ, Kim K, Kwon IC, Jeong SY, Lee SC (2012). The tumor accumulation and therapeutic efficacy of doxorubicin carried in calcium phosphate-reinforced polymer nanoparticles. *Biomaterials*, 33, 5788-5797.
233. Na JH, Koo H, Lee S, Min KH, Park K, Yoo H, Lee SH, Park JH, Kwon IC, Jeong SY, Kim K (2011). Real-time and non-invasive optical imaging of tumor-targeting glycol chitosan nanoparticles in various tumor models. *Biomaterials*, 32, 5252-5261.
234. Vasquez KO, Casavant C, Peterson JD (2011). Quantitative whole body biodistribution of fluorescent-labeled agents by non-invasive tomographic imaging. *Plos One*, 6.
235. Kahr B, Gurney RW (2001). Dyeing crystals. *Chemical Reviews*, 101, 893-951.
236. Hajek R, Vorlicek J, Slavik M (1996). Paclitaxel (Taxol<sup>®</sup>): A review of its antitumor activity in clinical studies - Minireview. *Neoplasma*, 43, 141-154.

237. ten Tije AJ, Verweij J, Loos WJ, Sparreboom A (2003). Pharmacological effects of formulation vehicles - Implications for cancer chemotherapy. *Clinical Pharmacokinetics*, 42, 665-685.
238. Ibrahim NK, Desai N, Legha S, Soon-Shiong P, Theriault RL, Rivera E, Esmali B, Ring SE, Bedikian A, Hortobagyi GN, Ellerhorst JA (2002). Phase I and pharmacokinetic study of ABI-007, a cremophor-free, protein-stabilized, nanoparticle formulation of paclitaxel. *Clinical Cancer Research*, 8, 1038-1044.
239. Hennenfent KL, Govindan R (2006). Novel formulations of taxanes: a review. Old wine in a new bottle? *Annals of Oncology*, 17, 735-749.
240. Center for Drug Policy at the University of Wisconsin Hospitals and Clinics 2007. Abraxane<sup>®</sup> Paclitaxel Protein-Bound Particles. Pharmacy Society of Wisconsin. [http://www.nm-pharmacy.com/Rx\\_Publications/iRx\\_-\\_New\\_Mexico/iRx-NewMexico-Abraxane.pdf](http://www.nm-pharmacy.com/Rx_Publications/iRx_-_New_Mexico/iRx-NewMexico-Abraxane.pdf). March 1, 2013.
241. De Smet L, Colin P, Ceelen W, Bracke M, Van Bocxlaer J, Remon JP, Vervaet C (2012). Development of a nanocrystalline paclitaxel formulation for HIPEC treatment. *Pharmaceutical Research*, 29, 2398-2406.
242. Liu F, Park J-Y, Zhang Y, Conwell C, Liu Y, Bathula SR, Huang L (2010). Targeted cancer therapy with novel high drug-loading nanocrystals. *Journal of Pharmaceutical Sciences*, 99, 3542-3551.
243. Wani MC, Taylor HL, Wall ME, Coggon P, McPhail AT (1971). Plant antitumor agents .6. Isolation and structure of Taxol, a novel antileukemic and antitumor agent from *Taxus-Brevifolia*. *Journal of the American Chemical Society*, 93, 2325-&.

244. Schiff PB, Fant J, Horwitz SB (1979). Promotion of microtubule assembly in vitro by Taxol. *Nature*, 277, 665-667.
245. Singla AK, Garg A, Aggarwal D (2002). Paclitaxel and its formulations. *International Journal of Pharmaceutics*, 235, 179-192.
246. Liu Y, Huang L, Liu F (2010). Paclitaxel nanocrystals for overcoming multidrug resistance in cancer. *Molecular Pharmaceutics*, 7, 863-869.
247. Yuan F, Dellian M, Fukumura D, Leunig M, Berk DA, Torchilin VP, Jain RK (1995). Vascular-permeability in a human tumor xenograft - molecular-size dependence and cutoff size. *Cancer Research*, 55, 3752-3756.
248. Tian J, Stella VJ (2008). Degradation of paclitaxel and related compounds in aqueous solutions II: Nonpimerization degradation under neutral to basic pH conditions. *Journal of Pharmaceutical Sciences*, 97, 3100-3108.
249. Reddy SR, Fogler HS (1980). Emulsion stability of acoustically formed emulsions. *Journal of Physical Chemistry*, 84, 1570-1575.
250. Liggins RT, Hunter WL, Burt HM (1997). Solid-state characterization of paclitaxel. *Journal of Pharmaceutical Sciences*, 86, 1458-1463.
251. Grant DJW, Brittain HG, Solubility of Pharmaceutical Solids, In *Physical Characterization of Pharmaceutical Solids, Drugs, and the Pharmaceutical Sciences*, ed. Brittain, HG, Marcel Dekker, Inc., New York, 1995, 321-386.
252. Paal K, Muller J, Hegedus L (2001). High affinity binding of paclitaxel to human serum albumin. *European Journal of Biochemistry*, 268, 2187-2191.

253. Park Y, Franses EI (2010). Effect of a PEGylated lipid on the dispersion stability and dynamic surface tension of aqueous DPPC and on the interactions with albumin. *Langmuir*, 26, 6932-6942.
254. Tian J, Stella VJ (2008). Degradation of paclitaxel and related compounds in aqueous solutions I: Epimerization. *Journal of Pharmaceutical Sciences*, 97, 1224-1235.
255. Tian JH, Stella VJ (2010). Degradation of Paclitaxel and Related Compounds in Aqueous Solutions III: Degradation Under Acidic pH Conditions and Overall Kinetics. *Journal of Pharmaceutical Sciences*, 99, 1288-1298.
256. Dordunoo SK, Burt HM (1996). Solubility and stability of taxol: Effects of buffers and cyclodextrins. *International Journal of Pharmaceutics*, 133, 191-201.
257. Aderem A, Underhill DM (1999). Mechanisms of phagocytosis in macrophages. *Annual Review of Immunology*, 17, 593-623.
258. Rabinovitch M (1995). Professional and nonprofessional phagocytes - An introduction. *Trends in Cell Biology*, 5, 85-87.
259. Iversen T-G, Skotland T, Sandvig K (2011). Endocytosis and intracellular transport of nanoparticles: Present knowledge and need for future studies. *Nano Today*, 6, 176-185.
260. Sahay G, Alakhova DY, Kabanov AV (2010). Endocytosis of nanomedicines. *Journal of Controlled Release*, 145, 182-195.
261. Hillaireau H, Couvreur P (2009). Nanocarriers' entry into the cell: relevance to drug delivery. *Cellular and Molecular Life Sciences*, 66, 2873-2896.

262. Mercer J, Helenius A (2009). Virus entry by macropinocytosis. *Nature Cell Biology*, 11, 510-520.
263. Conner SD, Schmid SL (2003). Regulated portals of entry into the cell. *Nature*, 422, 37-44.
264. Mayor S, Pagano RE (2007). Pathways of clathrin-independent endocytosis. *Nature Reviews Molecular Cell Biology*, 8, 603-612.
265. Chithrani BD, Ghazani AA, Chan WCW (2006). Determining the size and shape dependence of gold nanoparticle uptake into mammalian cells. *Nano Letters*, 6, 662-668.
266. Muro S, Garnacho C, Champion JA, Leferovich J, Gajewski C, Schuchman EH, Mitragotri S, Muzykantov VR (2008). Control of endothelial targeting and intracellular delivery of therapeutic enzymes by modulating the size and shape of ICAM-1-targeted carriers. *Molecular Therapy*, 16, 1450-1458.
267. Gratton SEA, Napier ME, Ropp PA, Tian S, DeSimone JM (2008). Microfabricated particles for engineered drug therapies: Elucidation into the mechanisms of cellular internalization of PRINT particles. *Pharmaceutical Research*, 25, 2845-2852.
268. Gratton SEA, Ropp PA, Pohlhaus PD, Luft JC, Madden VJ, Napier ME, DeSimone JM (2008). The effect of particle design on cellular internalization pathways. *Proceedings of the National Academy of Sciences of the United States of America*, 105, 11613-11618.
269. Park JW, Kim Y, Lee K-J, Kim DJ (2012). Novel cyanine dyes with vinylsulfone group for labeling biomolecules. *Bioconjugate Chemistry*, 23, 350-362.

270. Voigt W, Sulforhodamine B assay and chemosensitivity ed. Blumenthal, RD, Humana Press, 2005, 39-48.
271. Chou TC, Zhang XG, Harris CR, Kuduk SD, Balog A, Savin KA, Bertino JR, Danishefsky SJ (1998). Desoxyepothilone B is curative against human tumor xenografts that are refractory to paclitaxel. *Proceedings of the National Academy of Sciences of the United States of America*, 95, 15798-15802.
272. Meng H, Yang S, Li Z, Xia T, Chen J, Ji Z, Zhang H, Wang X, Lin S, Huang C, Zhou ZH, Zink JJ, Nel AE (2011). Aspect ratio determines the quantity of mesoporous silica nanoparticle uptake by a small GTPase-dependent macropinocytosis mechanism. *Acs Nano*, 5, 4434-4447.
273. Jones AT (2007). Macropinocytosis: searching for an endocytic identity and role in the uptake of cell penetrating peptides. *Journal of Cellular and Molecular Medicine*, 11, 670-684.
274. Zauner W, Farrow NA, Haines AMR (2001). In vitro uptake of polystyrene microspheres: effect of particle size, cell line and cell density. *Journal of Controlled Release*, 71, 39-51.
275. Saovapakhiran A, D'Emanuele A, Attwood D, Penny J (2009). Surface modification of PAMAM dendrimers modulates the mechanism of cellular internalization. *Bioconjugate Chemistry*, 20, 693-701.
276. Wang CH, Chang CW, Peng CA (2011). Gold nanorod stabilized by thiolated chitosan as photothermal absorber for cancer cell treatment. *Journal of Nanoparticle Research*, 13, 2749-2758.

277. Hatakeyama H, Akita H, Kogure K, Oishi M, Nagasaki Y, Kihira Y, Ueno M, Kobayashi H, Kikuchi H, Harashima H (2007). Development of a novel systemic gene delivery system for cancer therapy with a tumor-specific cleavable PEG-lipid. *Gene Therapy*, 14, 68-77.
278. Hatakeyama H, Akita H, Harashima H (2011). A multifunctional envelope type nano device (MEND) for gene delivery to tumours based on the EPR effect: A strategy for overcoming the PEG dilemma. *Advanced Drug Delivery Reviews*, 63, 152-160.
279. Kelkar SS, Reineke TM (2011). Theranostics: Combining Imaging and Therapy. *Bioconjugate Chemistry*, 22, 1879-1903.
280. Kozlowski JM, Fidler IJ, Campbell D, Xu ZL, Kaighn ME, Hart IR (1984). Metastatic behavior of human-tumor cell-lines grown in the nude-mouse. *Cancer Research*, 44, 3522-3529.
281. Morikawa K, Walker SM, Nakajima M, Pathak S, Jessup JM, Fidler IJ (1988). Influence of organ environment on the growth, selection, and metastasis of human-colon carcinoma-cells in nude-mice. *Cancer Research*, 48, 6863-6871.
282. Volpe JPG, Milas L (1990). Influence of tumor-transplantation methods on tumor-growth rate and metastatic potential of solitary tumors derived from metastases. *Clinical & Experimental Metastasis*, 8, 381-389.
283. Meyvisch C (1983). Influence of implantation site on formation of metastases. *Cancer and Metastasis Reviews*, 2, 295-306.
284. Singer CF, Kronsteiner N, Marton E, Kubista M, Cullen KJ, Hirtenlehner K, Seifert M, Kubista E (2002). MMP-2 and MMP-9 expression in breast cancer-

- derived human fibroblasts is differentially regulated by stromal-epithelial interactions. *Breast Cancer Research and Treatment*, 72, 69-77.
285. Poulson R, Hanby AM, Pignatelli M, Jeffery RE, Longcroft JM, Rogers L, Stamp GW (1993). Expression of gelatinase A and TIMP-2 mRNAs in desmoplastic fibroblasts in both mammary carcinomas and basal cell carcinomas of the skin. *J Clin Pathol*, 46, 429-436.
286. Iwata H, Kobayashi S, Iwase H, Masaoka A, Fujimoto N, Okada Y (1996). Production of matrix metalloproteinases and tissue inhibitors of metalloproteinases in human breast carcinomas. *Jpn J Cancer Res*, 87, 602-611.
287. Clapper ML, Hensley HH, Chang WC, Devarajan K, Nguyen MT, Cooper HS (2011). Detection of colorectal adenomas using a bioactivatable probe specific for matrix metalloproteinase activity. *Neoplasia*, 13, 685-691.
288. Keren S, Gheysens O, Levin CS, Gambhir SS (2008). A Comparison Between a Time Domain and Continuous Wave Small Animal Optical Imaging System. *Medical Imaging, IEEE Transactions on*, 27, 58-63.
289. Communication with Perkin Elmer indicates that the MMPsense 750 FAST is negatively charged. Jan 31, 2013.
290. Weissleder R, Tung CH, Mahmood U, Bogdanov A (1999). *In vivo* imaging of tumors with protease-activated near-infrared fluorescent probes. *Nature Biotechnology*, 17, 375-378.
291. Groves K, Kossodo S, Handy E, Jensen J, Blusztajn A, Cuneo G, Peterson JD, Rajopadhye M. 2009. *In vivo* imaging of treatment effects using a novel near

- infrared labeled agent: MMPSense™ 750 FAST. In *AACR Annual Meeting*. Denver.
292. Kleiner DE, Stetler-Stevenson WG (1999). Matrix metalloproteinases and metastasis. *Cancer Chemotherapy and Pharmacology*, 43, S42-S51.
293. Maeda H, Fang J, Inutsuka T, Kitamoto Y (2003). Vascular permeability enhancement in solid tumor: various factors, mechanisms involved and its implications. *International Immunopharmacology*, 3, 319-328.
294. Nagamitsu A, Greish K, Maeda H (2009). Elevating blood pressure as a strategy to increase tumor-targeted delivery of macromolecular drug SMANCS: Cases of advanced solid tumors. *Japanese Journal of Clinical Oncology*, 39, 756-766.
295. Maki S, Konno T, Maeda H (1985). Image-enhancement in computerized-tomography for sensitive diagnosis of liver-cancer and semiquantitation of tumor selective drug targeting with oily contrast-medium. *Cancer*, 56, 751-757.
296. Maeda H (2010). Nitroglycerin enhances vascular blood flow and drug delivery in hypoxic tumor tissues: Analogy between angina pectoris and solid tumors and enhancement of the EPR effect. *Journal of Controlled Release*, 142, 296-298.
297. Suzuki M, Hori K, Abe I, Saito S, Sato H (1981). A new approach to cancer-chemotherapy - selective enhancement of tumor blood-flow with angiotensin-II. *Journal of the National Cancer Institute*, 67, 663-669.
298. Hori K, Suzuki M, Tanda S, Saito S, Shinozaki M, Zhang QH (1991). Fluctuations in tumor blood-flow under normotension and the effect of antiotensin-II-induced hypertension. *Japanese Journal of Cancer Research*, 82, 1309-1316.

299. Hori K, Saito S, Takahashi H, Sato H, Maeda H, Sato Y (2000). Tumor-selective blood flow decrease induced by an angiotensin converting enzyme inhibitor, temocapril hydrochloride. *Japanese Journal of Cancer Research*, 91, 261-269.
300. Li CJ, Miyamoto Y, Kojima Y, Maeda H (1993). AUGMENTATION OF TUMOR DELIVERY OF MACROMOLECULAR DRUGS WITH REDUCED BONE-MARROW DELIVERY BY ELEVATING BLOOD-PRESSURE. *British Journal of Cancer*, 67, 975-980.
301. Feelisch M, Noack EA (1987). Correlation between nitric-oxide formation during degradation of organic nitrates and activation of guanylate-cyclase. *European Journal of Pharmacology*, 139, 19-30.
302. Mitchell JB, Wink DA, Degraff W, Gamson J, Keefer LK, Krishna MC (1993). Hypoxic mammalian-cell radiosensitization by nitric-oxide. *Cancer Research*, 53, 5845-5848.
303. Seki T, Fang J, Maeda H (2009). Enhanced delivery of macromolecular antitumor drugs to tumors by nitroglycerin application. *Cancer Science*, 100, 2426-2430.
304. Piao YJ, Choi JS (2008). Effects of morin on the pharmacokinetics of nicardipine after oral and intravenous administration of nicardipine in rats. *Journal of Pharmacy and Pharmacology*, 60, 625-629.
305. Sarkadi B, Szakacs G (2010). Understanding transport through pharmacological barriers - are we there yet? *Nature Reviews Drug Discovery*, 9.
306. Iwai K, Maeda H, Konno T (1984). Use of oily contrast-medium for selective drug targeting to tumor-enhanced therapeutic effect and X-ray Image. *Cancer Research*, 44, 2115-2121.

307. Konno T, Maeda H, Iwai K, Maki S, Tashiro S, Uchida M, Miyauchi Y (1984). SELECTIVE TARGETING OF ANTI-CANCER DRUG AND SIMULTANEOUS IMAGE-ENHANCEMENT IN SOLID TUMORS BY ARTERIALLY ADMINISTERED LIPID CONTRAST-MEDIUM. *Cancer*, 54, 2367-2374.
308. Maeda H (2001). SMANCS and polymer-conjugated macromolecular drugs: advantages in cancer chemotherapy. *Advanced Drug Delivery Reviews*, 46, 169-185.
309. Yang Z, Leon J, Martin M, Harder JW, Zhang R, Liang D, Lu W, Tian M, Gelovani JG, Qiao A, Li C (2009). Pharmacokinetics and biodistribution of near-infrared fluorescence polymeric nanoparticles. *Nanotechnology*, 20.
310. de la Zerda A, Bodapati S, Teed R, Schipper ML, Keren S, Smith BR, Ng JST, Gambhir SS (2010). A comparison between time domain and spectral imaging systems for imaging quantum dots in small living animals. *Molecular Imaging and Biology*, 12, 500-508.
311. Keren S, Gheysens O, Levin CS, Gambhir SS (2008). A comparison between a time domain and continuous wave small animal optical imaging system. *Ieee Transactions on Medical Imaging*, 27, 58-63.
312. Leblond F, Davis SC, Valdes PA, Pogue BW (2010). Pre-clinical whole-body fluorescence imaging: Review of instruments, methods and applications. *Journal of Photochemistry and Photobiology B-Biology*, 98, 77-94.

313. Ntziachristos V, Bremer C, Weissleder R (2003). Fluorescence imaging with near-infrared light: new technological advances that enable in vivo molecular imaging. *European Radiology*, 13, 195-208.
314. Stuker F, Ripoll J, Rudin M (2011). Fluorescence molecular tomography: Principles and potential for pharmaceutical research. *Pharmaceutics*, 3, 229-274.
315. Ntziachristos V, Weissleder R (2001). Experimental three-dimensional fluorescence reconstruction of diffuse media by use of a normalized Born approximation. *Optics Letters*, 26, 893-895.
316. Graves EE, Ripoll J, Weissleder R, Ntziachristos V (2003). A submillimeter resolution fluorescence molecular imaging system for small animal imaging. *Med Phys*, 30, 901-911.
317. Elson D, Requejo-Isidro J, Munro I, Reavell F, Siegel J, Suhling K, Tadrous P, Benninger R, Lanigan P, McGinty J, Talbot C, Treanor B, Webb S, Sandison A, Wallace A, Davis D, Lever J, Neil M, Phillips D, Stamp G, French P (2004). Time-domain fluorescence lifetime imaging applied to biological tissue. *Photochemical & Photobiological Sciences*, 3, 795-801.
318. Kumar ATN, Skoch J, Bacsikai BJ, Boas DA, Dunn AK (2005). Fluorescence-lifetime-based tomography for turbid media. *Optics Letters*, 30, 3347-3349.
319. Lee J, Sevick-Muraca EM (2002). Three-dimensional fluorescence enhanced optical tomography using referenced frequency-domain photon migration measurements at emission and excitation wavelengths. *Journal of the Optical Society of America a-Optics Image Science and Vision*, 19, 759-771.

320. Ait-Oudhia S, Straubinger RM, Mager DE (2012). Meta-analysis of nanoparticulate paclitaxel delivery system pharmacokinetics and model prediction of associated neutropenia. *Pharmaceutical Research*, 29, 2833-2844.
321. Sparreboom A, vanTellingen O, Nooijen WJ, Beijnen JH (1996). Nonlinear pharmacokinetics of paclitaxel in mice results from the pharmaceutical vehicle Cremophor EL. *Cancer Research*, 56, 2112-2115.
322. Eiseman JL, Eddington ND, Leslie J, Macauley C, Sentz DL, Zuhowski M, Kujawa JM, Young D, Egorin MJ (1994). Plasma pharmacokinetics and tissue distribution of paclitaxel in CD2F1 mice. *Cancer Chemotherapy and Pharmacology*, 34, 465-471.
323. Sparreboom A, vanTellingen O, Nooijen WJ, Beijnen JH (1996). Tissue distribution, metabolism and excretion of paclitaxel in mice. *Anti-Cancer Drugs*, 7, 78-86.
324. Gref R, Minamitake Y, Peracchia MT, Trubetskoy V, Torchilin V, Langer R (1994). Biodegradable long-circulating polymeric nanospheres. *Science*, 263, 1600-1603.
325. Rabinow B, Kipp J, Papadopoulos P, Wong J, Glosson J, Gass J, Sun CS, Wielgos T, White R, Cook C, Barker K, Wood K (2007). Itraconazole IV nanosuspension enhances efficacy through altered pharmacokinetics in the rat. *International Journal of Pharmaceutics*, 339, 251-260.
326. Frank MM, Fries LF (1991). The role of complement in inflammation and phagocytosis. *Immunology Today*, 12, 322-326.

327. Owens DE, Peppas NA (2006). Opsonization, biodistribution, and pharmacokinetics of polymeric nanoparticles. *International Journal of Pharmaceutics*, 307, 93-102.
328. Howard MD, Jay M, Dziublal TD, Lu XL (2008). PEGylation of nanocarrier drug delivery systems: State of the art. *Journal of Biomedical Nanotechnology*, 4, 133-148.
329. Frank MM, Fries LF (1991). The role of complement in inflammation and phagocytosis. *Immunology Today*, 12, 322-326.
330. Owens DE, Peppas NA (2006). Opsonization, biodistribution, and pharmacokinetics of polymeric nanoparticles. *Int. J. Pharm.*, 307, 93-102.
331. Wang YL, Li XM, Wang LY, Xu YL, Cheng XD, Wei P (2011). Formulation and pharmacokinetic evaluation of a paclitaxel nanosuspension for intravenous delivery. *Int. J. Nanomed.*, 6, 1497-1507.
332. Gao L, Zhang DR, Chen MH, Duan CX, Dai WT, Jia LJ, Zhao WF (2008). Studies on pharmacokinetics and tissue distribution of oridonin nanosuspensions. *Int. J. Pharm.*, 355, 321-327.
333. Ganta S, Paxton JW, Baguley BC, Garg S (2009). Formulation and pharmacokinetic evaluation of an asulacrine nanocrystalline suspension for intravenous delivery. *Int. J. Pharm.*, 367, 179-186.
334. Fujii T, Tachibana M, Dhar DK, Ueda S, Kinugasa S, Yoshimura H, Kohno H, Nagasue N (2003). Combination therapy with paclitaxel and thalidomide inhibits angiogenesis and growth of human colon cancer xenograft in mice. *Anticancer Research*, 23, 2405-2411.

335. Fujii T, Tachibana M, Dhar DK, Ueda S, Kinugasa S, Yoshimura H, Kohno H, Nagasue N (2003). Combination therapy with paclitaxel and thalidomide inhibits angiogenesis and growth of human colon cancer xenograft in mice. *Anticancer Research*, 23, 2405-2411.
336. Moghimi SM, Hunter AC, Murray JC (2001). Long-circulating and target-specific nanoparticles: Theory to practice. *Pharmacol. Rev.*, 53, 283-318.
337. Du SZ, Zhu L, Du B, Shi XF, Zhang ZZ, Wang SY, Zhang CF (2012). Pharmacokinetic evaluation and antitumor activity of 2-methoxyestradiol nanosuspension. *Drug Dev. Ind. Pharm.*, 38, 431-438.
338. Hao LL, Wang XY, Zhang DR, Xu QY, Song SY, Wang FH, Li CY, Guo HJ, Liu Y, Zheng DD, Zhang Q (2012). Studies on the preparation, characterization and pharmacokinetics of Amoitone B nanocrystals. *Int. J. Pharm.*, 433, 157-164.
339. Liu Y, Tseng Y-c, Huang L (2012). Biodistribution studies of nanoparticles using fluorescence imaging: A qualitative or quantitative method? *Pharm. Res.*, 29, 3273-3277.
340. Hilderbrand SA, Weissleder R (2010). Near-infrared fluorescence: application to *in vivo* molecular imaging. *Curr. Opin. Chem. Biol.*, 14, 71-79.
341. Pham W, Medarova Z, Moore A (2005). Synthesis and application of a water-soluble near-infrared dye for cancer detection using optical imaging. *Bioconj. Chem.*, 16, 735-740.
342. Fuhrmann K, Schulz JD, Gauthier MA, Leroux JC (2012). PEG nanocages as non-sheddable stabilizers for drug nanocrystals. *Acs Nano*, 6, 1667-1676.

343. Sharma P, Brown S, Walter G, Santra S, Moudgil B (2006). Nanoparticles for bioimaging. *Advances in Colloid and Interface Science*, 123–126, 471-485.
344. Sukhanova A, Nabiev I (2008). Fluorescent nanocrystal-encoded microbeads for multiplexed cancer imaging and diagnosis. *Critical Reviews in Oncology Hematology*, 68, 39-59.
345. Weng KC, Noble CO, Papahadjopoulos-Sternberg B, Chen FF, Drummond DC, Kirpotin DB, Wang DH, Hom YK, Hann B, Park JW (2008). Targeted tumor cell internalization and imaging of multifunctional quantum dot-conjugated immunoliposomes in vitro and in vivo. *Nano Letters*, 8, 2851-2857.
346. Basu S, Li GM, Alavi A (2009). PET and PET-CT imaging of gynecological malignancies: present role and future promise. *Expert Review of Anticancer Therapy*, 9, 75-96.
347. Choi HJ, Ju W, Myung SK, Kim Y (2010). Diagnostic performance of computer tomography, magnetic resonance imaging, and positron emission tomography or positron emission tomography/computer tomography for detection of metastatic lymph nodes in patients with cervical cancer: Meta-analysis. *Cancer Science*, 101, 1471-1479.
348. Weber WA, Grosu AL, Czernin J (2008). Technology insight: advances in molecular imaging and an appraisal of PET/CT scanning. *Nature Clinical Practice Oncology*, 5, 160-170.
349. Christiansen C (2005). X-ray contrast media - an overview. *Toxicology*, 209, 185-187.

350. Eck W, Nicholson AI, Zentgraf H, Semmler W, Bartling S (2010). Anti-CD4-targeted gold nanoparticles induce specific contrast enhancement of peripheral lymph nodes in X-ray computed tomography of live mice. *Nano Letters*, 10, 2318-2322.
351. Katayama H, Yamaguchi K, Kozuka T, Takashima T, Seez P, Matsuura K (1990). Adverse reactions to ionic and nonionic contrast-media - A report from the Japanese-committee-on-the-safety-of-contrast media. *Radiology*, 175, 621-628.
352. Hosoya T, Yamaguchi K, Akutsu T, Mitsuhashi Y, Kondo S, Sugai Y, Adachi M (2000). Delayed adverse reactions to iodinated contrast media and their risk factors. *Radiation Medicine*, 18, 39-45.
353. Hainfeld JF, Slatkin DN, Focella TM, Smilowitz HM (2006). Gold nanoparticles: a new X-ray contrast agent. *British Journal of Radiology*, 79, 248-253.
354. Hainfeld JF, Slatkin DN, Smilowitz HM (2004). The use of gold nanoparticles to enhance radiotherapy in mice. *Physics in Medicine and Biology*, 49, N309-N315.
355. Garcia-Fuentes M, Alonso MJ, Torres D (2005). Design and characterization of a new drug nanocarrier made from solid-liquid lipid mixtures. *Journal of Colloid and Interface Science*, 285, 590-598.
356. Sriram D, Yogeeswari P, Thirumurugan R, Bal TR (2005). Camptothecin and its analogues: a review on their chemotherapeutic potential. *Natural Product Research*, 19, 393-412.
357. Garcia-Carbonero R, Supko JG (2002). Current perspectives on the clinical experience, pharmacology, and continued development of the camptothecins. *Clinical Cancer Research*, 8, 641-661.

358. Adams VR, Burke TG, *Camptothecin in Cancer Therapy*, Humana Press Inc. Danvers, MA, 2005.
359. Chen WX, Bardhan R, Bartels M, Perez-Torres C, Pautler RG, Halas NJ, Joshi A (2010). A molecularly targeted theranostic probe for ovarian cancer. *Molecular Cancer Therapeutics*, 9, 1028-1038.
360. Guo R, Li RT, Li XL, Zhang LY, Jiang XQ, Liu BR (2009). Dual-functional alginic acid hybrid nanospheres for cell imaging and drug delivery. *Small*, 5, 709-717.
361. McFarland AD, Haynes CL, Mirkin CA, Van Duyne RP, Godwin HA (2004). Color my nanoworld. *Journal of Chemical Education*, 81, 544A.
362. Liu YL, Shipton MK, Ryan J, Kaufman ED, Franzen S, Feldheim DL (2007). Synthesis, stability, and cellular internalization of gold nanoparticles containing mixed peptide-poly(ethylene glycol) monolayers. *Analytical Chemistry*, 79, 2221-2229.
363. Dilmanian FA, Wu XY, Parsons EC, Ren B, Kress J, Button TM, Chapman LD, Coderre JA, Giron F, Greenberg D, Krus DJ, Liang Z, Marcovici S, Petersen MJ, Roque CT, Shleifer M, Slatkin DN, Thomlinson WC, Yamamoto K, Zhong Z (1997). Single- and dual-energy CT with monochromatic synchrotron x-rays. *Physics in Medicine and Biology*, 42, 371-387.
364. Eck W, Nicholson AI, Zentgraf H, Semmler W, Bartling S (2010). Anti-CD4-targeted Gold Nanoparticles Induce Specific Contrast Enhancement of Peripheral Lymph Nodes in X-ray Computed Tomography of Live Mice. *Nano Letters*, 10, 2318-2322.

365. Rychahou PG, Jackson LN, Silva SR, Rajaraman S, Evers BM (2006). Targeted molecular therapy of the PI3K pathway - Therapeutic significance of PI3K subunit targeting in colorectal carcinoma. *Annals of Surgery*, 243, 833-844.
366. Johnson SM, Gulhati P, Rampy BA, Han Y, Rychahou PG, Doan HQ, Weiss HL, Evers BM (2010). Novel Expression Patterns of PI3K/Akt/mTOR Signaling Pathway Components in Colorectal Cancer. *Journal of the American College of Surgeons*, 210, 767-776.
367. Yaguchi SI, Fukui Y, Koshimizu K, Yoshimi H, Matsuno T, Gouda H, Hirono S, Yamazaki K, Yamori T (2006). Antitumor activity of ZSTK474, a new phosphatidylinositol 3-kinase inhibitor. *Journal of the National Cancer Institute*, 98, 545-556.
368. Yamori T, Matsunaga A, Sato S, Yamazaki K, Komi A, Ishizu K, Mita I, Edatsugi H, Matsuba Y, Takezawa K, Nakanishi O, Kohno H, Nakajima Y, Komatsu H, Andoh T, Tsuruo T (1999). Potent antitumor activity of MS-247, a novel DNA minor groove binder, evaluated by an in vitro and in vivo human cancer cell line panel. *Cancer Research*, 59, 4042-4049.

## VITA

### CHRISTIN PRAMUDIATI HOLLIS

Birthplace: Semarang, Indonesia

#### EDUCATION

2001 – 2006      B.S. in Chemical Engineering, University of Kentucky, Lexington, KY

#### PROFESSIONAL EXPERIENCES

2012 – present    Development Scientist, Catalent Pharma Solutions, Winchester, KY  
2007 – 2012      Research Assistant – University of Kentucky, College of Pharmacy  
2006 – 2007      Teaching Assistant – University of Kentucky, College of Pharmacy  
2005 – 2006      Undergraduate Research – University of Kentucky, Department of  
Chemical Engineering  
2003 – 2004      Industrial Internship – ISP Chemical Inc., Calvert City, KY

#### HONORS AND AWARDS

- ◆ NCI Cancer Nanotechnology Training Center (CNTC) Predoctoral Fellow (2010-2012)
- ◆ Physical Pharmacy and Biopharmaceutics (PPB) Section of American Association of Pharmaceutical Scientists (AAPS) Travel Award (2008)
- ◆ NSF Integrative Graduate Education and Research Traineeship (IGERT) Fellow (2007-2009)
- ◆ Runner up, Physical and Engineering Sciences category, University of Kentucky Oswald Research and Creativity Program (2006)
- ◆ University of Kentucky Nanoscale Engineering Certificate Program (NECP) Fellowship (2005)

## PATENT

Arsenescu, R.; Hilt, J.Z.; and **Pramudiati, C.** US Patent Application Serial Number 60/863,777 (Patent Pending): Biodegradable PLGA seton for Crohn's disease treatment.

## PUBLICATIONS

**Hollis, C.P.**; Weiss, H.L.; Evers, B.M.; Gemeinhart, R.A.; Li, T. *In Vivo* Investigation of Hybrid Paclitaxel Nanocrystals with Dual Fluorescent Probes for Cancer Theranostics. *Pharmaceutical Research* **2013**, DOI: 10.1007/s 11095-013-1048-x.

**Hollis, C.P.**; Li, T. Nanocrystals: Production, Characterization, and Application for Cancer Therapy in *Nanoparticulate Drug Delivery Systems: Strategies, Technologies, and Applications*, ed. Y. Yeo, John Wiley and Sons, Inc.: Hoboken, NJ, 2013, 183-208.

Zhao, R.; **Hollis, C.P.**; Zhang, H.; Sun, L.; Gemeinhart, R.A.; Li, T. Hybrid Nanocrystals: Achieving Concurrent Therapeutic and Bioimaging Functionalities toward Solid Tumors. *Molecular Pharmaceutics* **2011**, 8(5), 1985-1991.

Zhang, H.; **Hollis, C.P.**; Zhang, Q.; Li, T. Preparation and Antitumor Study of Camptothecin Nanocrystals. *International Journal of Pharmaceutics* **2011**, 415, 293-300.

**Pramudiati, C.**; Hilt, J.Z. The Study of PLGA Drug Delivery Systems: Implication for Management of Crohn's Diseases. *Kaleidoscope, UK Journal of Undergraduate Scholarship* **2006**, 5, 41-47.

## PRESENTATIONS

**Hollis, C.P.**; Valentino, J.; Rychahou, P.; Evers, M.; Li, T. "Nanocrystals of PI3K and MEK Inhibitors for the Therapy of Colon Cancer." Poster at AAPS Annual Meeting, Washington, DC, Oct 23-27, 2011.

**Hollis, C.P.**; Zhao, R.; Zhang, H.; Sun, L.; Gemeinhart, R.; Li, T. "Development of Multifunctional Hybrid Nanocrystals for Cancer Therapy and Diagnosis." Poster at AAPS Annual Meeting, Washington, DC, Oct 23-27, 2011.

**Hollis, C.P.**; Dozier, A.; Knutson, B.; Li, T. "Preparation and Characterization of Multimodal Hybrid Nanocrystals of Camptothecin and Gold." Poster at AAPS Annual Meeting, Washington, DC, Oct 23-27, 2011.

**Hollis, C.P.**; Raetz, E.; Li, T. "Using Surface Energy of Eutectic Melt to Understand the Interaction between Eutectic Constituents." Poster at AAPS Annual Meeting, New Orleans, LA, Nov 14-18, 2010.

**Hollis, C.P.**; Mattei, A.; Li, T. "A Surface Energy Model of Eutectic Formation." Poster at AAPS Annual Meeting, Atlanta, GA, Nov 16-20, 2008.

- Hollis, C.P.;** Aubrey-Medendorp, C.; and Li, T. “Surface Energy Measurement of Acetaminophen Crystals with AFM.” Poster at AAPS Annual Meeting, San Diego, CA, Nov 11-15, 2007.
- Aubrey-Medendorp, C.; **Hollis, C.P.;** and Li, T. “A Novel Method for Measuring Surface Energy with the Atomic Force Microscope.” Poster at AAPS Annual Meeting, San Diego, CA, Nov 11-15, 2007.
- Patel, D.; **Hollis, C.P.;** and Jay, M. “Theophylline Molecularly Imprinted Polymer: Effect of Formulation Variables on its Binding to Theophylline.” Poster at AAPS Annual Meeting, San Diego, CA, Nov 11-15, 2007.
- Pramudiati, C.;** Arsenescu, R.; Hilt, J.Z. “Preparation and Analysis of a PLGA Drug Delivery System for Polyphenols.” Poster at American Institute of Chemical Engineers (AIChE) National Meeting, Cincinnati, OH, Oct 30 – Nov 4, 2005.